NUREG/CR--4295

TI91 009035

Bond Strength of Cementitious Borehole Plugs in Welded Tuff

Manuscript Completed: June 1990
Date Published: February 1991

Prepared by
H. Akgun, J. J. K. Daemen

Department of Mining and Geological Engineering
University of Arizona
Tucson, AZ 85721

Prepared for
Division of Engineering
Office of Nuclear Regulatory Research
U.S. Nuclear Regulatory Commission
Washington, DC 20555
NRC FIN D1192

DISCLAIMER

ABSTRACT

This study includes a systematic investigation of the bond strength of cementitious borehole plugs in welded tuff. Analytical and numerical analysis of borehole plug-rock stress transfer mechanics is performed. The interface strength and deformation are studied as a function of Young's modulus ratio of plug and rock, plug length and rock cylinder outside-to-inside radius ratio. The tensile stresses in and near an axially loaded plug are analyzed. The frictional interface strength of an axially loaded borehole plug, the effect of axial stress and lateral external stress, and thermal effects are also analyzed. Implications for plug design are discussed. The main conclusion is a strong recommendation to design friction plugs in shafts, drifts, tunnels or boreholes with a minimum length to diameter ratio of four. Such a geometrical design will reduce tensile stresses in the plug and in the host rock to a level which should minimize the risk of long-term deterioration caused by excessive tensile stresses.

Push-out tests have been used to determine the bond strength by applying an axial load to cement plugs emplaced in boreholes in welded tuff cylinders. A total of 130 push-out tests have been performed as a function of borehole size, plug length, temperature, and degree of saturation of the host tuff. The use of four different borehole radii enables evaluation of size effects. A well-defined exponential strength decrease with increasing plug diameter results. While these extrapolated strengths can be used for the design of large diameter plugs, e.g. in shafts or drifts, it would be desirable to confirm the extrapolations by tests on larger plugs.

TABLE OF CONTENTS

TABLE OF CONTENTS--Continued

(cont.)

TABLE OF CONTENTS--Continued

TABLE OF CONTENTS--Continued

LIST OF FIGURES

LIST OF FIGURES--Continued

LIST OF FIGURES--Continued

LIST OF FIGURES--Continued

LIST OF TABLES

LIST OF TABLES--Continued

ACKNOWLEDGMENTS

The research reported on has been performed by the University of Arizona, Department of Mining and Geological Engineering, for the U.S. Nuclear Regulatory Commission (NRC). Project monitor for the NRC is Mr. Jacob Philip. The project is under Mr. M. Silberberg, Chief, Waste Management Branch, Division of Engineering, Office of Nuclear Regulatory Research.

Dr. Jaak J.K. Daemen, Associate Professor, Department of Mining and Geological Engineering, University of Arizona, is the Principal Investigator. Dr. James G. McCray, Acting Director, Nuclear Fuel Cycle Research Program, Department of Nuclear and Energy Engineering, University of Arizona, has provided project management assistance and nuclear waste technical assistance. Haluk Akgun has performed the theoretical and experimental work as part of his Ph.D. degree requirements. Experimental assistance has been provided by Robert Morgan. Mike Porter has typed, assembled, and produced the report.

We gratefully acknowledge the assistance of Dowell-Schlumberger in donating cement and additives, and especially the technical help provided by Dr. P. Parcevaux, Dr. Ruediger Oberste-Padtberg and Mr. Tom Griffin.

We gratefully acknowledge the cooperation of Magma Copper Co., and in particular of Mr. Frank Florez, in providing access to their Superior, AZ, property and for allowing us to collect tuff blocks.

LIST OF SYMBOLS

Roman Letter Symbols

a = plug radius

A, B = integration constants

A_p, A_R = plug and rock cross-sectional area

A_s = effective pile surface area

b_i = effective interface width

c = cohesion

c_p, c_r = peak and residual cohesion along plug/rock interface, respectively

c_2 = y-intercept of the second stage of the bond stress-slip curve

dz, dz_t = element thickness

e_p, e_f = void ratio of push-out cylinder prior to and following push-out test, respectively

E, E_p = Young's modulus of plug

E', E_R = Young's modulus of rock

E_s, ν_s = Young's modulus and Poisson's ratio of steel pipe, respectively

f_s = skin friction

G_i and G_R = shear modulus of the interface and rock, respectively

H = geometric constant

I_z, I_c = normalization factors due to an axial stress applied to the plug and lateral stress, respectively

k_s = spring constant

K = coefficient of lateral earth pressure

K_o = coefficient of lateral earth pressure at rest

L, L_c = plug or pile length

L_h = length of top borehole

L_r = length of rock core

m_1, m_2 = slopes of the first and second stages of the bond stress-slip curve, respectively

n_p, n_f = porosity of push-out cylinder prior to and following push-out test, respectively

P_1, P_2 = applied internal and external radial stress, respectively

P_{po} = axial force applied to the plug

$P_{max}^{\Delta T}$ = maximum axial thermal force in rock and plug due to temperature increase

P_{pz}, P_{rz} = axial force in plug and rock cylinder at a distance z from initial location of loaded end of plug

P_s = pile skin resistance capacity

$P_{pz}^{\Delta T}$, $P_{rz}^{\Delta T}$ = axial force in plug and rock due to elevated temperature

$\frac{dP_{pz}^{\Delta T}}{dz_t}dz_t$, $\frac{dP_{rz}^{\Delta T}}{dz_t}dz_t$ = axial thermal force increment within plug and rock due to a temperature increase over section dz_t, respectively

$\frac{dP_{pz}}{dz}dz$ = axial force increment within plug (over section dz) due to an axial stress applied to the plug

$P_{pz,u}$ and $P_{pz,l}$ = axial force acting above and below plug section dz

$P_{rz,u}$ and $P_{rz,l}$ = axial force acting above and below rock section dz

q_s = surcharge

$\bar{q}$ = average vertical stress acting on pile element of length ΔL

r = radial coordinate

r_i, r_o = inside and outside radius, respectively

r_m = effective radius

R = rock radius

s_u = undrained shear strength

S_p, S_f = degree of saturation of push-out cylinder prior to and following push-out test, respectively

T_{rz} = shear force

u, l = subscripts referring to upper and lower, respectively

u, v, w = displacement components in the r, θ, and z directions

u_p, u_R = radial displacement of plug and rock

$u_{p,c}$ = radial (inward) displacement of plug due to an applied lateral external stress

$u_{p,z}$ = radial (outward) displacement of plug due to an applied axial stress

$u_{p,o}^{\Delta T}$ = the (outward) radial displacement on the outside periphery of an unconstrained cement plug due to temperature increase

$u_{p,i}^{\Delta T}$ = the (inward) radial displacement on the outside periphery of an unconstrained cement plug due to a compressive radial stress

$u_p^{\Delta T}$ = resultant radial displacement on the outside periphery of a cement plug emplaced in a rock core due to temperature increase

$u_R^{\Delta T}$ = resultant radial displacement on the inside periphery of a plugged rock core due to temperature increase

$u_{r,o}^{\Delta T}$ = the (outward) radial displacement on the inside periphery of an unconstrained rock cylinder due to temperature increase

$u_{r,i}^{\Delta T}$ = the (outward) radial displacement on the inside periphery of a plugged rock cylinder due to compressive radial stress resulting from plug-rock interaction

VSF = vertical stress function

w_{max} = resultant maximum axial plug displacement due to an axial stress applied to the plug and due to temperature increase

w_p, w_R = vertical displacement of plug and rock

w_p, w_f = water content of push-out cylinder prior to and following push-out test, respectively

w_p^r = vertical displacement of a rigid plug

$w_{p.T}^{\Delta T}$, $w_{R.T}^{\Delta T}$ = total axial displacement of plug and rock due to temperature increase

$\frac{dw_p}{dz}dz$ = axial plug displacement increment within plug (over section dz) due to an axial stress applied to the plug

w_{po} = axial plug displacement at the loaded end of plug

$w_{P,R}$ = resultant axial plug displacement due to an axial stress applied to the plug and due to temperature increase

w_T = vertical linear deformation due to temperature change

$W_3, W_6, W_9, W_{14f}, W_{18}$ = weight parameters of push-out cylinders

z = distance from initial location of loaded end of plug

z_t = the coordinate along the axis of the plug of a push-out cylinder with origin at the symmetry plane

Greek Letter Symbols

$\alpha, \alpha_l, \beta, \lambda$ = coefficients used to calculate the interface shear stress distribution in a borehole plug-rock system

α = coefficient of linear thermal expansion

α, λ, β = empirical methods to determine the skin friction along an axially loaded pile

α_p, α_R = coefficient of linear thermal expansion of plug and rock

γ_{rz} = shear strain

γ_l = shear strain at the plug-rock interface

$\gamma_{l.\Delta T}$ = interface shear strain induced by temperature change

Δ = slip at plug-rock interface

Δ_0 = slip at the loaded end of plug

ΔL = embedment increment

ΔP_{pz} = net axial plug load over plug section dz

ΔT = temperature increase

δ = effective friction angle between soil and pile material

$\epsilon_r, \epsilon_\theta, \epsilon_z$ = radial, tangential and axial strain components

$\epsilon_r^p, \epsilon_\theta^p, \epsilon_z^p$ = radial, tangential and axial strains in plug

$\epsilon_p^{\Delta T}$, $\epsilon_R^{\Delta T}$ = total axial strain in plug and in rock due to a temperature increase, respectively

ϵ_z^R = vertical strain in rock

$\epsilon_{\theta(r-a)}$ = average induced tangential strain on the plug (steel pipe inside walls)

$\epsilon_{\theta(r-R)}$ = average induced tangential strain on the steel pipe outside walls

$d\epsilon_p^{\Delta T}$, $d\epsilon_R^{\Delta T}$ = axial strain increment in the plug and in the rock at section dz_t, due to a temperature increase, respectively

λ_R = Lame's constant for rock

ν_p, μ = Poisson's ratio of plug

ν_R, μ' = Poisson's ratio of rock

ρ_p, ρ_f = density of push-out cylinder prior to and following push-out test, respectively.

σ_i = radial stress at plug/rock interface due to an applied external stress

σ_0 = applied external lateral stress

σ_{po} = axial stress applied to plug

$\sigma_r, \sigma_\theta, \sigma_z$ = radial, tangential and axial stress components

$\sigma_r^p, \sigma_\theta^p, \sigma_z^p$ = radial, tangential and axial stress components in plug

$\sigma_r^R, \sigma_\theta^R, \sigma_z^R$ = radial, tangential and axial stress components in rock

σ_n = normal (radial) stress across interface

$\sigma_{n,i}$ = peak normal stress across plug/rock interface

$\sigma_{\theta(r=R)}$ = tangential stress on the steel pipe outside walls

σ_t = tensile strength of push-out cylinder

$\sigma_{n,\Delta T}$ = thermally induced total normal (radial) stress at the plug/rock interface due to temperature increase

$\sigma^p_{z,f}$ = axial strength or axial stress at failure

σ_s = cement swelling stress

$\sigma^p_{z,\Delta T}, \sigma^R_{z,\Delta T}$ = axial thermal stress in plug and rock due to temperature increase

$\sigma_r^{\Delta T}$ = thermally induced radial stress at plug/rock interface due to a thermal axial stress in plug

$\sigma^p_{r,\Delta T}$ = thermal radial stress along plug/rock interface due to the differences in the thermal radial expansions of plug and rock

$\frac{d\sigma^p_z}{dz}dz$ = axial stress increment within plug over section dz due to an axial stress applied to the plug

τ_R = resultant shear stress along the plug-rock interface due to an axial stress applied to the plug and due to temperature increase

τ_{rz} = vertical shear stress in rock

$\tau^{av}_{rz,l}$ = bond strength or average shear stress along plug-rock interface

$\tau_{rz,l}$ = exponential shear stress along plug-rock interface

$\tau^{min}_{rz,l}, \tau^{max}_{rz,l}$ = resultant minimum and maximum extreme exponential interface shear stress along the plug-rock interface due to an axial stress applied to the plug and due to a temperature increase

$\tau^{\Delta T}_{rz,l}$ = thermal shear stress at the plug-rock interface due to temperature increase

$|\tau|$ = interface shear strength

$|\tau|_P$ = peak interface shear strength

ϕ = angle of friction along the interface

ϕ_p, ϕ_r = peak and residual angle of friction along the interface, respectively.

EXECUTIVE SUMMARY

I. Summary

This study includes a systematic investigation of the bond strength of cement borehole plugs in welded tuff. Axial loads on plugs due to gas or water pressures, or due to rock mass deformations induced subsequent to plug installation generate shear stresses along the plug/rock contact. Under extreme conditions, these stresses could cause failure, dislodging or slippage of plugs. Therefore, the interface, or the bond between the plug and rock, is a critical element of any seal system,

The objective of this study is to determine the bond strength of expansive cement plugs in welded tuff. This objective is pursued by a combination of theoretical and experimental approaches.

Selected published analyses on inclusion-host stress transfer mechanics (i.e. composite materials, reinforced concrete, rock bolts and piles) are utilized to obtain closed-form solutions for borehole plug-host rock interactions. Various mechanistically related models are analyzed as their derivations involve different simplifications or assumptions. Such models assist in calculating the theoretical stress and displacement distributions along an axially loaded borehole plug. The frictional interface strength of an axially loaded plug, the effect of axial stress and lateral external stress, thermal effects, and the stress distribution along an axially loaded rigid borehole plug are also studied.

An axisymmetric finite element analysis is performed to assess the validity of the closed-form solution(s) and to study the tensile stresses in and near axially loaded borehole plugs.

Push-out tests are used to determine the bond strength by applying an axial load to the cement plugs. Over 130 push-out tests have been performed on cement plugs cured for eight days. Recorded during push-out testing are the axial load applied to the plug and the top and bottom plug displacements. Failure occurs through shear along the plug/rock interface after periods ranging from 3 to 30 minutes. The tests are continued for up to 2 hours. Residual strengths range from 10 to 33% of the peak strengths, and average about 20%. Seven (out of 34) of the 50.8 mm inside diameter samples and 17 (out of 27) of the 101.6 mm inside diameter samples split in tension during push-out testing.

The interface (bond) strength and deformation are tested as a function of borehole size, plug length, temperature (up to 90°C) and degree of saturation. The tuff cylinders have inside radii of 6.35, 12.7, 25.4 or 50.8 mm, and outside radii of 38.1, 76.2 or 94.0 mm. The tuff cylinders are plugged with cement plugs having length-to-diameter ratios ranging from 1 to 4, but approximately 1 in most cases. Seven of the push-out

cylinders are presaturated (by injecting water into the cylinders) prior to plug emplacement. Other cores are cured at relatively dry, partially and highly saturated conditions, following plugging.

Push-out tests on tuff rock bridges provide a reference strength against which to compare cement axial strength. The 25.4, 50.8 and 101.6 mm inside diameter specimens plugged with cement give a mean axial strength of 12.5, 13.1 and 8.8% of that of samples with rock bridges of the same diameter and rock bridge length-to-diameter ratios of approximately 1. The axial stress, uniform shear stress and maximum exponential shear stress at failure range from 4.4 to 171.2 MPa, 1.29 to 12.96 MPa, and 5.1 to 115.47 MPa, respectively. The average degree of saturation in the low, intermediate, presaturated, and highly saturated push-out cylinders (prior to push-out testing) is 29, 43, 78 and 73%, respectively.

II. Conclusions

Plugs with smaller diameters and grater lengths give higher strengths. The curves of the best fit of the bond strengths as a function of diameter for the highly saturated samples, rock bridge specimens and for the upper bounds for the partially saturated samples obey a power law, with exponents in the neighborhood of 0.5. An exponent of 0.5 has implications in the strength-size relationship and hence in borehole plug design.

There is no discernible difference between the strengths of the highly and partially saturated samples. The low saturated samples cured and tested at 36°C show lower strength than the more saturated samples cured and tested at 44-45°C. This suggests that as long as the plugs are not allowed to dry out, their performance may not deteriorate. The extrapolated strengths of cement plugs emplaced in highly saturated host tuff are higher than those of plugs in partially saturated tuff. The push-out cylinders show moderate changes in strength from samples cured and tested at ambient temperature to 70°C. The pronounced strength drop at 90°C (Tables 4.1-4.3, Ch. 4) is attributed to the weakening of the cement gel structure due to induced saturated steam pressure.

The closed-form solution used for mechanical plug-rock interaction analysis is linearly elastic. It ignores the normal stress distribution in rock and neglects the axial rock displacement. As the closed-form solution is valid up to failure initiation, it gives high peak shear stresses and is conservative for plug design. An axisymmetric finite element analysis has been performed to assess the validity of the simplifications used in the derivation of the closed-form solution. The closed-form solution always overestimates the peak interface shear stress compared to the finite element analysis, with overestimation ranges of 1 to 32%.

The interface shear stress at the loaded end of a borehole plug increases with decreasing Young's modulus ratio of plug and rock, decreasing plug length-to-radius ratio, and decreasing cylinder outside-to-inside radius ratio. The axial stresses within the plug become less linear with the same trends of the parameters. The axial stresses and interface shear stresses do not affect the entire length of plugs having

length-to-radius ratios larger than 4. The radial (contact) stress at the plug/rock interface, due to an axial stress applied to the plug decreases with increasing ratio of plug modulus to rock modulus and with decreasing cylinder inside-to-outside ratio.

The closed-form solution underestimates the axial plug displacement per axial stress at failure compared to the experimental data (by an average of 30%), most probably due to deformation of the test system.

Radial stresses may be created at the plug/rock interface due to an axial stress applied to the plug, due to cement swelling pressures, or due to deformations of the host rock. Such radial stresses may widen fractures or may lead to tensile fracturing of the rock and cause preferential pathways around seals for water flow or for gaseous radionuclides.

The results of the finite element analysis show that, for an axially loaded borehole plug, the most critical areas for the tensile stresses in the plug are the topmost corner, and the bottom center for relatively short plugs. The maximum tensile stresses in rock occur adjacent to the top plug corner. For a push-out sample with a modulus ratio of 0.233, the peak tensile stress occurs at the top plug corner. The tensile stress in this location is uniaxial and reaches up to 74% of the applied axial stress for a borehole plug with a length-to-radius ratio of 2.0. The tensile stress at this location decreases with increased plug length (the peak tensile stress reduces to 26% of the applied axial stress for a plug length-to radius ratio of 8) and increased modulus ratio. A modulus ratio of 10.0 leads to peak tensile stresses at the bottom center of the plug with a peak tensile stress up to 41% of the axial stress applied to the plug. A biaxial tensile stress develops at this location. The tensile stresses decrease with decreasing modulus ratio and with increasing plug length.

The maximum tensile stresses in rock occur adjacent to the top plug corner and decrease with increased modulus ratio and increased plug length. A borehole plug with a length-to-radius ratio of 2.0 and a modulus ratio of 0.233 shows maximum tensile stress of 80% of the applied axial stress at this location.

The results of the theoretical analysis show that a borehole plug with a modulus ratio of 0.233 and plug length-to-radius ratio of 8 shows smaller maximum exponential shear stresses and shows little probability of tensile failure in the plug (when compared to shorter plugs). Hence, it provides an attractive geometrical design criterion for borehole plugs. It is of considerable interest that a very similar geometrical design recommendation results from detailed hydrological analyses of flow through plugs and host rock (Greer and Daemen, 1990), assuming reasonably similar hydraulic conductivities of plug and rock. This may not be surprising in light of the parallelisms between the governing equations.

III. Recommendations for Further Research

The test plan as completed uses a somewhat narrow range of test geometries and specimen stiffnesses. Because of the narrow range of test geometries (plug diameters up to 187.3 mm (7.4 in)), the axial strengths should be extrapolated only with extreme caution. It would be desirable to obtain a firmer basis for extrapolating, by performing tests on larger diameter plugs. Samples should have similar stiffnesses (i.e. outside-to-inside cylinder radius ratios) for a firmer extrapolation.

In this study, the rock cylinders are not confined. It can be assumed that the strengths measured are lower bounds. Due to the possibility of varying lateral stressfield conditions for the sealing of openings in or near a repository, there is a need to perform confined push-out tests. Confined push-out testing also should provide better insight into the relative contribution of adhesive and frictional interface strengths.

Push-out testing provides an estimate of the mechanical bond between a borehole plug and the surrounding rock. The uncertainties in the relations between the mechanical and hydraulic bond, a subject that needs considerable attention in borehole plug performance evaluations, might be resolved by performing simultaneous push-out tests and flow tests. This can be accomplished by loading the plug by means of fluid pressure, rather than by a steel rod. Such fluid pressurization would have considerable advantages, by corresponding more realistically to likely in-situ conditions, and by allowing simultaneous fluid flow and strength testing. It would complicate the experimental arrangement (e.g. measurements of the top and bottom axial plug displacements). In all probability, it would require confining the cylinders, in order to prevent tensile splitting.

The exponential shear stress distribution used in this study appears to be fundamentally more attractive than the average shear stress, but is difficult to validate directly. An effort at such a validation, e.g. by means of strain gages at multiple points along the plug/rock interface, would be warranted.

All push-out tests reported on are short-term tests (minutes to hours) and are performed on neat cement grouts cured for only a short time, typically eight days. Performing long-term quasi-static loading would aid in understanding any stress corrosion effects, creep, and true long-term strength. Push-out tests on cement plugs mixed with crushed tuff or on concrete should be performed to simulate plugs in larger excavations. A desirable feature of stiffening the plugs, i.e. increasing the modulus ratio, is the resulting decrease in the peak interface shear stress.

This study made no attempt to predict the relation between axial strength and cement curing period. Push-out tests should be performed on cement plugs with a variety of relatively long curing times (i.e. months to years). This would be particularly helpful to identify any reactions that might take place between plug, host rock, and water. It also would be a more realistic approach to assess the influence of the degree of saturation in the host rock on bond strength.

CHAPTER ONE

( ) = delete material within

INTRODUCTION

1.1 Objectives

Axial loads on plugs or seals in an underground repository due to gas, water pressures and temperature changes induced subsequent to waste and plug emplacement lead to shear stresses at the plug/rock contact. (These shear stresses may cause cracking and increased permeability along the plug/rock interface. Under extreme conditions they could cause dislodging or slippage of plugs.) Therefore, the bond between the plug and rock is a critical element for the design and effectiveness of plugs in boreholes, shafts or tunnels.

The objective of this study is to determine the bond strength of cement borehole plugs in welded tuff cores. An additional objective is to evaluate the interface strength and deformation as a function of borehole size, plug length, temperature (up to 90°C) and degree of saturation of the tuff cylinder. The tuff cylinders tested have inside diameters of 12.7, 25.4, 50.8, or 101.6 mm, outside diameters ranging from 76.2 to 187.3 mm, and lengths ranging from 101.6 to 177.8 mm. The use of four different inside hole diameters enables evaluation of size effects. The tuff cores are plugged with Self-Stress II cement plugs having length to diameter ratios ranging from 1.0 to 4.0, but approximately 1.0 in most cases.

The bond strength of cement[1] borehole plugs in tuff cores is determined experimentally by means of push-out tests. The push-out test involves the use of a cylindrical steel rod to apply an axial load to a cement plug emplaced within the borehole of a hollow rock cylinder. The applied axial load and the axial displacements at the top and bottom of the cement plug are measured during push-out testing.

Push-out testing provides an estimate of the quality of the mechanical bond between a borehole plug and the surrounding rock. Push-out tests can be used for the design of seals in: 1) water dams, barriers, waterwells, mine drifts or shafts, to prevent flooding of underground operations (e.g. Garrett and Campbell Pitt (1961); Loofbourow (1973)); 2) diversion tunnels for the construction of hydroelectric power plants (e.g. Mitchell (1982); Kinstler (1983); Pettman (1984)); 3) oil, gas and chemical waste disposal wells (e.g. Smith (1976); Calvert (1980)); 4)

---

1 Self-stress II cement, provided by Dowell-Schlumberger, is an expansive cement formulation composed of Ideal Type I/II Portland cement (from Tijeras Canyon, New Mexico), mixed with 50% distilled water, 10% D53 (an expansive agent) and 1% D65 (a dispersant). All percentages are weight percent with respect to cement.

blasthole stemming (e.g. Konya et al. (1982); Otuonye et al. (1983)); and 5) high-level radioactive waste repositories (e.g. U.S. Nuclear Regulatory Commission (1983; 1985)).

In the previous paragraphs, one of the main objectives is identified as investigating the push-out strength in partially saturated welded tuff. Some seals at Yucca Mountain, the proposed site for a high level radioactive waste (HLW) site, quite possibly the major ones, are likely to be emplaced in an unsaturated rock mass. It is not obvious what the consequences of this might be for seal performance. The sealing performance of cement plugs deteriorates drastically in a dry environment (Adisoma and Daemen, 1988). The conditions at Yucca Mountain are far from dry, however. Therefore, this study includes testing of seal performance in partially saturated tuff. Partial saturation requires the curing of welded tuff specimens in a controlled environment (e.g. in an environmental chamber) with the assumption that the degree of saturation throughout the push-out specimen (i.e. within the cement plug and the tuff core) is uniform.

Two methods have been developed in the oil industry to determine the bond strength of set cement, the hydraulic bond strength test and the mechanical bond strength test. The hydraulic bond strength is determined from a test that uses fluid pressure to measure the bond strength of cement either to pipe or to a simulated formation. The test results are generally expressed as the amount of pressure required to break the bond. The results of the mechanical bond strength test are expressed as the shear stress at the interface required to shear the cement bond along a pipe or along a simulated formation (Smith and Calvert, 1980, p. 93). In the mechanical bond strength test, it is assumed that the shear stress is uniform along the interface. Bond strength tests performed in this study are very similar to the mechanical bond strength tests except that the cement is dislodged from tuff cores by means of a rigid cylindrical steel rod. The tests are referred to as shear or interface bond strength tests and are analyzed by calculating the shear stress along the cement plug-rock interface assuming a uniform or an exponential shear stress distribution.

1.2 Scope and Limitations

This study includes an extensive laboratory investigation of the bond strength of cement borehole plugs in welded tuff cores. A total of 130 push-out tests are performed to evaluate the bond strength and deformation as a function of borehole size, plug length, elevated temperature, and degree of saturation of the tuff cylinder. The tuff cylinders tested have inside radii of 6.35, 12.7, 25.4, or 50.8 mm, outside radii ranging from 38.1 to 94.0 mm, and lengths ranging from 71.5 to 229 mm. The tuff cylinders are plugged with nearly centered cement plugs having length-to-diameter ratios ranging from 1.0 to 4.0, but approximately 1.0 in most cases. The use of four different borehole radii enables evaluation of size effects.

In addition to experimental work, analytical and finite element analysis for borehole plug-rock mechanical interaction are performed. The interface strength and deformation are studied as a function of Young's modulus ratio of plug and rock, plug length, rock cylinder outside-to-inside radius ratio, and Poisson's ratio of the plug. The tensile stresses in and near the vicinity of an axially loaded borehole plug are also analyzed.

All of the push-out tests are performed on unconfined rock cylinders, so it can be assumed that the bond strengths measured are lower bounds. The tests are very short-term tests (i.e. up to 2 hours) and are performed on plugs cured for a short time, typically eight days.

1.3 Host Rock and Sealing Materials

The rock used in this study is from the densely welded brown unit of Apache Leap tuff. Tuff is a volcanic ash which has been compressed under its own weight and sometimes is welded due to its high temperature during deposition. The physical properties of tuff can vary from soft, relatively unconsolidated and highly porous material to more compacted and less porous material referred to as welded tuff. Due to the low permeability and high sorptive capacities of the more consolidated tuffs, welded tuff is considered a primary candidate for disposal of high-level nuclear waste (Organization for Economic Cooperation and Development, 1982, p. 15).

Materials used to seal a radioactive waste repository constitute an essential component of the repository system. Cementitious materials (cements, grouts,[2] concretes) have been used in underground sealing in the oil and gas, and mining industries (Roy et al., 1985, p. 3; South and Daemen, 1986, pp. 27-28; Wakeley et al., 1981, p. 4), as well as in other underground storage facilities. Major requirements for repository-seal materials include the following: The materials should 1) be mechanically adequate, 2) be well-bonded to the host rock, 3) provide a very low permeability to fluids, particularly in the interfacial zone between seal material and host rock, 4) be stable and chemically durable, 5) be compatible with the surrounding rock, 6) be resistant to destructive expansion and contraction, and 7) be resistant to radionuclide transport (D'Appolonia Consulting Engineers, 1981, p. 107; Coons et al., 1982, p. 7; Gulick et al., 1980a, p. 278, 1980b, p. 10; Kelsall et al., 1983, pp. 25-26; Wakeley et al., 1981, p. 4, 1986, p. 5). Some authors argue that repository-seal materials should maintain their integrity for periods comparable to the life of the rock formations in which they are emplaced (Gulick et al., 1980a, p. 278, 1980b, p. 9; Kelsall et al., 1983, p. 55). Hence, the seal should bond to the rock and should exclude fluid flow for some (as yet rather uncertain, but considerable) time.

---

2 The term "grout" means a mixture of pourable and pumpable consistency and fluidity. Hydraulic-cement based grouts may or may not include aggregate. Thus, grouts may be either (a) neat cement (or cementitious material blend) pastes, (b) mortars, or (c) concretes, of pourable consistencies (Buck and Mather, 1982, p. 6).

Cementitious materials, because of their engineering properties, combined with their potential for long-term geochemical stability, may satisfy the above requirements. Concretes discovered in the remains of many ancient structures have maintained their mechanical integrity and can function in their intended capacity today. Despite centuries of use and exposure to adverse environmental conditions such as atmospheric carbon dioxide, dissolved species in ore treatment liquids, and warm climatic conditions, such materials have endured "better than the natural stone or brick found in the same structures" (Malinowski, 1982; Moore et al., 1978, p. 71; Roy and Langton, 1983, pp. 1 and 81). During an investigation of the Troy Lock and Dam, New York, Rhoderick (1981, pp. 3 and 4) recovered a core containing part of a metal anchor grouted into foundation rock. The 63 year old grout, which remained continuously below the water table, provides an opportunity to study the effect of an adverse environment on the longevity (phase composition and microstructure) of the grout. X-ray diffraction (XRD), scanning electron microscopy (SEM) studies and visual examinations show that the adverse environmental conditions did not have a significant effect on grout composition or microstructure and that the grout-anchor bond is tight. Buck and Burkes (1979, pp. 1-5) petrographically examine a 17-year old grout specimen surrounded by rock salt. The grout contains Class C cement, brine and calcium chloride. They conclude that the grout-rock salt interface is tight. The XRD and SEM analyses also show that the composition and microstructure of the grout is normal.

Notwithstanding the considerable evidence that cements and concretes can age gracefully, i.e. without significant deterioration, for millenia, it can not be assumed that this is always true, or even frequently. Malinowski (1982), from whom the above quote is taken, also points out that ancient mortars and concretes have sometimes survived even better than modern concretes exposed to similar conditions. He continues with a discussion of the extreme care with which many of the old concretes were prepared, providing at least part of the explanation why extrapolation of the past record to future expectations needs to be done with considerable care. Selective preservation, and hence selective sampling, also complicates interpretation of the archaelogical record with respect to predicting future performance (Winograd, 1986). Durability problems with concrete have been the subject of extensive investigations, in itself an indication that, in general, concrete and cement longevity needs to be designed, and certainly cannot be assumed to be a given intrinsic characteristic of cementitious materials.

The interface is considered a critical element of the seal system for borehole plugging. The interface should be strong enough to resist a site-specific water pressure [1.85 MPa at the WIPP site (Van Sambeek, 1987, p. 1); 11 MPa for the Gorleben site (Jezierski, 1984)] without shear failure. The interface should have a relatively low permeability (Calvert, 1980, p. 194; Rhoderick and Buck, 1981, p. 1; Roy et al., 1983, p. 135; Wakeley and Roy, 1985, p. 3; Wakeley et al., 1985, p. 951; Wakeley and Roy, 1986, p. 1). The interface shear strength should exceed all reasonably calculated requirements and should be investigated as a function of time, pressure, temperature and groundwater conditions (Roy et al., 1979, p. 17).

A cementitious seal can develop mechanically or chemically. The mechanical bonding is established once the matrix hardens and can be enhanced by using expansive cement formulations. From that point on, the cement plug must remain firmly in place against the host rock to prevent annular separation, at least until chemical bonding is established (so that no undesirable phase changes take place). Hence, the interface (bond) strength of the cement plug/rock contact is one indicator of the mechanical and chemical compatibility between these materials (Roy et al., 1983, pp. 40 and 135; Wakeley and Roy, 1985, p. 7; Wakeley et al., 1985, p. 955; Wakeley and Roy, 1986, p. 27).

1.4 Organization

The first section of this first chapter identifies the objectives of the work reported on. The second section describes scope and limitations. The third section gives the properties of the rock and seal materials used in rock mass sealing. This fourth section gives a chapter by chapter overview of the contents.

The first part of Chapter Two presents theoretical models to calculate the interfacial shear stress, axial stress, and axial displacement distributions along an axially loaded borehole plug in rock. The related theoretical models studied are composite materials, rock bolts, piles, and reinforced concrete. The second part of Chapter Two studies the frictional interface strength of an axially loaded borehole plug, the effect of axial stress and lateral external stress, thermal effects ad the stress distribution along an axially loaded rigid borehole plug. Appendix A gives the interfacial shear stress distribution along an axially loaded rigid plug.

Chapter Three gives the results of the finite element analysis for mechanical borehole plug-rock interaction. The results of the finite element analysis are compared with those of the closed-form solution. The tensile stresses in and near the vicinity of an axially loaded borehole plug are analyzed. Appendix B gives the finite element meshes and stress distributions.

Experimental procedures and results are summarized in Chapter Four, while details are included in Appendices C through M.

Chapter Five analyzes and interprets the results of the experimental results. Axial and radial stresses and deformations are analyzed as a function of the axial stress applied to the plug, applied lateral external stress, and elevated temperature. Implications of tensile stresses in and near an axially loaded borehole plug are analyzed.

Chapter Six gives the summary, conclusions and recommendations.

CHAPTER TWO

ANALYTICAL SOLUTIONS FOR THE MECHANICAL INTERACTION BETWEEN BOREHOLE PLUGS AND HOST ROCK

2.1 Introduction

Composite materials, reinforced concrete, rock bolts and piles are mechanistically similar to an axially loaded borehole plug. In all structures of these types, axial load is transferred from the inclusion to the host (or vice versa) in the form of shear stresses along the interface. Figure 2.1 illustrates the general geometry of such cylindrical inclusion problems.

The first part of this chapter presents theoretical models applicable to push-out testing. Such models can assist in calculating theoretical stress distributions along an axially loaded borehole plug. Both the plug and the rock are treated as elastic materials, and elastic continuity is assumed along the interface in most of the calculations. The second part of this chapter studies the frictional interface strength of an axially loaded plug, the effect of axial stress and lateral external stress, thermal effects, and the stress distribution along an axially loaded rigid borehole plug.

This Chapter Two presents a comprehensive set of closed form solutions for the plug-rock interaction mechanics. A detailed numerical evaluation of the solutions is deferred to Chapter Five, which also includes extensive discussions of the implications with regard to the design and performance of plugs.

2.2 Related Mechanical Analyses for Borehole Plug-Rock Interaction

A vast literature exists on stress-transfer mechanics in composite materials, reinforced concrete, rock bolts an piles. It is beyond the limits of this study to summarize that literature. In this section, selected published analyses on inclusion-host stress transfer mechanics are utilized to obtain closed-form solutions for borehole plug-host rock interactions. No attempt is made to reproduce these models, but only to modify them for a plug-rock system. Various mechanistically related problems are analyzed as they involve different simplifications or assumptions in their theoretical derivations. Modifications (i.e. in terms of boundary conditions) are made whenever necessary. Sign conventions are those presented by Jaeger and Cook (1979, pp. 10 and 33-37), where compressive stresses and displacements in the negative directions of the axes are reckoned positive. Some empirical solutions are presented for piles.

Element ABCD, in Figure 2.2, is common to all the models considered. As an axial force (P_{po}) is applied to the plug, load transfer occurs through shear stresses at the interface between host and inclusion. This results in differential deformation of the inclusion.

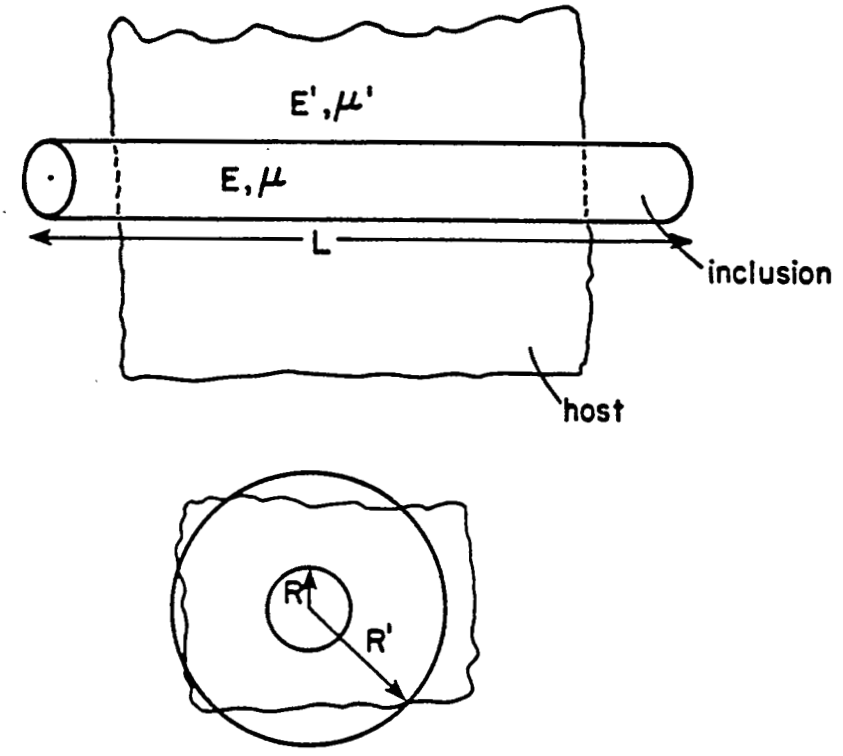

Figure 2.1 Cylindrical inclusion problem. Inclusion of radius (R), length (L), Young's modulus (E) and Poisson's ratio (μ) embedded in host of radius (R'), Young's modulus (E') and Poisson's ratio (μ').

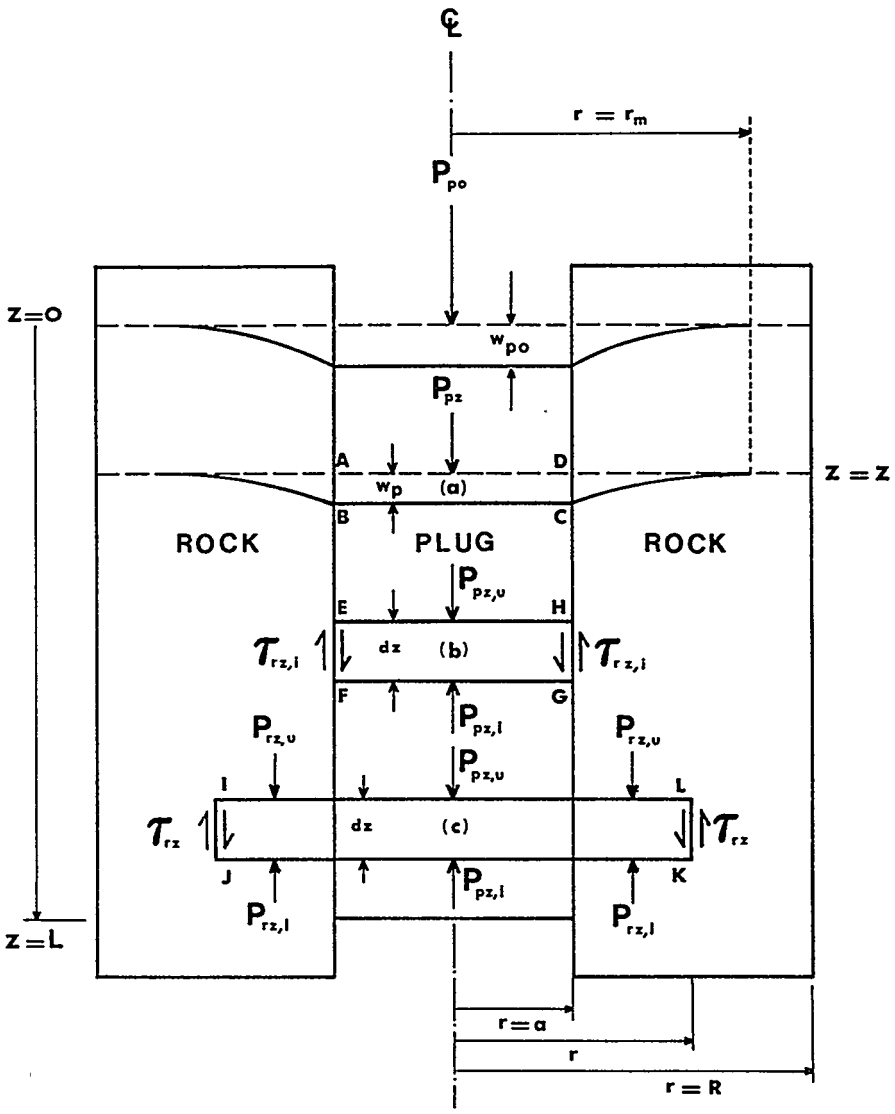

Figure 2.2 (a) Model used to develop theoretical stress distribution for borehole plug-rock system.

(b) Plug element EFGH (of thickness dz and radius a), showing force distribution along plug ($P_{pz,u}$; $P_{pz,l}$) and shear stress at interface ($\tau_{rz,l}$).

(c) Element IJKL (of thickness dz and radius r), showing force distribution in plug and shear stress in rock (τ_{rz}).

P_{po} = axial force applied to the plug
P_{pz}, P_{rz} = axial force in plug and rock at distance z from initial location of loaded end of plug, respectively
u, l = subscripts indicating upper and lower surfaces, respectively.

2.2.1 Derivation of Exponential Load Transfer Along Plug-Rock Interface Using Composite Material Solutions

The analysis by Cox (1952, pp. 72-79) results in an exponential shear stress distribution along the plug-rock interface. Holister and Thomas (1966, pp. 14-19); Kelly (1973, pp. 175-179); Piggott (1980, pp. 83-87); and Kelly and Macmillan (1986, pp. 258-262) present similar analyses.

P_{pz} is the vertical load in the plug at a distance z below the top of the plug (Figures 2.2(a) and 2.3). The transfer of load from the plug to the rock is assumed to take place as:

$$\frac{dP_{pz}}{dz} = -H(w_p - w_R) \tag{2.1}$$

where w_p is the vertical displacement in the plug and w_R is the vertical displacement of the rock at the same vertical position. H is a constant which depends on the geometrical arrangement of the plug and rock and on their respective elastic moduli. The geometric constant H can be obtained by considering the equilibrium of the plug slice ABCD in Figures 2.2(a) and 2.3. Solving at equilibrium between z and z + dz, i.e. $\Sigma F_z = 0$:

$$\sum F_z = \left(P_{pz} - P_{pz} - \frac{dP_{pz}}{dz} dz \right) - \tau_{rz,i} 2\pi a dz = 0 \tag{2.2}$$

$$\frac{dP_{pz}}{dz} = -2\pi a \tau_{rz,i} \tag{2.3}$$

where $\tau_{rz,i}$ = shear stress at rock-plug interface
a = plug radius.

Equating (2.1) and (2.3) results in:

$$H = 2\pi a \frac{\tau_{rz,i}}{w_p - w_R} \tag{2.4}$$

Considering the equilibrium of the plug element EFGH, Figure 2.2(b), and solving for the interface shear stress, $\tau_{rz,i}$, results in:

$$\sum F_z = P_{pz,u} - P_{pz,l} - 2\pi a \tau_{rz,i} dz = 0 \tag{2.5}$$

and

$$\tau_{rz,i} = (P_{pz,u} - P_{pz,l})/(2\pi a dz) \tag{2.6}$$

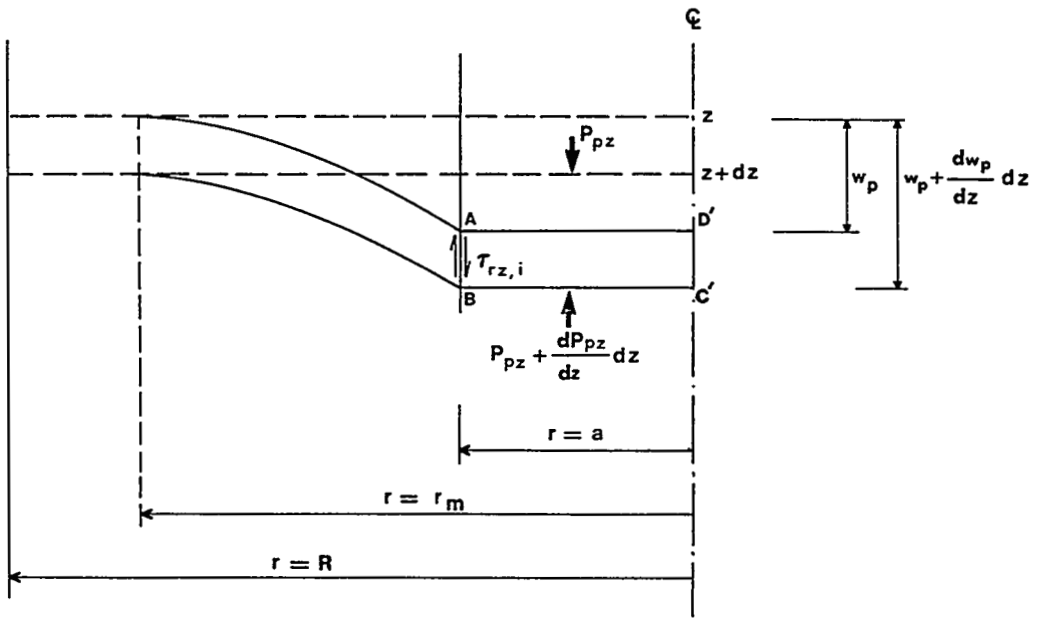

Figure 2.3 Enlarged section of half of element ABCD in Figure 2.2(a), showing deformations and stresses in plug-rock section.

where $P_{pz,u}$ and $P_{pz,l}$ are the vertical forces acting on the upper and lower surfaces of the plug slice.

Equilibrium of element IJKL, Figure 2.2(c), leads to:

$$\sum F_z = 0 = (P_{pz,u} - P_{pz,l}) + (P_{rz,u} - P_{rz,l}) - \tau_{rz} 2\pi r\, dz = 0 \qquad (2.7)$$

and

$$\tau_{rz} = \frac{(P_{pz,u} - P_{pz,l}) + (P_{rz,u} - P_{rz,l})}{2\pi r\, dz} \qquad (2.8)$$

where τ_{rz} = vertical shear stress at radius r from plug center

$P_{rz,u}$ and $P_{rz,l}$ = vertical force acting on the upper and lower surfaces of the rock section.

Neglecting the vertical load difference in the rock (i.e. assuming $P_{rz,u} = P_{rz,l}$), and equating (2.6) and (2.8) results in:

$$\tau_{rz} = \tau_{rz,i}(a/r) \qquad (2.9)$$

The shear strain in the rock (at radius r) is given by:

$$\frac{dw_R}{dr} = \frac{\tau_{rz}}{G_R} = \frac{\tau_{rz,i} a}{G_R r} \qquad (2.10)$$

where G_R = shear modulus of rock.

Integrating Eq. (2.10) from plug radius a to rock cylinder outside radius R, results in:

$$-(w_p - w_R) = \frac{\tau_{rz,i} a}{G_R} \ln(R/a) \qquad (2.11)$$

Using Eq. (2.4):

$$H = -\frac{2\pi G_R}{\ln(R/a)} = -\frac{\pi E_R}{(1+\nu_R)\ln(R/a)} \qquad (2.12)$$

where E_R and ν_R = Young's modulus and Poisson's ratio of rock
a = plug radius
R = rock cylinder radius.

If the deformations are assumed to be elastic and one-dimensional, then:

$$P_{pz} = E_p A_p \frac{dw_p}{dz} \qquad (2.13)$$

where E_p and A_p are the Young's modulus and cross-sectional area of the plug.

Similarly,

$$P_{rz} = E_R A_R \frac{dw_R}{dz} = E_R A_R \epsilon_z^R \tag{2.14}$$

where P_{rz} = vertical load at any point z in rock
E_R = Young's modulus of rock
ϵ_z^R = vertical strain in rock (assumed to be constant for simplicity (Cox, 1952)).

Differentiating Eq. (2.1), using Eq. (2.13) in (2.1) and substituting the geometric constant H from Eq. (2.12) into the resultant equation leads to:

$$\frac{d^2 P_{pz}}{dz^2} = -H\left[\frac{P_{pz}}{E_p A_p} - \epsilon_z^R\right] = \frac{\pi E_R}{(1+\nu_R)\ln(R/a)}\left[\frac{P_{pz}}{E_p A_p} - \epsilon_z^R\right] \tag{2.15}$$

The solution of this differential equation is:

$$P_{pz} = E_p A_p \epsilon_z^R + A\sinh(\beta z) + B\cosh(\beta z) \tag{2.16}$$

where

$$\beta = \left[\frac{E_R}{(1+\nu_R)E_p a^2 \ln(R/a)}\right]^{1/2}$$

A and B are integration constants.

The constants in Eq. (2.16) can be determined by introducing the boundary conditions. For the borehole plug-rock system, $P_{pz} = P_{po}$ at $z = 0$ (on top of plug) and $P_{pz} = 0$ at $z = L$ (at bottom of plug, L = plug length). A and B can be written as:

$$A = -\left[\frac{(P_{po} - E_p A_p \epsilon_z^R)\cosh(\beta L) + E_p A_p \epsilon_z^R}{\sinh(\beta L)}\right] \tag{2.17}$$

$$B = P_{po} - E_p A_p \epsilon_z^R \tag{2.18}$$

which upon substitution into Eq. (2.16) yields:

$$P_{pz} = E_p A_p \epsilon_z^R\left[\frac{\sinh(\beta L)[1-\cosh(\beta z)] + \sinh(\beta z)[\cosh(\beta L) - 1]}{\sinh(\beta L)}\right]$$

$$+ P_{po}\left[\frac{\sinh(\beta(L-z))}{\sinh(\beta L)}\right] \tag{2.19}$$

Equation (2.19) can be written in terms of stresses as:

$$\sigma_z^P = E_p \epsilon_z^R \left[\frac{\sinh(\beta L)[1-\cosh(\beta z)]+\sinh(\beta z)[\cosh(\beta L)-1]}{\sinh(\beta L)} \right]$$

$$+\sigma_{po}\left[\frac{\sinh(\beta(L-z))}{\sinh(\beta L)} \right] \qquad (2.20)$$

where σ_z^P = axial stress at any depth z in plug
σ_{po} = axial stress applied to the plug.

Differentiating equation (2.19), equating it with (2.3), and expressing the resultant equation in terms of stresses leads to the solution of the shear stress at any depth z along the interface ($\tau_{rz,i}$):

$$\tau_{rz,i} = E_p \beta \epsilon_z^R \left[\frac{\sinh(\beta z)\sinh(\beta L)+\cosh(\beta z)[\cosh(\beta L)-1]}{\sinh(\beta L)} \right]$$

$$+\frac{\sigma_{po}\beta\alpha}{2}\left[\frac{\cosh(\beta(L-z))}{\sinh(\beta L)} \right] \qquad (2.21)$$

Greszczuk (1969, pp. 49-52) uses a similar approach as Cox (1952). He expresses the shear strain at the interface (γ_i) as:

$$\gamma_i = -\frac{(w_p - w_R)}{b_i} = -\frac{w_p}{b_i} \qquad (2.22)$$

where w_p = vertical displacement in plug
w_R = vertical displacement in rock (assumed to be negligible)
b_i = effective interface width.

Using the relationship between the interface shear stress ($\tau_{rz,i}$) and the shear strain (γ_i) and combining with equation (2.22):

$$\gamma_i = \frac{\tau_{rz,i}}{G_i} = -\frac{w_p}{b_i} \qquad (2.23)$$

$$\tau_{rz,i} = -\frac{w_p G_i}{b_i} \qquad (2.24)$$

where G_i = shear modulus of the interface.

Substituting Eqs. (2.24) and (2.13) into Eq. (2.3) yields:

$$\frac{d^2 w_p}{dz^2} - \alpha_i^2 w_p = 0 \qquad (2.25)$$

where w_p = vertical displacement of plug
$\alpha_i = [(2G_i)/(b_i \alpha E_p)]^{1/2}$.

The solution of Eq. (2.25) is:

$$w_p = Ae^{\alpha_i z} + Be^{-\alpha_i z} \tag{2.26}$$

where A and B are constants of integration that can be evaluated from the boundary conditions:

at z = 0, $P_{pz} = P_{po}$
at z = L, $P_{pz} = 0$.

Differentiating Eq. (2.26) and using Eq. (2.13) with these boundary conditions leads to the solution of the axial displacement at any depth z along the plug (w_p) as:

$$w_p = \frac{P_{po}}{E_p A_p \alpha_i} \frac{\cosh[\alpha_i(L-z)]}{\sinh(\alpha_i L)} \tag{2.27}$$

where P_{po} = axial load applied to the plug.

The average vertical load at any point z in the plug (P_{pz}) is calculated by differentiating Eq. (2.27) and by substituting the resultant equation into Eq. (2.13):

$$P_{pz} = P_{po} \frac{\sinh[\alpha_i(L-z)]}{\sinh(\alpha_i L)} \tag{2.28}$$

The average vertical stress at any point z in the plug (σ_z^P) is calculated by dividing both sides of Eq. (2.28) by the plug area:

$$\sigma_z^P = \sigma_{po} \frac{\sinh[\alpha_i(L-z)]}{\sinh(\alpha_i L)} \tag{2.29}$$

Differentiating Eq. (2.27) and equating it to Eq. (2.3) (also using Eq. (2.13) in Eq. (2.3)) gives the shear stress at any point z along the interface ($\tau_{rz,i}$):

$$\tau_{rz,i} = \frac{\sigma_{po} \alpha_i a}{2} \frac{\cosh[\alpha_i(L-z)]}{\sinh(\alpha_i L)} \tag{2.30}$$

where σ_{po} = axial stress applied to the plug
L = plug length
a = plug radius
α_i is given by Eq. (2.25).

The analysis presented by Greszczuk (1969) requires the use of interface properties (e.g. b_i, G_i) which are not obvious and are not easily determined.

2.2.2 Analyses of Mechanical Interaction Between Borehole Plugs and Host Rock Derived from Rock Bolt Interaction Analyses

The stress distribution along an axially stressed grouted rock bolt is similar to that along an axially loaded borehole plug (i.e. Daemen, 1974; Farmer, 1975). The model considered to derive the theoretical stress distribution is given in Figures 2.2(a) and 2.3. Previously presented derivations are not repeated.

Considering the equilibrium of the diametral plug slice ABC'D' in Figure 2.3 (in terms of stresses) and solving at equilibrium between z and z + dz, $\sum F_z = 0$:

$$\sum F_z = \left(\sigma_z^P - \sigma_z^P - \frac{d\sigma_z^P}{dz} dz \right) \pi a^2 - \tau_{rz,i} 2\pi a dz = 0 \qquad (2.31)$$

$$\frac{d\sigma_z^P}{dz} = -\frac{2}{a} \tau_{rz,i} \qquad (2.32)$$

If the deformations are elastic and three-dimensional, the vertical strain in a plug (ϵ_z^P) loaded axially, from Hooke's Law is:

$$\epsilon_z^P = \frac{\sigma_z^P - \nu_p(\sigma_r^P + \sigma_\theta^P)}{E_p} \qquad (2.33)$$

where σ_z^P = axial stress at any point z along the plug
σ_r^P = radial stress
σ_θ^P = tangential stress in plug
E_p, ν_p = Young's modulus and Poisson's ratio of plug.

If the radial strain in a plug (ϵ_r^P) equals the tangential strain (ϵ_θ^P), and $\sigma_r^P = \sigma_\theta^P$, the radial strain in a plug loaded axially is:

$$\epsilon_r^P = \frac{\sigma_r^P - \nu_p(\sigma_z^P + \sigma_r^P)}{E_P} \qquad (2.34)$$

The radial displacement in the plug (u_p) equals the radial strain times the plug radius (a):

$$u_p = \left[\frac{(1-\nu_p)\sigma_r^P - \nu_p \sigma_z^P}{E_p} \right] a \qquad (2.35)$$

The radial displacement (u) in a hollow rock cylinder with an internal radius a and external radius R, subjected to a radial stress P_1 at a and P_2 at R, for a plane strain configuration is given by (Jaeger and Cook, 1979, p. 135; Timoshenko, 1956, pp. 205-210):

$$u = \frac{(1+\nu_R)}{E_R(R^2-a^2)}\left[(1-2\nu_R)(P_2R^2-P_1a^2)r + \frac{(P_2-P_1)R^2a^2}{r}\right] \qquad (2.36a)$$

Eq. (2.36a) can be converted to the case of plane stress by expressing the plane strain solution in terms of the shear modulus of the rock, G_R, and the Poisson's ratio of the rock, ν_R, and by replacing ν_R by $\nu_R/(1+\nu_R)$ (Jaeger and Cook, 1979, p. 115):

$$u = \frac{1}{E_R(R^2-a^2)}\left[(1-\nu_R)(P_2R^2-P_1a^2)r + \frac{(1+\nu_R)(P_2-P_1)R^2a^2}{r}\right] \qquad (2.36b)$$

where R = outside radius of rock cylinder
E_R, ν_R = Young's modulus and Poisson's ratio of rock
r = radial coordinate.

The radial displacement in the rock (u_R) at the plug/rock contact (r = a) due to an internal stress (σ_r^p) follows from Eq. (2.36a) for a plane strain solution:

$$u_R = -\frac{\sigma_r^p(1+\nu_R)a}{E_R(R^2-a^2)}[(1-2\nu_R)a^2+R^2] \qquad (2.37a)$$

and from Eq. (2.36b) for a plane stress solution:

$$u_R = -\frac{\sigma_r^p a}{E_R(R^2-a^2)}[(1-\nu_R)a^2+(1+\nu_R)R^2] \qquad (2.37b)$$

A compressive axial stress applied to a plug generates a radial (normal) stress along the plug/rock contact and an outward radial displacement of the plug. The normal stress along the interface is proportional to the axial stress applied to the plug. The radial contact stress (σ_r^p) can be determined by equating the plug and rock radial displacements along the interface (i.e. $u_p = u_R$). For a plane strain solution, equating (2.35) and (2.37a) yields:

$$\sigma_r^P = \sigma_z^P \frac{\nu_p(1-(a/R)^2)}{(1-\nu_p)(1-(a/R)^2)+(E_P/E_R)(1+\nu_R)[(1-2\nu_R)(a/R)^2+1]} \tag{2.38a}$$

Equating Eqs. (2.35) and (2.37b) results in a plane stress solution for the radial contact stress along the plug/rock interface (σ_r^P):

$$\sigma_r^P = \sigma_z^P \frac{\nu_p(1-(a/R)^2)}{(1-\nu_p)(1-(a/R)^2)+(E_P/E_R)[(1-\nu_R)(a/R)^2+(1+\nu_R)]} \tag{2.38b}$$

For the case of an infinite rock mass, substituting $R \to \infty$ into Eq. (2.38a or b) leads to the same solution of the radial stress along the plug/rock contact for plane strain and for plane stress:

$$\sigma_r^P = \sigma_z^P \frac{\nu_P}{(1-\nu_P)+(E_P/E_R)(1+\nu_R)} \tag{2.38c}$$

The relations between σ_r^P and σ_z^P can thus be written as:

$$\sigma_r^P = \sigma_z^P (VSF) \tag{2.39}$$

where VSF is called the vertical stress function. VSF is selected from the appropriate equation in accordance with geometrical and constraint conditions.

Substituting Eq. (2.39) into (2.33) and solving for σ_z^P yields (noting that $\sigma_r^P = \sigma_\theta^P$):

$$\sigma_z^P = \frac{E_p \epsilon_z^P}{[1-2\nu_p(VSF)]} = \frac{E_p}{[1-2\nu_p(VSF)]} \frac{dw_p}{dz} \tag{2.40}$$

where w_p = vertical displacement in plug.

Combining equations (2.32) and (2.40) yields:

$$\frac{d^2 w_p}{dz^2} = -\frac{2[1-2\nu_p(VSF)]}{aE_p} \tau_{rz,i} \tag{2.41}$$

Assuming that the vertical rock displacement (w_R) is negligible at a radius r_m from the plug center, the interface shear stress given in Eq. (2.11) can be written as:

$$\tau_{rz,i} = -\frac{w_p G_R}{a \ln(r_m/a)} \tag{2.42}$$

where r_m = effective (critical) radius beyond which shear stresses are negligible (Figures 2.2 and 2.3). Determination of r_m is discussed in Ch. 3.

For the modulus ratio (E_p/E_R) range of 0.1 to 5.0, the effective radius (r_m) can be expressed as:

$$r_m/a = [2.1 - 0.38(E_p/E_R)]L/a + 1 \tag{2.42a}$$

For a modulus ratio of 10.0 or greater, r_m is given by:

$$r_m/a = 0.1(L/a) + 1 \tag{2.42b}$$

Eqs. (2.42a and b) are applicable for a plug length-to-radius ratio range of $2.0 \leq L/a \leq 8.0$ (Ch. 3).

After substitution of Eq. (2.42), Eq. (2.41) becomes:

$$\frac{d^2 w_p}{dz^2} - \alpha^2 w_p = 0 \tag{2.43}$$

$$\alpha^2 = \frac{[1 - 2\nu_p(VSF)]E_R}{(1+\nu_R)E_p a^2 \ln(r_m/a)} \tag{2.43a}$$

The vertical stress function (VSF) is given by Eq. (2.38a) for a plane strain configuration and by Eq. (2.38b) for plane stress.

In Eq. (2.43a):

r_m = effective radius beyond which shear stresses are considered negligible
ν_p, ν_R = Poisson's ratio of plug and rock, respectively
E_p, E_R = Young's modulus of plug and rock, respectively
a = plug radius.

The solution of Eq. (2.43) is:

$$w_p = Ae^{\alpha z} + Be^{-\alpha z} \tag{2.44}$$

where A and B are the integration constants that can be evaluated from the boundary conditions:

at z = 0, $\sigma_z^p = \sigma_{po}$
at z = L, $\sigma_z^p = 0$.

Substituting equation (2.44) into (2.40) and introducing the boundary conditions leads to:

$$A = \frac{\sigma_{po}[1-2\nu_p(VSF)]}{E_p\alpha}\frac{e^{-\alpha L}}{e^{\alpha L}-e^{-\alpha L}} \tag{2.45}$$

$$B = \frac{\sigma_{po}[1-2\nu_p(VSF)]}{E_p\alpha}\frac{e^{\alpha L}}{e^{\alpha L}-e^{-\alpha L}} \tag{2.46}$$

where σ_{po} = axial stress applied to plug
VSF = given in Eq. (2.39)
L = plug length

Combining equations (2.45) and (2.46) in (2.44) gives the vertical displacement at any point z in the plug:

$$w_p = \frac{\sigma_{po}[1-2\nu_p(VSF)]}{E_p\alpha}\frac{\cosh[\alpha(L-z)]}{\sinh(\alpha L)} \tag{2.47}$$

Substituting Eq. (2.47) into (2.42) gives the shear stress ($\tau_{rz,i}$) along the interface:

$$\tau_{rz,i} = \frac{\sigma_{po}\alpha\alpha}{2}\frac{\cosh[\alpha(L-z)]}{\sinh(\alpha L)} \tag{2.48}$$

The axial stress (σ_z^p) in the plug can be calculated by substituting equation (2.48) into (2.32) and by integrating over the appropriate limits:

$$\frac{d\sigma_z^p}{dz} = -\sigma_{po}\alpha\frac{\cosh[\alpha(L-z)]}{\sinh(\alpha L)} \tag{2.49}$$

$$\sigma_z^p = -\int_0^z \sigma_{po}\alpha\frac{\cosh[\alpha(L-z)]}{\sinh(\alpha L)}dz \tag{2.50}$$

$$\sigma_z^p = \sigma_{po}\frac{\sinh[\alpha(L-z)]}{\sinh(\alpha L)} + A \tag{2.51}$$

Evaluating the boundary conditions: $\sigma_z^p = \sigma_{po}$ at z = 0 and $\sigma_z^p = 0$ at z = L indicates that the integration constant A = 0 and:

$$\sigma_z^p = \sigma_{po}\frac{\sinh[\alpha(L-z)]}{\sinh(\alpha L)} \tag{2.52}$$

The radial stress (σ_r^p) at the interface can be computed by substituting equation (2.52) into (2.39):

$$\sigma_r^P = \sigma_{po}(VSF)\frac{\sinh[\alpha(L-z)]}{\sinh(\alpha L)} \tag{2.53}$$

where VSF = vertical stress function given in equation (2.39).

The analysis presented by Cox (1952) reduces to that presented in this section if the vertical rock strain (ϵ_z^R, Eqs. (2.20) and (2.21)), is taken to be equal to zero, and if a three-dimensional stress field is assumed (Eq. (2.39)).

The average shear stress along the plug-rock interface can be expressed as:

$$\tau_{rz,i}^{av} = \frac{P_{po}}{2\pi a L} = \frac{\sigma_{po} a}{2L} \tag{2.54}$$

or

$$\sigma_{po} = \frac{2\tau_{rz,i}^{av} L}{a} \tag{2.55}$$

Substituting Eq. (2.55) into Eq. (2.47), (2.48), (2.52), and (2.53) expresses w_p, $\tau_{rz,i}$, σ_z^P and σ_r^P as a function of $\tau_{rz,i}^{av}$:

$$w_p = \frac{\tau_{rz,i}^{av} 2L[1-2\nu_p(VSF)]}{E_p \alpha a}\frac{\cosh[\alpha(L-z)]}{\sinh(\alpha L)} \tag{2.56}$$

$$\tau_{rz,i} = \tau_{rz,i}^{av} \alpha L \frac{\cosh[\alpha(L-z)]}{\sinh(\alpha L)} \tag{2.57}$$

$$\sigma_z^P = \frac{\tau_{rz,i}^{av} 2L}{a}\frac{\sinh[\alpha(L-z)]}{\sinh(\alpha L)} \tag{2.58}$$

$$\sigma_r^P = \frac{\tau_{rz,i}^{av} 2L(VSF)}{a}\frac{\sinh[\alpha(L-z)]}{\sinh(\alpha L)} \tag{2.59}$$

2.2.3 Study of Borehole Plug-Rock Interaction Derived from Pile Analyses

Piles are structural members of timber, concrete and/or steel, used to transmit surface loads to lower levels in a soil mass. Their load is transferred to the surrounding soil through skin friction and tip resistance (Bowles, 1977, p. 575). Tip resistance, or end bearing capacity, is not a mechanism involved in a plug-rock system; therefore, emphasis in this section is on predictions of stress distributions resulting from skin friction or interface shear stress ($\tau_{rz,i}$).

Most theories developed to predict stress distributions along the pile-soil interface are empirical. The α, λ and β methods are used for computing the skin resistance of piles in soils. The α and λ methods are used only for cohesive soils. In all three methods, the skin resistance capacity (P_S) is computed as:

$$P_S = \sum A_s f_s (\Delta L) \tag{2.60}$$

where A_s = pile surface area on which the skin friction (f_s) acts
ΔL = embedment increment
f_s = skin friction or interface shear stress, computed by the α, λ or β method
$\sum$ = summation of contributions from several strata or pile segments.

In the α method, proposed by Tomlinson (1971, pp. 107-114), the skin friction (f_S) of a pile in clay is computed as:

$$f_s = \alpha s_u + \bar{q} K \tan\delta \tag{2.61}$$

where α = adhesion factor between pile and soil (the value of the α coefficient depends on the type of soil and on the depth of penetration into the soil)
s_u = undrained shear strength for the soil stratum of interest
$\bar{q}$ = average vertical stress on element ΔL
K = coefficient of lateral earth pressure (generally taken as K_o: coefficient of lateral earth pressure at rest)
δ = effective friction angle between soil and pile materials.

Vijayvergiya and Focht (1972, pp. 865-874) present the λ method for obtaining the skin friction (f_S) of a pile in clay as:

$$f_s = \lambda(\bar{q} + 2s_u) \tag{2.62}$$

where $\bar{q}$, s_u = average vertical stress and average undrained shear strength over the entire length of pile
λ = coefficient with a value depending on the depth of pile penetration.

The λ coefficient is obtained from a regression analysis of a plot with a large number of pile-load tests.

Bowles (1977, pp. 604-608) presents the β method, by which the skin friction (f_s) is computed as:

$$f_s = \beta(\bar{q} + q_s) \tag{2.63}$$

where $\beta = K \tan\delta$ (where K, δ are defined with Eq. (2.61))
q_s = surcharge on element ΔL
$\bar{q}$ = defined in Eq. (2.61).

The empirical α, λ and β methods depend on variables such as soil stratification, soil penetration ratio and surcharge, parameters not involved in push-out testing. All three methods show increase in skin friction with depth, most likely due to the increase in horizontal pressure. In push-out testing the skin friction and the interface shear stress decrease with depth as a result of decreasing vertical stress in the plug. Decreasing axial stress leads to decreasing radial stress on the interface (as given in Eq. (2.53)) and hence to decreasing skin friction with depth.

Amir (1986, pp. 53-56) proposes an exponential skin friction or exponential interface shear stress distribution at the pile-soil interface. His analysis is very similar to that discussed in Section 2.3. He examines a linearly elastic pile loaded axially at its top. The soil friction is represented by axial Winkler springs. A Winkler spring is assumed to exist at every point of the pile side (uniformly distributed springs). The spring constant, k_S, relates the side friction of the pile $\tau_{rz,i}$ to the relative displacement of the pile, w_p:

$$\tau_{rz,i} = -k_s w_p \tag{2.64}$$

According to Scott (1981), as quoted by Amir (1986, p. 54), the spring constant k_s is given by:

$$k_s = E_R / 8a \tag{2.65}$$

where E_R = Young's modulus of surrounding rock
a = pile or plug radius.

The spring constant, k_S, given by Eq. (2.65) results from Eq. (2.42), with the assumption that the Poisson's ratio of the soil is negligible and that the critical radius (r_m in Eq. (2.42)) is equal to 60 plug radii from the center of an axially loaded pile in an infinite medium.

Combining Eqs. (2.64) and (2.65) gives an expression for the interface shear stress ($\tau_{rz,i}$) as a function of the vertical plug (pile) displacement (w_p):

$$\tau_{rz,i} = -(w_p E_R)/8a \tag{2.66}$$

The solution can be modified for a three-dimensional stress field (as discussed in Section 2.3) by substituting equation (2.66) into (2.41):

$$\frac{d^2 w_p}{dz^2} - \lambda^2 w_p = 0 \tag{2.67}$$

where

$$\lambda^2 = \frac{[1 - 2\nu_p(VSF)]E_R}{4a^2 E_p} \tag{2.67a}$$

VSF = vertical stress function (given in Eq. (2.39)).

The solution for the vertical displacement follows from Eqs. (2.43) through (2.46) as:

$$w_p = \frac{\sigma_{po}[1 - 2\nu_p(VSF)]}{E_p \lambda} \frac{\cosh[\lambda(L-z)]}{\sinh(\lambda L)} \tag{2.68}$$

Substituting equation (2.68) into (2.66) gives $\tau_{rz,i}$ as:

$$\tau_{rz,i} = \frac{\sigma_{po} \lambda a}{2} \frac{\cosh[\lambda(L-z)]}{\sinh(\lambda L)} \tag{2.69}$$

The axial stress can be calculated by substituting equation (2.69) into (2.32) and by integrating over the appropriate limits (as for Eq. (2.49):

$$\sigma_z^P = \sigma_{po} \frac{\sinh[\lambda(L-z)]}{\sinh(\lambda L)} \tag{2.70}$$

This analysis suggests an exponential decay of skin friction (or interface shear stress) with depth which is contradictory to the skin friction distribution proposed by the α, λ and β methods.

Randolph and Wroth (1978, pp. 1474-1476) use an analysis similar to that of Amir (1986). Their solution leads to an exponentially decaying skin friction with depth (if the tip resistance of the pile is zero). The only difference is that they consider an effective radius, r_m (Figure 2.2(a)), as included in Eqs. (2.43a and b), at which the shear stress is negligible. The effective radius, r_m, is given as:

$$r_m = 2.5L(1 - \nu_p)\psi \tag{2.71}$$

where L = pile or plug length
ψ = inhomogeneity factor, which is the ratio of the shear modulus of the rock at the pile mid-depth to that at the base (equal to unity for push-out testing).

Randolph and Wroth (1978, p. 1470) also suggest that the increase in the shear stress (τ_{rz}) in the pile shaft is much greater than the increase in the vertical stress in the rock (σ_z^R). Thus, they neglect the vertical stress in the rock and assume that the vertical load in the pile is transferred to the host rock only through shear stresses (as presented in Eq. (2.9)). The remainder of their analysis is similar to that discussed in this section and in Section 2.2.2.

2.2.4 Exponential Load Transfer Along Plug-Rock Interface Using Concrete Reinforcement Interaction Solutions

Reinforced concrete provides another inclusion bond strength problem similar to a plug-rock system. Morley and Royles (1983c, pp. 660-662) present a theoretical study on bond stresses in the anchorage zone of reinforced concrete structures. The following section gives the application of their analysis to a plug-rock system.

The slip (Δ) at any plug-rock section can be written in terms of the vertical displacements in the plug, w_p, and rock, w_R, at that section as:

$$\Delta = -(w_p - w_R) \tag{2.72}$$

and so,

$$\frac{d\Delta}{dz} = -\left(\frac{dw_p}{dz} - \frac{dw_R}{dz}\right) = -(\epsilon_z^P - \epsilon_z^R) \tag{2.73}$$

where ϵ_z^P and ϵ_z^R are the vertical plug and rock strains in any plug-rock section.

Assuming that the rock strains are relatively small under slipping, then from the one-dimensional Hooke's law:

$$\frac{d\Delta}{dz} = -\epsilon_z^P = -\frac{\sigma_z^P}{E_p} \tag{2.74}$$

and

$$\frac{d^2\Delta}{dz^2} = -\frac{1}{E_p}\frac{d\sigma_z^P}{dz} \tag{2.75}$$

where σ_z^P = axial stress within plug
E_p = Young's modulus of plug.

Equilibrium of element ABC'D' between z and z + dz (Fig. 2.3) leads to:

$$\sum F_z = \left(\sigma_z^P - \sigma_z^P - \frac{\sigma_z^P}{dz}dz\right)\frac{\pi D^2}{4} - \tau_{rz,i}\pi D\,dz = 0 \tag{2.76}$$

where D = plug diameter.

$$\frac{d\sigma_z^p}{dz} = -\frac{4}{D}\tau_{rz,i} \tag{2.77}$$

Substituting Eq. (2.77) into (2.75) gives:

$$\frac{d^2\Delta}{dz^2} = \tau_{rz,i}k^2 \tag{2.78}$$

where

$$k^2 = \frac{4}{E_p D}$$

Equation (2.78) can be solved by breaking the interface shear stress-slip curve into three parts. The curve is made up of two linear and one polynomial parts, as shown in Figure 2.4. The differential equation (2.78) can be solved by considering each part or stage in turn.

Stage 1 (Figure 2.4). Consider:

$$\tau_{rz,i} = m_1\Delta \tag{2.79a}$$

where m_1 = slope of the curve representing Stage 1 (Figure 2.4).

and from Eq. (2.78):

$$\frac{d^2\Delta}{dz^2} = k_1^2\Delta \tag{2.79b}$$

where $k_1^2 = k^2 m_1$. A solution to the above equation can be written in the form:

$$\Delta = Ae^{k_1 z} + Be^{-k_1 z} \tag{2.79c}$$

and

$$\frac{d\Delta}{dz} = Ak_1 e^{k_1 z} - Bk_1 e^{-k_1 z} \tag{2.79d}$$

Boundary conditions at z = 0 (at top of plug) are $\Delta = -\Delta_o$ and $d\Delta/dz = -\sigma_{po}/E_p$. Δ_o is the axial plug displacement and σ_{po} is the axial stress applied at slip initiation. Therefore, from Eqs. (2.79c and d):

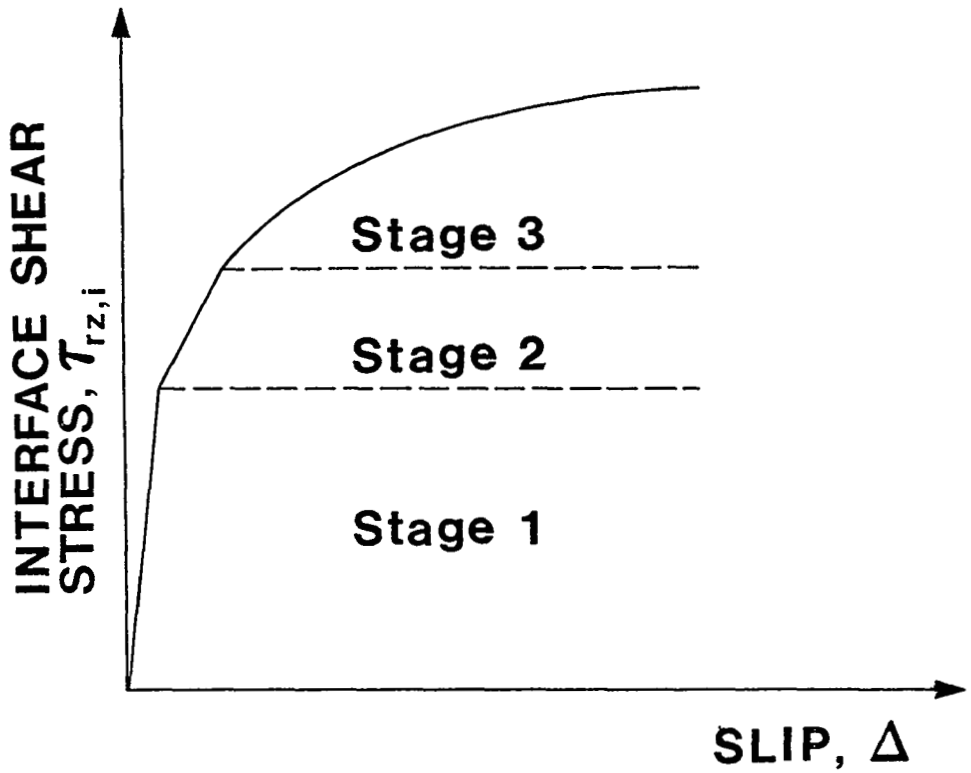

Figure 2.4 Breakdown of the interface shear stress - slip curve into three stages.

(Reprinted by permission of the Institution of Civil Engineers, From P.D. Morley and R. Royles, Proc. Instn. Civ. Engrs., Part 2, 1983, 75, Dec., Paper 8701, Fig. 10, p. 667.
Copyright 1983, Institution of Civil Engineers, London.)

$$\Delta = -(\Delta_o/2 + \sigma_{po}/2E_p k_1)e^{k_1 z} - (\Delta_o/2 - \sigma_{po}/2E_p k_1)e^{-k_1 z} \quad (2.79e)$$

and

$$\sigma_z^p = E_p k_1\left[(\Delta_o/2 + \sigma_{po}/2E_p k_1)e^{k_1 z} - (\Delta_o/2 - \sigma_{po}/2E_p k_1)e^{-k_1 z}\right] \quad (2.79f)$$

where σ_z^p = axial stress within plug
Δ = slip at any plug-rock section
$k_1 = (4m_1/E_p D)^{1/2}$.

Substituting Eq. (2.79e) into (2.79a) gives the expression for $\tau_{rz,i}$.

Stage 2 (Figure 2.4). Consider:

$$\tau_{rz,i} = m_2\Delta + C_2 \quad (2.80a)$$

where m_2 = slope of the curve representing Stage 2 (Figure 2.4)..
C_2 = y-intercept.

and from Eq. (2.78):

$$\frac{d^2\Delta}{dz^2} - k_2^2\Delta = k^2 C_2 \quad (2.80b)$$

where $k_2^2 = k^2 m_2$. The general solution of the above equation is:

$$\Delta = Ae^{k_2 z} + Be^{-k_2 z} - C_2/m_2 \quad (2.80c)$$

Introducing the boundary conditions given in Stage 1 yields:

$$\Delta = -(\Delta_o/2 - C_2/2m_2 + \sigma_{po}/2E_p k_2)e^{k_2 z} - (\Delta_o/2 + C_2/2m_2 - \sigma_{po}/2E_p k_2)e^{-k_2 z} - \frac{C_2}{m_2} \quad (2.80d)$$

and

$$\sigma_z^p = E_p k_2\left[(\Delta_o/2 - C_2/2m_2 + \sigma_{po}/2E_p k_2)e^{k_2 z} + (\Delta_o/2 + C_2/2m_2 - \sigma_{po}/2E_p k_2)e^{-k_2 z}\right] \quad (2.80e)$$

where Δ = slip at any plug-rock section
σ_z^p = axial stress within plug
$k_2 = (4m_2/E_p D)^{1/2}$.

Substituting Eq. (2.80d) into (2.80a) gives the expression for $\tau_{rz,i}$.

Stage 3 (Figure 2.4). Morley and Royles (1983c, p. 661) assume a polynomial relation between the interface shear stress ($\tau_{rz,i}$) and plug slip (Δ) for Stage 3. They state that a numerical integration scheme leads to the solution of the plug slip, which in turn yields a solution for the axial stress within the plug and for the interface shear stress. The method presents an interesting approach to the nonlinear interaction, which is postulated here to be less important in the context of a design approach which is recommended to remain quite conservative, i.e. well below the elastic limit.

Equations (2.72) through (2.80e) give different Δ, $\tau_{rz,i}$ and σ_z^p values for each stage of the shear stress-slip curve presented in Figure 2.4. The boundary conditions given below Eq. (2.79d) show that not all of the stress applied to the plug (σ_{po}) transfers to the rock. This solution does not completely satisfy the boundary condition of the borehole plug system (i.e. $\sigma_z^p = 0$ at $z = L$).

2.3 Interactions Between Plug and Host Rock Under Combined Axial, Lateral, and Thermal Loading

The main objective of this section is to study the influence of axial stress and lateral external stress along a loaded borehole plug in rock and thermal effects. Additional objectives are to study the resultant interfacial shear stress and axial plug displacement due to an axial load applied to the plug and due to thermal effects.

2.3.1 Influence of Axial Stress Applied to the Plug and Lateral External Stress on Radial Contact Stress

The push-out tests reported in Chapter 4 are performed on plugs in unconfined rock cylinders. A change in the lateral stressfield can either increase or decrease the radial contact (normal) stress across the interface (Jeffrey, 1980, pp. 18-60; Jeffrey and Daemen, 1981). Changes in the transverse direction can result from slow or rapid tectonic deformations, from thermally induced rock mass deformation resulting from high-level radioactive waste emplacement, or from pressurization by magmatic intrusions.

The main objective of this section is to study the effects of the axial stress applied to the plug and of lateral external stresses or stress changes on the normal stress across the plug/rock interface, and on the radial displacement along the plug-rock interface. The solutions are presented for cases of plane strain and plane stress. The plane strain solution is used for an infinite rock mass.

2.3.1.1 Influence of Axial Stress Applied to the Plug on Radial Contact Stress

A compressive axial stress (σ_{po}) applied to a plug generates a radial stress (σ_r^p) along the plug/rock contact and an outward radial displacement of the plug ($u_{p,z}/a$). The solution for σ_r^p/σ_{po} is presented in Eq. (2.53) as:

$$\frac{\sigma_r^P}{\sigma_{po}} = (VSF)\frac{\sinh[\alpha(L-z)]}{\sinh(\alpha L)} \tag{2.81}$$

The radial displacement in the plug ($u_{p,z}$) due to an applied axial plug stress may be expressed for the case of plane strain by combining Eq. (2.35) or (2.37a) into (2.38a):

$$\frac{u_{P,Z}}{a} = -\frac{\sinh[\alpha(L-z)]}{\sinh(\alpha L)}$$

$$\frac{(\sigma_{po}/E_R)\nu_P(1+\nu_R)[(1-2\nu_R)(a/R)^2+1]}{(1-\nu_P)(1-(a/R)^2)+(E_p/E_R)(1+\nu_R)[(1-2\nu_R)(a/R)^2+1]} \tag{2.82}$$

For the case of plane stress in the confining rock cylinder, the radial displacement in the plug ($u_{P,Z}/a$) due to an applied axial plug stress may be obtained by combining Eq. (2.35) or (2.37b) into (2.38b):

$$\frac{u_{P,Z}}{a} = -\frac{\sinh[\alpha(L-z)]}{\sinh(\alpha L)}$$

$$\frac{(\sigma_{po}/E_R)\nu_P[(1-\nu_R)(a/R)^2+(1+\nu_R)]}{(1-\nu_P)(1-(a/R)^2)+(E_p/E_R)[(1-\nu_R)(a/R)^2+(1+\nu_R)]} \tag{2.83}$$

2.3.1.2 Influence of Lateral External Stress

A lateral external stress (σ_o) applied to a plugged rock cylinder generates a normal (radial) contact stress (σ_i) and an inward radial plug displacement ($u_{P,C}$) along the plug/rock contact. The radial displacement ($u_{R,C}$) in the rock at the plug/rock contact, due to an external stress (σ_o) and internal stress (σ_i) follows from Eq. (2.36a) for a plane strain configuration and from Eq. (2.36b) for a plane stress assumption.

The radial displacement in the plug at the plug/rock contact can be calculated from Hooke's law. For plane strain ($\epsilon_z^P = 0$):

$$u_{P,C} = \frac{(1+\nu_P)(1-2\nu_P)a}{E_p}\sigma_i \tag{2.84}$$

and for plane stress ($\sigma_z^P = 0$):

$$u_{P,C} = \frac{(1-\nu_P)a}{E_p}\sigma_i \tag{2.85}$$

where $u_{P,C}$ = radial displacement in the plug at the plug/rock contact

σ_i = radial stress developed along the plug/rock contact due to an applied external lateral stress

E_p = Young's modulus of plug

ν_P = Poisson's ratio of plug

a = plug radius

ϵ_z^P = axial strain in plug

σ_z^P = axial stress in plug.

Equating the rock and plug displacements gives the solution for the normal stress at the plug/rock contact as a fraction of the applied lateral external stress. Equating Eq. (2.36a) and (2.84) for a plane strain solution yields:

$$\frac{\sigma_i}{\sigma_o} = \frac{2(E_p/E_R)(1+\nu_R)(1-\nu_R)}{(E_p/E_R)(1+\nu_R)[(1-2\nu_R)(a/R)^2+1]+(1+\nu_P)(1-2\nu_P)(1-(a/R)^2)} \tag{2.86a}$$

Equating (2.36b) and (2.85) gives σ_i/σ_o for a plane stress approximation:

$$\frac{\sigma_i}{\sigma_o} = \frac{2(E_p/E_R)}{(E_p/E_R)[(1+\nu_R)+(1-\nu_R)(a/R)^2]+(1-\nu_P)(1-(a/R)^2)} \tag{2.86b}$$

The radial displacement in the plug, for a plane strain approximation, may be calculated from Eq. (2.36a) or (2.84) by substituting for σ_i from Eq. (2.86a):

$$\frac{u_{P,C}}{a} = \frac{2(\sigma_o/E_R)(1+\nu_P)(1-2\nu_P)(1+\nu_R)(1-\nu_R)}{(E_p/E_R)(1+\nu_R)[(1-2\nu_R)(a/R)^2+1]+(1+\nu_P)(1-2\nu_P)(1-(a/R)^2)} \tag{2.87a}$$

For a plane stress approximation, the radial displacement in the plug may be calculated from Eq. (2.36b) or (2.84) by substituting σ_i from Eq. (2.86b):

$$\frac{u_{P,c}}{a} =$$

$$\frac{2(\sigma_o/E_R)(1-\nu_P)}{(E_p/E_R)[(1+\nu_R)+(1-\nu_R)(a/R)^2]+(1-\nu_P)(1-(a/R)^2)} \qquad (2.87b)$$

2.3.2 Theoretical Analysis of Mechanical Plug-Rock Interactions Caused by Temperature Changes

Some push-out samples are heated in order to study the influence of elevated temperatures on borehole plug performance (Chapter 4). Thermal stresses are induced when a borehole plug-rock composite is heated. A linear deformation w_T is expressed by the relation (e.g. Drucker, 1967, p. 84):

$$w_T = \alpha L(\Delta T) \qquad (2.88)$$

in which α is the coefficient of linear thermal expansion, usually expressed in units of meter per meter·per degree of temperature change, L is the initial length of the body, and ΔT is the temperature change. The analysis presented here assumes a uniform temperature increase throughout the push-out sample.

2.3.2.1 Theoretical Analysis of Thermally Induced Axial Stresses and Displacements

Figure 2.5 gives the model used for thermal stress calculations in the axial direction. The model is valid in the interval within which the plug is emplaced (i.e. $-L/2 \le z_t \le L/2$). The axial displacement of the plug ($w_p^{\Delta T}$) and of the rock ($w_R^{\Delta T}$) due to a temperature change ΔT, assuming that they are free to expand axially (i.e. that no interface restraint develops), is shown in Figure 2.5b. From Eq. (2.88):

$$w_p^{\Delta T} = -\int_0^{z_t} \alpha_p \Delta T \, dz_t = -\alpha_p \Delta T z_t \qquad (2.89a)$$

$$w_R^{\Delta T} = -\int_0^{z_t} \alpha_R \Delta T \, dz_t = -\alpha_R \Delta T z_t \qquad (2.89b)$$

where α_p = coefficient of linear thermal expansion of the plug
α_R = coefficient of linear thermal expansion of the rock
dz_t = thickness of element ABCD (Figure 2.5)
z_t = the coordinate along the axis of the plug of a push-out cylinder with origin at the symmetry plane ($-L/2 \le z_t \le L/2$).

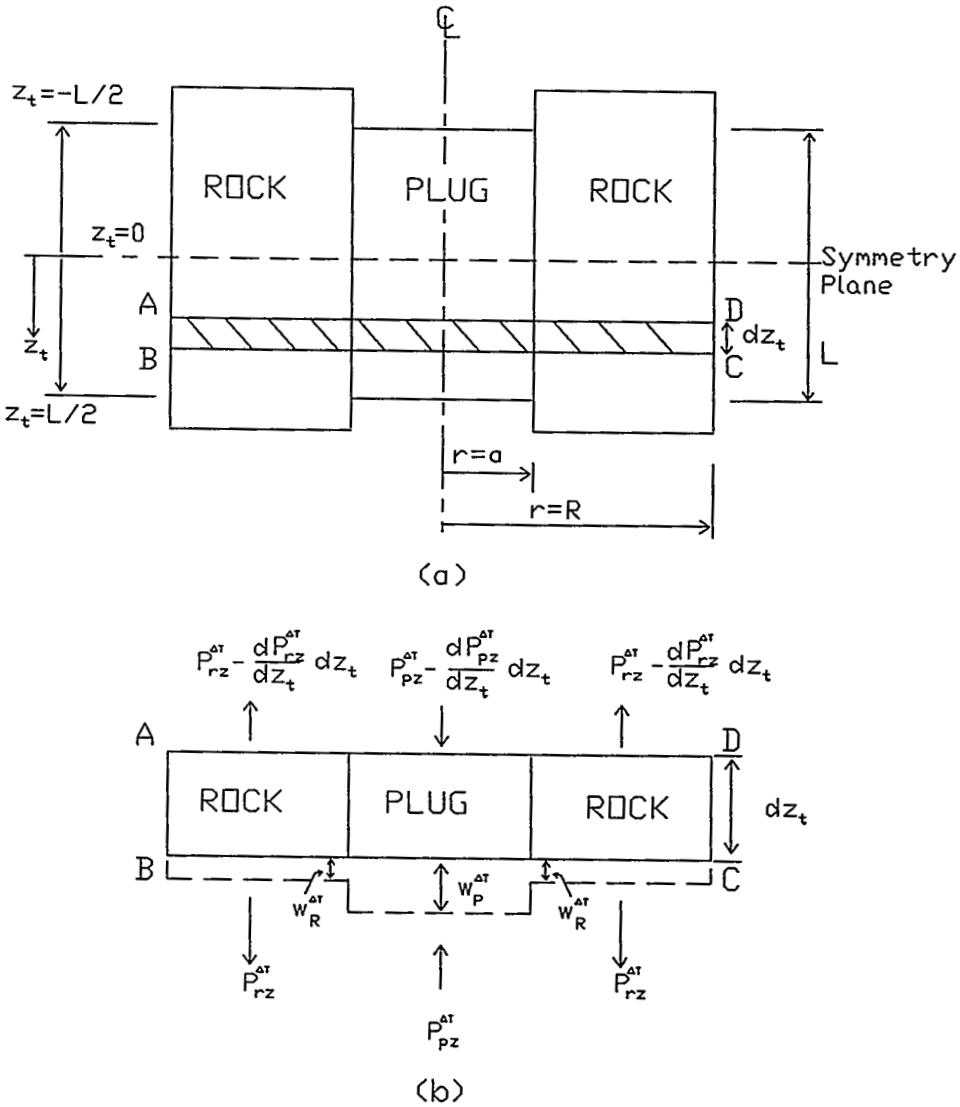

Figure 2.5 Model used for thermal stress calculations (in the axial direction). Displacements w in (b) indicate the elongation at the level BC assuming that no interaction between plug and host rock cylinder restrains the thermal expansion. Forces P develop as a result of the restraining interaction.

If the coefficient of thermal expansion of the plug material is larger than that of the rock, the forces in the plug and in the rock must be such that they shorten the plug and stretch the rock until the final elongations of the plug and the rock are the same (a compatibility requirement if no slip occurs along the interface). A greatly simplified distribution of these forces is shown in Figure 2.5b, where $P_{pz}^{\Delta T}$ denotes the axial force in the plug and $P_{rz}^{\Delta T}$ denotes the axial force in the rock (e.g. Drucker, 1967, pp. 101-102). Assuming uniaxial stress-strain states in the plug and in the rock, the corresponding axial strain increment in the plug ($d\epsilon_p^{\Delta T}$) and in the rock ($d\epsilon_R^{\Delta T}$) at section dz_t (Figure 2.5) is:

$$d\epsilon_p^{\Delta T} = \frac{\frac{dP_{pz}^{\Delta T}}{dz_t} dz_t}{E_p A_p} \tag{2.90a}$$

and

$$d\epsilon_R^{\Delta T} = -\frac{\frac{dP_{rz}^{\Delta T}}{dz_t} dz_t}{E_R A_R} \tag{2.90b}$$

where $\frac{dP_{pz}^{\Delta T}}{dz_t} dz_t, \frac{dP_{rz}^{\Delta T}}{dz_t} dz_t$ = axial thermal force increment over section dz_t within plug and rock, respectively (Figure 2.5)

E_p, E_R = Young's modulus of plug and rock, respectively

A_p, A_R = Cross-sectional area of plug and rock, respectively.

Considering equilibrium of element ABCD, Figure 2.5b, $\sum Fz_t = 0$:

$$P_{pz}^{\Delta T} = P_{rz}^{\Delta T} \tag{2.91a}$$

Assuming a fourth-order distribution (symmetric about the mid-plane of the plug) for the axial thermal forces in the plug and in the rock leads to:

$$P_{pz}^{\Delta T} = P_{rz}^{\Delta T} = f(z_t) \tag{5.9b}$$

where $f(z_t) = A + Bz_t^2 + Cz_t^4$

A, B and C are constants that can be evaluated from the boundary conditions:

$$f(0) = P_{\max}^{\Delta T}; f\left(\pm\frac{L}{2}\right) = 0; \frac{df}{dz_t}\left(\pm\frac{L}{2}\right) = 0$$

The first condition expresses that the axial thermal forces are maximum at the symmetry plane. The second set of conditions assure that the ends of the plug are free of normal stress. The last conditions impose freedom from shear stresses of the plug ends.

Substituting for the constants A, B and C into Eq. (2.91b) yields:

$$P_{pz}^{\Delta T} = P_{rz}^{\Delta T} = P_{\max}^{\Delta T}\left(1 - \frac{8z_t^2}{L^2} + \frac{16z_t^4}{L^4}\right) \tag{2.91c}$$

where $P_{\max}^{\Delta T}$ = maximum axial thermal force in rock and plug.

Combining Eq. (2.91c) into (2.90a and b) yields:

$$d\epsilon_p^{\Delta T} = \frac{P_{\max}^{\Delta T}\left[-\frac{16z_t}{L^2} + \frac{64z_t^3}{L^4}\right]dz_t}{E_p A_p} \tag{2.92a}$$

and

$$d\epsilon_R^{\Delta T} = -\frac{P_{\max}^{\Delta T}\left[-\frac{16z_t}{L^2} + \frac{64z_t^3}{L^4}\right]dz_t}{E_R A_R} \tag{2.92b}$$

where $d\epsilon_p^{\Delta T}, d\epsilon_R^{\Delta T}$ = axial strain increments in plug and in rock at section dz_t, respectively.

The total axial strain in the plug ($\epsilon_p^{\Delta T}$) and in the rock ($\epsilon_R^{\Delta T}$) due to the interaction between rock and plug is:

$$\epsilon_p^{\Delta T} = \int_0^{z_t} d\epsilon_p^{\Delta T} = \frac{P_{\max}^{\Delta T}}{E_p A_p}\left[-\frac{8z_t^2}{L^2} + \frac{16z_t^4}{L^4}\right] \tag{2.93a}$$

and

$$\epsilon_R^{\Delta T} = \int_0^{z_t} d\epsilon_R^{\Delta T} = -\frac{P_{\max}^{\Delta T}}{E_R A_R}\left[-\frac{8z_t^2}{L^2} + \frac{16z_t^4}{L^4}\right] \tag{2.93b}$$

The total axial plug displacement ($w_{p,T}^{\Delta T}$) due to the relative shortening of the plug caused by the restraint exerted by the rock and due to a uniform temperature increase (ΔT) follows from Eqs. (2.89a) and (2.93a):

$$w_{p,T}^{\Delta T} = \int_0^{z_t} (\epsilon_p^{\Delta T} - \Delta T \alpha_p) dz_t = \frac{P_{max}^{\Delta T}}{E_p A_p}\left[\frac{-8z_t^3}{3L^2} + \frac{16z_t^5}{5L^4}\right] - \Delta T \alpha_p z_t \qquad (2.94a)$$

or

$$\frac{w_{p,T}^{\Delta T}}{(L/2)} = s\left[\frac{P_{max}^{\Delta T}}{E_p A_p}\left(-\frac{16s^2}{3} + \frac{32s^4}{5}\right) - 2\Delta T \alpha_p\right] \qquad (2.94b)$$

where $z_t = sL$ $\quad -0.5 \le s \le 0$ for $-L/2 \le z_t \le 0$
$\quad 0 \le s \le 0.5$ for $0 \le z_t \le L/2$

The total axial rock displacement ($w_{R,T}^{\Delta T}$) due to the elongation of the rock and due to a uniform temperature increase (ΔT) follows from Eqs. (2.89b) and (2.93b):

$$w_{R,T}^{\Delta T} = \int_0^{z_t} (\epsilon_R^{\Delta T} - \Delta T \alpha_R) dz_t = -\frac{P_{max}^{\Delta T}}{E_R A_R}\left[-\frac{8z_t^3}{3L^2} + \frac{16z_t^5}{5L^4}\right] - \Delta T \alpha_R z_t \qquad (2.94c)$$

or

$$\frac{w_{R,T}^{\Delta T}}{(L/2)} = s\left[-\frac{P_{max}^{\Delta T}}{E_R A_R}\left(-\frac{16s^2}{3} + \frac{32s^4}{5}\right) - 2\Delta T \alpha_R\right] \qquad (2.94d)$$

Inspection of the equations for the axial plug and rock displacements (Eqs. 2.94a,c) indicates that they are not equal (or compatible) along the plug/rock interface. This is due to the error introduced by the selection of a fourth-order function for the axial thermal forces (Eq. 2.91b). One way to reduce the error is to assume compatibility at various locations along the interface (e.g. s = 0.05, 0.1, ..., 0.5) and to obtain the location that gives the smallest difference in the axial plug and rock displacements.[1]

The difference in the axial plug and rock displacements along the interface (Eqs. 2.94b and d) as a function of the point selected for compatibility is plotted in Figure 2.6. The area under the displacement difference is minimum (i.e. the error is minimized) when assuming compatibility at s = 0.40 (Figure 2.6).

Substituting s = 0.4 into Eqs. (2.94b and d) and equating Eqs. (2.94b and d) gives the solution for the axial thermal force in the plug ($P_{pz}^{\Delta T}$) and in the rock ($P_{rz}^{\Delta T}$) (noting that $z_t = sL$):

---

1 Kiousis, P.D., 1990, personal communication, Assistant Professor, Department of Civil Engineering and Engineering Mechanics, University of Arizona, Tucson.

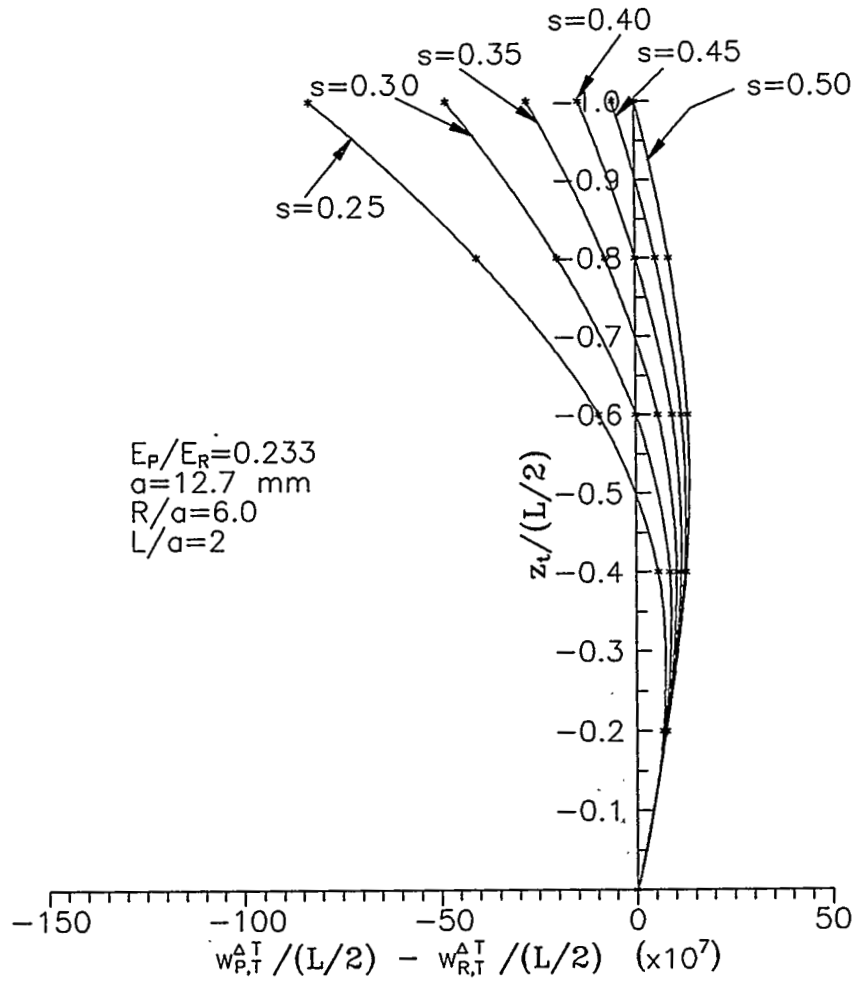

Figure 2.6 The difference in the axial plug ($w^{\Delta T}_{P,T}/(L/2)$) and axial rock ($w^{\Delta T}_{R,T}/(L/2)$) displacements along the interface as a function of the point selected for compatibility (z_t = sL; -0.5 ≤ s ≤ 0). Definitions for all variables are given in Eq. (2.85).

$$P_{pz}^{\Delta T} = -P_{rz}^{\Delta T} = \frac{2.9(\Delta T)(\alpha_p - \alpha_R)}{\left[\frac{1}{E_R A_R} + \frac{1}{E_p A_p}\right]}\left(1 - \frac{8z_l^2}{L^2} + \frac{16z_l^4}{L^4}\right) \tag{2.95}$$

where ΔT = uniform temperature increase

α_p, α_R = coefficient of linear thermal expansion of plug and rock, respectively

E_p, E_R = Young's modulus of plug and rock

A_p, A_R = cross-sectional area of plug and rock

L = plug length

$-L/2 \le z_l \le L/2$.

Substituting $A_p = \pi a^2$, $A_R = \pi(R^2 - a^2)$, $z_l = sL$, $\sigma_{z,\Delta T}^p = P_{pz}^{\Delta T}/A_p$ and $\sigma_{z,\Delta T}^R = P_{rz}^{\Delta T}/A_R$ into Eq. (2.95) yields:

$$\sigma_{z,\Delta T}^p = \frac{2.9(\Delta T)(\alpha_p - \alpha_R)E_p(1-(a/R)^2)}{(E_p/E_R)(a/R)^2 + (1-(a/R)^2)}(1 - 8s^2 + 16s^4) \tag{2.96a}$$

and

$$\sigma_{z,\Delta T}^R = \frac{-2.9(\Delta T)(\alpha_p - \alpha_R)E_p(a/R)^2}{(E_p/E_R)(a/R)^2 + (1-(a/R)^2)}(1 - 8s^2 + 16s^4) \tag{2.96b}$$

where $\sigma_{z,\Delta T}^p, \sigma_{z,\Delta T}^R$ = axial thermal stress in the plug and in the rock due to a temperature increase, ΔT

R = rock radius

a = plug radius.

Substituting Eq. (2.95) into (2.91c) gives the solution for $P_{\max}^{\Delta T}$:

$$P_{\max}^{\Delta T} = \frac{2.9(\Delta T)(\alpha_p - \alpha_R)}{\left[\frac{1}{E_R A_R} + \frac{1}{E_p A_p}\right]} \tag{2.97a}$$

Substituting Eq. (2.97a) into (2.94b and d) gives the total axial thermal plug displacement ($w_{P,T}^{\Delta T}$) and the total thermal axial rock displacement ($w_{R,T}^{\Delta T}$) at $z_l = \pm L/2$ as:

$$\frac{w_{P,T}^{\Delta T}}{(L/2)} = s\Delta T\left[\frac{-2.9(\alpha_p - \alpha_R)(1-(a/R)^2)}{(E_p/E_R)(a/R)^2 + (1-(a/R)^2)}\left[-\frac{16s^2}{3} + \frac{32s^4}{5}\right] - 2\alpha_p\right] \tag{2.97b}$$

and

$$\frac{w_{R,T}^{\Delta T}}{(L/2)} = s\Delta T\left[\frac{2.9(\alpha_p-\alpha_R)(E_p/E_R)(a/R)^2}{(E_p/E_R)(a/R)^2+(1-(a/R)^2)}\left[-\frac{16s^2}{3}+\frac{32s^4}{5}\right]-2\alpha_R\right] \tag{2.97c}$$

The thermal shear stress at the plug-rock interface ($\tau_{rz,i}^{\Delta T}$) follows from the equilibrium equation for an axially loaded borehole plug (Eq. 2.32):

$$\frac{d\sigma_{z,\Delta T}^{p}}{dz_i} = -\frac{2}{a}\tau_{rz,i}^{\Delta T} \tag{2.98a}$$

Substituting for $\sigma_{z,\Delta T}^{p}$ from Eq. (2.96a) (noting that $s = z_i/L$) into Eq. (2.98a) and differentiating yields:

$$\tau_{rz,i}^{\Delta T} = \frac{(2.9a/2L)\Delta T(\alpha_p-\alpha_R)E_p(1-(a/R)^2)}{(E_p/E_R)(a/R)^2+(1-(a/R)^2)}(64s^3-16s) \tag{2.98b}$$

where $z_i = sL$ $\quad -0.5 \le s \le 0$ for $-L/2 \le z_i \le 0$
$\quad 0 \le s \le 0.5$ for $0 \le z_i \le L/2$

The interface shear stress given by Eq. (2.98b) is zero at the top, middle (at the symmetry plane) and bottom of the plug/rock interface.

An alternative solution for the interface shear stress is to evaluate the interface shear strain induced by elevated temperature ($\gamma_{i,\Delta T}$) (Greszczuk, 1969, p. 49):

$$\gamma_{i,\Delta T} = \frac{w_{P,T}^{\Delta T} - w_{R,T}^{\Delta T}}{b_i} \tag{2.99a}$$

where b_i = effective interface width

The interface shear stress due to the shear strain is:

$$\tau_{rz,i}^{\Delta T} = \gamma_{i,\Delta T}G_i = \frac{w_{P,T}^{\Delta T} - w_{R,T}^{\Delta T}}{b_i}G_i \tag{2.99b}$$

where G_i = shear modulus of the interface.
$w_{P,T}^{\Delta T}$, $w_{R,T}^{\Delta T}$ = axial thermal displacements in plug and rock, respectively.

Eq. (2.99b) requires terms that involve interface properties (e.g. b_i, G_i), which are not obvious and are not easily determined.

2.3.2.2 Theoretical Analysis of Thermally Induced Lateral Stresses and Displacements

The thermally induced total normal stress at the plug/rock interface due to a uniform temperature increase is given by:

$$\sigma_{n,\Delta T} = \sigma_r^{\Delta T} + \sigma_{r,\Delta T}^{P} \qquad (2.100)$$

where $\sigma_r^{\Delta T}$ = thermally induced radial stress at plug/rock interface due to the thermal axial stress in the plug ($\sigma_{z,\Delta T}^{P}$) (not constant along plug/rock interface)

$\sigma_{r,\Delta T}^{P}$ = thermally induced radial stress at plug/rock interface due to the differences in the thermal radial expansions of plug and rock (assumed constant along interface).

The axial thermal stress in a plug due to a uniform temperature increase ($\sigma_{z,\Delta T}^{P}$) is given by Eq. (2.96a). The relation between the axially induced thermal stress in a plug ($\sigma_{z,\Delta T}^{P}$) and the resulting compressive radial stress at the plug/rock interface follows from Eq. (2.39) as:

$$\sigma_r^{\Delta T} = (VSF)\sigma_{z,\Delta T}^{P} \qquad (2.101a)$$

where VSF = vertical stress function (given in Eq. (2.39)).

Combining Eq. (2.96a) into (2.101a) gives the thermally induced radial stress at the plug/rock interface due to a thermal vertical stress in the plug:

$$\sigma_r^{\Delta T} = \frac{2.9(\Delta T)(\alpha_p - \alpha_R)E_p(1-(a/R)^2)}{(E_p/E_R)(a/R)^2 + (1-(a/R)^2)}(VSF)(1-8s^2+16s^4) \qquad (2.101b)$$

where VSF = vertical stress function

α_p, α_R = coefficient of linear thermal expansion of plug and rock, respectively.

E_p, E_R = Young's modulus of plug and rock

A_p, A_R = cross-sectional area of plug and rock

a = plug radius

L = plug length

R = rock cylinder radius

s = described by Eq. (2.98b).

The thermally induced radial stress at the plug/rock interface due to the differences in the thermal radial expansions of plug and rock (along the interface); as a result of a uniform temperature increase ($\sigma_{r,\Delta T}^{P}$), can be calculated from thermal elasticity (e.g. Sokolnikoff, 1956, p. 359; Burgreen, 1971, pp. 1-5).

The resultant radial displacement on the inside periphery of a plugged rock cylinder ($u_R^{\Delta T}$ at r = a), due to the difference in the coefficient of linear thermal expansion of plug and rock (for a rock core subjected to a uniform temperature increase, ΔT), is the summation of (1) the (outward) radial displacement ($u_{r,0}^{\Delta T}$) of the unconstrained rock core at r = a, due to a uniform temperature increase ΔT, and (2) the (outward) radial displacement ($u_{r,i}^{\Delta T}$) of the rock core due to a (compressive) radial stress ($\sigma_{r,\Delta T}^{P}$) resulting from the plug-rock interaction, acting at r = a:

$$u_R^{\Delta T} = u_{r,0}^{\Delta T} + u_{r,i}^{\Delta T} \qquad (2.102a)$$

(1) The outward radial displacement of the rock core at r = a due to ΔT can be calculated from the formula derived from Timoshenko and Goodier (1970, p. 448) or from Hearn (1977, pp. 210-212), for a uniformly heated cylinder with a concentric hole, subjected to free expansion (assuming plane strain) as:

$$u_{r,0}^{\Delta T} = -(1+\nu_R)\alpha_R \Delta T a \qquad (2.102b)$$

where ν_R = Poisson's ratio of rock
α_R = coefficient of linear thermal expansion of rock
ΔT = uniform temperature increase
a = rock core inside (plug) radius.

(2) The (outward) radial displacement of the rock cylinder at the plug/rock contact due to a radial stress can be calculated from the formula given by Jaeger and Cook (1979, p. 135, Eq. (8)) for plane strain as:

$$u_{r,i}^{\Delta T} = -\frac{\sigma_{r,\Delta T}^{P}(1+\nu_R)a}{E_R(R^2-a^2)}[(1-2\nu_R)a^2+R^2] \qquad (2.102c)$$

The resultant radial displacement on the inside periphery of the plugged rock cylinder ($u_R^{\Delta T}$ at r = a), subjected to a uniform temperature increase, is the combination of Eqs. (2.102b and c) into (2.102a):

$$u_R^{\Delta T} = -(1+\nu_R)\alpha_R \Delta T a - \frac{\sigma_{r,\Delta T}^{P}(1+\nu_R)a}{E_R(R^2-a^2)}[(1-2\nu_R)a^2+R^2] \qquad (2.102d)$$

The resultant radial displacement on the outside periphery of the cement plug ($u_P^{\Delta T}$ at r = a) can be calculated in a similar way to that of the rock core:

$$u_p^{\Delta T} = -u_{p,0}^{\Delta T} + u_{p,i}^{\Delta T} \qquad (2.102e)$$

where $u_{p,0}^{\Delta T}$ = the (outward) radial displacement of an unconstrained cement plug at $r = a$ due to a uniform temperature increase ΔT

$u_{p,i}^{\Delta T}$ = the (inward) radial displacement of the cement plug due to a (compressive) radial stress ($\sigma_{r,\Delta T}^{p}$) acting at r = a

$u_{p,0}^{\Delta T}$ can be calculated from the formula derived from Timoshenko and Goodier, 1970, p. 445, for a uniformly heated solid cylinder free to expand laterally under axial plane strain:

$$u_{p,0}^{\Delta T} = (1+\nu_p)\alpha_p \Delta T a \qquad (2.102f)$$

where ν_p = Poisson's ratio of plug
α_p = coefficient of linear thermal expansion of plug
ΔT = uniform temperature increase
a = plug radius.

The (inward) radial displacement on the outside of the plug ($u_{p,i}^{\Delta T}$ at r = a), due to a compressive radial stress ($\sigma_{r,\Delta T}^{p}$) along the plug/rock contact, can be derived from Hooke's law for a plane strain configuration as:

$$u_{p,i}^{\Delta T} = \frac{\sigma_{r,\Delta T}^{p}}{E_p}(1-2\nu_p)(1+\nu_p)a \qquad (2.102g)$$

The resultant radial displacement on the outside of the plug ($u_p^{\Delta T}$ at r = a), subjected to a uniform temperature increase ΔT, is the combination of Eqs. (2.102f and g) into (2.102e):

$$u_p^{\Delta T} = -(1+\nu_p)\alpha_p \Delta T a + \frac{\sigma_{r,\Delta T}}{E_p}(1-2\nu_p)(1+\nu_p)a \qquad (2.102h)$$

Equating the resultant rock and plug radial displacements along the plug/rock contact ($u_R^{\Delta T} = u_p^{\Delta T}$) gives the (compressive) radial stress ($\sigma_{r,\Delta T}^{p}$; assumed constant along the interface):

$$\sigma_{r,\Delta T}^{p} =$$

$$\frac{E_p \Delta T[(1+\nu_p)\alpha_p - (1+\nu_R)\alpha_R](1-(a/R)^2)}{(1-2\nu_p)(1+\nu_p)(1-(a/R)^2)+(1+\nu_R)(E_p/E_R)[(1-2\nu_R)(a/R)^2+1]} \qquad (2.103)$$

where ν_p, ν_R = Poisson's ratio of plug and rock, respectively
α_p, α_R = coefficient of linear thermal expansion of plug and rock

E_p, E_R = Young's modulus of plug and rock
ΔT = uniform temperature increase
a = plug radius
R = rock cylinder radius

Substituting Eq. (2.103) into (2.102a or e) gives the resultant radial displacement at the plug/rock contact, due to a uniform temperature increase ($u_R^{\Delta T}$ or $u_p^{\Delta T}$):

$$u_R^{\Delta T} = u_p^{\Delta T} = -(1+\nu_p)(1+\nu_R)\Delta T a$$

$$\left[\frac{\alpha_p\{(E_p/E_R)[(1-2\nu_R)(a/R)^2+1]\}+\alpha_R\{(1-2\nu_p)(1-(a/R)^2)\}}{(1-2\nu_p)(1+\nu_p)(1-(a/R)^2)+(1+\nu_R)(E_p/E_R)[(1-2\nu_R)(a/R)^2+1]}\right] \quad (2.104)$$

The equation for the radial stress ($\sigma_{r,\Delta T}^p$; Eq. (2.103)) has been substituted into both Eqs. (2.102d and h) to verify the solutions for the resultant rock and plug radial displacements (i.e. $u_R^{\Delta T} = u_P^{\Delta T}$, Eq. (2.104)).

2.3.3 Resultant Shear Stresses and Axial Plug Displacements due to a Combination of Axial Loading and Uniform Temperature Increase

The interfacial shear stresses and the axial plug displacements in a borehole plug-rock system are the sum of 1) the shear stresses and axial plug displacements due to an applied axial stress ($\tau_{rz,I}$ from Eq. (2.48), and w_p from Eq. (2.47)), and 2) shear stresses and displacements due to a temperature increase ($\tau_{rz,I}^{\Delta T}$ from Eq. (2.98b), and $w_{P,T}^{\Delta T}$ from Eq. (2.97a)). The resultant interface shear stress (τ_R) is given by:

$$\tau_R = \frac{\sigma_{po}\alpha a}{2}\frac{\cosh[\alpha(L-z)]}{\sinh(\alpha L)} + \frac{(2.9a/2L)(\Delta T)(\alpha_p-\alpha_R)E_p(1-(a/R)^2)}{(E_p/E_R)(a/R)^2+(1-(a/R)^2)}(64s^3-16s) \quad (2.105)$$

The resultant axial plug displacement ($w_{P,R}$) is given by:

$$w_{P,R} = \frac{(\sigma_{po}/E_p)(1-2\nu_p(VSF))}{\alpha}\frac{\cosh[\alpha(L-z)\,]}{\sinh(\alpha L)}$$

$$+ s(L/2)\Delta T\left[\frac{-2.9(\alpha_p-\alpha_R)(1-(a/R)^2)}{(E_p/E_R)(a/R)^2+(1-(a/R)^2)}\left[\frac{-16s^2}{3}+\frac{32s^4}{5}\right]-2\alpha_p\right] \quad (2.106)$$

All symbols are defined with Eqs. (2.39), (2.43a), (2.46), (2.89b), and (2.94b).

It follows from Eq. (2.105) (as presented in Section 5.4, Ch. 5) that the maximum resultant shear stress ($\tau_{rz,i}^{max}$) occurs at the top of the plug (i.e. z = 0, z_t = -L/2):

$$\tau_{rz,i}^{max} = \frac{\sigma_{po}\alpha a}{\tanh(\alpha L)} \tag{2.107}$$

Similarly, the maximum resultant axial plug displacement (w_{max}) occurs at the top of the plug (i.e. z = 0, z_t = - L/2):

$$w_{max} = \frac{(\sigma_{po}/E_p)(1-2\nu_p(VSF))}{\alpha\tanh(\alpha L)}$$

$$-\Delta T(L/2)\left[-\frac{1.353(\alpha_p-\alpha_R)(1-(a/R)^2)}{(E_p/E_R)(a/R)^2+(1-(a/R)^2)}+\alpha_p\right] \tag{2.108}$$

where definition of all symbols is given with Eqs. (2.39), (2.43a), (2.46), and (2.89b).

2.4 Strength of the Interface

The shear strength of the interface is given by:

$$|\tau| = c + \sigma_n \tan\phi \tag{2.109}$$

where c = cohesion (or adhesion)
ϕ = angle of friction along the interface
σ_n = normal stress across the interface.

The normal stress across the interface is the sum of the radial stress (σ_r^p) due to an applied axial plug stress σ_{po}, the thermally induced normal stress, and the cement swelling pressure (σ_s):

$$\sigma_n = \sigma_r^p + \sigma_{n,\Delta T} + \sigma_s \tag{2.110}$$

The radial stress due to an applied axial stress is given by Eq. (2.53):

$$\sigma_r^p = \sigma_{po}(VSF)\frac{\sinh[\alpha(L-z)]}{\sinh(\alpha L)} \tag{2.111}$$

All variables are defined in Eqs. (2.39), (2.43a) and (2.46).

The thermally induced total normal stress at the plug/rock interface due to a uniform temperature increase is given by:

$$\sigma_{n,\Delta T} = \sigma_r^{\Delta T} + \sigma_{r,\Delta T}^p \tag{2.112}$$

where $\sigma_r^{\Delta T}$ = thermally induced radial stress at the plug/rock interface due to the thermal axial stress in the plug ($\sigma_{z,\Delta T}^{p}$) (Eq. (2.101b))

$\sigma_{r,\Delta T}^{p}$ = thermally induced radial stress at plug/rock interface due to the difference in the thermal radial expansion of plug and rock (Eq. (2.103)).

The cement swelling stresses, generated by Self-Stress II cement are given in Section 4.2.3 and are assumed uniform along the plug/rock interface.

The peak strength along the plug-rock interface ($|\tau|_p$) occurs at the loaded end of the plug ($z = 0$, $z_t = -L/2$) as the radial stress due to an applied axial stress is maximum at $z = 0$ (Eq. (2.111)). The thermally induced radial stress at the plug/rock interface due to the thermal axial stress in the plug ($\sigma_r^{\Delta T}$; Eq. (2.101b)) is maximum at the symmetry plane, but is up to an order of magnitude smaller than the radial stress due to an applied axial stress. The cement swelling stress and thermally indued radial stress at the plug/rock interface due to the differences in the thermal radial expansions of plug and rock ($\sigma_{r,\Delta T}$; Eq. (2.103)) are assumed constant along the interface. The peak strength follows from Eq. (2.109):

$$|\tau|_p = c_p + \sigma_{n,t} \tan\phi_p \qquad (2.113)$$

where c_p = peak cohesion

ϕ_p = peak angle of friction

$\sigma_{n,t}$ = peak normal stress across plug/rock interface (occurs at the loaded end of plug (at $z = 0$, $z_t = -L/2$)).

The peak normal stress across the plug/rock interface is obtained by substituting Eqs. (2.111), (2.103) and the cement swelling stress (σ_s; Ch. 4) into (2.113) (with $z = 0$):

$$\sigma_{n,t} = \sigma_{po}(VSF) + \sigma_s + \frac{E_p \Delta T[(1+\nu_p)\alpha_p - (1+\nu_R)\alpha_R](1-(a/R)^2)}{(1-2\nu_p)(1+\nu_p)(1-(a/R)^2) - (1+\nu_R)(E_p/E_R)[(1-2\nu_R)(a/R)^2+1]} \qquad (2.114)$$

where σ_{po} = axial stress applied to the plug

VSF = vertical stress function (Eq. (2.39))

σ_s = cement swelling stress

E_p, E_R = Young's modulus of plug and rock, respectively

ν_p, ν_R = Poisson's ratio of plug and rock, respectively

α_p, α_R = coefficient of linear thermal expansion of plug and rock, respectively
a = plug radius
R = rock cylinder radius
ΔT = uniform temperature increase.

Substituting Eq. (2.114) into (2.113) gives the peak strength along the plug/rock interface.

2.5 Axially Loaded Rigid Borehole Plug

In the case of a rigid plug, the analysis for the axial stress and displacement distributions is particularly simple since the plug displaces a uniform distance along its entire length. As a limiting case of the mechanical interaction between plugs and rock, a rigid plug is defined as a plug much stiffer than the rock in which it is emplaced ($E_p/E_R \gg 1.0$). Neglecting end effects, the vertical plug displacement w_p^r under the applied axial stress σ_{po} generates a uniform shear stress ($\tau_{rz,i}^{av}$) along the plug-rock interface (e.g. Fleming et al, 1985, pp. 128-129; Scott, 1981, pp. 274-284).

For an axially loaded rigid borehole plug, neglecting end effects, the shear stress distribution at the plug/rock contact is uniform:

$$\frac{\tau_{rz,i}^{av}}{\sigma_{po}} = \frac{a}{2L} \tag{2.115}$$

where a = plug radius
L = plug length.

Equation (2.115) may also be obtained from Eq. (2.48) by taking the limit when the Young's modulus of the plug (E_p) tends to infinity (App. A).

Eq. (2.32) gives the equilibrium equation for an axially loaded borehole plug:

$$\frac{d\sigma_z^p}{dz} = -\frac{2}{a}\,\tau_{rz,i} \tag{2.116}$$

Substituting Eq. (2.115) into the equilibrium equation (2.116) and introducing the boundary conditions (at z = 0, $\sigma_z^p = \sigma_{po}$; at z = L, $\sigma_z^p = 0$) gives a linear axial stress distribution (σ_z^p) along an axially loaded rigid plug:

$$\frac{\sigma_z^p}{\sigma_{po}} = \left(1 - \frac{z}{L}\right) \tag{2.117}$$

where σ_{po} = axial stress applied to the plug
z = distance from initial location of loaded end of plug
L = plug length.

The interface shear stress is related to the axial plug displacement (Eq. (2.42)) by:

$$\tau_{rz,i} = \frac{w_p E_R}{2(1+\nu_R)\alpha \ln(r_m/\alpha)} \tag{2.118}$$

where r_m = critical radius (Eq. (2.42b)).

The solution for the uniform vertical displacement of an axially loaded rigid borehole plug (w_p^r) can be obtained by substituting Eq. (2.115) into (2.118):

$$\frac{w_p^r}{\alpha} = \frac{(\sigma_{po}/E_R)(1+\nu_R)\alpha \ln(r_m/\alpha)}{L} \tag{2.119}$$

where E_R, ν_R = Young's modulus and Poisson's ratio of rock
α, R = plug and rock cylinder radius.

2.6 Concluding Comments

The main objective of this chapter is to derive theoretical formulations for the stress and axial displacement distributions along an axially loaded borehole plug in rock. For this reason, mechanistically similar problems such as composite materials, rock bolts, piles and concrete reinforcement have been used as starting points for plug-rock interaction analyses. In all of these rather simplified analyses, the axial displacement of the host rock is either assumed to be zero, constant or negligible beyond a certain radial distance from the plug center. The majority of the models studied neglect the normal stress distribution in the rock. All of the models lead to exponential stress and axial displacement distributions.

The models have the limitation of assuming behavior is elastic. They usually assume that two adjacent points along the interface deform such that compatibility is maintained. They predict high stress concentrations at the loaded end of a borehole plug prior to slip initiation and are valid up to a certain load level where slip has not yet occurred. Hence, they lead to a more conservative plug design. The models that assume constant or negligible axial rock displacements at the plug/rock interface are valid at plug slip and are more realistic than the former analysis. At high loads, slip can occur and two initially adjacent points may no longer have the same displacements. However, they require the use of terms that involve interface properties (e.g. b_i, G_i) which are not obvious or are not easily determined (Section 2.2.1); or they require the installation of strain gages at the plug/rock interface to obtain the interface shear stress-axial plug displacement curve (e.g. concrete reinforcement analysis). For these reasons, the analysis given

in Section 2.2.2 will be used as a framework for the closed-form solutions of the theoretical stress and axial plug displacement distributions. The model neglects normal stress distribution in rock and assumes that the axial rock displacement is negligible at a critical radius, r_m, from the plug center.

CHAPTER THREE

FINITE ELEMENT ANALYSIS AND COMPARISON OF THE RESULTS WITH THE CLOSED-FORM SOLUTION

3.1 Introduction

The main objective of the finite element analysis is to study the detailed stress distribution in plugs and host rock. A secondary objective is to assess the validity of the simplified analytical models presented in Chapter 2. In order to validate the analytical solutions, the shear stress distribution at the plug-rock interface and within the rock, along with the vertical stress distribution within the plug and rock, as a function of the axial stress applied to the plug, is analyzed. The results of the finite element analysis is compared with the analytical solutions.

A vast literature is available on the finite element method (i.e Zienkiewicz, 1977; Cook, 1981; and Kardestuncer, 1987), and on inclusion-host mechanical interactions. Coates and Yu (1970) use two materials to study the behavior of rock anchors. Randolph and Wroth (1978) and Potts and Martins (1982) model axially loaded piles using two materials. Hollingshead (1971), Nitzsche and Haas (1976), Yap and Rodger (1984), and Tadolini (1986) use three material systems to analyze grouted rock bolts and rock anchors. Goodman et al. (1968) and Zienkiewicz et al. (1970) present a joint element which can be used along the interface. Desai and Holloway (1972), Desai (1974 ad 1977), Arya and Hegemier (1982) and Katona (1983) use double-node pairs along the interface. Desai et al. (1984) propose the use of a thin solid element along the interface. They show that an interface element with a thickness-to-length ratio range of 0.01 to 0.1 shows satisfactory agreement with observations of the direct shear tests.

3.2 Finite Element Analysis of Borehole Plug-Rock Interaction

3.2.1 Introduction

One objective of the finite element analysis is to determine the shear stress distribution along the plug/rock interface and within the rock, as well as the vertical stress distribution within the plug and rock. The finite element analysis is performed to assess the validity of the simplified analytical models presented in Chapter 2. The results of the finite element method and of the analytical solutions are compared as a function of Young's modulus ratio of plug and rock, rock cylinder outside-to-inside radius ratio, and plug length-to-radius ratio.

An axisymmetric finite element program, PLANE-2DFE, is used to determine the stress distribution within an axially loaded push-out specimen. The finite element analysis simulates a push-out test on elastic material for an applied axial plug stress of 1 MPa (145 psi). Desai (1979, pp.

335-357) and Desai and Abel (1972, pp. 136-139) give the finite element formulation for the four-node isoparametric axisymmetric elements used in this analysis.

Figure 3.1 gives the finite element mesh and boundary conditions for a plugged cylinder with an outside-to-inside radius ratio of 6 and plug length-to-radius ratio of 2. The model is designed for a 76.2 mm (3 in) radius tuff cylinder, 127 mm (5 in) long and with a 12.7 mm (0.5) radius coaxial hole. The cement plug located in the middle of the hole has a length of 25.4 mm (1 in). The mesh consists of 256 elements and 295 nodal points. The shaded region in the mesh gives the location where the stress distribution within the rock is analyzed.

Figures B.1 through B.3 (Appendix B) give the finite element mesh and boundary conditions for plugged tuff cylinders with outside-to-inside radius ratios of 60 and plug length-to-radius ratios (L/a) of 2, 4 and 8, respectively. All models are designed for 12.7 mm (0.5 in) radius coaxial holes centrally plugged with cement. The shaded regions in the meshes show the locations where the stress distributions in the rock are obtained. The objective of using finite element meshes with cylinder outside-to-inside radius ratios of 60 is to simulate an in-situ rock mass (e.g. as presented by Randolph and Wroth, 1978, pp. 1474-1476; Amir, 1986, p. 54; Scott, 1981, pp. 282-283, and Baguelin and Frank, 1979, as quoted by Fleming et al., 1985, p. 129). The mesh presented in Figure B.1 (App. B) consists of 313 elements and 342 nodal points, those in Figures B.2 and B.3 of 298 elements and 329 nodal points, and 318 elements and 351 nodal points, respectively.

The Young's modulus (E_R) and Poisson's ratio (ν_R) of Apache Leap tuff are 22.6 GPa and 0.20, respectively (Fuenkajorn and Daemen, 1990). The Self-Stress II cement has Young's modulus (E_P) and Poisson's ratio (ν_P) of 5.25 GPa and 0.22, respectively (Chapter 4). Therefore, push-out specimens used in this study have a modulus ratio (E_P/E_R) of 0.233. Later discussions that compare the results of the finite element analysis with those of the closed-form solution involve modulus ratio ranges from 0.1 to 10.0. The Poisson's ratio of the rock and of the plug cement is taken to be 0.20 and 0.22, respectively.

3.2.2 Validity of the Closed-Form Solutions

Most of the simplified analytical solutions presented in Chapter 2 ignore the normal stress distribution in the rock. The finite element method is used to check the validity of this simplification.

The plug-rock interface shear stress ($\tau_{rz,i}$) distribution is obtained from the finite element analysis by considering the equilibrium of each plug element (i.e. element EFGH, Figure 2.2(b)) along the interface. Equilibrium of element EFGH yields:

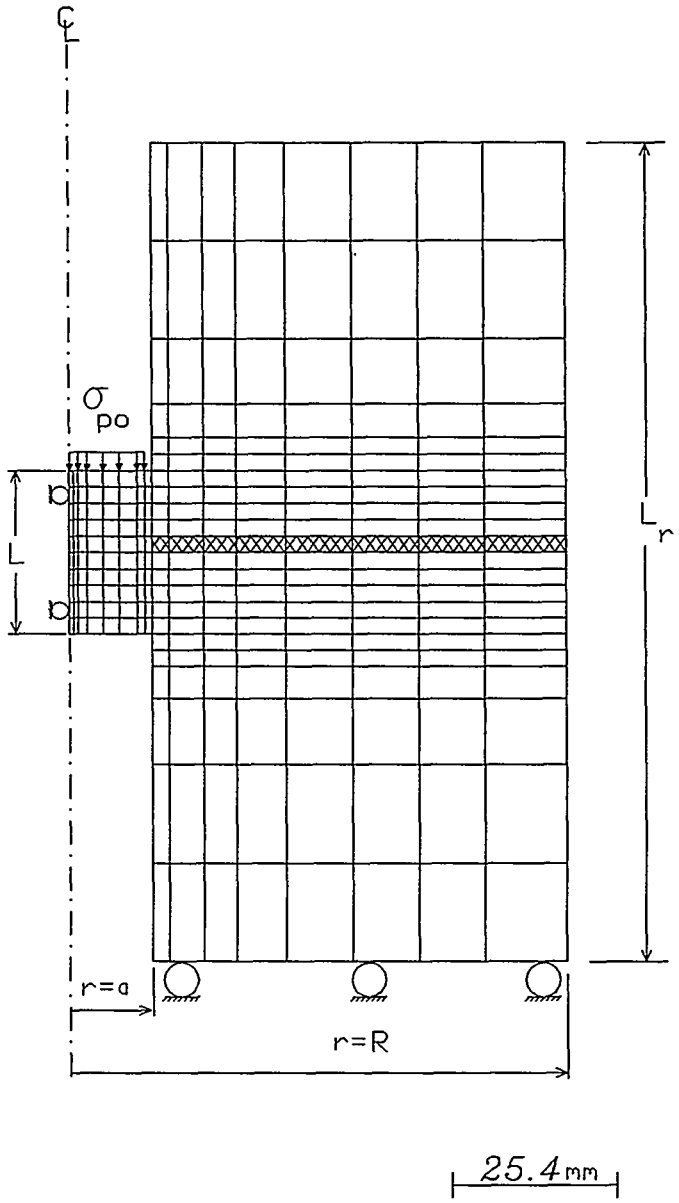

Figure 3.1 Finite element mesh and boundary conditions for a push-out specimen with a plug radius (a) of 12.7 mm, cylinder length (L_r) of 127 mm, cylinder outside-to-inside radius ratio (R/a) of 6 and plug length-to-radius ratio (L/a) of 2. The mesh represents a laboratory-size push-out specimen and consists of 256 elements and 295 nodal points. The shaded region shows the location where the axial stress and shear stress distribution within rock is studied in detail. σ_{po} = axial stress applied to the plug.

$$\sum F_z = P_{pz,u} - P_{pz,l} - 2\pi a \tau_{rz,l} dz = 0 \qquad (3.1a)$$

and

$$\tau_{rz,l} = \frac{P_{pz,u} - P_{pz,l}}{2\pi a dz} \qquad (3.1b)$$

where $P_{pz,u}$ and $P_{pz,l}$ = axial force acting on top and bottom of a plug slice of thickness dz (Figure 2.2(b))
a = plug radius.

Figure 3.2 presents an example to calculate $\tau_{rz,l}$ for a particular plug element, ABCD, with a thickness of dz_4. The vertical stress (σ_z^P) at each plug element centroid is obtained from the finite element output. σ_z^P is assumed to be uniform in each element and is converted to the axial force (P_{pz}) by:

$$P_{pz} = \pi(r_0^2 - r_i^2)\sigma_z^P \qquad (3.1c)$$

where P_{pz} = axial force (in plug) at distance z from the loaded end of plug.
r_o = outside radius of element
r_i = inside radius of element.

The axial force acting on the upper and lower surfaces of the plug slice dz_4 ($P_{pz,u}$ and $P_{pz,l}$) is calculated as follows (Figure 3.3):

$$P_{pz,u} = P_7 + P_{17} + P_{27} + P_{37} + P_{47} + P_{57} + P_{67} + P_{77} \qquad (3.2a)$$

$$P_{pz,l} = P_6 + P_{16} + P_{26} + P_{36} + P_{46} + P_{56} + P_{66} + P_{76} \qquad (3.2b)$$

Using Eqs. (3.2a and b) in (3.1b) gives the interface shear stress, $\tau_{rz,l}$, along the plug-rock interface CD (Figure 3.3). The shear stress distribution along the entire interface is obtained by determining $\tau_{rz,l}$ for each plug-rock interface section (dz_1 through dz_9) and by plotting $\tau_{rz,l}$ as a function of the vertical distance z from the initial location of the loaded end of the plug. Note that $P_{pz,u}$ for plug slice dz_4 is $P_{pz,l}$ for the upper slice, dz_3, and $P_{pz,l}$ for plug slice dz_4 is $P_{pz,u}$ for the lower slice, dz_5 (Figure 3.2).

Figure 3.4 shows the distribution of the interface shear stress ($\tau_{rz,l}$) and axial stress within the plug (σ_z^P). The results are for an applied plug stress (σ_{po}) of 1 MPa (145 psi) and for the ratio of the plug to rock Young's modulus of 0.233. Figure 3.4 gives the distribution of $\tau_{rz,l}$ and σ_z^P, according to the finite element analysis (curves 1 and 4);

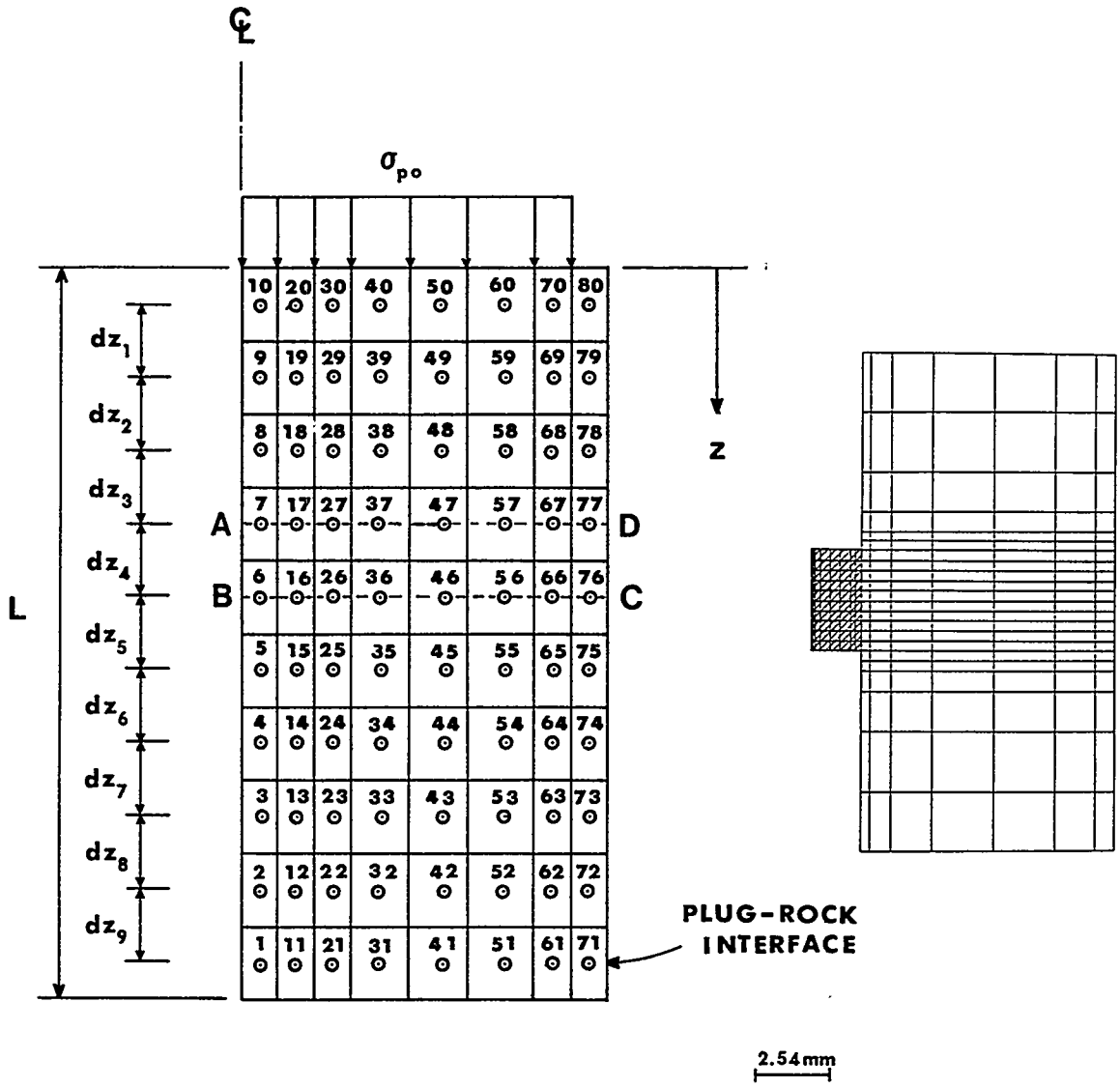

Figure 3.2 Right: shaded region shows the plug in the push-out cylinder. Left: enlarged section of the push-out plug showing element centroids (⊙) and element numbers.

σ_{po} = axial stress applied to the plug
L = plug length
z = distance from initial location of loaded end of plug.

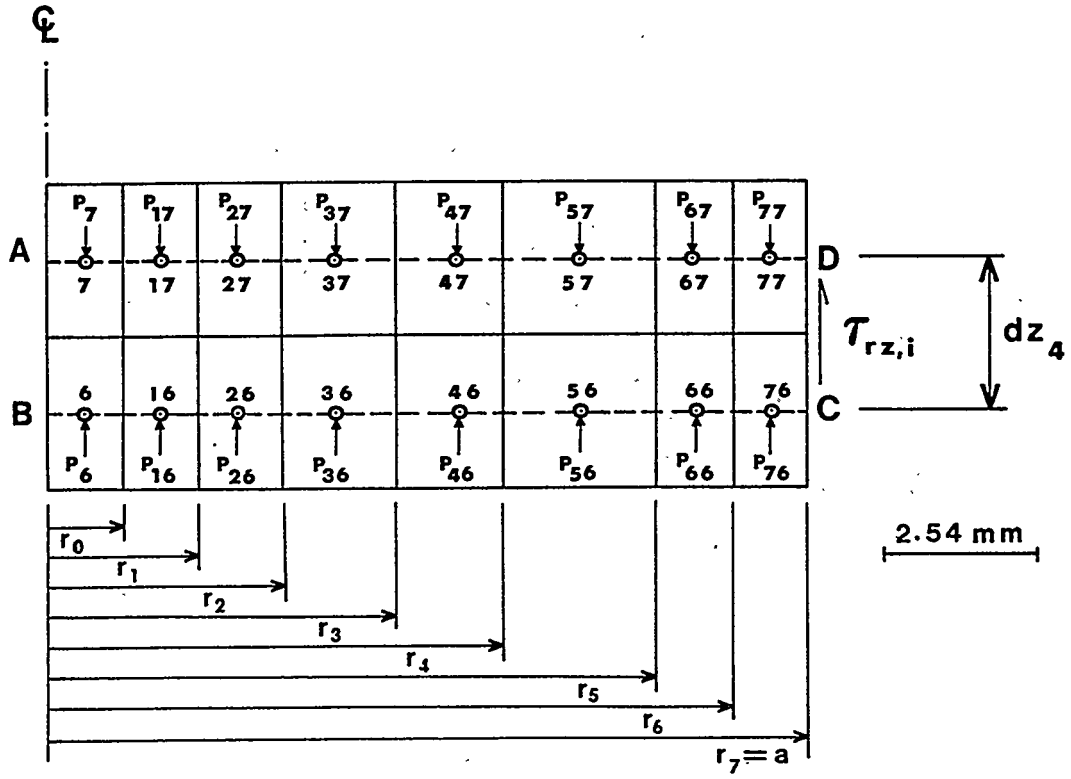

Figure 3.3 Enlarged section of element ABCD of Figure 3.2. The section shows force distribution on plug elements (P_6 through P_{77}): vertical forces acting on plug elements; $\tau_{rz,i}$ = interface shear stress; r_0 - r_7: radii of plug elements; dz_1 through dz_9: thickness of plug elements.

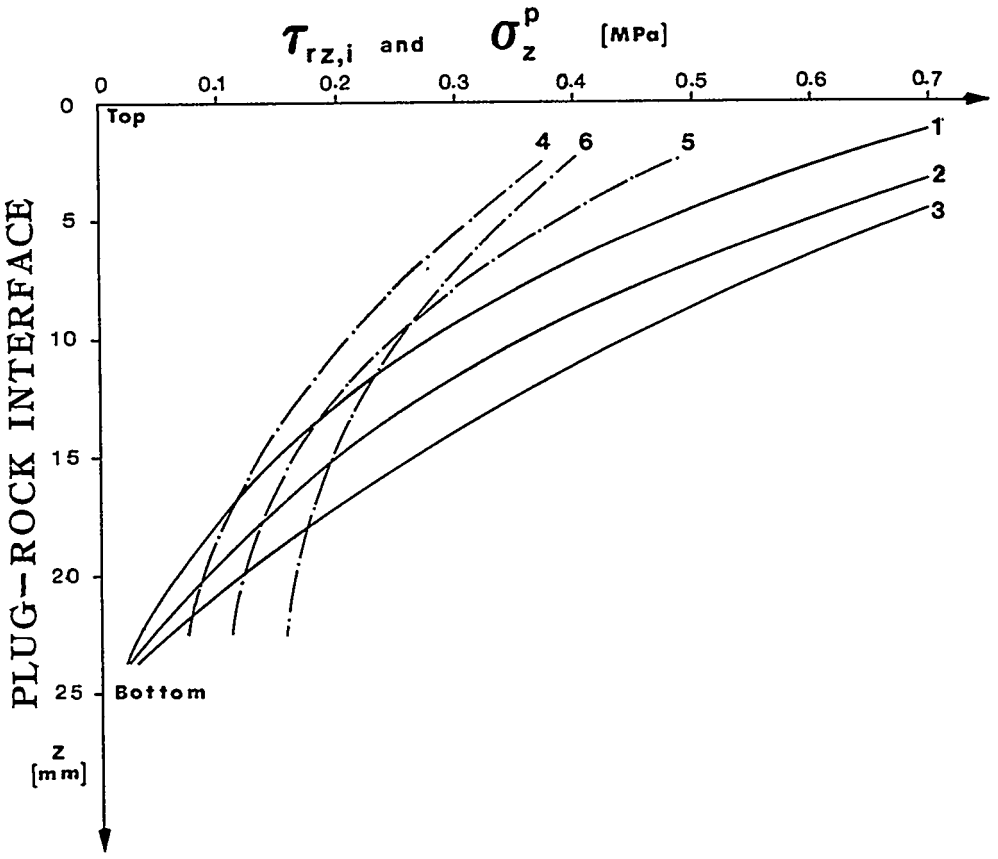

Solid lines (1,2,3): normal stress (σ_z^p)
Broken lines (4,5,6): interface shear stress ($\tau_{rz,i}$)

Figure 3.4 Distribution of the interface shear stress ($\tau_{rz,i}$) and axial stress within the plug (σ_z^p). The plots are according to the finite element analysis (curves 1 and 4), according to the rock bolt analysis (curves 2 and 5), and according to Amir (1986) (curves 3 and 6). The results are presented as a fraction of the applied plug stress (σ_{po}). Curves 1, 2, and 3 tend to 1 MPa at z = 0 (top of plug) and tend to 0 at z = L (bottom of plug).

E_p/E_R = ratio of Young's moduli of plug and rock = 0.233
ν_p, ν_R = Poisson's ratios of plug and rock = 0.22 and 0.20, respectively
L/a = plug length-to-radius ratio = 2
a = plug radius = 12.7 mm
R = rock cylinder radius = 76.2 mm.

according to the rock bolt analysis (curves 2 and 5) and according to Amir (curves 3 and 6). Sections 2.2.2 and 2.2.3 give the solutions proposed by the rock bolt analysis and Amir's analysis.

Figure 3.4 indicates that the σ_z^f distribution becomes more linear going from the curve obtained by the finite element analysis to Amir's analysis (i.e. going from curve 1 to curve 3). The shear stress distribution is slightly overestimated both by the rock bolt analysis and Amir's analysis. The reason for the overestimated $\tau_{rz,l}$ obtained by both analytical solutions (curves 5 and 6) is the assumption that the vertical load in rock is negligible, as given by Eqs. (2.8) and (2.9). This assumption leads to overestimated vertical shear stresses in rock (Eq. 2.8) and hence, to overestimated interfacial shear stresses (Eq. 2.9). As the peak interfacial shear stress calculated by the rock bolt solution (Section 2.2.2) is higher than that calculated by Amir (1986), it is more conservative and brings an additional factor of safety for design purposes. For this reason, subsequent discussions on the analytical solution vs. the finite element analysis will be confined to the rock bolt solution.

The radial distribution of the shear stress (τ_{rz}) within the rock is obtained by considering the equilibrium of a plug-rock element (i.e. element IJKL, Figure 2.2c). Equilibrium of element IJKL yields:

$$\sum F_z = 0 = (P_{pz,u} - P_{pz,l}) + (P_{rz,u} - P_{rz,l}) - \tau_{rz} 2\pi r\, dz = 0 \qquad (3.3a)$$

and

$$\tau_{rz} = \frac{(P_{pz,u} - P_{pz,l}) + (P_{rz,u} - P_{rz,l})}{2\pi r\, dz} \qquad (3.3b)$$

where τ_{rz} = vertical shear stress at radius r from plug center
$P_{rz,u}$ and $P_{rz,l}$ = vertical force acting above and below the rock portion of element IJKL
$P_{rz,u}$ and $P_{rz,l}$ = vertical force acting above and below the plug portion of element IJKL
dz = thickness of element IJKL (Figure 2.2c)

The shear force at radius r from plug center (T_{rz}) can be written as:

$$T_{rz} = (P_{pz,u} - P_{pz,l}) + (P_{rz,u} - P_{rz,l}) \qquad (3.3c)$$

Figure 3.5 gives an example to calculate the shear force (T_{rz}) for the plug-rock element, IJKL, with a thickness of dz. The vertical stress (σ_z^f) at each rock element centroid is obtained from the finite element output. σ_z^f, assumed to be uniform in each element, is converted to axial force (P_{rz}) using Eq. (3.1c).

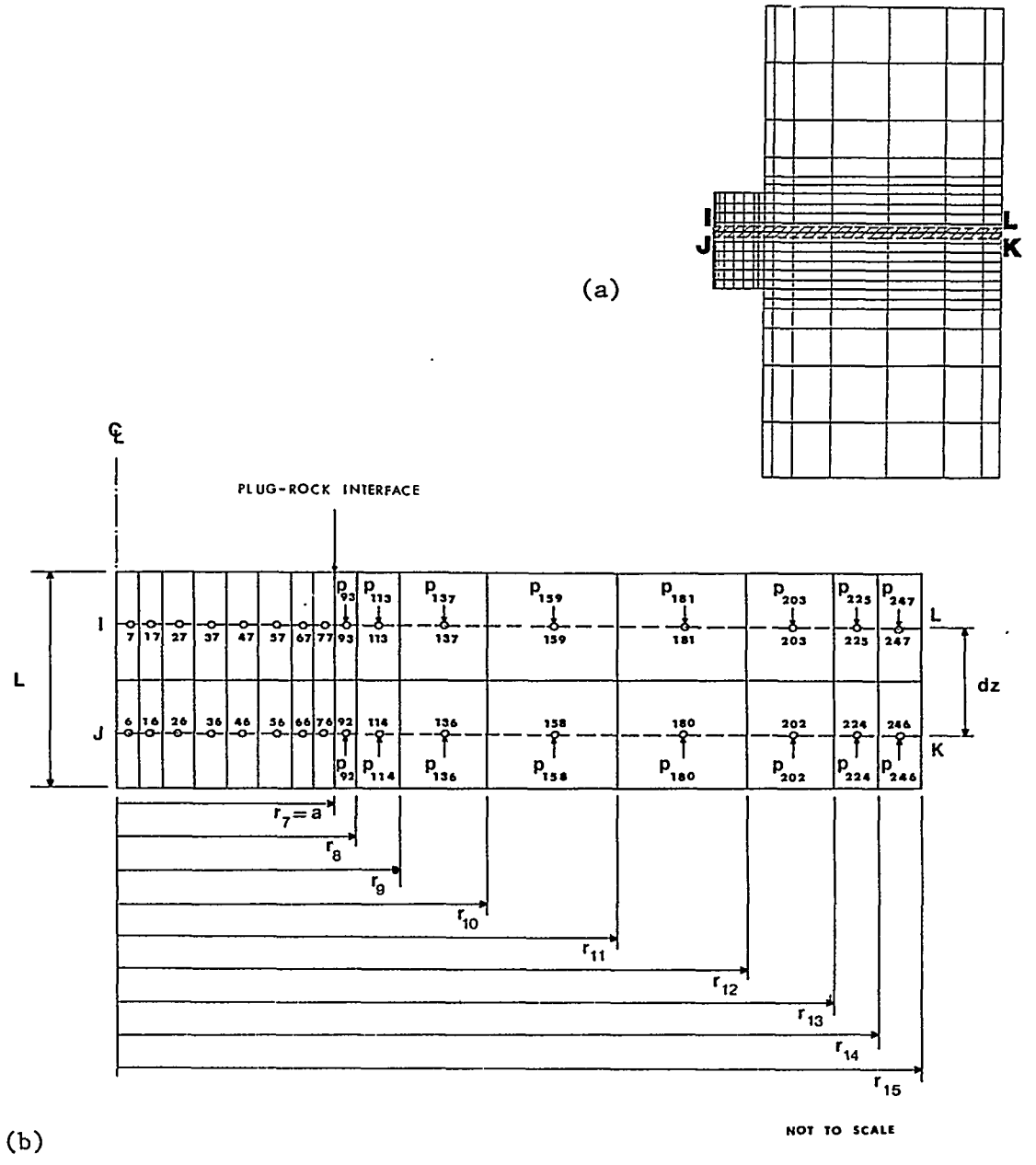

Figure 3.5 (a) Push-out sample showing location of element IJKL (shaded region). (b) Enlarged section of element IJKL of 3.5a, showing element centroids (⊙), element numbers, and force distribution on rock elements (P_{92} - P_{247}: vertical forces acting on rock elements; r_7 - r_{15}: radii from plug center to rock elements; L = plug length; a = plug radius). Force distribution and radii of plug elements are given in Figure 3.3.

For example, the axial force acting above and below the first rock element of IJKL ($P^1_{rz,u}$ and $P^1_{rz,l}$) is calculated as follows (Figure 3.5b):

$$P^1_{rz,u} = \pi(r_8^2 - r_7^2)\sigma_{93} \qquad (3.3d)$$

and

$$P^1_{rz,l} = \pi(r_8^2 - r_7^2)\sigma_{92} \qquad (3.3e)$$

where r_8 = outside radius of first element
r_7 = inside radius of first element
σ_{92}, σ_{93} = vertical stress acting at centroid of elements 92 and 93 (i.e. acting below and above the first rock section of element IJKL). σ_{92} and σ_{93} are obtained from the finite element output.

Similarly, the axial force acting above and below the second rock element of IJKL ($P^2_{rz,u}$ and $P^2_{rz,l}$) is calculated as follows:

$$P^2_{rz,u} = P^1_{rz,u} + \pi(r_9^2 - r_8^2)\sigma_{113} \qquad (3.3f)$$

and

$$P^2_{rz,l} = P^1_{rz,l} + \pi(r_9^2 - r_8^2)\sigma_{114} \qquad (3.3g)$$

As indicated by Eqs. (3.3d through g), the axial force acting above and below the rock section of element IJKL can be calculated as a function of the radial distance, r. The vertical force on the upper and lower surfaces of the plug portion of element IJKL is given in Eqs. (3.2a and b). Combining Eqs. (3.2a and b) with (3.3d through g), in Eq. (3.3c) gives the shear force in the rock cylinder as a function of the radial distance, r.

Figure 3.6 gives the distribution of the shear force and the axial forces ($P_{pz,u}$ and $P_{pz,l}$), as a function of radial distance, r. The plot is for a net axial plug load ($\Delta P_{pz} = P_{pz,u} - P_{pz,l}$) across the plug slice of 41 N. T_{rz} becomes negligible at two plug radius away from the interface. Figure 3.7 presents the distribution of the shear stress within the rock (as a function of radial distance r). The shear stress is calculated from Eq. (3.3b). Curve 1 assumes that axial stress as well as shear stress exists in the rock. Curve 2, which represents the closed-form solution, neglects normal stresses in the rock, and overestimates the shear stress in the rock.

Tables 3.1 and 3.2 give the axial stress and shear stress distributions in the rock due to an axial stress applied on the plug. The stress distributions are obtained from the shaded regions of the meshes in Figures 3.1 and B.1 through B.3 (App. B). One objective of studying the axial and shear stress distributions in rock is to find the location where the axial stresses in rock are negligible (i.e. to find the radius of influence). The shaded regions are selected at the midsection of the plug/rock interface. At the top of the interface, the resultant axial

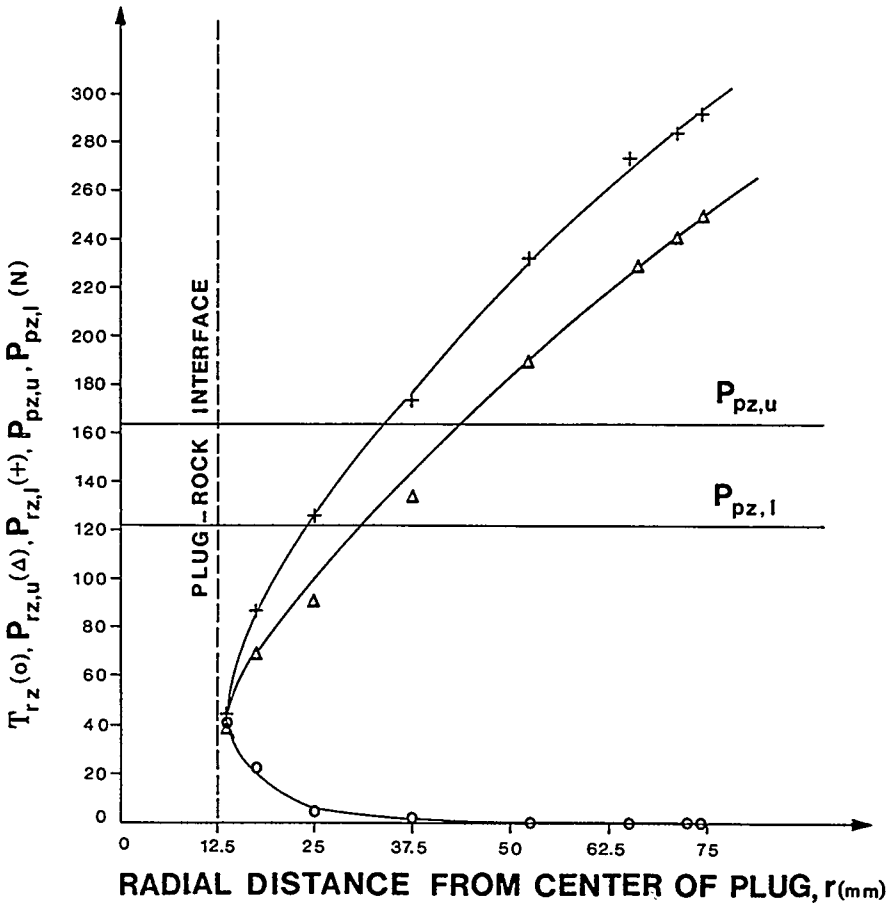

Figure 3.6 Distribution of the shear force (T_{rz}) and the axial force acting above ($P_{rz,u}$) and below ($P_{rz,l}$) the rock section of element IJKL (shown in Figure 3.5). $P_{pz,u}$ and $P_{pz,l}$ are the axial forces acting above and below the plug section of element IJKL. The plot is for a differential net (localized) axial plug load ($\Delta P_{po} = P_{pz,u} - P_{pz,l}$) of 41 N.

Table 3.1 Axial Stress Distribution within Rock (σ_z^R/σ_{po}) due to an Axial Stress Applied to a Borehole Plug. The axial stress, obtained from the shaded regions of the finite element meshes presented in Figs. 3.1 and B.1 through B.3 (Appendix B), is a function of Young's modulus ratio of plug and rock (E_p/E_R), tuff cylinder outside-to-inside radius ratio (R/a), and plug length-to-radius ratio (L/a). σ_{po} = axial stress applied to the plug. Poisson's ratio of plug and rock (ν_P, ν_R) = 0.22 and 0.20, plug radius (a) = 12.7 mm.

Young's Modulus Ratio of Plug to Rock (E_p/E_R)	Plug Length to Radius Ratio (L/a)	Tuff Cylinder Radius Ratio (R/a)	Axial Stress Distribution within Rock (σ_z^R/σ_{po}) x 10^2								
			Radial Distance from Center of Plug (r) (mm):								
			14.0	17.8	22.9	29.2	38.1	48.3	58.4	69.9	86.4
0.1	2	6	26.0	12.6	4.54	2.37	1.76	1.50	1.33	1.05	-
0.1	2	60	24.5	11.5	3.45	1.29	0.706	0.484	0.394	0.175	0.042
0.233	2	6	23.3	11.6	4.31	2.32	1.76	1.51	1.31	1.03	-
0.233	2	60	23.3	10.6	3.25	1.26	0.702	0.479	0.394	0.171	0.042
10	2	6	3.62	2.31	1.63	1.58	1.56	1.45	1.29	1.02	-
10	2	60	3.35	1.74	0.841	0.684	0.614	0.468	0.385	0.139	0.041
			Radial Distance from Center of Plug (r) (mm):								
			14.0	20.4	31.8	40.7	50.8	63.5	86.4	107.0	127.0
0.1	4	60	15.5	9.5	3.55	2.05	1.33	0.833	0.432	0.211	0.097
0.233	4	60	15.1	9.13	3.43	2.01	1.31	0.831	0.431	0.210	0.088
10	4	60	3.4	2.62	1.53	1.21	0.984	0.710	0.414	0.206	0.083

Table 3.1 Axial Stress Distribution within Rock (σ_z^R/σ_{po}) due to an Axial Stress Applied to a Borehole Plug--Continued. The axial stress, obtained from the shaded regions of the finite element meshes presented in Figures 3.1 and B.1 through B.3 (Appendix B), is a function of Young's modulus ratio of plug and rock (E_p/E_R), tuff cylinder outside-to-inside radius ratio (R/a), and plug length-to-radius ratio (L/a). σ_{po} = axial stress applied to the plug. Poisson's ratio of plug and rock (ν_P, ν_R) = 0.22 and 0.20, plug radius (a) = 12.7 mm.

Young's Modulus Ratio of Plug to Rock (E_p/E_R)	Plug Length to Radius Ratio (L/a)	Tuff Cylinder Radius Ratio (R/a)	Axial Stress Distribution within Rock (σ_z^R/σ_{po}) x 10^2								
			Radial Distance from Center of Plug (r) (mm):								
			14.0	25.4	45.7	55.9	68.6	83.8	102.0	122.0	142.0
0.1	8	60	5.93	4.10	1.96	1.32	0.858	0.512	0.280	0.121	0.038
0.233	8	60	5.07	4.08	1.92	1.30	0.847	0.508	0.279	0.121	0.037
10	8	60	3.09	2.03	1.02	0.767	0.559	0.377	0.228	0.110	0.035

Table 3.2 Shear Stress Distribution within Rock (τ_{rz}/σ_{po}) due to an Axial Stress Applied to a Borehole Plug. The shear stress, obtained from the shaded regions of the finite element meshes presented in Figs. 3.1 and B.1 through B.3 (Appendix B), is a function of Young's modulus ratio of plug and rock (E_p/E_R), tuff cylinder outside-to-inside radius ratio (R/a), and plug length-to-radius ratio (L/a). σ_{po} = axial stress applied to the plug. Poisson's ratio of plug and rock (ν_P, ν_R) = 0.22 and 0.20, plug radius (a) = 12.7 mm.

Young's Modulus Ratio of Plug to Rock (E_p/E_R)	Plug Length to Radius Ratio (L/a)	Tuff Cylinder Radius Ratio (R/a)	Shear Stress Distribution within Rock (τ_{rz}/σ_{po}) x 10^2								
			Radial Distance from Center of Plug (r) (mm):								
			14.0	17.8	22.9	29.2	38.1	48.3	58.4	69.9	86.4
0.1	2	6	18.5	12.9	6.23	3.50	1.00	0.46	0.176	0.020	-
0.1	2	60	18.5	13.0	6.40	2.80	1.48	1.07	0.790	0.348	0.005
0.233	2	6	18.4	12.8	6.22	2.53	0.990	0.440	0.175	0.02	-
0.233	2	60	18.5	12.9	6.40	2.80	1.40	1.00	0.78	0.345	0.003
10	2	6	16.5	11.3	6.31	3.01	1.25	0.53	0.206	0.019	-
10	2	60	16.6	11.4	6.45	3.25	1.63	1.07	0.734	0.328	0.002
			Radial Distance from Center of Plug (r) (mm):								
			14.0	20.4	31.8	40.7	50.8	63.5	86.4	107.0	127.0
0.1	4	60	6.5	6.12	3.34	1.90	1.13	0.610	0.280	0.119	0.032
0.233	4	60	6.5	6.00	3.30	1.90	1.10	0.600	0.270	0.110	0.030
10	4	60	6.4	5.47	2.68	1.58	0.938	0.486	0.211	0.081	0.023

Table 3.2 Shear Stress Distribution within Rock (τ_{rz}/σ_{po}) due to an Axial Stress Applied to a Borehole Plug--Continued. The shear stress, obtained from the shaded regions of the finite element meshes presented in Figures 3.1 and B.1 through B.3 (Appendix B), is a function of Young's modulus ratio of plug and rock (E_p/E_R), tuff cylinder outside-to-inside radius ratio (R/a), and plug length-to-radius ratio (L/a). σ_{po} = axial stress applied to the plug. Poisson's ratio of plug and rock (ν_p, ν_R) = 0.22 and 0.20, plug radius (a) = 12.7 mm.

Young's Modulus Ratio of Plug to Rock (E_p/E_R)	Plug Length to Radius Ratio (L/a)	Tuff Cylinder Radius Ratio (R/a)	Shear Stress Distribution within Rock (τ_{rz}/σ_{po}) x 10^2								
			Radial Distance from Center of Plug (r) (mm):								
			14.0	25.4	45.7	55.9	68.6	83.8	102.0	122.0	142.0
0.1	8	60	4.72	2.57	1.43	1.11	0.803	0.550	0.353	0.194	0.084
0.233	8	60	3.98	1.98	1.40	1.09	0.790	0.540	0.350	0.190	0.082
10	8	60	3.60	1.90	1.16	0.859	0.604	0.410	0.260	0.142	0.058

stress within the rock is negligible; at the bottom, the resultant shear stress is negligible. For longer plugs (e.g. L/a ≥ 8) the shaded regions should be selected near the top of the plug. The precise location of the section where the influence radius is determined deserves further investigation. Tables 3.1 and 3.2 give the stresses as a function of modulus ratio of plug and rock, plug length-to-radius ratio and tuff cylinder outside-to-inside radius ratio. Figures 3.8 and 3.9 give the axial stress and shear stress distributions across a section through the rock cylinder for an axially loaded Self-Stress II cement plug emplaced in an Apache Leap tuff cylinder.

One objective of Tables 3.1 and 3.2 and Figures 3.8 and 3.9 is to find the effective radius (r_m in Eq. (2.42), Ch. 2) beyond which axial stresses and shear stresses within the rock may be considered negligible (e.g. 0.1% of the applied axial plug stress). The critical radii are analyzed at the midsection of the plug/rock interface. The axial stress and shear stress within the rock decrease away from the plug/rock interface. They become negligible (for any modulus ratio between 0.1 and 10.0) approximately four plug radii away from the interface for a push-out cylinder outside-to-inside radius ratio (R/a) of 6.0 and plug length-to-radius ratio (L/a) of 2.0; about five plug radii, eight plug radii, and ten plug radii away from the interface for samples with R/a = 60.0 and L/a of 2.0, 4.0 and 8.0, respectively. Specimens with a modulus ratio (E_p/E_R) of 0.1 show the highest stress transfer to the rock. Close to the interface, samples with a modulus ratio of 0.1 show a stress up to 16% higher than those with a modulus ratio of 0.233 and up to 86% higher than those with a modulus ratio of 10.0.

Substituting the critical radii (or effective radii) obtained from the finite element analyses into the closed-form solution leads to overestimated axial stress distributions within the plug and underestimated peak shear stress at the plug/rock interface for modulus ratios equal to or greater than 5.0.

The relation between the axial plug and rock displacements (w_p and w_R) and the interfacial shear stress ($\tau_{rz,i}$) is given by Eq. (2.11), Ch. 2, as:

$$\tau_{rz,i} = \frac{(w_p - w_R)E_R}{2(1+\nu_R)a\ln(R/a)} \tag{3.4}$$

where R = rock cylinder outside radius
a = plug radius
E_R = Young's modulus of rock
ν_R = Poisson's ratio of rock.

As discussed in Chapter 2 and in the previous paragraphs, Eq. (3.4) is derived with the assumption that no normal stress in rock exists. With an additional assumption that the vertical rock displacement is negligible beyond a distance r_m from the plug center, Eq. (3.4) can be reduced to:

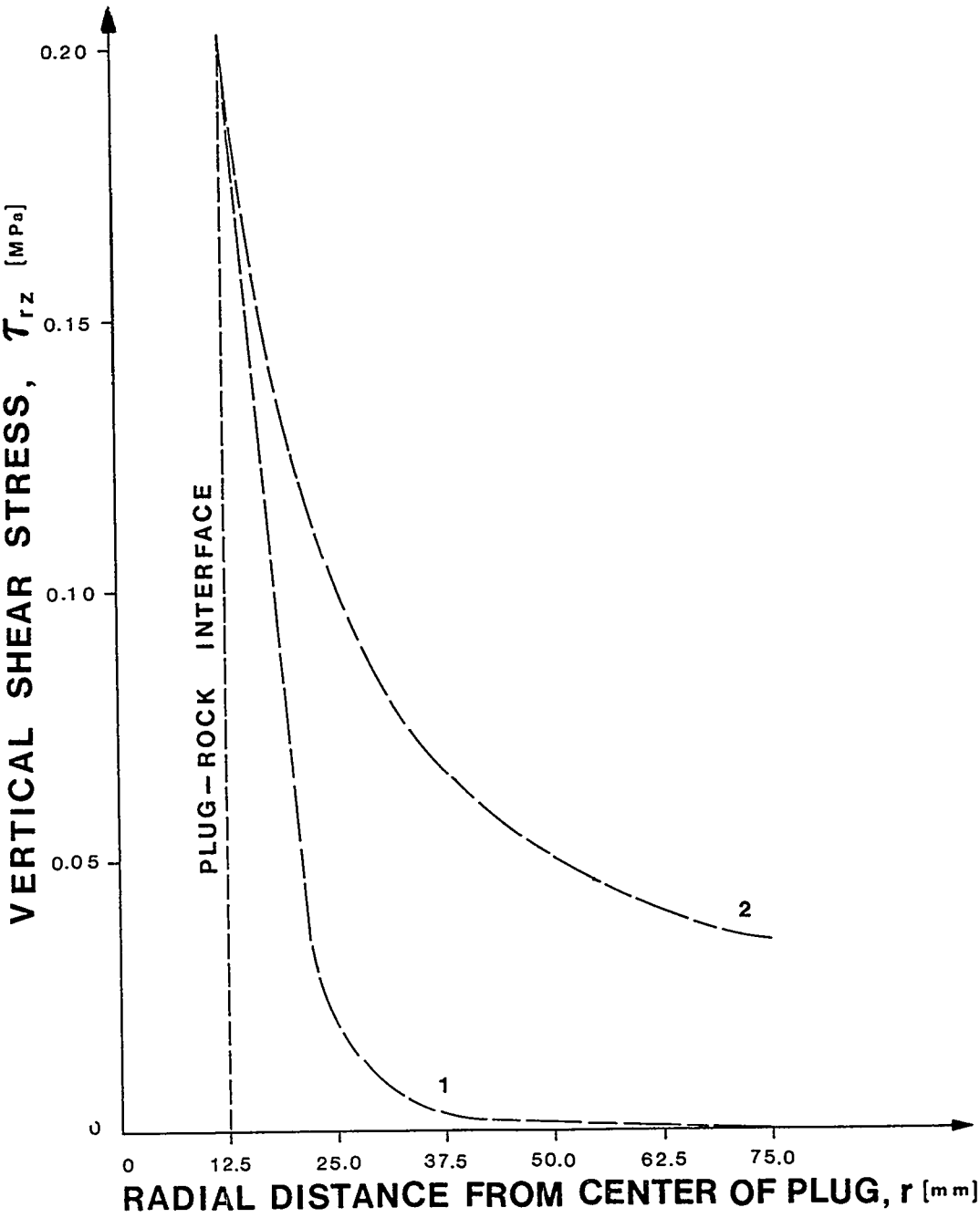

Figure 3.7 Shear stress (τ_{rz}) distribution in Section IJKL of the rock cylinder shown in Figure 3.5. Curve 1 gives the shear stress distribution, assuming that axial stress as well as shear stress exists in the rock. Curve 2 neglects normal stresses in the rock.

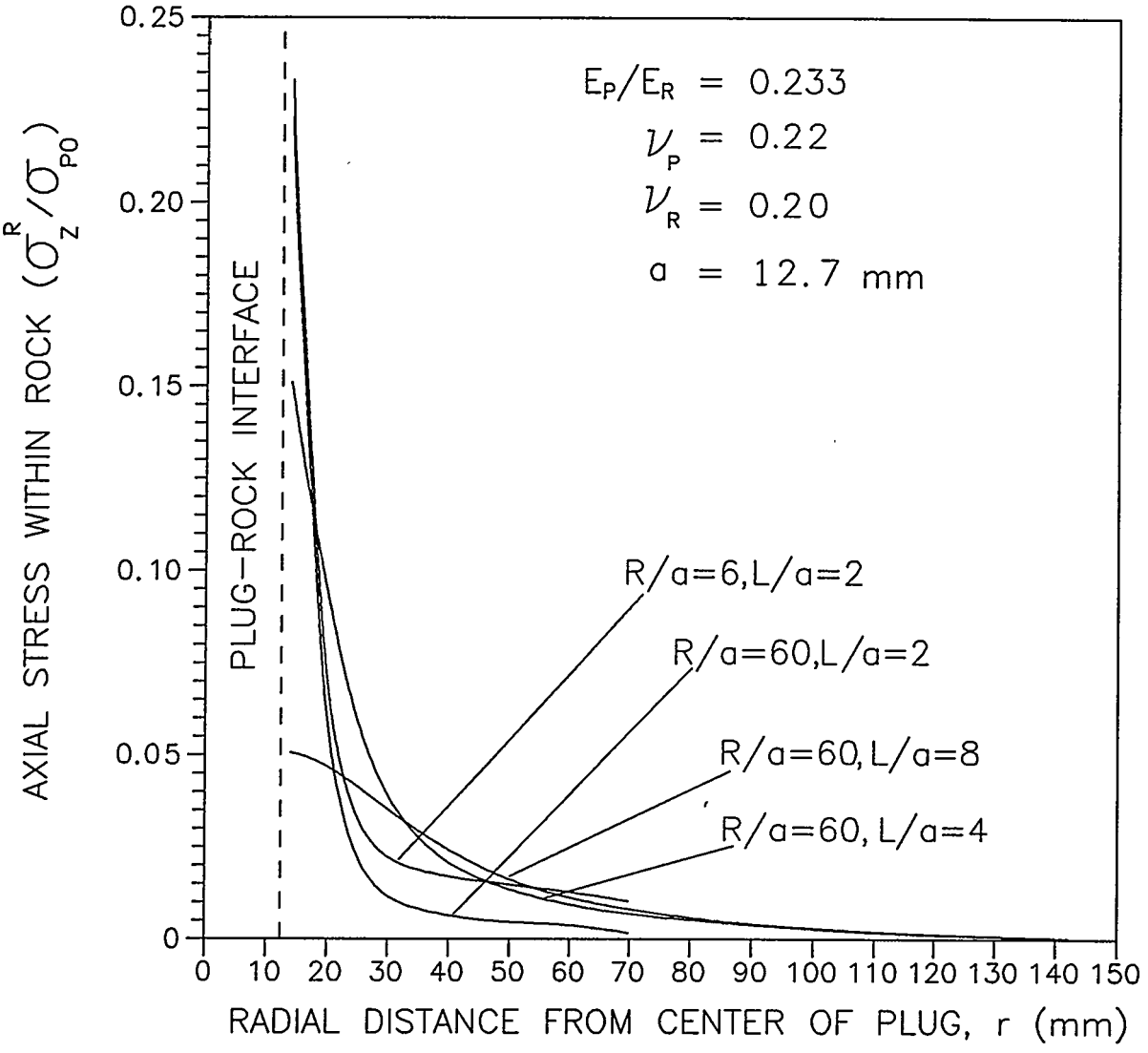

Figure 3.8 Axial stress distribution within rock (σ_z^R/σ_{po}) for a Self-Stress II cement plug emplaced in an Apache Leap welded tuff cylinder. The stress is plotted as a fraction of the axial stress applied to the plug (σ_{po}), and as a function of plug length-to-radius ratio (L/a), tuff cylinder outside-to-inside radius ratio (R/a) and radial distance from center of plug (r). The shaded regions in the finite element meshes presented in Figures 3.1 and B.1 through B.3 (Appendix B) show the location of rock sections where the σ_z^R/σ_{po} distribution is obtained. E_p/E_R = Young's modulus ratio of plug and rock. ν_p, ν_R = Poisson's ratios of plug and rock. a = plug radius.

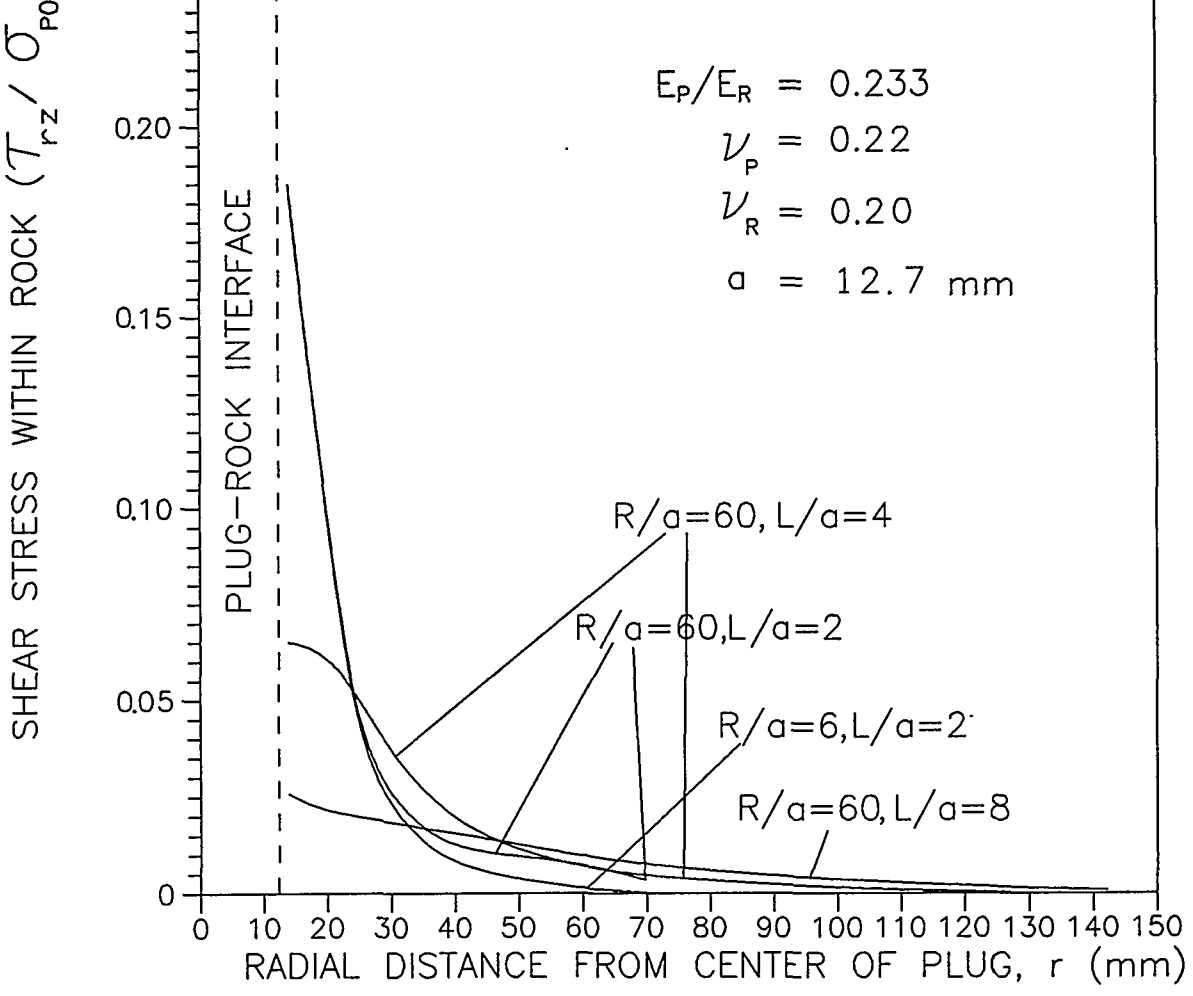

Figure 3.9 Shear stress distribution within rock (τ_{rz}/σ_{po}) for an axially loaded Self-Stress II cement plug emplaced in an Apache Leap welded tuff cylinder. The shear stress is plotted as a fraction of the stress applied to the plug (σ_{po}), and as a function of plug length-to-radius ratio (L/a), tuff cylinder outside-to-inside radius ratio (R/a) and radial distance from center of plug (r). The shaded regions in the finite element meshes in Figures 3.1 and B.1 through B.3 (Appendix B) show the rock sections where the shear stress distribution is obtained. E_p/E_R = Young's modulus ratio of plug and rock. ν_p, ν_R = Poisson's ratios of plug and rock. a = plug radius.

$$\tau_{rz,i} = \frac{w_p E_R}{2(1+\nu_R)a \ln(r_m/a)} \qquad (3.4a)$$

and

$$r_m = a e^{\frac{w_p E_R}{2(1+\nu_R)a\tau_{rz,i}}} \qquad (3.4b)$$

where r_m = effective or critical radius
a = plug radius
E_R = Young's modulus of rock
ν_R = Poisson's ratio of rock.

Comparing the two extreme cases for modulus ratios (E_P/E_R) of 0.1 and 10.0 in Eq. (3.4b), and substituting the values for the peak interface shear stress and axial plug displacement from the finite element analysis into Eq. (3.4b), indicates that the effective radial distance starting from the plug/rock interface for a modulus ratio of 0.1 is up to 20 times larger than that for a modulus ratio of 10.0. Hence, the effective radius increases with decreasing modulus ratio. For the modulus ratio range of 0.1 to 5.0, the effective radius can be expressed in the form of a linear interpolation as:

$$r_m/a = [2.1 - 0.38(E_P/E_R)]L/a + 1 \qquad (3.5a)$$

where L/a = plug length-to-radius ratio ($2.0 \leq L/a \leq 8.0$)

For a modulus ratio of 10.0, the effective radius is given by:

$$r_m/a = 0.1(L/a) + 1 \qquad (3.5b)$$

for $2.0 \leq L/a \leq 8.0$. (Eqs. (3.5a through c) are based on the observation that the length of the critical radius starting from the plug/rock interface ($r_m - a$) for $E_P/E_R = 0.1$ is 20 times that of $E_P/E_R = 10$, as observed from the finite element analysis.) Figure 3.10 gives a plot of the critical radius starting from the plug/rock interface, as a function of modulus ratio.

The effective radius can be expressed in the form of an exponential interpolation as:

$$r_m/a = [1.99e^{-0.33(E_P/E_R)}]L/a + 1 \qquad (3.5c)$$

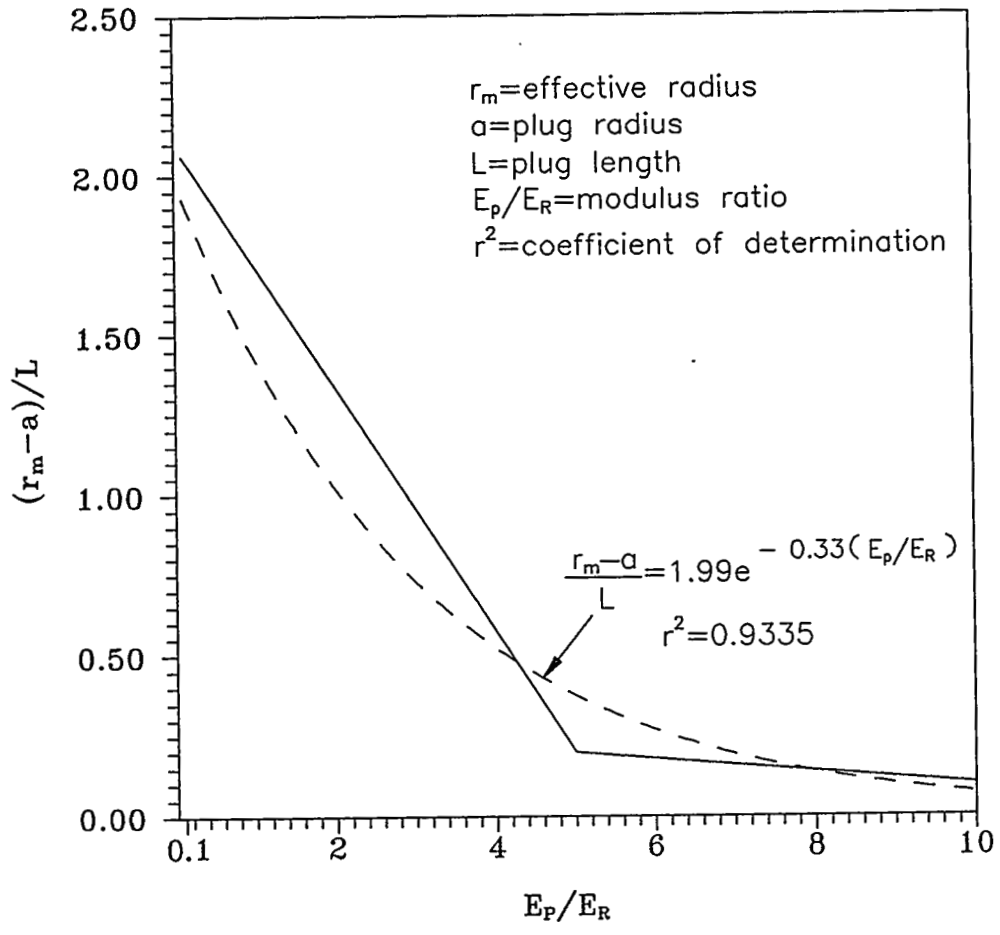

Figure 3.10 The critical radius starting from the plug/rock interface as a function of modulus ratio. Plots for linear and exponential interpolations.

3.3 Analysis of the Stress Distribution Along an Axially Loaded Borehole Plug

Figure 3.11 gives the axial stress distribution along the plug and the interfacial shear stress distribution for a modulus ratio of 0.233. Figures B.4 through B.7 (App. B) give the axial stress distribution along the plug and the interface shear stress distribution for modulus ratios of 0.1, 1.0, 5.0 and 10.0, respectively. These plots compare the stress distributions obtained by the finite element analysis (solid lines) with those of the closed-form solution (dashed lines, obtained through Eqs. (2.52), (2.48), (3.5a) and (3.5b)). The plots are given for a plug radius of 12.7 mm (0.5 in), for several tuff cylinder outside-to-inside radius ratios and plug length-to-radius ratios. The stress distributions for a 12.7 mm radius plug with a plug length-to-radius ratio of 2 and tuff cylinder outside-to-inside radius ratios of 6 (representing a laboratory push-out specimen) and 60 (representing an in-situ push-out configuration) are given as a single curve in Figures 3.11 and B.4 through B.7 (App. B). The stress distributions for cylinder ratios of 6 and 60, as determined through the finite element analysis, virtually coincide. The analytical solution (Eqs. (2.52), (2.48), (3.5a), and (3.5b)) gives the same stress distributions for cylinder ratios of 6 and 60 due to the use of an identical radius of influence. A push-out specimen with a cylinder ratio of 6 shows a slightly higher interface shear stress distribution and a slightly lower axial stress distribution within the plug (a difference of not more than 0.078% to 2.34%) than that with a cylinder radius ratio of 60. The axial stress distribution within the plug tends to become slightly more nearly linear with increasing cylinder ratio.

The shear stress at the loaded end of a plug is higher for smaller plug length-to-radius ratios (L/a) (Figures 3.11 and B.4 through B.7 (App. B)). The axial stresses and the interface shear stresses do not affect the entire length of the longer plugs (i.e. plugs with L/a of 8).

Figures 3.12a and 3.12b give the axial stress along the plug and the interface shear stress for several modulus ratios. Both plots are for a 12.7 mm radius borehole plug with a plug length-to-radius ratio of 2 and cylinder radius ratio of 60. The axial stress distribution becomes more nearly linear with increasing modulus ratio (Figure 3.12a). The interface shear stress at the loaded end of the plug increases with decreasing modulus ratio. The shear stress distribution becomes more uniform with increasing modulus ratio (Figure 3.12b).

Figure 3.13 gives the interface shear stress near the loaded end of the plug (at $z/L = 0.1$, where z is the distance from the initial location of the loaded end of the plug, L = plug length) as a function of modulus ratio and plug length-to-radius ratios, as obtained by the finite element analysis and by the closed-form solution. The plot is for a 12.7 mm radius borehole plug with a cylinder radius ratio of 60 and for a Poisson's ratio of the plug and rock of 0.22 and 0.20, respectively. The peak interface shear stress decreases with increased modulus ratio and increased plug length-to-radius ratio. The analytical solution always overestimates the peak interface shear stress when compared to

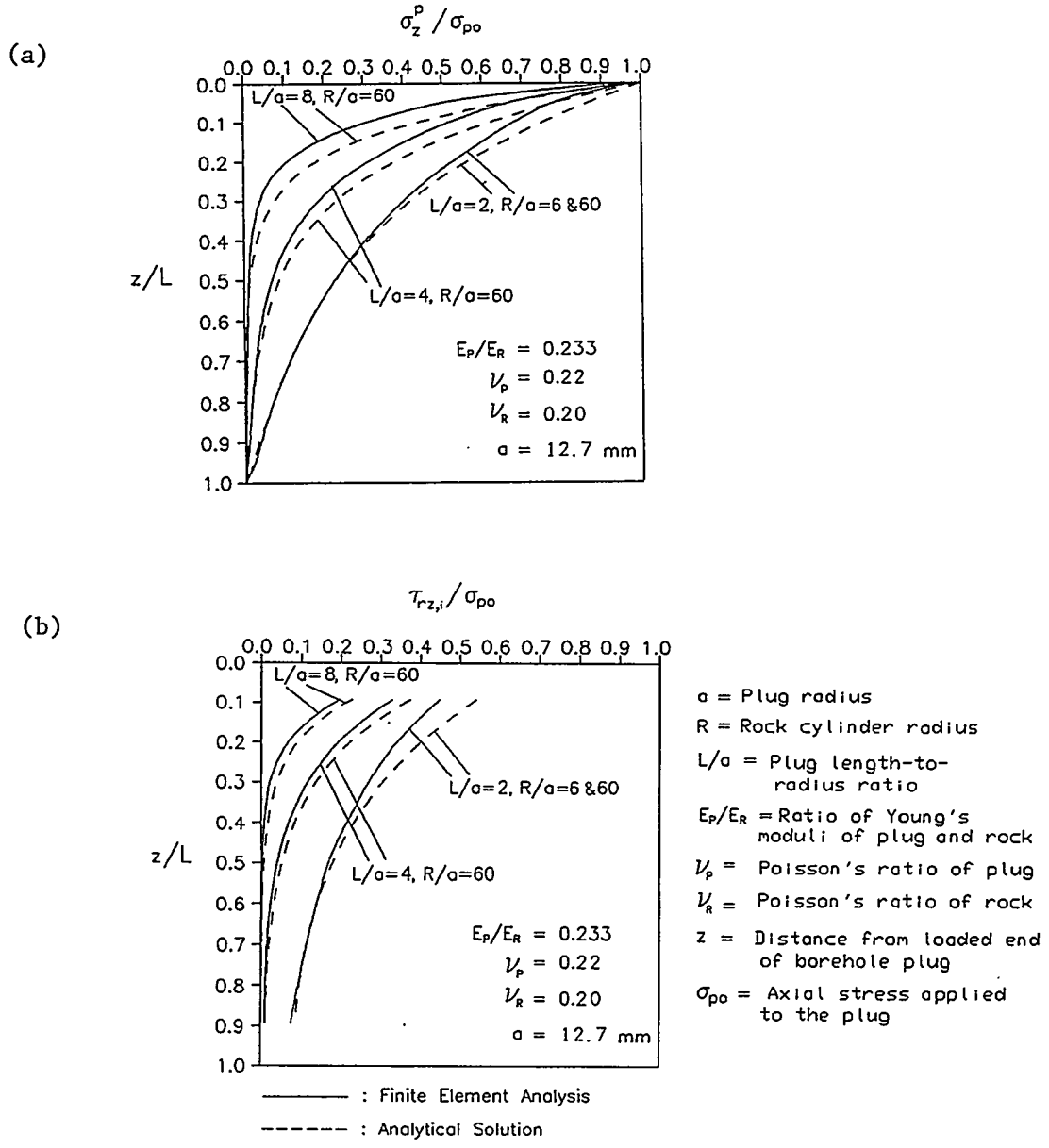

Figure 3.11 (a) Axial stress distribution along a plug (σ_z^p/σ_{po}), and (b) shear stress distribution along the plug/rock interface ($\tau_{rz,i}/\sigma_{po}$) for a modulus ratio (E_p/E_R) of 0.233.

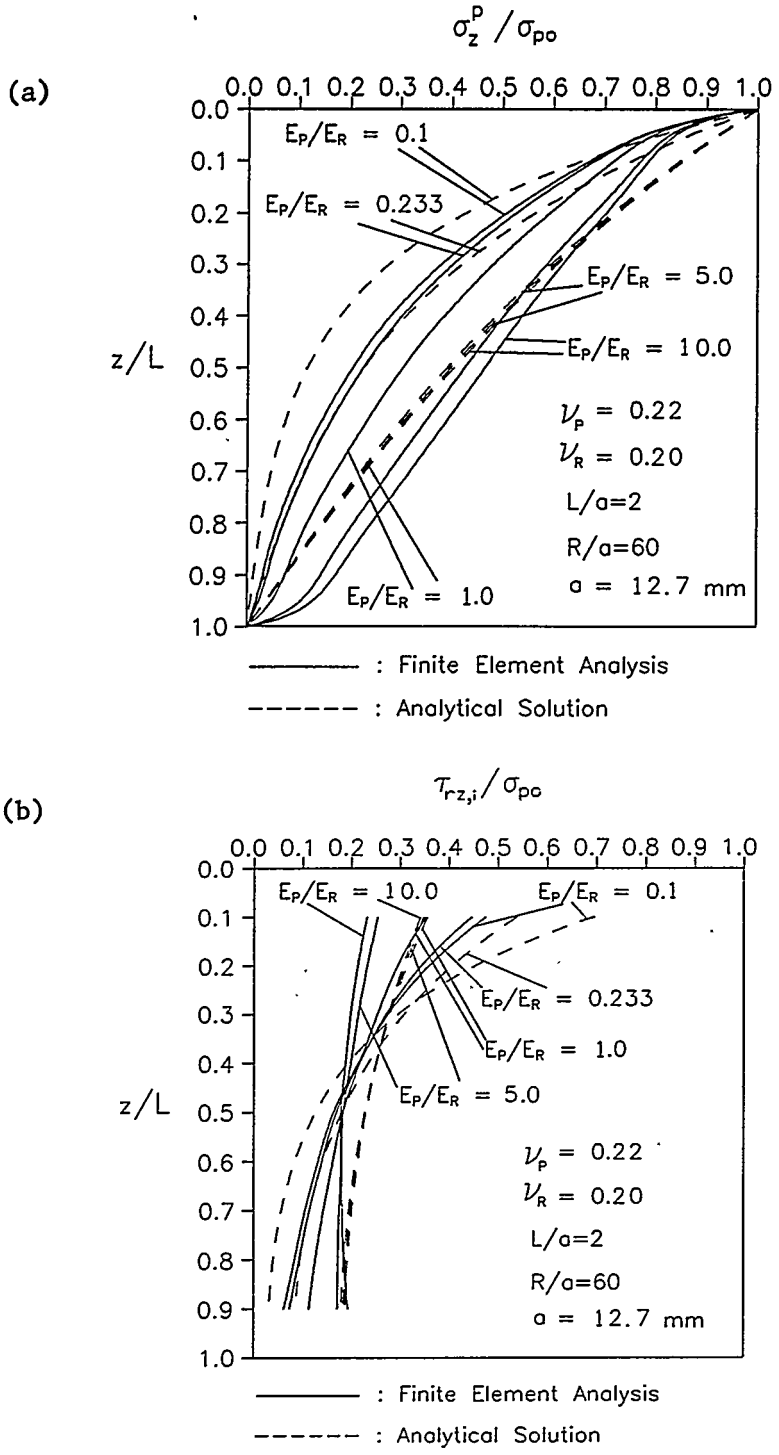

Figure 3.12 (a) Axial stress distribution along a plug (σ_z^p/σ_{po}), and (b) shear stress distribution along the plug/rock interface ($\tau_{rz,i}/\sigma_{po}$), as a function of modulus ratio (E_p/E_R). Figure 3.11 gives definitions for all variables.

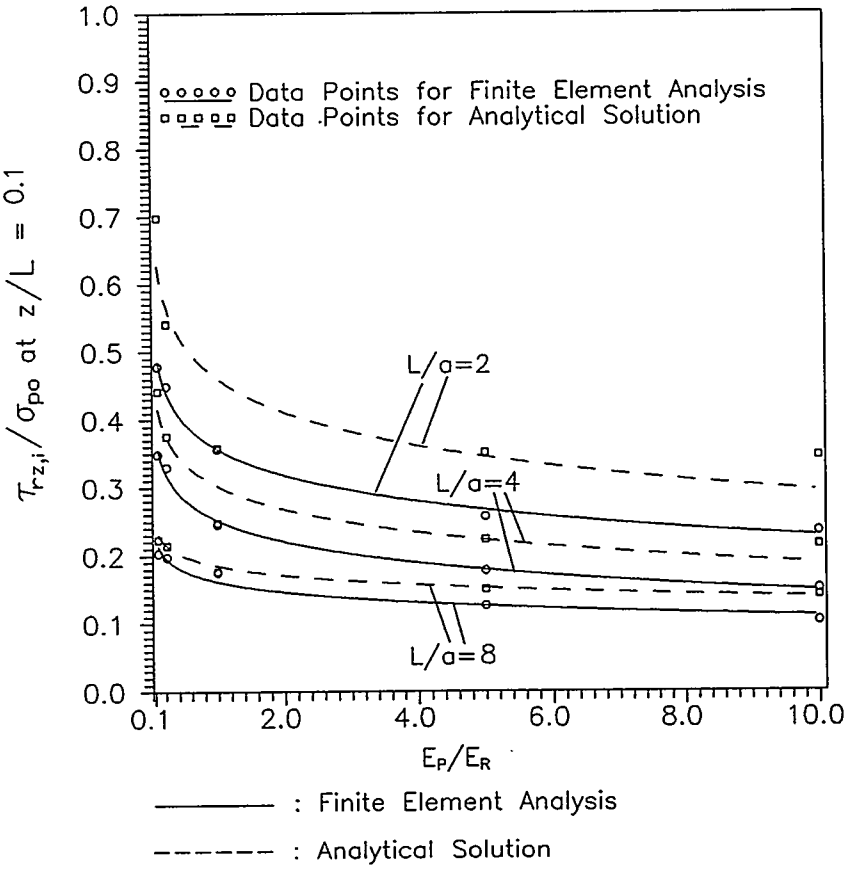

Figure 3.13 Interface shear stress ($\tau_{rz,i}/\sigma_{po}$) near the loaded end of the plug (i.e. z/L = 0.1) as a function of modulus ratio and plug length-to-radius ratio, as determined by the finite element analysis and by closed-form solution. Figure 3.11 gives definitions for all variables.

the finite element analysis, with overestimation ranges of 1 to 32%. Hence, the interface shear stress calculated by the analytical solution brings an additional factor of safety for design purposes.

Figure 3.14 gives the shear stress and normal stress distributions (within the rock) along sections I-L (upper rock elements) and J-K (lower rock elements) of element IJKL (Figure 3.5b). The data (at element centroids) are obtained from the finite element analysis. The lower rock elements give lower shear stress and higher normal stress distributions in the radial direction (r). The results of the finite element analysis indicates that when an axial stress is applied to a borehole plug: 1) the shear stresses in the rock are a maximum at $z = 0$ and minimum at $z = L$ at a fixed radial distance; 2) the normal stresses in the rock are maximum at $z = L$ and minimum at $z = 0$ at a fixed radial distance; and 3) both the shear stress and normal stress decrease going from the plug-rock interface towards the outside of the rock core (i.e. in the radial direction).

3.4 Tensile Stresses in and near an Axially Loaded Borehole Plug

The determination of the tensile stress in rock hosting a plug is important. Tensile fracturing may cause preferential pathways around seals. The objective of this section is to analyze the tensile zone in the vicinity of an axially loaded borehole plug. The finite element meshes given in Figures B.1 through B.3 (Appendix B) are used to analyze the tensile radial and tangential stress distributions. The meshes represent 12.7 mm radius borehole plugs with length-to-radius ratios of 2,4 and 8, respectively. All meshes have a cylinder outside-to-inside radius ratio of 60 and represent borehole plugs in an infinite medium. The stress distributions are investigated as a function of plug length-to-radius ratio and modulus ratio. The Poisson's ratio of the plug and rock are 0.22 and 0.20, respectively

Figure 3.15 gives the tensile radial and tensile tangential stress distribution in a specimen with a plug length-to-radius ratio of 2 and a modulus ratio of 0.233, representative of a Self-Stress II cement plug emplaced in an Apache Leap tuff cylinder. The tensile radial stress contours (on the right in Figure 3.15) and the tensile tangential stress contours (on the left in Figure 3.15) are plotted as a percentage of the axial stress applied to the plug. The axial stress applied to the plug produces biaxial tension in the bottom center of the plug. The peak tensile radial and tangential stresses at this location are in the range of 10-20% of the applied axial stress. Biaxial tension develops along the axis of the plug from the bottom to over half the plug height. The peak tensile tangential stress occurs in the bottom center of the plug and has a magnitude of 11% of the applied axial stress; the peak tensile radial stress occurs at the top corner of the plug, and is 26.8% of the applied axial stress. The maximum tension in the rock occurs adjacent to the top corner of the plug and has a magnitude of 76.3% of the applied axial stress. At this location the rock is in triaxial tension (Table 3.3). There are no tensile axial stresses within the plug.

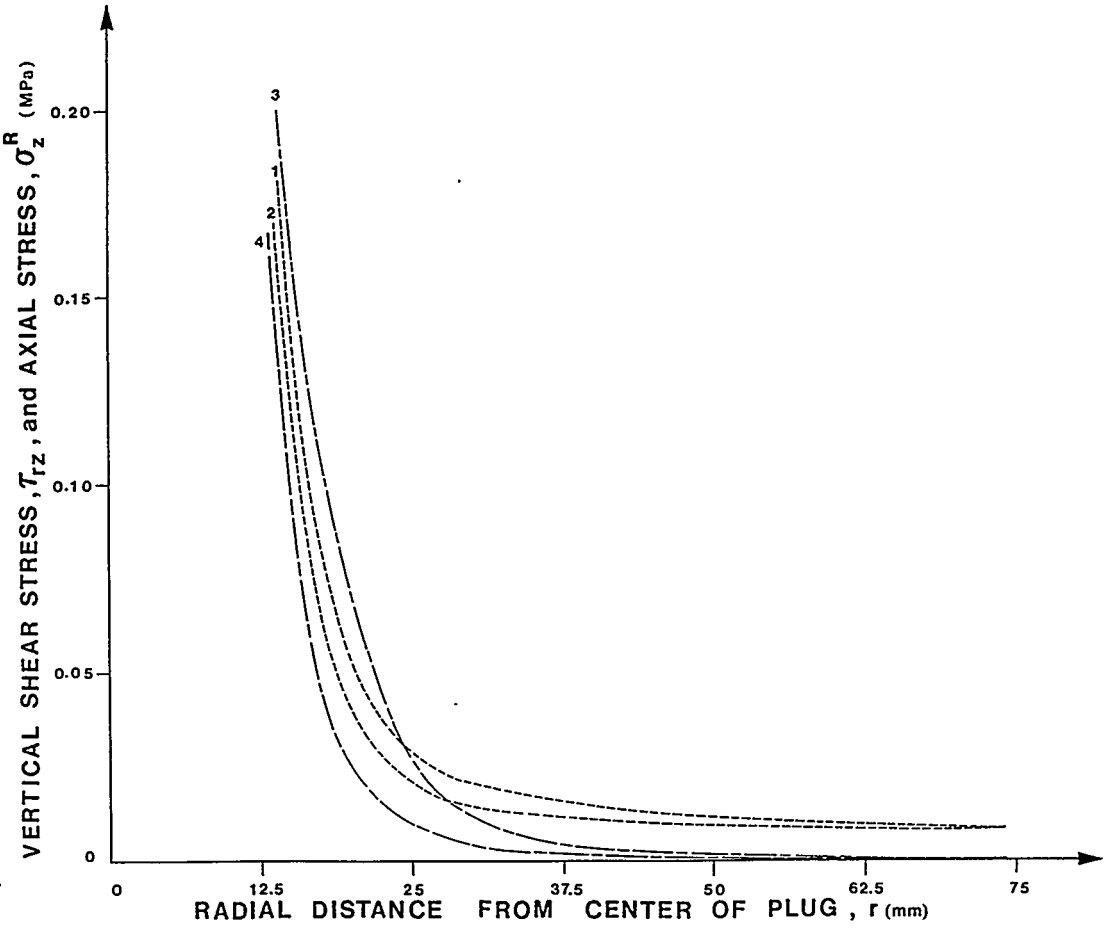

Figure 3.14 Shear stress (τ_{rz}) and normal stress (σ_z^R) distributions within rock. Curves 2 and 3 give the normal stress and shear stress distributions along section I - L (upper rock elements) of element IJKL (Figure 3.5b). Curves 1 and 4 are the normal stress and shear stress distributions along section J - K (lower rock elements).

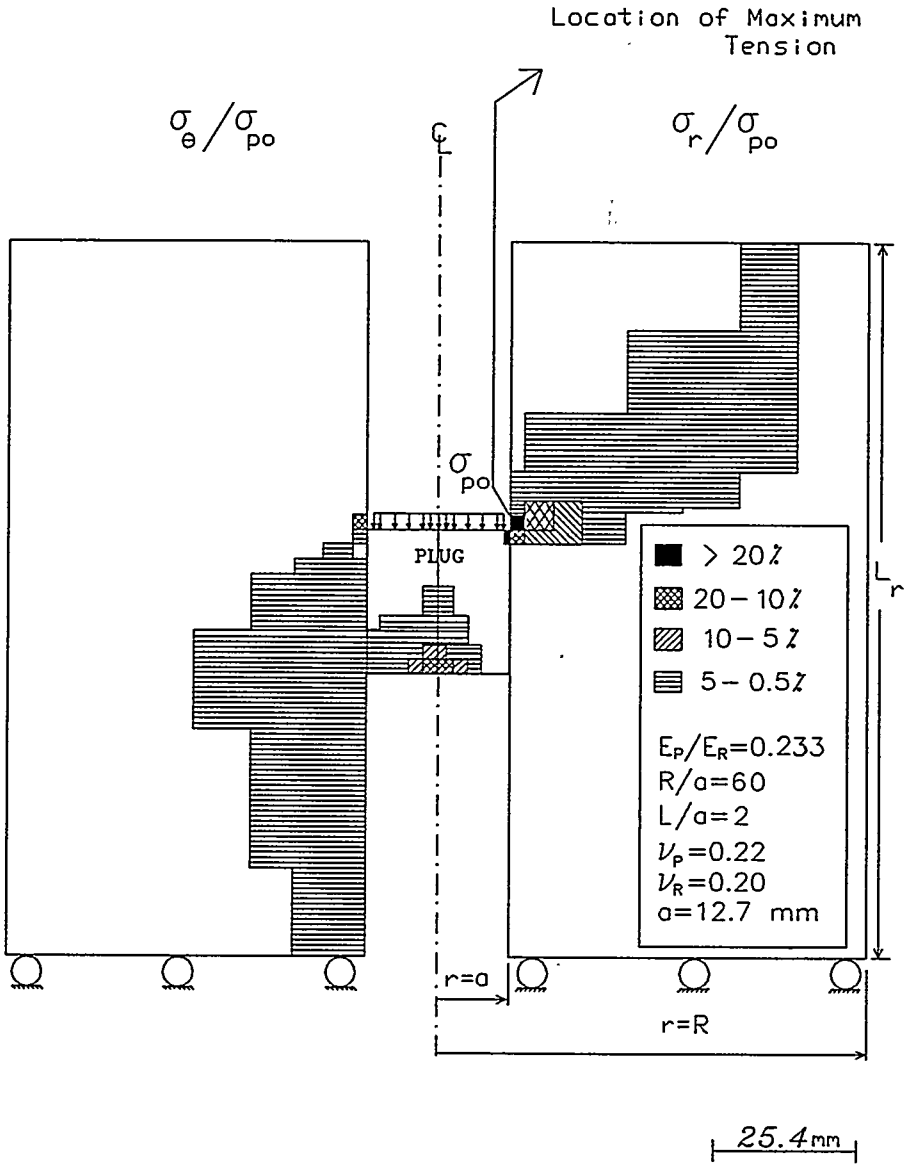

Figure 3.15 Percentage normalized tensile radial stress (σ_r/σ_{po}; right) and tensile tangential stress ($\sigma_\theta/\sigma_{po}$; left) contours for an axially loaded borehole plug in rock. Modulus ratio of 0.233 and plug length-to-radius ratio of 2. A portion of the mesh, from center to section XX', is given in Figure B.1 (Appendix B).

Table 3.3 Principal Stresses in Plug and in Rock as a Fraction of the Axial Stress (σ_{po}) Applied to a Borehole Plug. Locations A, B and C are the locations where at least one of the principal stress components give maximum tension. Compressive stresses are reckoned positive and tensile stresses negative.

		Principal Stresses in Plug						Principal Stresses in Rock		
		Location A			Location B			Location C		
E_p/E_R	L/a	σ_1/σ_{po} (%)	σ_2/σ_{po} (%)	σ_3/σ_{po} (%)	σ_1/σ_{po} (%)	σ_2/σ_{po} (%)	σ_3/σ_{po} (%)	σ_1/σ_{po} (%)	σ_2/σ_{po} (%)	σ_3/σ_{po} (%)
0.1	2	1.0	-9.0	-9.1	68.9	1.65	-73.6	-7.4	-9.7	-80.0
0.233	2	10.12	-11.13	-11.14	67.6	3.1	-68.7	-7.0	-9.0	-76.3
0.233	4	0.3	-1.14	-1.15	63.5	3.74	-49.4	-4.5	-5.0	-60.0
0.233	8	0.1	-0.18	-0.19	54.8	5.50	-26.1	-0.75	-1.8	-41.0
10	2	0.18	-41.2	-41.3	57.6	23.4	-9.6	0.44	-4.3	-42.0

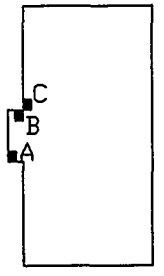

Figures B.8 and B.9 (Appendix B) give the percentage normalized tensile radial stress and tensile tangential stress distributions in specimens with plug length-to-radius ratios of 4 and 8, respectively. The tensile stress contours are for a modulus ratio of 0.233. The magnitudes of the tensile stresses and the volume under tension decrease with increased plug length-to-radius ratio. The tensile stress in the cement plugs moves upward with increased plug length (Figures 3.15 and B.9 (App. B)) because less of the plug is stressed in specimens with greater length-to-radius ratios. The specimen with L/a = 8 (Fig. B.9 (App. B)) has tension in about one-third of the top of the cement plug; the specimen with L/a = 2 (Fig. 3.15) has tension in the bottom half of the plug. Hence, less of the plug is utilized with increased plug length-to-radius ratio. The maximum tension in specimens with L/a of 4 and 8 occurs in the rock adjacent to the top corners of the plugs with a magnitude of 60% and 41% of the applied axial plug stress, respectively (Table 3.3). The magnitude of the maximum tension and the volume in tension decrease with increased plug length-to-radius ratio. No tensile axial stresses develop in the plugs.

Figure B.10 (Appendix B) gives the tensile radial and tensile tangential stress distribution in a specimen with a plug length-to-radius ratio of 2 and a modulus ratio of 10. The axial stress applied to the plug produces higher biaxial tension in the bottom half of the plug compared to that in the plug of a specimen with a modulus ratio of 0.233 (Figure 3.15). The peak tensile radial and tangential stresses in the bottom quarter of the plug center are greater than 20% of the applied axial plug stress (Figure B.10 (App. B)). More than half of the plug is in biaxial tension. The peak tensile radial and tangential stresses occur at the bottom center of the plug with a magnitude of 41% of the applied axial plug stress. The maximum tension in the rock occurs adjacent to the top corner of the plug and reaches 42% of the applied axial stress (Table 3.3). The volume in tension is larger than for a modulus ratio of 0.233 (Fig. 3.15). There are no tensile axial stresses in the plug.

Table 3.3 summarizes principal stresses in regions in the plug and rock where large tensions develop. A, B and C are the locations where at least one of the principal stress components gives maximum tension. Maximum tension in the plug for a modulus ratio of 0.233 occurs at the top corner of the plug (location B) and decreases with increasing plug length-to-radius ratio. At location B, only one stress component is tensile. At this location a plug with a modulus ratio of 10 shows smaller tension than a plug with a modulus ratio of 0.10 (Table 3.3, location B).

At the bottom center of the plug (location A), the plug is in biaxial tension. The magnitude of the tension at this location decreases with increasing plug length-to-radius ratio and with decreasing modulus ratio (Table 3.3, location A).

The maximum tension in rock occurs at location C (Table 3.3). For a modulus ratio of 0.10, the rock is under triaxial tension; for a modulus ratio of 10, there is biaxial tension at location C. At this location, the tension decreases with increasing modulus ratio and with increased plug length-to-radius ratio.

3.5 Summary and Conclusions

The simplified analytical solution(s) for borehole plug-rock mechanical interaction (presented in Chapter 2) ignore the normal stress in the rock (i.e. assume stress distribution only in the form of shear stresses). The finite element analysis shows that: 1) ignoring the normal stress in the rock overestimates the shear stresses in the rock and along the plug/rock interface; 2) the shear stresses in rock are maximum at the loaded end of the plug ($z = 0$) and minimum at the bottom of the plug ($z = L$) at a fixed radial distance r; 3) the normal stresses in rock are maximum at $z = L$ and minimum at $z = 0$ at a fixed radial distance; and 4) both the vertical stress and shear stress in rock decrease going from the plug/rock interface towards the outside of the rock core in the radial direction.

The interface shear stresses at the loaded end of the borehole plug increase with decreasing modulus ratio, decreasing plug length-to-radius ratio, and decreasing cylinder outside-to-inside radius ratio. The axial stresses within the plug become less linear with the above parameters. The axial stresses and the interface shear stresses do not affect the entire length of the longer plugs (i.e. less of the plug is utilized with increased plug length-to-radius ratios). The closed-form solution always overestimates the peak interface shear stress when compared to the finite element analysis, with overestimation ranges of 1 to 32%. Hence, the interface shear stress calculated by the analytical solution brings an additional factor of safety for design purposes.

An axial stress applied to a borehole plug in rock creates tension both in the plug and in the rock. The volume under tension increases with increased modulus ratio and decreased plug length-to-radius ratio. The maximum tension occurs in the rock adjacent to the top corners of the plugs and the magnitude increases with decreased modulus ratio and with decreased plug length. The most severe case of biaxial tension at the bottom center of the plug is observed in a specimen with a plug length-to radius ratio of 2 and a modulus ratio of 10. The peak tensile principal stress occurs at this location with a magnitude of 41% of the axial stress applied to the plug. The highest uniaxial tension in the top corner of the cement plug is observed in a specimen with a plug length-to-radius ratio of 2 and a modulus ratio of 0.1. The peak tensile principal stress occurs at this location with a magnitude of 74% of the axial stress applied to the plug.

CHAPTER FOUR

EXPERIMENTAL PROCEDURES AND RESULTS

4.1 Push-Out Tests

4.1.1 Introduction

Figures 4.1 and 4.2 show the push-out test arrangement. A cylindrical steel rod applies an axial load to a cement plug[1] installed in a rock cylinder. The LVDT and dial gage that measure the vertical displacement of the top of the plug are mounted on horizontal arms connected to the loading rod. The top LVDT and dial gage displacement monitoring points rest on horizontal brackets clamped to fixed vertical reference bars. The steel platen underneath the sample has a slit on one side to allow the downward movement of the horizontal arm of the bottom vertical displacement monitoring assembly. A vertical rod, screwed into the bottom of the cement plug, is connected to the horizontal arm, which supports the bottom LVDT and dial gage monitoring points for bottom plug displacement measurements. The bottom LVDT and dial gage are clamped to fixed vertical reference bars. A heating controller and heating tape are used to perform tests at elevated temperatures. Appendix D gives a detailed description of the push-out test set-up.

Push-out samples are stored in relatively dry (RD), in intermediately saturated (PS), or in highly saturated (FS) conditions for eight days at ambient room temperatures (24 ± 2°C), at 44 to 45°C, at 65 to 70°C, or at 90°C. The average degree of saturation ± one standard deviation for the relatively dry, intermediately saturated, and highly saturated push-out samples are 28.9 ± 20.4%, 43.0 ± 18.2%, and 72.6 ± 12.3%, respectively. Highly saturated samples are prepared by keeping the specimens under water at the desired temperature. The relatively dry or intermediately saturated samples are prepared by keeping the specimens in an environmental chamber at the desired relative humidity and temperature. Constant chamber relative humidities of 45[2] and 80%, respec-

---

1 Self-Stress II cement, provided by Dowell-Schlumberger, is an expansive cement formulation composed of Ideal Type I/II Portland cement (from Tijeras Canyon, New Mexico), mixed with 50% distilled water, 10% D53 (an expansive agent), and 1% D65 (a dispersant). All percentages are weight percent with respect to cement. Appendix C gives the procedure for preparing Self-Stress II cement borehole plugs.

2 It was originally proposed to store the relatively dry samples at 20% r.h. As the dry bulb and wet bulb temperatures of the environmental chamber can not be reduced below 36°C and 26°C, respectively, the relatively dry samples are stored at 45% r.h. (The wet bulb temperature can not be lowered below the ambient room temperature (26°C); a dry bulb temperature of 36°C and a wet bulb temperature of 26°C correspond to 45% r.h. If the dry bulb temperature is lowered below 36°C, the r.h. in the environmental chamber goes above 45%.)

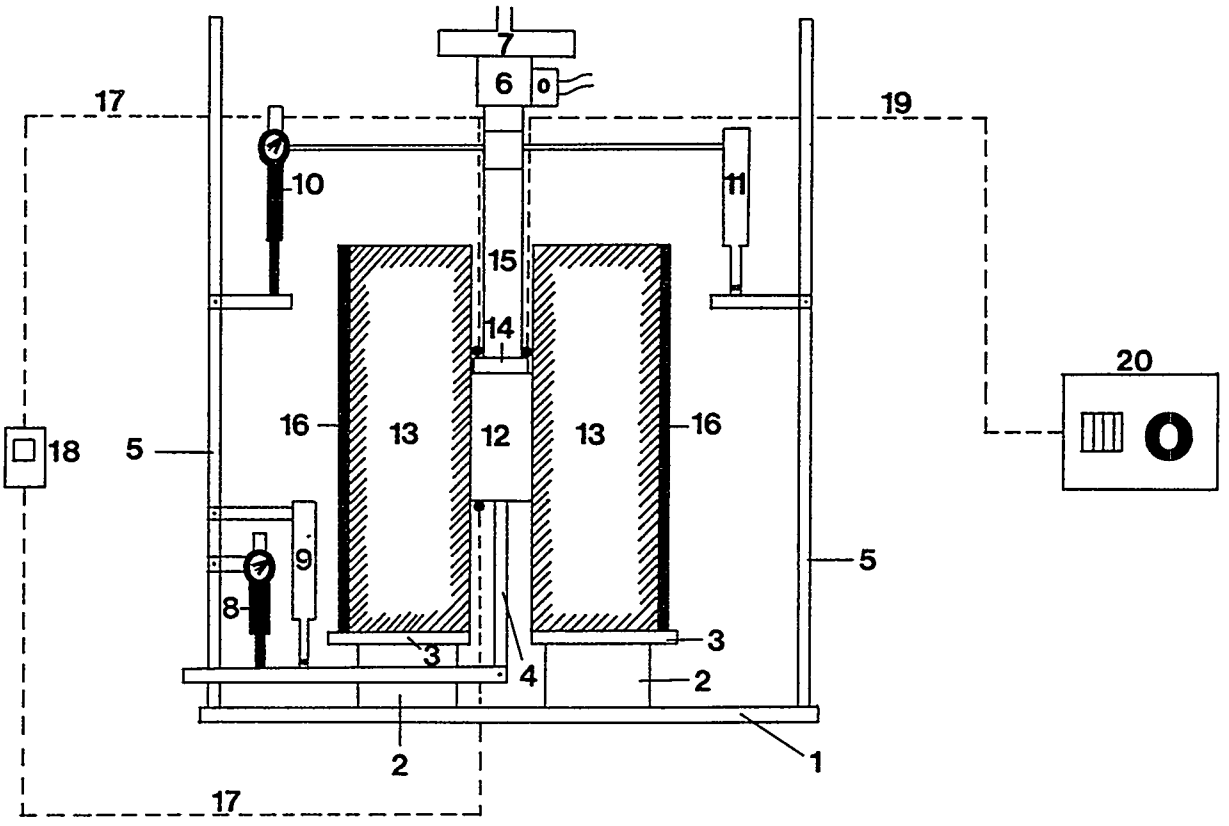

Not to scale.

1. Cylindrical steel plate
2. Circular steel plate with a slit
3. Square steel plate
4. Section for bottom displacement transfer
5. Vertical steel bars
6. Load cell
7. Loading platen
8,10. Bottom and top dial gages
9,11. Bottom and top LVDT's
12. Cement plug
13. Rock sample
14. Steel cylinder
15. Axial bar
16. Steel pipe with heating tape wrapped around
17. Thermocouple sensor and wire
18. Digital thermometer
19. Heater probe and wire
20. Heater controller

Figure 4.1 Schematic drawing of push-out test set-up.

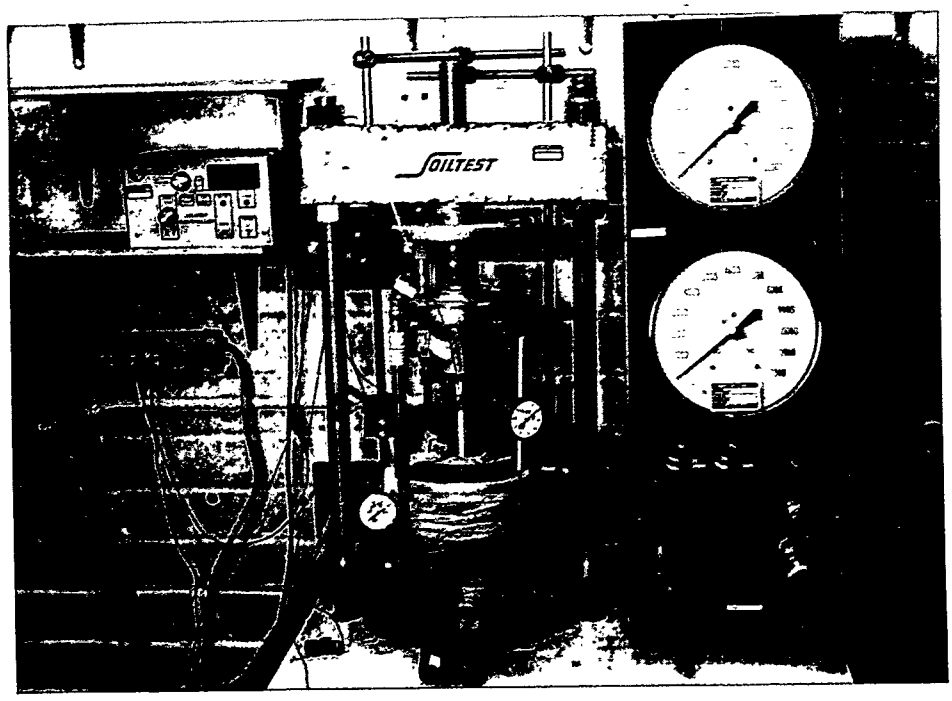

Figure 4.2 Equipment and instrumentation setup for a typical push-out test. Far right: SoilTest compression testing machine. Bottom and above: cylindrical steel plate, circular steel plate with a slit, square steel plate, rock specimen, heating tape, cylindrical axial bar, load cell, loading platen. Right: top dial gage. Left: section for bottom displacement transfer, bottom dial gage, and LVDT. Background: vertical steel bar, heater controller (to the left), top LVDT (to the right). Foreground: digital thermometer.

tively, are used in preparing dry and partially saturated samples. Sample preparation for all three curing conditions consists of the following steps: 1) leave in the oven for at least a week at 100-105°C, 2) take out of the oven and weigh (for determination of the weight of the dry tuff solids), 3) leave at room conditions (24 ± 2°C, 42-46% r.h.) for at least 4 hours to cool down (this step normally requires a desiccator to keep the sample dry and bring the temperature down. Due to the lack of a desiccator, step 3 is performed by allowing the sample to cool down at room conditions), 4) plug with cement. Then, a thin film of water is poured on top of the cement plugs. The highly saturated samples are cured underwater. A rubber stopper is placed tightly in the top boreholes of the intermediately saturated samples prior to placing them into the environmental chamber. The rubber stopper prevents the evaporation of water on top of the cement plugs, which might lead to cracking. The relatively dry samples are placed in the environmental chamber without a rubber stopper in the top boreholes (i.e. to investigate the drying effects on cement plugs). A limited number of tuff cylinders have been saturated (for a period of up to 164 days) under a water injection pressure of 0.35 MPa (50 psi) prior to cement plug emplacement. These tuff cores have degrees of saturation ranging from 68.5 to 93.7% prior to plugging and are referred to as presaturated samples. The objective of testing cement plugs in presaturated tuff cylinders is to study the influence of presaturation on bond strength, as determined by push-out tests. The cement plugs of the presaturated samples are cured underwater. Appendices D and E give the detailed procedures for push-out testing and for determining the water content and degree of saturation of push-out specimens.

4.1.2 Push-Out Test Results

Push-out tests have been performed on 130 Apache Leap tuff cylinders plugged with Self-Stress II cement. The Apache Leap tuff push-out specimens have inside diameters of 12.7 mm (0.5 in), 25.4 mm (1 in), 50.8 mm (2 in) and 101.6 mm (4 in), outside diameters of 76.2 mm (3 in), 152.4 mm (6 in) and 187.3 mm (7.375 in), and lengths ranging from 71.5 mm (2.82 in) to 228.9 mm (9.01 in). The tuff cylinders are plugged with nearly centered Self-Stress II cement plugs having length to diameter ratios ranging from 1.0 to 4.0, but approximately 1.0 in most cases. Seven tuff cylinders have been presaturated prior to plug pouring. (Appendix D gives the procedure for presaturating the tuff cylinders.) Other push-out cores are cured at relatively dry, partially and highly saturated conditions following plugging. Figure F.1 (App. F) gives the dimensions of the tested cylinders. The 50.8 mm (2 in) inside diameter samples are prepared by over-coring the 25.4 mm samples after they are tested in order to reduce sample preparation requirements.

The degree of saturation (S), water content (w), void ratio (e), porosity (n) and density (ρ) of the samples are determined prior to and following push-out testing, according to the procedure given in Appendix E. Appendix G gives the weight parameters used to determine the above variables. Appendix H gives the physical properties of each specimen. The average degree of saturation in the low, intermediate, presaturated, and highly saturated samples (prior to push-out testing) ± one standard

deviation is 28.9 ± 20.4%, 43.0 ± 18.2%, 78.0 ± 8.4% and 72.6 ± 12.3%, respectively. The presaturated samples have average degrees of saturation ± one standard deviation of 81.6 ± 9.0% prior to plug emplacement.

The variables recorded during push-out testing are the axial load applied to the plug along with the top and bottom axial plug displacements. The applied axial stress and the plug displacements of a typical push-out test are plotted against each other in Figure 4.3. In all tests, the bottom axial plug displacements are small prior to bond failure compared to the top axial plug displacements. Upon slip, the difference between the top and bottom axial plug displacements starts to decrease; i.e., the plugs start to recover their length, most probably due to stress relief. Appendix I gives additional axial stress-axial plug displacement plots.

The push-out specimens fail after periods ranging from 3 minutes to 1/2-hour. The tests are continued for up to 2 hours. Residual axial strengths range from 10 to 33% of the peak axial strengths. On the average, the tests give a residual axial strength of about 20%.

Table F.1 (Appendix F) summarizes the axial stress at failure, plug length, average and exponential shear stresses along with the top and bottom axial plug displacements at failure. The average shear stresses at the interface are calculated from Eq. (2.54). The extreme exponential shear stress distributions at the interface are calculated from Eq. (2.48). The maximum and minimum exponential shear stresses are the shear stresses at the loaded end ($z = 0$) and at the unloaded end ($z = L$) of the plug, respectively. The axial stress, uniform shear stress, and maximum exponential shear stress at failure range from 4.4 to 171.2 MPa, 1.29 to 12.96 MPa, and 5.1 to 115.47 MPa, respectively. Samples showing high axial stresses at failure generally tend to give high average shear stresses. Samples with smaller inside diameters and longer plugs (Table F.1 (App. F)) give higher axial stresses and maximum exponential shear stresses at failure.

Tables 4.1 through 4.3 give the mean axial stress, mean average shear stress, and mean maximum exponential shear stress at failure. The axial stress, average shear stress and maximum exponential shear stress in the 25.4 and 101.6 mm samples show a moderate increase in going from ambient temperature (24 ± 2°C) to 44-45°C and then a decrease with increasing temperature. The 50.8 mm highly saturated samples generally show a decrease in all three strength measures with elevated temperatures. A pronounced strength drop occurs at 90°C. The 101.6 mm specimens may show a slight decrease in strength with decreasing degree of saturation. There is no discernible difference between the bond strengths of highly and partially saturated samples. The bond strengths of the presaturated samples may be somewhat lower than those of samples cured at other conditions (Table 4.2), although the results are not statistically conclusive. The three strength measures decrease with increasing plug diameter and with decreasing plug length.

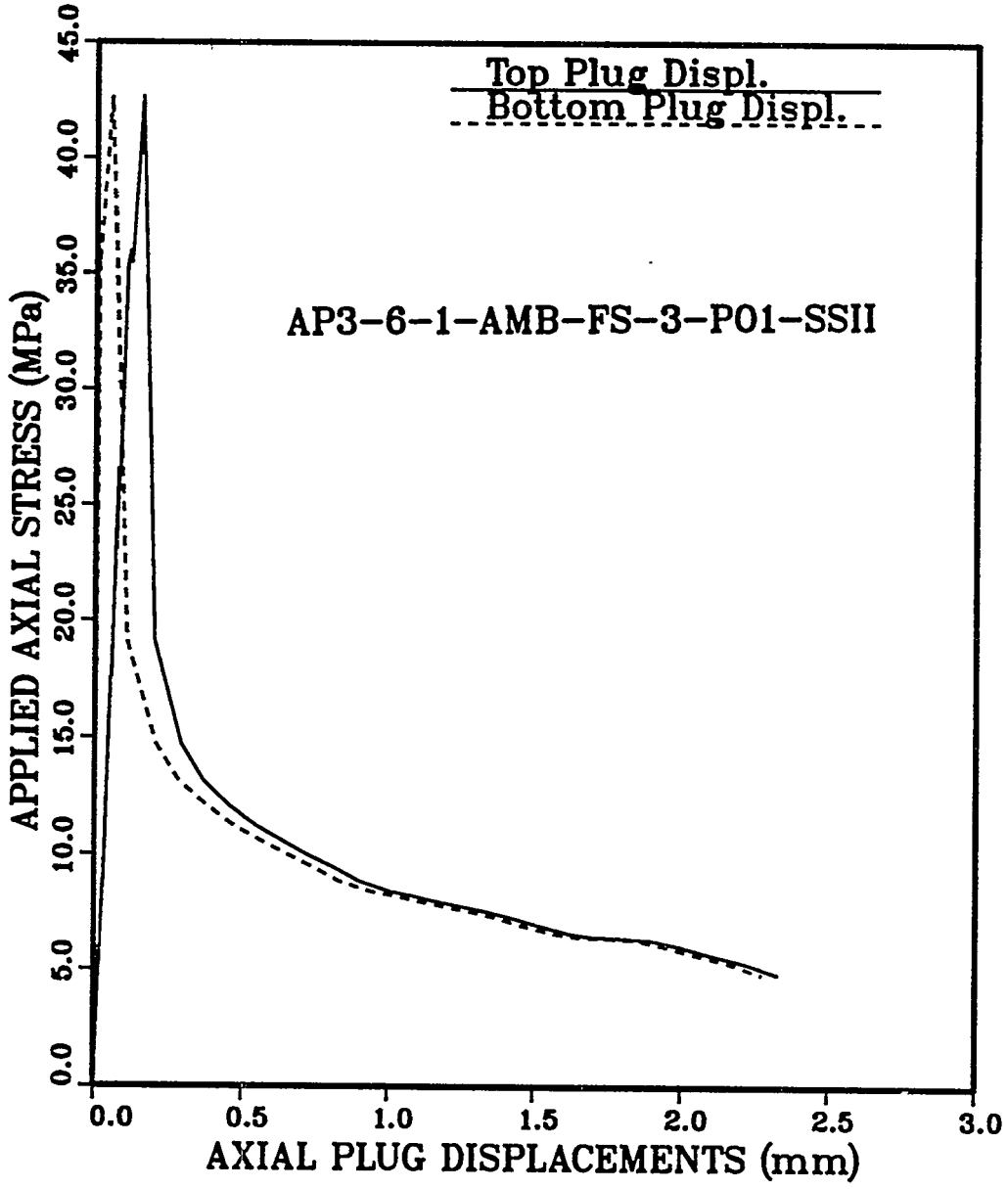

Figure 4.3 Applied axial stress vs. top and bottom axial plug displacement for push-out sample AP3-6-1-AMB-FS-3-P01-SSII. Figure F.1 (Appendix F) gives sample dimensions.

Table 4.1 Mean Axial Stress at Failure for Cement Plugs in Apache Leap Tuff Cylinders. In parentheses are given the number of samples tested. Data is for the 130 push-out tests performed. L/D = cement plug length-to-diameter ratio.

Apache Leap Tuff Cylinder		Mean Axial Stress at Failure ± One Standard Deviation (MPa)					
	Curing and	Tuff Cylinder Inside Diameter (mm)					
Saturation Condition	Test Temp. (°C)	12.7 L/D = 1	25.4 L/D = 1	25.4 L/D = 2	25.4 L/D = 4	50.8 L/D = 1	101.6 L/D = 1
Presaturated	24 ± 2	-	26.4 ± 3.9 (4)	-	-	19.3 ± 6.2 (3)	-
Highly Saturated	24 ± 2	50.5 ± 6.2 (14)	35.2 ± 4.4 (6)	65.7 ± 9.0 (5)	169.7 ± 2.5 (3)	22.7 ± 5.5 (3)	14.9 ± 1.7 (3)
	45	-	41.3 ± 4.0 (5)	-	-	21.7 ± 5.9 (3)	16.1 ± 1.2 (3)
	70	-	29.5 ± 5.1 (4)	-	-	21.7 ± 4.3 (3)	13.1 ± 3.6 (3)
	90	-	17.7 ± 3.7 (3)	-	-	10.2 ± 3.4 (4)	6.5 ± 2.1 (3)
Partially Saturated	24 ± 2	-	34.7 ± 6.4 (7)	-	-	26.4 ± 8.1 (5)	14.6 ± 5.9 (3)
	44	-	45.2 ± 9.4 (5)	-	-	20.1 ± 4.0 (4)	14.8 ± 5.1 (3)
	70	-	40.9 ± 10.9 (3)	-	-	24.3 ± 5.9 (3)	12.8 ± 1.7 (3)

Table 4.1 Mean Axial Stress at Failure for Cement Plugs in Apache Leap Tuff Cylinders.--Continued
In parentheses are given the number of samples tested. Data is for the 130 push-out tests performed. L/D = cement plug length-to-diameter ratio.

Apache Leap Tuff Cylinder		Mean Axial Stress at Failure ± One Standard Deviation (MPa)					
	Curing and	Tuff Cylinder Inside Diameter (mm)					
Saturation Condition	Test Temp. (°C)	12.7 L/D = 1	25.4 L/D = 1	25.4 L/D = 2	25.4 L/D = 4	50.8 L/D = 1	101.6 L/D = 1
Relatively Dry	24 ± 2*	-	35.4 ± 0.3 (3)	-	-	26.3 ± 4.4. (3)	14.9 ± 1.0 (3)
	36	-	25.4 ± 6.4 (7)	-	-	22.7 ± 1.4 (3)	13.5 ± 2.2 (3)

*Cylinders cured at room conditions (i.e. not in environmental chamber) at 24 ± 2°C, 36 ± 2% relative humidity with a thin film of water remaining on the top boreholes.

Table 4.2 Mean Bond Strengths of Cement Plugs in Apache Leap Tuff Cylinders. In parentheses are given the number of samples tests (130 push-out tests have been performed). L/D = cement plug length-to-diameter ratio.

Apache Leap Tuff Cylinder		Mean Average Shear Stress at Failure ± One Standard Deviation (MPa)					
	Curing and	Tuff Cylinder Inside Diameter (mm)					
Saturation Condition	Test Temp. (°C)	12.7 L/D = 1	25.4 L/D = 1	25.4 L/D = 2	25.4 L/D = 4	50.8 L/D = 1	101.6 L/D = 1
Presaturated	24 ± 2	-	6.1 ± 0.7 (4)	-	-	4.8 ± 1.5 (3)	-
Highly Saturated	24 ± 2	10.9 ± 1.2 (14)	7.3 ± 1.0 (6)	8.1 ± 1.0 (5)	10.5 ± 0.4 (3)	6.3 ± 1.9 (3)	3.9 ± 0.7 (3)
	45	-	8.6 ± 0.9 (5)	-	-	6.5 ± 2.1 (3)	4.3 ± 0.6 (3)
	70	-	6.6 ± 1.2 (4)	-	-	5.6 ± 0.9 (3)	3.3 ± 0.8 (3)
	90	-	3.7 ± 0.7 (3)	-	-	2.7 ± 1.0 (4)	1.7 ± 0.4 (3)
Partially Saturated	24 ± 2	-	7.6 ± 1.0 (7)	-	-	6.6 ± 2.0 (5)	3.7 ± 1.6 (3)
	44	-	9.3 ± 2.4 (5)	-	-	5.2 ± 0.7 (4)	3.8 ± 1.2 (3)
	70	-	8.5 ± 2.5 (3)	-	-	6.0 ± 1.2 (3)	3.0 ± 0.8 (3)

Table 4.2 Mean Bond Strengths of Cement Plugs in Apache Leap Tuff Cylinders.--Continued In parentheses are given the number of samples tests (130 push-out tests have been performed). L/D = cement plug length-to-diameter ratio.

Apache Leap Tuff Cylinder		Mean Average Shear Stress at Failure ± One Standard Deviation (MPa)					
	Curing and	Tuff Cylinder Inside Diameter (mm)					
Saturation Condition	Test Temp. (°C)	12.7 L/D = 1	25.4 L/D = 1	25.4 L/D = 2	25.4 L/D = 4	50.8 L/D = 1	101.6 L/D = 1
Relatively Dry	24 ± 2*	-	7.5 ± 0.1 (3)	-	-	6.6 ± 1.1 (3)	4.0 ± 0.2 (3)
	36	-	5.6 ± 1.2 (7)	-	-	5.4 ± 0.5 (3)	3.7 ± 0.2 (3)

*Cylinders cured at room conditions (i.e. not in environmental chamber) at 24 ± 2°C, 36 ± 2% relative humidity with a thin film of water remaining on the top boreholes.

Table 4.3 Mean Maximum Exponential Shear Stress at Failure along Cement-Rock Interface for Apache Leap Tuff Push-out Tests. In parentheses are given the number of tests. Data is for the 130 push-out tests performed. L/D = cement plug length-to-diameter ratio.

Apache Leap Tuff Cylinder		Mean Maximum Exponential Shear Stress at Failure ± One Standard Deviation (MPa)					
	Curing and	Tuff Cylinder Inside Diameter (mm)					
Saturation Condition	Test Temp. (°C)	12.7 L/D = 1	25.4 L/D = 1	25.4 L/D = 2	25.4 L/D = 4	50.8 L/D = 1	101.6 L/D = 1
Presaturated	24 ± 2	-	18.5 ± 2.6 (4)	-	-	16.7 ± 5.3 (3)	-
Highly Saturated	24 ± 2	34.8 ± 4.1 (14)	24.0 ± 3.0 (6)	44.3 ± 6.1 (5)	114.5 ± 1.7 (3)	19.7 ± 4.8 (3)	17.3 ± 1.9 (3)
	45	-	28.2 ± 2.7 (5)	-	-	18.9 ± 5.2 (3)	18.8 ± 1.4 (3)
	70	-	20.5 ± 3.6 (4)	-	-	18.8 ± 1.7 (3)	15.2 ± 4.2 (3)
	90	-	12.1 ± 2.4 (3)	-	-	8.8 ± 3.0 (4)	7.5 ± 2.4 (3)
Partially Saturated	24 ± 2	-	24.0 ± 4.1 (7)	-	-	22.8 ± 7.0 (5)	17.0 ± 6.9 (3)
	44	-	30.9 ± 6.7 (5)	-	-	17.4 ± 3.4 (4)	17.2 ± 5.9 (3)
	70	-	28.1 ± 7.3 (3)	-	-	21.0 ± 5.1 (3)	14.9 ± 2.0 (3)

Table 4.3 Mean Maximum Exponential Shear Stress at Failure along Cement-Rock Interface for Apache Leap Tuff Push-out Tests.--Continued In parentheses are given the number of tests. Data is for the 130 push-out tests performed. L/D = cement plug length-to-diameter ratio.

Apache Leap Tuff Cylinder		Mean Maximum Exponential Shear Stress at Failure ± One Standard Deviation (MPa)					
	Curing and	Tuff Cylinder Inside Diameter (mm)					
Saturation Condition	Test Temp. (°C)	12.7 L/D = 1	25.4 L/D = 1	25.4 L/D = 2	25.4 L/D = 4	50.8 L/D = 1	101.6 L/D = 1
Relatively Dry	24 ± 2*	-	24.2 ± 0.2 (3)	-	-	22.8 ± 3.8 (3)	17.3 ± 1.2 (3)
	36	-	19.7 ± 1.2 (7)	-	-	17.4 ± 4.2 (3)	15.7 ± 2.6 (3)

*Cylinders cured at room conditions (i.e. not in environmental chamber) at 24 ± 2°C, 36 ± 2% relative humidity with a thin film of water remaining on the top boreholes.

The relatively dry 25.4 mm samples cured and tested at 36°C show lower strength measures than the more saturated samples cured and tested at 44°C (Tables 4.1 through 4.3). This parallels conclusions from previous studies (e.g. Daemen et al., 1986, pp. 338-360; Adisoma and Daemen, 1988). A common observation in these previous studies is that if the push-out samples are allowed to dry out, their cement plugs show significant shrinkage and drastic strength reduction after moderately long periods of time (e.g. more than 2 years). The relatively dry samples cured and tested at ambient conditions (24 ± 2°C, 36 ± 2% r.h.) show comparable strength measures to the more saturated samples (Tables 4.1 through 4.3). This is most probably because these samples are not allowed to dry out. They are cured and tested at room conditions (24 ± 2°C, 36 ± 2% r.h.) with a film of water in their top boreholes during the initial 3 to 5 days of cement curing. The free water (in the top specimen boreholes) of the relatively dry samples cured in the environmental chamber at 36°C, 45% r.h. evaporates within one day after the samples are placed in the environmental chamber. This might explain why the relatively dry samples cured in the environmental chamber give lower strengths than those cured under room conditions.

Tables 4.4 and 4.5 give the mean axial top plug displacement per applied axial stress at failure and the mean peak interface shear strength at failure, respectively. The mean peak interface shear strength is calculated from Eq. (2.113), using 0.05 MPa for cohesion and 25° for the angle of friction (Section 4.2.4). The displacement increases with increasing plug diameter and decreasing plug length. The strength decreases with increasing plug diameter and decreasing plug length. The highly saturated and partially saturated samples give comparable frictional strengths. The mean frictional shear strengths at failure are 13.3 to 31.8% of the mean maximum exponential shear stresses at failure (Table 4.3).

Seven (out of 34) of the 50.8 mm samples and 17 (out of 27) of the 101.6 mm samples split in tension during push-out testing (Table F.1) (App. F). The mean tensile strengths of the 50.8 and 101.6 mm specimens ± one standard deviation (calculated from Eq. (J.2) (App. J)) are 8.98 ± 1.7 MPa and 9.16 ± 1.2 MPa respectively.

4.1.2.1 Push-Out Tests on Rock Bridges

Push-out tests on tuff rock bridges provide a reference strength against which to compare cement axial strength. Eleven rock bridge push-out tests have been performed. The rock bridge cylinders have inside diameters of 25.4 mm (1 in), 50.8 mm (2 in) and 101.6 mm (4 in), outside diameters of 152.4 mm (6 in) and 187.3 mm (7.375 in). The tuff cylinders have nearly centered rock bridges left in place with length-to-diameter ratios of approximately 1.0. Figure F.2 (App. F) gives the dimensions of the tuff cylinders with rock bridges.

Table F.2 (App. F) summarizes the axial stress at failure, plug length, and average and exponential shear stresses at failure for the rock

Table 4.4 Mean Axial Top Plug Displacement per Applied Axial Stress at Failure. The number of tests is given in parentheses. L/D = cement plug length-to-diameter ratio.

Apache Leap Tuff Cylinder		Mean Axial Top Plug Displacement per Applied Axial Stress at Failure ± One Standard Deviation (mm/MPa x 10^3)					
	Curing and	Tuff Cylinder Inside Diameter (mm)					
Saturation Condition	Test Temp. (°C)	12.7 L/D = 1	25.4 L/D = 1	25.4 L/D = 2	25.4 L/D = 4	50.8 L/D = 1	101.6 L/D = 1
Presaturated	24 ± 2	-	6.1 ± 0.2 (4)	-	-	12.5 ● 6.6 (3)	-
Highly Saturated	24 ± 2	2.6 ± 0.4 (14)	4.6 ± 1.7 (6)	4.3 ± 0.7 (5)	4.3 ± 0.4 (3)	10.5 ± 6.1 (3)	13.9 ± 5.0 (3)
	45	-	4.0 ± 1.5 (5)	-	-	11.1 ± 5.0 (3)	11.6 ± 1.8 (3)
	70	-	7.3 ± 2.0 (4)	-	-	7.7 ± 2.0 (3)	17.4 ± 9.0 (3)
	90	-	8.8 ± 1.8 (3)	-	-	22.0 ± 10.0 (4)	27.0 ± 17.5 (3)
Partially Saturated	24 ± 2	-	4.3 ± 2.0 (7)	-	-	8.9 ± 3.6 (5)	21.5 ± 11.0 (3)
	44	-	5.8 ± 3.1 (5)	-	-	17.0 ± 11.0 (4)	18.7 ± 4.3 (3)
	70	-	3.8 ± 2.1 (3)	-	-	13.9 ± 5.1 (3)	16.1 ± 8.5 (3)

Table 4.4 Mean Axial Top Plug Displacement per Applied Axial Stress at Failure.--Continued In parentheses are given the number of tests. Data is for the 130 push-out tests performed. L/D = cement plug length-to-diameter ratio.

Apache Leap Tuff Cylinder		Mean Axial Top Plug Displacement per Applied Axial Stress at Failure ± One Standard Deviation (mm/MPa x 10^3)					
	Curing and	Tuff Cylinder Inside Diameter (mm)					
Saturation Condition	Test Temp. (°C)	12.7 L/D = 1	25.4 L/D = 1	25.4 L/D = 2	25.4 L/D = 4	50.8 L/D = 1	101.6 L/D = 1
Relatively Dry	24 ± 2*	-	5.3 ± 2.7 (3)	-	-	5.5 ± 0.9 (3)	23.1 ± 6.0 (3)
	36	-	5.9 ± 1.7 (7)	-	-	6.6 ± 2.5 (3)	17.3± 6.6 (3)

*Cylinders cured at room conditions (i.e. not in environmental chamber) at 24 ± 2°C, 36 ± 2% relative humidity with a thin film of water remaining on the top boreholes.

Table 4.5 Mean Peak Interface Shear Strength at Failure for Apache Leap Tuff Push-Out Tests. In parentheses are given the number of samples tested. Data is for the 130 push-out tests performed. L/D = cement plug length-to-diameter ratio.

Apache Leap Tuff Cylinder		Mean Peak Interface Shear Strength at Failure ± One Standard Deviation (MPa)					
	Curing and	Tuff Cylinder Inside Diameter (mm)					
Saturation Condition	Test Temp. (°C)	12.7 L/D = 1	25.4 L/D = 1	25.4 L/D = 2	25.4 L/D = 4	50.8 L/D = 1	101.6 L/D = 1
Presaturated	24 ± 2	-	3.5 ± 0.4 (4)	-	-	2.8 ± 0.6 (3)	-
Highly Saturated	24 ± 2	5.8 ± 0.6 (14)	4.4 ± 0.4 (6)	7.3 ± 0.9 (5)	17.3 ± 0.3 (3)	3.1 ± 0.5 (3)	2.3 ± 0.1 (3)
	45	-	5.2 ± 0.4 (5)	-	-	3.3 ± 0.6 (3)	2.6 ± 0.1 (3)
	70	-	4.4 ± 0.5 (4)	-	-	3.6 ± 0.4 (3)	2.7 ± 0.3 (3)
	90	-	3.6 ± 0.4 (3)	-	-	2.8 ± 0.3 (4)	2.3 ± 0.2 (3)
Partially Saturated	24 ± 2	-	4.3 ± 0.6 (7)	-	-	3.5 ± 0.8 (5)	2.3 ± 0.5 (3)
	44	-	5.6 ± 0.9 (5)	-	-	3.1 ± 0.4 (4)	2.5 ± 0.4 (3)
	70	-	5.5 ± 1.0 (3)	-	-	3.8 ± 0.6 (3)	2.6 ± 0.1 (3)

Table 4.5 Mean Peak Interface Shear Strength at Failure for Apache Leap Tuff Push-Out Tests.--Continued In parentheses are given the number of samples tested. Data is for the 130 push-out tests performed. L/D = cement plug length-to-diameter ratio.

Apache Leap Tuff Cylinder		Mean Peak Interface Shear Strength at Failure ± One Standard Deviation (MPa)					
	Curing and	Tuff Cylinder Inside Diameter (mm)					
Saturation Condition	Test Temp. (°C)	12.7 L/D = 1	25.4 L/D = 1	25.4 L/D = 2	25.4 L/D = 4	50.8 L/D = 1	101.6 L/D = 1
Relatively Dry	24 ± 2*	-	4.4 ± 0.03 (3)	-	-	3.5 ± 0.4 (3)	2.3 ± 0.1 (3)
	36	-	3.6 ± 0.6 (7)	-	-	3.3 ± 0.1 (3)	2.3 ± 0.2 (3)

*Cylinders cured at room conditions (i.e. not in environmental chamber) at 24 ± 2°C, 36 ± 2% relative humidity with a thin film of water remaining on the top boreholes.

bridge cylinders. The average shear stresses at the interface are calculated from Eq. (2.54). The extreme exponential shear stress distributions at the interface are calculated from Eq. (2.48). The average axial stress at failure ± one standard deviation for cylinders with inside diameters of 25.4, 50.8 and 101.6 mm are 272 ± 125, 166 ± 99 and 153 ± 80 MPa, respectively. Hence, samples with smaller rock bridge diameters give higher axial strengths. The 25.4, 50.8 and 101.6 mm Self-Stress II cement push-out samples (Table F.1 (App. F)) give a mean axial strength of 12.46, 13.12 and 8.79% of that of samples with rock bridges having the same inside diameters (Table F.2).

4.2 Mechanical Characterization of Cement

This section describes results of mechanical characterization tests on the Self-Stress II cement used in this sealing research. Appendix C gives the composition and procedure for preparing Self-Stress II cement borehole plugs. Cement slurry viscosity and density measurements, uniaxial compressive strength tests, cement swelling tests, and tuff-on-cement small-scale direct shear tests are performed.

4.2.1 Cement Slurry Viscosity and Density Measurements

Table L.1 (Appendix L) gives the viscosity and slurry density of Self-Stress II cement. Four viscosity and density measurements have been performed. The viscosity is measured with a Fann viscometer using the procedure given in Appendix C. The density of the cement slurry is measured with a hydrometer (Cole-Parmer Model J-8291-50) with a specific gravity range of 1.000 to 2.000.[3] Viscosity and density measurements are taken at a room temperature of 27°C, relative room humidity of 39 ± 1% and at atmospheric pressure. The viscosity of the cement slurry varies from 32 x 10^{-3} kg/m sec (32 centipoises) at 300 rpm rotor speed to 200 x 10^{-3} kg/m sec (200 centipoises) at 3 rpm. The average cement slurry density ± standard deviation is 1.86 ± 0.013 g/cc (Table L.1) (App. L).

4.2.2 Uniaxial Compressive Strength

Uniaxial compressive strength tests have been performed on eleven Self-Stress II cement specimens. Sample preparation and testing procedures are given in Appendix K. The cylindrical samples are prepared by curing cement paste in acrylic molds for eight days. The nominal diameter and length are 50.8 mm (2 in) and 127 mm (5 in), respectively. A SoilTest compression machine is used to load the specimens at a loading rate of 252 N/s. Three specimens have been tested with a deformation jacket in order to determine the Young's modulus and Poisson's ratio.

---

3 Procedure deviates from API Spec. No. 10, 1986, pp. 46-47, which requires the use of a pressurized fluid density balance for slurry density measurements.

Mean and standard deviation of the uniaxial compressive strength are 18.8 and 0.97 MPa, respectively (Table L.2) (App. L). All samples experience splitting failure. Figure 4.4 shows sample B-20 after failure. Note the absence of air voids and the uniform dense composition.

4.2.2.1 Elastic Modulus and Poisson's Ratio

A deformation jacket (Part No. DJC, Structural Behavior Engineering Laboratories) is placed around the cement specimens in order to monitor the lateral and axial displacement during uniaxial loading. Figure K.2 (Appendix K) shows sample B-20 instrumented with the deformation jacket. Appendix K gives the procedure for measuring the Young's modulus and Poissons's ratio of the cement paste specimens. The Young's modulus and Poisson's ratio for a specimen are calculated from the secant of the stress-strain curve at 50% of the strength (0 to 13344 N (3000 lbf)) (ISRM Suggested Methods, Bieniawski et al, 1978; ASTM D3148-80).

Figure L.1 (Appendix L) gives the axial stress and lateral strain vs. axial strain for sample B-20. Figures L.2 and L.3 give those for specimens B-24 and B-26. The Young's moduli for samples B-20, B-24 and B-26 are 5.0 GPa, 5.54 GPa and 5.23 GPa, respectively. The Poisson's ratios are 0.266, 0.239 and 0.167. The mean Young's modulus ± standard deviation is 5.25 ± 0.270 GPa. The Poisson's ratio is 0.22 ± 0.05.

4.2.3 Cement Swelling Tests

4.2.3.1 Introduction

The objective of these tests is to determine the radial expansive stresses generated by Self-Stress II cement. The swelling stresses are measured by monitoring the strains of steel pipes in which cement grout is emplaced and cured. Three pipes each with inside diameters of 25.4 mm (1 in), 50.8 mm (2 in) and 101.6 mm (4 in) have been monitored. All pipes have wall thickness-to-inside diameter ratios of 1/16, and hence have identical confining stiffnesses. The cement plugs installed in these pipes have length-to-diameter ratios (L/D) of approximately 1. The cement swelling stresses are determined with two tangential strain gages, placed 180° from each other on the outside walls of each pipe. The hydration temperature is monitored with thermocouple probes placed approximately at the center of each plug. Testing is performed at a room temperature of 24 ± 2°C. The tangential strains and cement hydration temperatures are monitored by means of an HP Data Acquisition System. Test results are presented as a function of time. The procedures for performing cement swelling tests in steel pipes and for monitoring the hydration temperatures are given in Appendix M. Figure 4.5 shows the steel pipes with strain gages and thermocouple wires.

4.2.3.2 Results

The expansive stress (σ_s) is calculated from Eq. (M.4) (Appendix M). The average tangential strain on the inside steel pipe walls ($\epsilon_{\theta(r=a)}$) is given by Eq. (M.7).

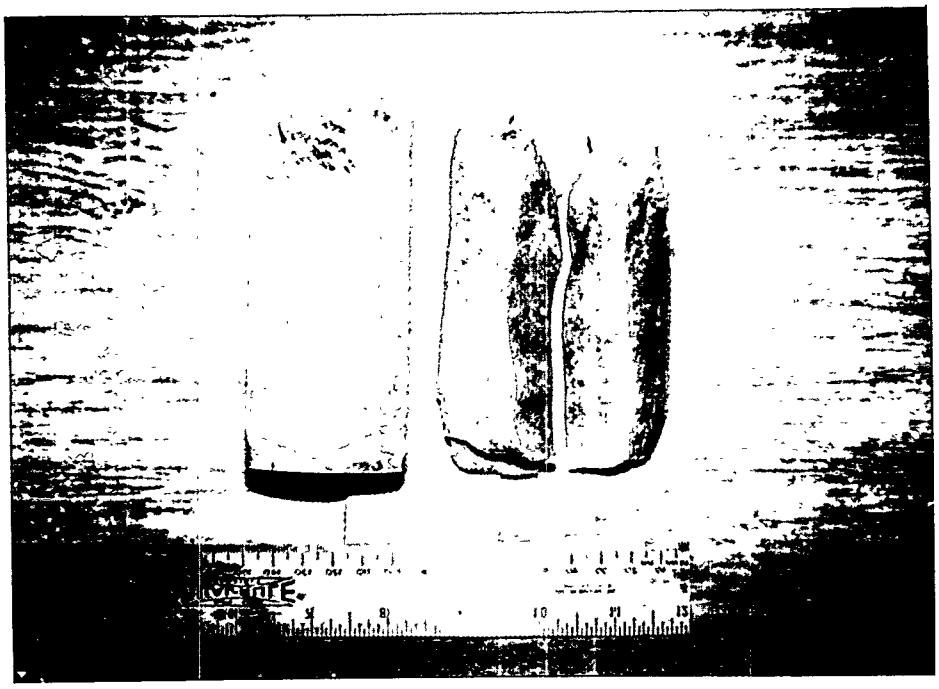

Figure 4.4 Failed uniaxial compressive strength test cement cylinder B-20. Note the splitting failure and the absence of air voids.

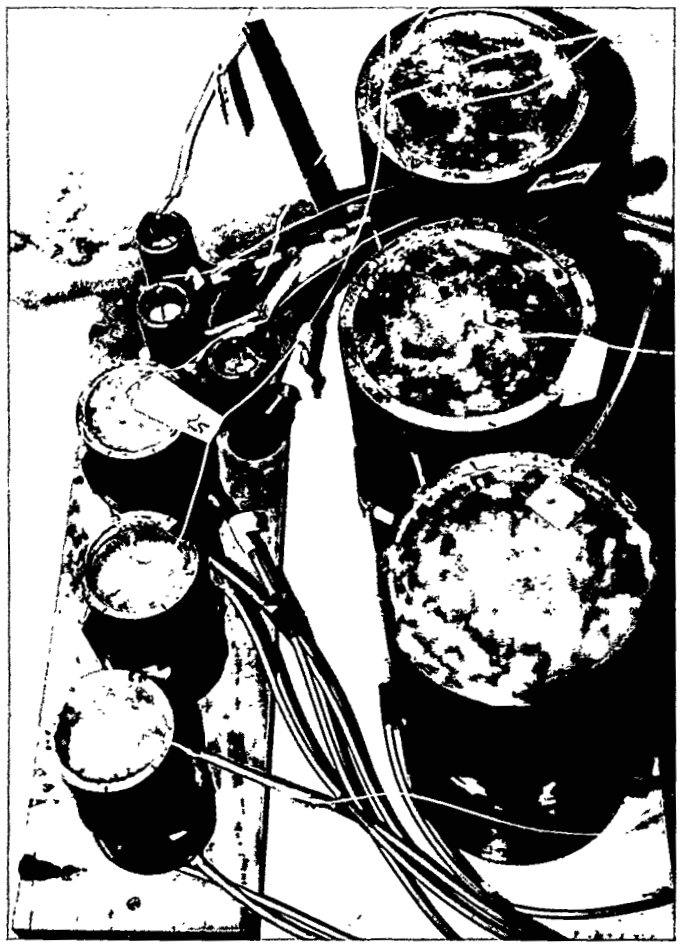

Figure 4.5 Steel pipes filled with Self-Stress II cement and instrumented for swelling stress and hydration temperature measurements. The pipes have inside diameters of 25.4, 50.8 and 101.6 mm (1, 2 and 4 in). Three plugs of each size are monitored.

All results are for a Young's modulus and Poisson's ratio of the steel pipe of 207 GPa and 0.27, respectively (Sandor, 1978, p. 414). Figures L.4 and L.5 (Appendix L) give the mean tangential strain on the steel pipe outside and inside walls respectively. The plots are given as a function of time for each pipe size. The swelling stress vs. time is presented in Figure 4.6. The strains and the swelling stresses give the steepest slopes between 12 hours to 1 day after cement paste emplacement. Swelling tends to increase with time, but at a decreasing rate. The mean swelling stress (σ_s) ± one standard deviation measured in the 25.4, 50.8 and 101.6 mm pipes after 8 days is 2.04 ± 0.09, 2.1 ± 0.05 and 2.19 ± 0.04 MPa, respectively. The mean swelling stress in the 25.4, 50.8 and 101.6 mm pipes after 335 days is 4.61, 4.81 and 4.97 MPa, respectively (Figure 4.6). Swelling increases slightly with increasing plug diameter.

The temperature of the cement paste at the time of pouring is ambient (23°C). The temperature increases gradually until 12 hours after emplacement. The mean maximum hydration temperature of the 25.4, 50.8 and 101.6 mm diameter plugs, 12 hours after cement pouring is 24, 25.3 and 31°C, respectively. The temperatures gradually decrease beyond 12 hours and return to room temperature (23°C) 27 hours after emplacement.

4.2.4 Cement-on-Rock Small-Scale Direct Shear Tests

The direct shear test measures the shear strength (peak and/or residual) as a function of the stress perpendicular to the sheared plane. Its purpose is to obtain shear strength parameters (cohesion, angle of friction) for sliding surfaces. Push-out tests induce a highly nonuniform shear stress, which complicates interpretation of the results. Direct shear tests allow a determination of the rock-cement interface shear strength under relatively uniform stress conditions.

Three tests have been conducted on Apache Leap tuff discs in contact with Self-Stress II cement discs. Cylindrical rock and cement samples of equal nominal diameter and length of 25.4 mm (1 in) are tested. The rock cores are obtained from Apache Leap Tuff Block No. APD-6. The rock discs are prepared by cutting rock cores to 25.4 mm length by means of a diamond saw. The cement discs are prepared according to the procedure given in Appendix K and are cured under water for eight days.

The rock and cement discs are cast in cement molds prior to placing them into the direct shear box. The tests are performed with a Wykeham Farrance 25302 direct shear machine following the procedure of Adisoma et al. (1990). Normal stresses of 0.172, 0.344, 0.689, and 1.38 MPa (25, 50, 100, and 200 psi) are applied. A displacement rate of 0.635 mm/min is maintained during testing. The Coulomb criterion is used to

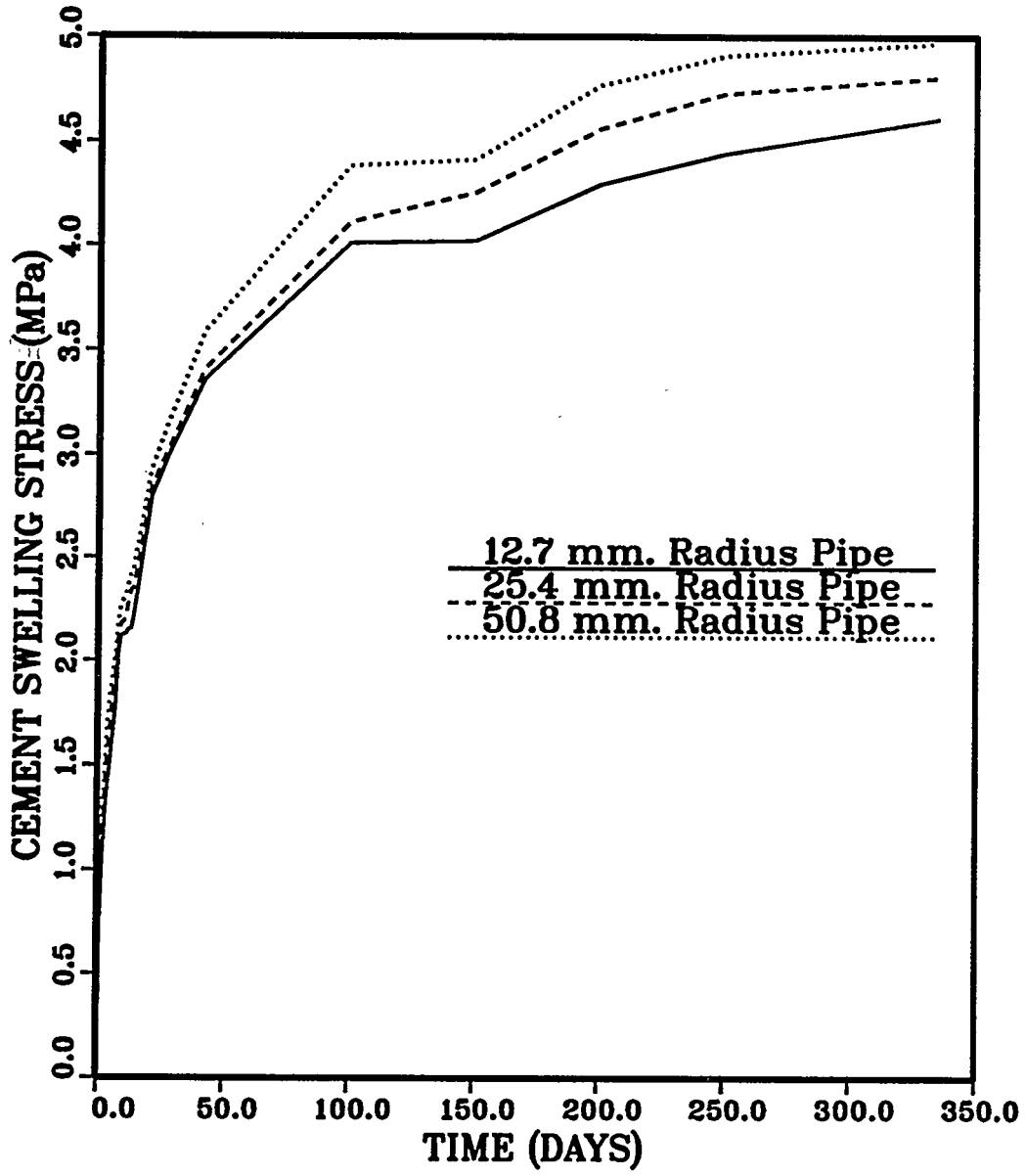

Figure 4.6 Mean cement swelling stress vs. curing time.

determine the cohesion and angle of friction (peak and residual[4]) of the rock/cement contact. Strength parameters are obtained using linear regression.

Table L.3 (Appendix L) gives the results. Figures L.6 through L.8 give a linear regression plot for the shear stress vs. normal stress.

4 There is strong doubt about the residual value, as it appears that the shear displacements were not sufficient to give a true residual value.

CHAPTER FIVE

ANALYSIS AND INTERPRETATION OF THE ANALYTICAL AND EXPERIMENTAL RESULTS

5.1 Introduction

This chapter analyzes and interprets the results of the push-out tests performed on cementitious borehole plugs in holes in welded tuff. The bond strength is more easily determined than is the hydraulic bond between such plugs and the rock. Because the permeability of such systems is usually low, its determination requires lengthy experiments. Measuring the bond strength provides an efficient alternative, as well as results that have direct relevance to plug performance. Analyzed in this chapter are the variables that influence the distributions of the axial stress and of the shear stress along an axially loaded borehole plug, bond strength of confined push-out cylinders, variables that influence push-out strength, and borehole stability under internal pressure.

5.2 Influence of the Axial Stress Applied to the Plug and the Applied External Lateral Stress on Contact Stress

5.2.1 Introduction

The push-out tests reported in Chapter 4, Section 4.1.2, have been performed on tuff cores with four different outside and inside radii: 1) cores with inside radius of 6.35 mm (0.25 in) and outside radius of 38.1 mm (1.5 in); 2) cores with inside radius of 12.7 mm (0.5 in) and outside radius of 76.2 mm (3 in); 3) cores with inside radius of 25.4 mm (1 in) and outside radius of 76.2 mm (3 in); and 4) cores with inside radius of 50.8 mm (2 in) and outside radius of 93.7 mm (3.7 in). These tuff cores have outside to inside radius ratios of 6, 3 and 1.84, respectively. They are plugged with nearly centered Self-Stress II cement plugs having length-to-diameter ratios of 1.0, in most cases. The push-out tests are performed on plugs in unconfined rock cylinders.

The main objective of this section is to investigate analytically the potential influence of push-out cylinder outside-to-inside radius ratio on the contact (radial) stress. Additional objectives are to study the effect of axial stress applied to the plug and the effect of lateral external stress on the normal stress across the plug/rock interface, and on the radial displacement along the plug-rock interface. The normal stress and the radial displacement along the plug/rock interface are analyzed as a function of ratio of the Young's modulus of the plug to that of the rock, cylinder outside to inside radius ratio, and Poisson's ratios of the plug and of the rock. The analysis leads to a formulation which allows for the differences in cylinder outside-to-inside radius

ratio, and provides a means for adjusting all results to a common reference basis. Sign conventions are those presented by Jaeger and Cook (1979, pp. 10 and 33-37), where compressive stresses and displacements in the negative directions of the axes are reckoned positive.

The Young's modulus and Poisson's ratio of the tuff are 22.6 ± 5.7 GPa and 0.20 ± 0.03, respectively (Fuenkajorn and Daemen, 1990, p. 36). The Self-Stress II cement plug has Young's modulus and Poisson's ratio of 5.25 ± 0.27 GPa and 0.22 ± 0.05, respectively (Chapter 4, Section 4.2.2). Using the lower and higher bounds for the material properties (instead of the average material properties) leads to a variation of not more than 0.6% in the calculated displacements and stresses. Hence, only the average values of the rock and plug material properties are used (i.e. $E_p/E_R = 0.223$, $\nu_p = 0.22$, $\nu_R = 0.20$).

Binnall et al. (1987, pp. 18 and 23) give the average value of the in-situ vertical and horizontal stresses for four stratigraphic units of the Yucca Mountain tuff at potential repository horizon depths. The ratio of the average in-situ vertical stress to the Young's modulus of the plug (σ_{po}/E_p) and that of the average in-situ horizontal stress to the Young's modulus of the rock (σ_o/E_R) are in the neighborhood of 0.001. Therefore, for displacement calculations, both σ_{po}/E_R and σ_o/E_R are taken equal to 0.001. The stress and axial displacement calculations using the plane strain assumption usually deviate not more than 5% from those calculated with the plane stress approximation. Because the difference is small, subsequent presentations and discussions are usually limited to the plane strain configuration.

5.2.2 Axially Loaded Borehole Plug

5.2.2.1 Theoretical Axial Stress and Axial Plug Displacement Distribution

Chapter Two, Section 2.2.2, presents analytical solutions for the axial stress and displacement distributions along an axially loaded, elastic borehole plug. The axial stress within an axially loaded borehole plug, the shear stress along the plug/rock interface, and the axial plug displacement is given by Eqs. (2.52), (2.48) and (2.47). A comprehensive numerical evaluation of these equations is given in the following sections. Implications in terms of plug design and performance are discussed.

5.2.2.2 Axial Stress and Axial Plug Displacement Distribution

Table 5.1 summarizes the results for the axial stress within the plug and for the interface shear stress along the plug as a function of modulus ratio, cylinder outside-to-inside radius ratio and distance from the loaded end of the plug. Tuff cylinders with radius ratios of 6, 3 and 1.84 represent push-out cylinders with inside radii of 12.7, 25.4 and 50.8 mm, respectively (Table 5.1). Table 5.2 summarizes the results for the relative and absolute axial plug displacements for an axially loaded borehole plug. The interface shear stresses at the loaded end of the borehole plug (at $z/L = 0$) increase with decreasing modulus ratio and (slightly) with decreasing cylinder outside-to-inside radius ratio.

Table 5.1 Axial Stress (σ_z^p) and Interface Shear Stress ($\tau_{rz,l}$) Distributions along an Axially Loaded Borehole Plug. The stresses are a function of Young's modulus ratio of plug and rock (E_p/E_R), tuff cylinder outside-to-inside radius ratio (R/a), and distance along the plug (z/L). σ_{po} = axial stress applied to the plug. Poissons' ratio of rock and plug (ν_p, ν_R) = 0.22 and 0.20, plug length-to-radius ratio (L/a) = 2.50.

Tuff Cylinder Radius Ratio (R/a)	Young's Modulus Ratio of Plug and Rock (E_p/E_R)	σ_z^p/σ_{po}			$\tau_{rz,l}/\sigma_{po}$	
		z/L = 0.25	z/L = 0.50	z/L = 0.75	z/L = 0	z/L = 1
1.84 (a = 50.8 mm)	10	0.6641	0.4045	0.1913	0.3860	0.1877
"	1	0.5513	0.2887	0.1235	0.5849	0.1170
"	0.233	0.3126	0.0970	0.0276	1.1621	0.0223
"	0.1	0.1736	0.03	0.0051	1.7513	0.0301
3.0 (a = 25.4 mm)	10	0.6642	0.4046	0.1913	0.3857	0.1878
"	1	0.6231	0.361	0.1653	0.4551	0.1604
"	0.233	0.4199	0.1725	0.0618	0.8648	0.0547
"	0.1	0.2716	0.0734	0.0186	1.3030	0.0142
6.0 (a = 12.7 mm)	10	0.6643	0.4047	0.1914	0.3856	0.1878
"	1	0.6517	0.3911	0.1832	0.4065	0.1793
"	0.233	0.4861	0.2281	0.0903	0.7156	0.083
"	0.1	0.3435	0.1167	0.036	1.068	0.0299

Table 5.2 Relative and Absolute Axial Plug Displacement Distributions along an Axially Loaded Borehole Plug. The displacements are a function of Young's modulus ratio of plug and rock (E_p/E_R), tuff cylinder outside-to-inside radius ratio (R/a), and distance along the plug (z/L). σ_{po} = axial stress applied to the plug. Poissons' ratio of cement and plug (ν_p, ν_R) = 0.22 and 0.20, plug length-to-radius ratio (L/a) = 2.0.

Tuff Cylinder Radius Ratio (R/a)	Young's Modulus Ratio of Plug and Rock (E_p/E_R)	Relative Axial Plug Displacement (x 10^6) ($w_p\alpha$)		Absolute Axial Plug Displacement (mm x 10^4) (w_p)	
		z/L = 0	z/L = 1	z/L = 0	z/L = 1
1.84 (a = 50.8 mm)	10	1139	554	858	417
"	1	985	197	437	87
"	0.233	922	18	202	4
"	0.1	901	2	131	0.2
3.0 (a = 25.4 mm)	10	1138	554	429	209
"	1	1022	360	305	107
"	0.233	918	58	135	9
"	0.1	895	10	87	1
6.0 (a = 12.7 mm)	10	1137	554	214	104
"	1	1061	468	185	81
"	0.233	916	106	82	10
"	0.1	894	25	53	1.5

The axial stresses within the plug become less linear with decreases of the above parameters (Table 5.1). The relative and absolute axial plug displacements at the loaded end of the borehole plug increase with increasing modulus ratio and with decreasing cylinder radius ratio (Table 5.2). Hence, a push-out specimen (E_p/E_R = 0.233, ν_p = 0.22, ν_R = 0.20) with an inside radius of 50.8 mm and outside radius of 93.7 mm (R/a = 1.84) shows the highest interfacial shear stress and axial displacement at the loaded end (Tables 5.1 and 5.2).

Table 5.3a summarizes the results for the axial stress within the plug and interface shear stress as a function of Poisson's ratio of the plug and distance along the loaded end of the plug. Table 5.3b summarizes the results for the relative and absolute axial plug displacements for an axially loaded borehole plug. The interface shear stress and axial plug displacements at the loaded of the plug increase with decreasing Poisson's ratio of the plug. The axial stress within the plug becomes less linear with decreasing Poisson's ratio of the plug.

5.2.2.3 Limiting Length and Post-Failure Behavior for an Axially Loaded Borehole Plug

Figure 3.11 (Chapter 3) gives the axial stress distribution along the plug and the interfacial shear stress distribution for a modulus ratio of 0.233 and as a function of the distance from the loaded end of the plug. The plot compares the finite element analysis and the closed-form solution. The plot is for a plug radius of 12.7 mm (0.5 in) and for several plug length-to-radius ratios.

The stresses do not distribute over the entire length of the longer plugs. The length beyond which no axial stress is present and hence no shear stress is transferred along the interface may be referred to as the limiting length. When the ratio of the axial stress within the plug to the applied axial plug stress (σ_z^p/σ_{po}) is 0.1%, the axial stress may be considered to be negligible. The limiting length can be calculated by setting σ_z^p/σ_{po} = 0.001 in Eq. (2.52) and solving for the distance from the initial location of the loaded end of the borehole plug. Figure 5.1 gives the limiting length as a function of σ_z^p/σ_{po} within the plug and plug length-to-radius ratio. The limiting length for a 12.7 mm radius plug with a length-to-radius ratio of 2 is 25.32 mm when considering σ_z^p/σ_{po} = 0.1% (99.7% of the plug carries stress), that with a length-to-radius ratio of 8 is 81 mm (80% of the plug has a stress exceeding 0.1% of the applied stress).

The advantage of a longer plug is realized at slip (at post-failure). When slip occurs, the interface no longer behaves elastically and the maximum shear stress moves down the interface in front of the failed (slip) zone (i.e. Hollingshead, 1971; Stormont and Daemen, 1983). The portion of the plug which fails still transfers some load to the rock through residual shear strength and the maximum shear stress drops below the shear strength at some point along the interface. The intact portion of the plug/rock interface below this particular point transfers the remainder of the load by an elastic, exponential shear stress

Table 5.3a Axial Stress (σ_z^p) and Interface Shear Stress ($\tau_{rz,i}$) Distributions along an Axially Loaded Borehole Plug. The stresses are a function of Poisson's ratio of plug (ν_p), and distance along the loaded end of plug (z/L). σ_{po} = axial stress applied to the plug. Young's modulus ratio of plug and rock (E_p/E_R) = 0.233. Poissons' ratio of rock (ν_R) = 0.20, plug length-to-radius ratio (L/a) = 2.0.

Tuff Cylinder Radius Ratio (R/a)	Poisson's Ratio of Plug (ν_p)	σ_z^p/σ_{po}			$\tau_{rz,i}/\sigma_{po}$	
		z/L = 0.25	z/L = 0.50	z/L = 0.75	z/L = 0	z/L = 1
6.0 (a = 12.7 mm)	0.1	0.47	0.22	0.08	0.74	0.08
"	0.2	0.48	0.23	0.09	0.72	0.08
"	0.3	0.50	0.24	0.10	0.68	0.09
"	0.4	0.54	0.28	0.12	0.61	0.11

Table 5.3b Relative and Absolute Axial Plug Displacement Distributions along an Axially Loaded Borehole Plug. The displacements are a function of Poisson's ratio of plug (ν_p), and distance along the loaded end of plug (z/L). Young's modulus ratio of plug and rock (E_p/E_R) = 0.233. Poissons' ratio of rock (ν_R) = 0.20, plug length-to-radius ratio (L/a) = 2.0.

Tuff Cylinder Radius Ratio (R/a)	Poisson's Ratio of Plug (ν_p)	Relative Axial Plug Displacement (x 10^4) ($w_p\alpha$)		Absolute Axial Plug Displacement (mm x 10^4) (w_p)	
		z/L = 0	z/L = 1	z/L = 0	z/L = 1
6.0 (a = 12.7 mm)	0.1	9.9	1.0	85	8.8
"	0.2	9.3	1.1	83	9.3
"	0.3	8.3	1.1	78	10.4
"	0.4	6.5	1.2	69	13.0

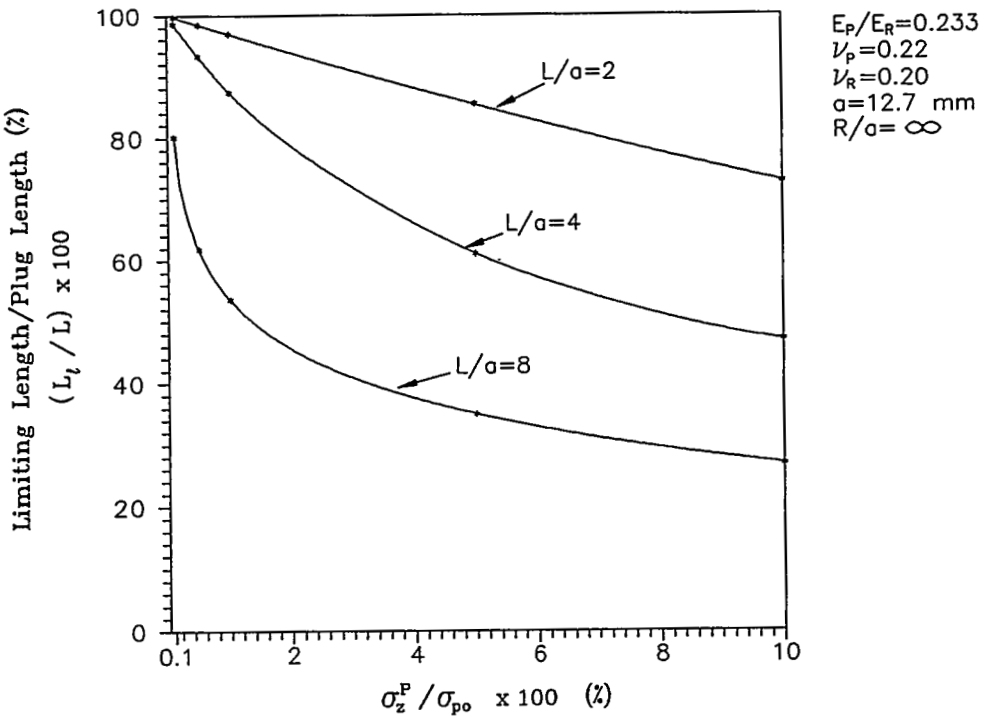

Figure 5.1 The limiting length of a borehole plug vs. the ratio of the axial stress within the plug to the applied axial plug stress (σ_z^p/σ_{po}). The plot is a function of plug length-to-radius ratio (L/a).

distribution with a reduced peak shear stress. Therefore, a longer plug has a longer limiting length and higher strength than a shorter plug upon failure. An elastic analysis leads to a high interfacial peak shear stress at the loaded end of the plug and hence is more conservative that a progressive failure analysis which leads to reduced peak shear stress.

5.2.2.4 Relation Between Normal Stress Across the Plug/Rock Interface and Axial Stress Applied to the Plug

5.2.2.4.1 Introduction. The main objective of this section is to express the ratio of the normal (radial) stress generated along the plug/rock interface to that of an axial stress applied to the plug (σ_r^p/σ_{po}). Results are given as a function of the ratio of the Young's modulus of the plug to that of the rock and the Poisson's ratio of the plug and rock and cylinder outside to inside radius ratio. All results are adjusted to a common cylinder radius ratio with the assumption of plane strain.

Equation (2.53) (Ch. 2) gives the ratio of the normal stress generated along the plug/rock interface to that of the axial stress applied to the plug (σ_r^p/σ_{po}). Equation (2.82) gives the radial plug displacement due to an axial stress applied to the plug ($u_{p,z}$) for plane strain.

5.2.2.4.2 Radial Stress and Displacement Distributions Induced by an Axial Plug Stress. Table 5.4 summarizes the effect of the axial stress applied to the plug and on the normal stress along the plug/rock contact and the outward radial plug displacement. Results are presented for different modulus ratios, different cylinder radius ratios and as a function of position along an axially loaded borehole plug (with the assumption of plane strain). The ratio of the normal stress along the plug/rock contact to the axial stress applied to the plug (σ_r^p/σ_{po}) decreases with increasing modulus ratio and with decreasing cylinder outside-to-inside radius ratio. The outward radial plug displacement ($u_{p,z}$) due to an axial stress applied to the plug decreases with increasing modulus ratio and with increasing cylinder outside-to-inside radius ratio (Table 5.4). σ_r^p/σ_{po} increases with increasing Poisson's ratio of the plug (Table 5.5). Therefore, the outward radial displacement also increases with increasing plug Poisson's ratio.

5.2.2.4.3 Normalized Radial Stress due to an Applied Axial Stress. Table 5.4 gives the interface contact stress due to an axial stress applied to a plug with a modulus ratio of 0.233. Inspecting Table 5.4 shows that a tuff cylinder with a radius ratio of 1.84 (corresponding to a 50.8 mm radius plug in a 93.7 mm radius rock cylinder) shows a 13.9% lower contact stress than a cylinder with a radius ratio of 6.0 (corresponding to a 12.7 mm radius plug in a 76.2 mm radius cylinder). Hence, cylinders with different radius ratios have different contact stress ratios along their plug/rock contacts, which should be normalized to a common cylinder ratio for assessment of size effects.

Table 5.4 Effect of Axial Stress Applied to Plug (σ_{po}) on Normal Stress along the Plug/Rock Contact (σ_r^p) and on the Outward Radial Plug Displacement ($u_{P,z}$). Results are presented as a function of plug-to-rock Young's modulus ratio (E_p/E_R), cylinder radius ratio (R/a), and distance along an axially loaded borehole plug (z/L). $\nu_R = 0.20$, $\nu_P = 0.22$, $\sigma_{po}/E_R = 0.001$, plug radius (a) = 12.7 mm, plug length-to-radius ratio (L/a) = 2.0.

Tuff Cylinder Radius Ratio (R/a)	E_p/E_R	σ_r^p/σ_{po}			$u_{P,z}/a$ (x 10^6)		
		z = 0	z = L/4	z = L/2	z = 0	z = L/4	z = L/2
1.84	10	0.01	0.007	0.004	0.15	0.11	7.49×10^{-2}
"	1	0.0791	0.0436	0.0228	105	58	30
"	0.233	0.176717	0.05523	0.0171	203	73	26
"	0.1	0.225	0.039	0.007	352	5.6×10^{-6}	8.9×10^{-14}
3.0	10	0.015	0.009	0.006	0.15	0.11	7.49×10^{-2}
"	1	0.099	0.0618	0.0356	94	58.5	34
"	0.233	0.19735	0.0829	0.0341	166	77	34
"	0.1	0.238	0.065	0.018	254	3.8×10^{-4}	5.8×10^{-10}
6.0	10	0.02	0.01	0.007	0.15	0.11	7.49×10^{-2}
"	1	0.108	0.0705	0.0423	89	59	36
"	0.233	0.205	0.1	0.0468	151	82	42
"	0.1	0.243	0.083	0.028	221	6.1×10^{-3}	1.7×10^{-7}

Table 5.4 Effect of Axial Stress Applied to Plug (σ_{po}) on Normal Stress along the Plug/Rock Contact (σ_r^p) and on the Outward Radial Plug Displacement ($u_{P,z}$).--Continued Results are presented as a function of plug-to-rock Young's modulus ratio (E_p/E_R), cylinder radius ratio (R/a), and distance along an axially loaded borehole plug (z/L). $\nu_R = 0.20$, $\nu_P = 0.22$, $\sigma_{po}/E_R = 0.001$, plug radius (a) = 12.7 mm, plug length-to-radius ratio (L/a) = 2.0.

Tuff Cylinder Radius Ratio		σ_r^p/σ_{po}			$u_{P,z}/a$ (x 10^6)		
(R/a)	E_p/E_R	z = 0	z = L/4	z = L/2	z = 0	z = L/4	z = L/2
10.0	10	0.017	0.0113	0.007	0.15	0.11	7.5×10^{-2}
"	1	0.110	0.0717	0.043	88	60	37
"	0.233	0.207	0.1006	0.472	148	85	46
"	0.1	0.2439	0.0838	0.028	215	2.1×10^{-2}	2×10^{-6}
∞	10	0.0172	0.0114	0.007	0.15	0.11	7.5×10^{-2}
"	1	0.1110	0.0724	0.0435	87.8	66	44
"	0.233	0.208	0.101	0.0474	147	110	73
"	0.1	0.244	0.084	0.029	212	133	78

Table 5.5 Effect of the Axial Stress Applied to the Plug (σ_{po}) on the Normal Stress along the Plug/Rock Contact (σ_r^p) as a Function of Poisson's ratio of the Plug and Distance along the Axially Loaded Borehole Plug (z/L). Modulus ratio (E_p/E_R) = 0.233, Poisson's ratio of rock (ν_R) = 0.20, plug radius (a) = 12.7 mm, plug length-to-radius ratio (L/a) = 2, tuff cylinder radius ratio (R/a) = 6.0.

Poisson's Ratio of Plug (ν_p)	σ_r^p/σ_{po}		
	z/L = 0	z/L = 0.25	z/L = 0.50
0.1	0.084	0.04	0.018
0.2	0.183	0.09	0.041
0.3	0.303	0.152	0.074
0.4	0.449	0.242	0.125

A tuff cylinder with a modulus ratio of 0.233 and tuff cylinder ratio of 1.84 gives a contact stress of 0.1767 at the loaded end of the plug/rock interface (i.e. z = 0, Table 5.4). A tuff cylinder with a modulus ratio of 0.233 and cylinder ratio of 6.0 gives a contact stress of 0.205 at the loaded end of the interface (i.e. z = 0, Table 5.4). Therefore, as the contact radial stress is related to the axial stress (Eq. (2.52)), a plug emplaced in a cylinder with a radius ratio of 6.0 will give an applied axial stress (σ_{po}) 1.16161 (0.205/0.1767) times that of a plug in a cylinder with a radius ratio of 1.84. The axial stress applied to the plug should be multiplied by a normalization factor (I_Z) of 1.16161 to normalize (adjust) the result to a cylinder ratio of 6.0.

The interface contact stress due to an axial stress applied on the plug can be adjusted to a common cylinder outside-to-inside radius ratio (R/a) as follows:

$$\sigma_{po\ \ normalized} = I_z \sigma_{po} \tag{5.1}$$

where I_Z = normalization factor to normalize the contact stress to a common cylinder radius ratio under the influence of an applied axial stress
= [(σ_r^p/σ_{po}) for the sample with the radius ratio for which the contact stress is to be calculated] divided by [(σ_r^p/σ_{po}) acting on the sample to be normalized]

σ_{po} = axial (compressive) stress applied to the plug of the sample to be normalized

$\sigma_{po\ normalized}$ = normalized (adjusted) axial stress.

The axial stress applied to the plugs of the push-out cylinders can be adjusted to a radius ratio of 6.0 (corresponding to a 25.4 mm push-out cylinder) by using a normalization factor of 1.16161 for the samples with an R/a of 1.84 (corresponding to a 101.6 mm push-out cylinder) and 1.0402 for samples with an R/a of 3.0 (corresponding to a 50.8 mm push-out cylinder). Adjustment to an infinite radius ratio leads to normalization factors of 1.012, 1.053 and 1.176 for the 25.4, 50.8 and 101.6 mm cylinders (Table 5.4).

5.2.3 Influence of Lateral External Stress on Radial Contact Stress

5.2.3.1 Introduction

Analyzed in this section is the effect of a lateral external stress (σ_o) applied to the cylinder periphery on the normal stress (σ_i) and radial displacement ($u_{P,C}$) along the plug/rock contact. The objective is to present a formulation that expresses the ratio of the normal stress generated along the plug/rock interface to that of the applied external stress. Results are given as a function of material properties (E_p/E_R, ν_P, ν_R), and for the cylinder radius ratios of 6, 3 and 1.84 used in the push-out tests. All results are adjusted to a common cylinder radius ratio.

Equations (2.86a and b) (Ch. 2) give the ratio of the normal stress along the plug/rock contact to that of the applied lateral external stress (σ_i/σ_o) for a plane strain and plane stress solution, respectively. Equation (2.87a) gives the radial plug displacement ($u_{P,c}$) due to an applied lateral external stress for a plane strain configuration.

5.2.3.2 Influence of Applied Lateral External Stress on Radial (Contact) Stress and Displacement Distribution

The ratio of the normal stress along the plug/rock contact to the applied external stress (σ_i/σ_o) increases with increasing plug-to-rock Young's modulus ratio (E_p/E_R) and with increasing Poisson's ratio of the plug (Figure 5.2). The stress ratio decreases with increasing cylinder radius ratio (R/a) for cylinders of E_p/E_R less than 1.0. The opposite is observed on cylinders with modulus ratios greater than 1.0 (Table 5.6).

The radial plug displacement due to the applied external stress decreases with increasing modulus ratio. The displacement decreases with increasing cylinder radius ratio for cylinders with modulus ratios less than 1.0. The opposite is observed for cylinders with E_p/E_R greater than 1.0. Table 5.6 summarizes the results for the interface normal stress and displacement due to an applied external stress.

5.2.3.3 Normalized Radial Interface Stress due to an Applied Lateral External Stress

The interface contact stress due to an applied lateral external stress can be adjusted to a common cylinder outside-to inside radius ratio (R/a, as described in Section 5.2.2.4.3) as follows:

$$\sigma_{o\ normalized} = I_c \sigma_o \qquad (5.2)$$

where I_C = normalization factor to normalize the contact stress to a common cylinder radius ratio under the influence of an applied external lateral stress
= [(σ_i/σ_o) for the sample with the radius ratio for which the contact stress is to be calculated] divided by [(σ_i/σ_o) acting on the sample to be normalized]

σ_o = external lateral stress applied to the sample to be normalized

$\sigma_{o\ normalized}$ = normalized (adjusted) external stress.

The external stress applied to the push-out cylinders can be adjusted to a radius ratio of 6.0 (corresponding to a 25.4 mm push-out cylinder) by using a normalization factor of 0.855 for the samples with an R/a of 1.84 (corresponding to a 50.8 mm push-out cylinder) and 0.955 for samples with an R/a of 3.0 (corresponding to a 25.4 mm push-out cylinder). Adjustment to an infinite radius ratio leads to normalization factors of 0.985, 0.940 and 0.842 for the 12.7, 25.4 and 50.8 mm cylinders (Table 5.6).

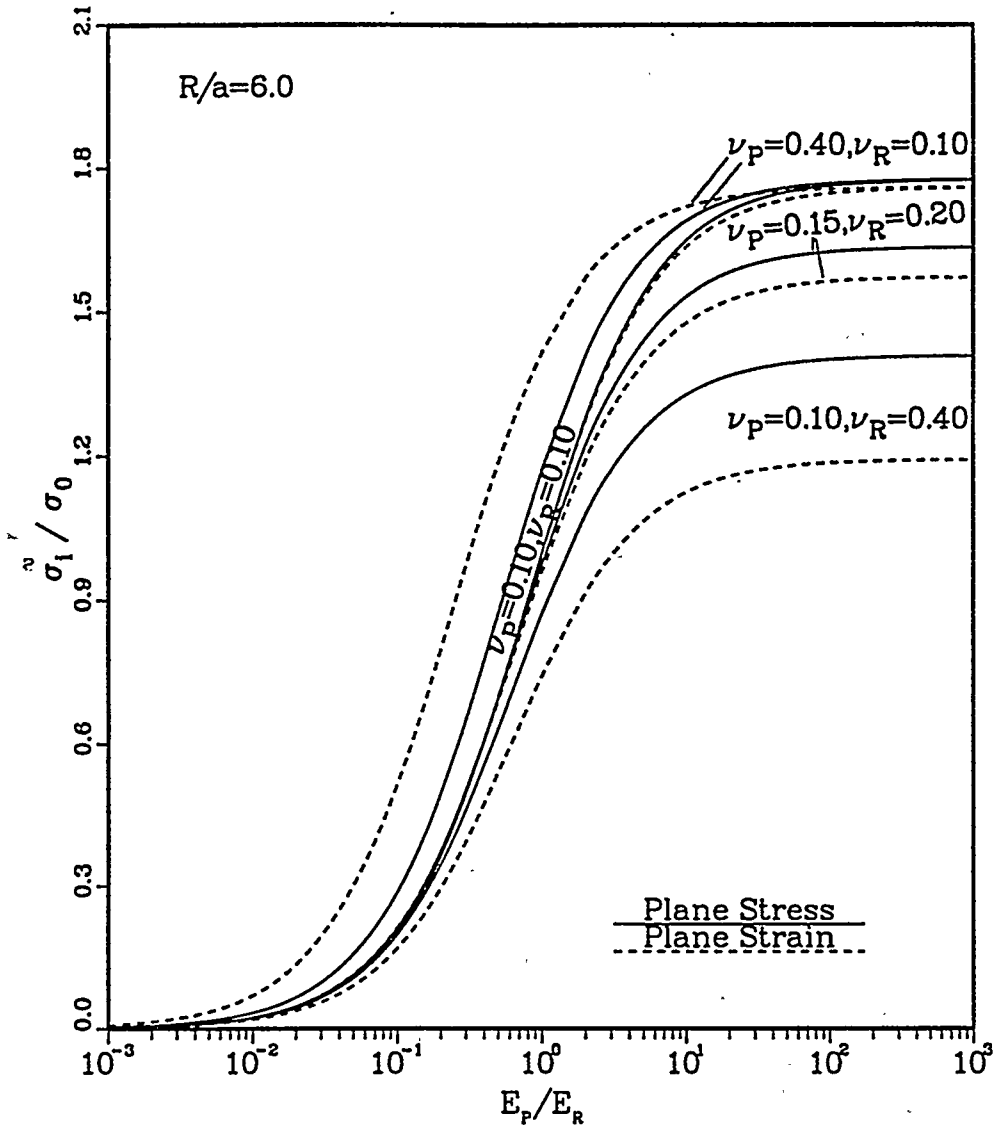

Figure 5.2 Ratio of normal stress along the plug/rock interface to applied lateral stress (σ_i/σ_o).

E_p/E_R = Young's modulus ratio of plug and rock
ν_p, ν_R = Poisson's ratios of plug and rock
a = plug radius = 12.7 mm
R/a = outside-to-inside cylinder radius ratio
L/a = plug length-to-radius ratio = 2.

Table 5.6 Effect of the External Stress (σ_o) on Normal Stress along the Plug/Rock Contact (σ_i) and on the Inward Radial Plug Displacement ($u_{P,C}$). Results are presented (for the case of plane strain) as a function of different cylinder radius raitos (R/a) and plug-to-rock Young's modulus ratios (E_p/E_R). Poisson's ratio of rock (ν_R) = 0.20, ν_P = 0.22, σ_o/E_R = 0.001, plug radius (a) = 12.7 mm, plug length-to-radius ratio (L/a) = 2.

Tuff Cylinder Radius Ratio (R/a)	E_p/E_R	σ_i/σ_o	$u_{P,C}/a$ (x 10^6)
1.84	10	1.320	1.09
"	1	1.020	781
"	0.233	0.550	1529
"	0.1	0.310	2713
3.0	10	1.432	1.21
"	1	1.02	775
"	0.233	0.493	1384
"	0.1	0.261	2156
6.0	10	1.493	1.27
"	1	1.02	772
"	0.233	0.47	1326
"	0.1	0.244	1972
10.0	10	1.506	1.28
"	1	1.02	771
"	0.233	0.466	1315
"	0.1	0.241	1937
∞	10	1.514	1.28
"	1	1.02	771
"	0.233	0.464	1308
"	0.1	0.239	1917

5.3 Thermal Stresses and Displacements

5.3.1 Theoretical Thermal Stress and Displacement Distribution

Equations (2.96a), (2.97b) and (2.98b) (Ch. 2) give the thermally induced axial thermal stress in a plug, thermal axial plug displacement, and thermal shear stress at the plug/rock interface. The radial thermal stresses and displacements at the plug/rock contact are given as Eqs. (2.103) and (2.104).

5.3.2 Results

Figure 5.3 gives the thermal axial stress distribution along the plug and the thermal interfacial shear stress distribution for a uniform temperature increase of 1°C, along the upper symmetrical half of the interface. The plot is given for push-out cylinders with several cylinder outside-to-inside radius ratios (R/a), for a modulus ratio of 0.233, and for a plug length-to-radius ratio of 2. The coefficient of linear thermal expansion of rock (α_R) is assigned the value for the average of the four stratigraphic units at the Yucca Mountain tuff site (α_R = 6.9 x 10^{-6} 1/°C; according to Lappin, 1980, as quoted by Binnall et al., 1987, p. 28). That for the cement plug (α_P) is assigned the value for medium strength concrete (α_P = 11 x 10^{-6} 1/°C; Gere and Timoshenko, 1984, p. 747). Cylinder outside-to-inside ratios of 1.84, 3 and 6 represent push-out cylinders with plug radii of 50.8, 25.4 and 12.7 mm, respectively. The thermal axial stresses and the thermal interface shear stresses slightly increase with increased cylinder ratio (possibly due to increased stiffness of the tuff cylinder). The peak axial stresses and interfacial shear stresses due to a temperature increase of 1°C have magnitudes of about 0.06 and 0.05 MPa, respectively. The thermally induced axial plug displacements (Figure 5.4) increase with decreased cylinder ratio. The peak thermal axial plug displacements for cylinder ratios of 1.84, 3 and 6 are 30 x 10^{-5}, 14 x 10^{-5}, and 7 x 10^{-5} mm, respectively.

The thermal radial stresses due to the differences in the thermal radial expansions of plug and rock increase with increasing cylinder ratios. The thermally induced radial plug displacements decrease with increasing cylinder ratios (Table 5.7).

5.4 Resultant Axial Stresses and Plug Displacements due to a Combination of Axial Loading and Uniform Temperature Increase

5.4.1 Introduction

The resultant axial stresses and plug displacements in a borehole plug-rock system are the sum of 1) the stresses and displacements due to an axial stress applied to the plug, and 2) stresses and displacements due to a uniform temperature increase. The resultant interfacial shear stress and axial plug displacement are given by Eqs. (2.105) and (2.106) (Ch. 2), respectively. The resultant axial stress within the plug is the sum of Eqs. (2.52) and (2.96a). A detailed numerical evaluation of these equations is presented in the following sections.

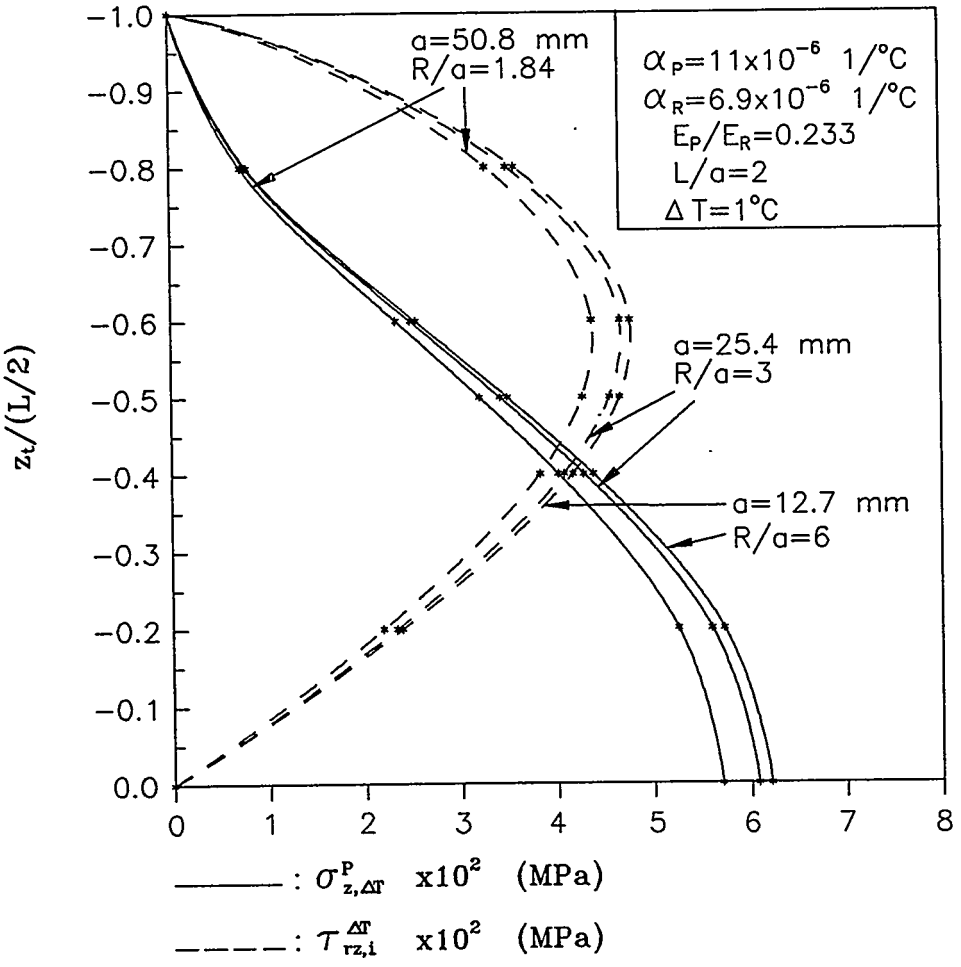

Figure 5.3 Thermal axial stress ($\sigma^P_{z,\Delta T}$) and thermal interfacial shear stress ($\tau^{\Delta T}_{rz,i}$) for a uniform temperature increase of 1°C. Plot is for the upper half of the plug/rock interface.

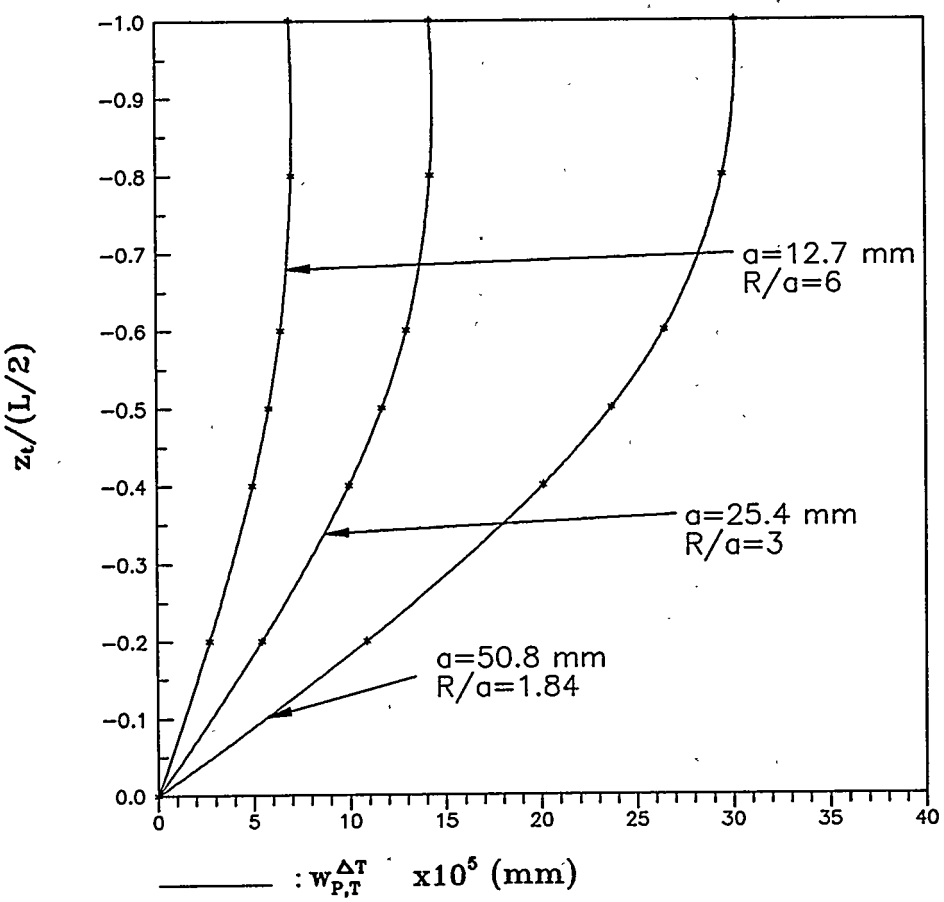

Figure 5.4 Thermally induced axial plug displacement ($w_{P,T}^{\Delta T}$) for a uniform temperature increase of 1°C. Plot is for the upper half of a symmetrical plug.

Table 5.7 The Thermal Radial Stresses and Thermally Induced Radial Plug Displacements per Unit Temperature Increase. Results are presented as a function of different cylinder radius ratios (R/a). Plug to rock Young's modulus ratio (E_p/E_R) = 0.233, Poisson's ratio of plug and rock (ν_p = 0.22, ν_R = 0.20), and plug length to radius ratio (L/a) = 2.

Tuff Cylinder Radius Ratio (R/a)	$\sigma^p_{r,\Delta T}$ (MPa) x 10^2	$u^{\Delta T}_p$ (mm) x 10^4
6 (a = 12.7 mm)	2.77	1.25
3 (a = 25.4 mm)	2.65	2.53
1.84 (a = 50.8 mm)	2.35	5.26

5.4.2 Results

Figures 5.5 through 5.7 give the resultant interfacial shear stress, resultant axial plug displacement, and resultant axial stress. The push-out tests reported in Section 4.1.2 are heated uniformly up to 90°C. With an average ambient temperature of 24°C, this leads to a uniform temperature increase of up to 66°C. This is the reason why the plots presented in Figures 5.5 through 5.7 give the resultant stresses and displacements for a temperature increase of 1°C and 66°C, respectively. The 12.7, 25.4 and 50.8 mm radius push-out specimens fail at a mean axial stress of 33.92, 21.79 and 13.47 MPa, respectively (Section 4.1.2). These stresses are used for Figures 5.5 through 5.7. The plots are given as a function of push-out cylinder outside-to-inside radius ratio, uniform temperature increase and distance from the loaded end of the plug (z/L). The specimens have plug-to-rock modulus ratios of 0.233, plug and rock Poisson's ratios of 0.22 and 0.20, and plug length-to-radius ratio of 2.

Figure 5.5 gives the resultant shear stresses at the plug/rock interface. The resultant interfacial shear stress increases with increasing cylinder outside-to-inside radius ratio. The thermal shear stresses reduce the resultant shear stress along the upper half of the interface, and increase the resultant shear stress along the lower half of the plug. The maximum resultant interfacial shear stress occurs at the loaded end of the plug (Figure 5.5).

Figure 5.6 presents the resultant axial plug displacement. There is no monotonic trend between the resultant displacement and cylinder radius ratio at a uniform temperature increase of 1°C; however, as presented in Section 4.1.2, the axial plug displacement per unit axial stress at failure increases with increasing plug radius. The reason for no monotonic trend between resultant axial plug displacement and cylinder radius ratio is the different axial stresses at failure for various cylinder ratios. At high temperature increases (ΔT = 66°C) the resultant axial plug displacements increase with increased cylinder ratio. A temperature increase of 66°C leads to reduced resultant axial plug displacement within the upper half of the plug. The maximum resultant axial plug displacement occurs at the loaded end of the plug (Figure 5.6).

Figure 5.7 shows the distribution of the resultant axial stress within the plug. The resultant axial stress is due to the axial stress applied to the plug and due to the axial thermal stress within the plug. The resultant axial stress increases with increasing cylinder radius ratio. The curves tend to become more linear with increased temperature (Figure 5.7).

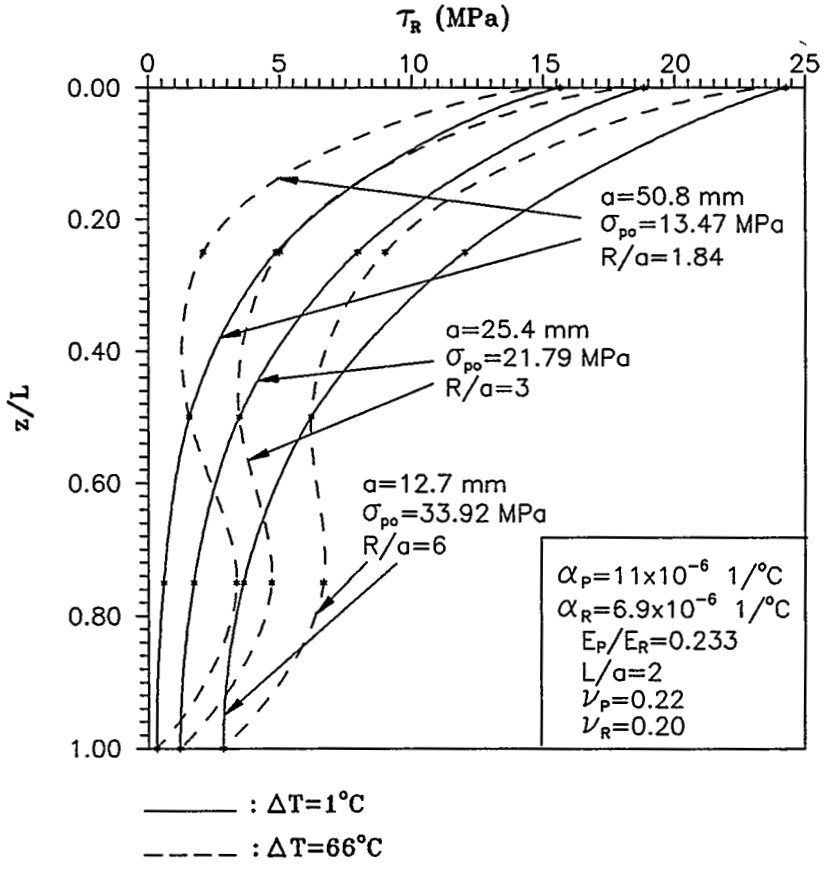

Figure 5.5 Resultant interfacial shear stress at the plug/rock contact (τ_R) as a function of uniform temperature increase, cylinder outside-to-inside radius ratio, and position along the loaded end of the plug. The resultant interfacial shear stress is due to an axial stress applied to the plug and thermal interfacial shear stress.

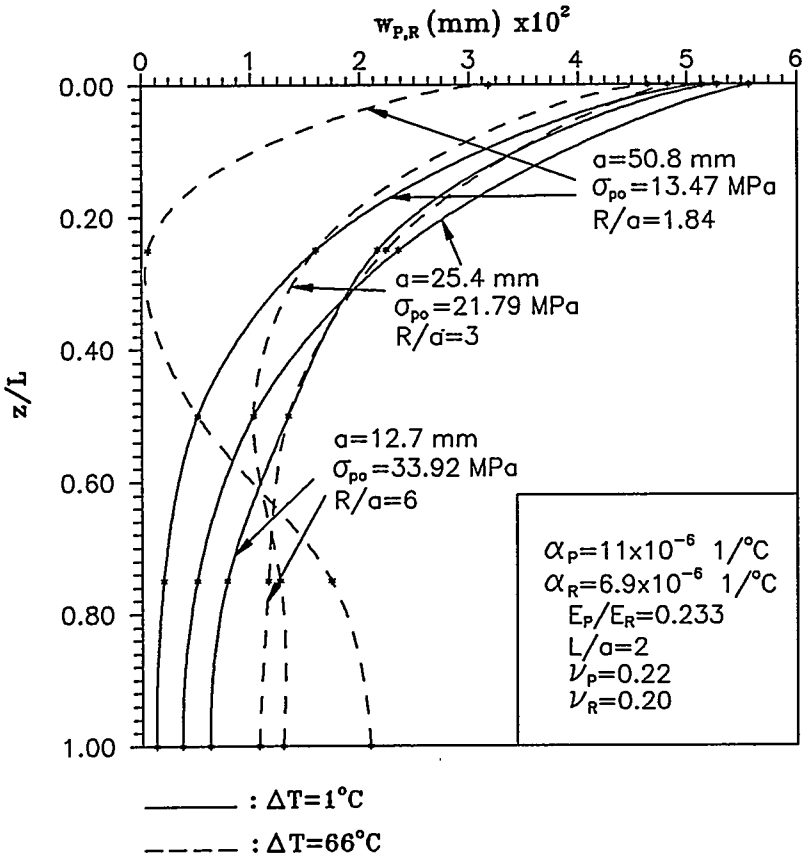

Figure 5.6 Resultant axial plug displacement ($w_{P,R}$) along a borehole plug due to an axial stress applied to the plug and thermally induced axial plug displacements.

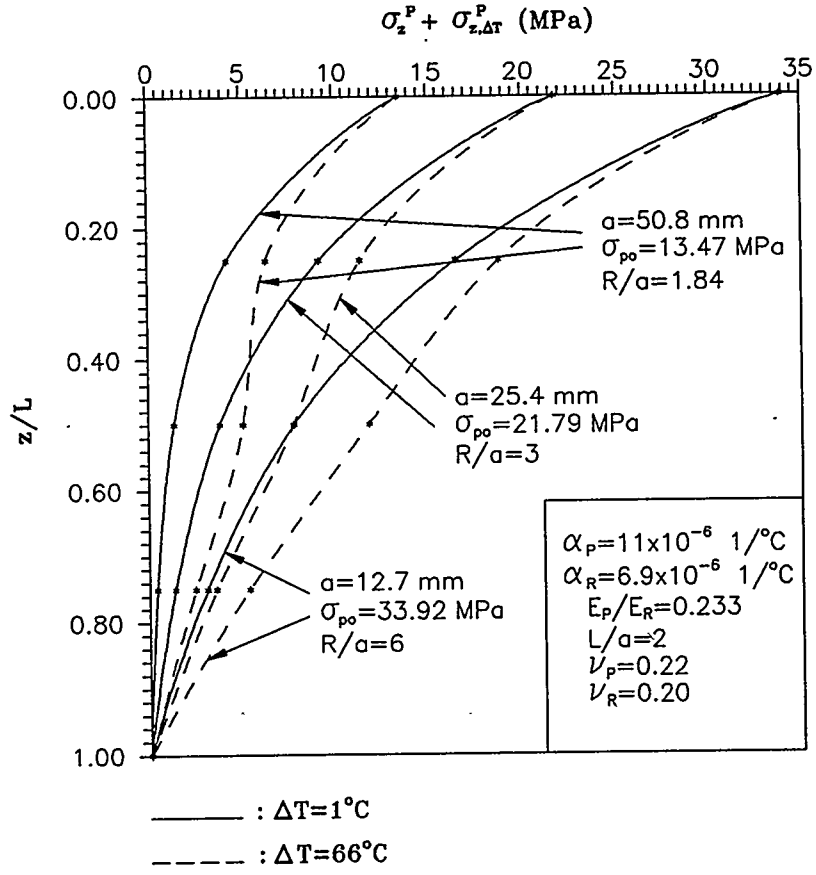

Figure 5.7 Resultant axial stress ($\sigma_z^P + \sigma_{z,\Delta T}^P$) along a borehole plug due to a combination of an axial stress applied to the plug with axially induced thermal stress.

5.5 Push-Out Tests

5.5.1 Introduction

The push-out test arrangement is given in Figures 4.1 and 4.2 (Ch. 4). Appendix D gives a detailed description of the test set-up, as well as of sample preparation, storage and curing conditions. Appendix C gives the composition and procedure for preparing Self-Stress II cement borehole plugs.

Section 4.1.2 reports the results of push-out tests performed on 130 Apache Leap tuff cylinders plugged with Self-Stress II cement. The cylinders have inside diameters of 12.7, 25.4, 50.8 and 101.6 mm (0.5, 1, 2 and 4 in), outside diameters of 76.2, 152.4 and 187.3 mm (3, 6 and 7.375 in), and lengths ranging from 71.5 to 228.9 mm (2.82 to 9.01 in). The cylinders are plugged with nearly centered Self-Stress II cement plugs having length-to-diameter ratios ranging from 1.0 to 4.0, but approximately 1.0 in most cases.

5.5.2 Normalized Stresses

5.5.2.1 Introduction

Table 4.1 gives the axial stress at failure ± one standard deviation for the 12.7, 25.4, and 50.8 mm plug radius highly saturated samples cured and tested at ambient conditions (24 ± 2°C) to be 35.2 ± 4.4, 22.7 ± 5.5, and 14.9 ± 1.7 MPa, respectively. These results are adjusted (normalized) to a common cylinder radius ratio (R/a) of infinity by the procedure given in Section 5.2.2.4.3. The axial stress applied to the plugs of the push-out cylinders can be adjusted to an infinite cylinder radius ratio by multiplying the above-mentioned axial stresses with a correction factor (I_z) of 1.1755 for the samples with R/a of 1.84 (corresponding to a 50.8 mm plug radius push-out sample), 1.0527 for 25.4 mm samples, and 1.012 for 12.7 and 6.35 mm samples. Equation (5.1), Section 5.2.2.4.3 gives the equation for normalization. Hence, the highly saturated, ambient samples with plug radii of 12.7, 25.4 and 50.8 mm give normalized axial stresses at failure ± one standard deviation of 35.6 ± 4.5, 23.9 ± 5.8, and 17.5 ± 1.9 MPa, respectively. Tables 5.8 through 5.10 give the mean normalized axial stress, mean normalized average shear stress, and mean normalized maximum exponential shear stress at failure. The trend of the results with respect to degree of saturation, curing and test temperature, plug radius and plug length is identical to those reported in Section 4.1.2.

5.5.2.2 Extrapolation of Normalized Axial Stresses at Failure

Figure 5.8 gives a best fit of the upper, mean and lower bounds of the normalized axial stresses at failure vs. plug radii for borehole plugs having length-to-radius ratios of 2.0, cured and tested at highly saturated, ambient conditions. The curves are extrapolated to plug radii of 6.35 and 120 mm. The highly saturated, ambient samples with plug radius of 6.35 mm give normalized axial stress at failure ± one standard deviation of 51.1 ± 6.3 MPa (Table 5.8). Plotting the upper, mean and lower

Table 5.8 Normalized Mean Axial Stress at Failure for Cement Plugs in Apache Leap Tuff Cylinders. In parentheses are given the number of samples tested. Data is for the 130 push-out tests performed. L/D = cement plug length-to-diameter ratio.

Apache Leap Tuff Cylinder		Normalized Mean Axial Stress at Failure ± One Standard Deviation (MPa)					
	Curing and	Tuff Cylinder Inside Diameter (mm)					
Saturation Condition	Test Temp. (°C)	12.7 L/D = 1	25.4 L/D = 1	25.4 L/D = 2	25.4 L/D = 4	50.8 L/D = 1	101.6 L/D = 1
Presaturated	24 ± 2	-	26.7 ± 4.0 (4)	-	-	20.3 ± 4.0 (3)	-
Highly Saturated	24 ± 2	51.1 ± 6.3 (14)	35.6 ± 4.5 (6)	66.5 ± 9.1 (5)	171.8 ± 2.6 (3)	23.9 ± 5.8 (3)	17.5 ± 1.9 (3)
	45	-	41.8 ± 4.0 (5)	-	-	22.9 ± 6.3 (3)	20.0 ± 1.5 (3)
	70	-	29.9 ± 5.2 (4)	-	-	22.8 ± 4.5 (3)	15.4 ± 4.3 (3)
	90	-	18.0 ± 3.7 (3)	-	-	10.7 ± 3.6 (4)	7.6 ± 2.4 (3)
Partially Saturated	24 ± 2	-	35.1 ± 6.5 (7)	-	-	27.8 ± 8.6 (5)	14.0 ± 5.2 (3)
	44	-	45.8 ± 9.5 (5)	-	-	21.1 ± 4.2 (4)	17.4 ± 6.0 (3)
	70	-	41.3 ± 11.0 (3)	-	-	25.6 ± 6.2 (3)	15.1 ± 2.0 (3)

Table 5.8 Normalized Mean Axial Stress at Failure for Cement Plugs in Apache Leap Tuff Cylinders.--Continued In parentheses are given the number of samples tested. Data is for the 130 push-out tests performed. L/D = cement plug length-to-diameter ratio.

Apache Leap Tuff Cylinder		Normalized Mean Axial Stress at Failure ± One Standard Deviation (MPa)					
	Curing and	Tuff Cylinder Inside Diameter (mm)					
Saturation Condition	Test Temp. (°C)	12.7 L/D = 1	25.4 L/D = 1	25.4 L/D = 2	25.4 L/D = 4	50.8 L/D = 1	101.6 L/D = 1
Relatively Dry	24 ± 2*	-	35.8 ± 0.3 (3)	-	-	27.7 ± 4.6 (3)	17.5 ± 1.2 (3)
	36	-	25.7 ± 6.5 (7)	-	-	23.9 ± 1.5 (3)	15.9 ± 2.6 (3)

*Cylinders cured at room conditions (i.e. not in environmental chamber) at 24 ± 2°C, 36 ± 2% relative humidity with a thin film of water remaining on the top boreholes.

Table 5.9 Normalized Mean Bond Strengths of Cement Plugs in Apache Leap Tuff Cylinders. In parentheses are given the number of samples tests (130 push-out tests have been performed). L/D = cement plug length-to-diameter ratio.

Apache Leap Tuff Cylinder		Normalized Mean Average Shear Stress at Failure ± One Standard Deviation (MPa)					
	Curing and	Tuff Cylinder Inside Diameter (mm)					
Saturation Condition	Test Temp. (°C)	12.7 L/D = 1	25.4 L/D = 1	25.4 L/D = 2	25.4 L/D = 4	50.8 L/D = 1	101.6 L/D = 1
Presaturated	24 ± 2	-	6.1 ± 0.7 (4)	-	-	5.0 ± 1.6 (3)	-
Highly Saturated	24 ± 2	11.03 ± 1.3 (14)	7.4 ± 1.0 (6)	8.2 ± 1.0 (5)	10.6 ± 0.4 (3)	6.6 ± 2.0 (3)	4.6 ± 0.9 (3)
	45	-	8.7 ± 0.9 (5)	-	-	6.8 ± 2.2 (3)	5.1 ± 0.7 (3)
	70	-	6.6 ± 1.3 (4)	-	-	5.9 ± 1.0 (3)	3.9 ± 1.0 (3)
	90	-	3.8 ± 0.7 (3)	-	-	2.8 ± 1.1 (4)	1.9 ± 0.5 (3)
Partially Saturated	24 ± 2	-	7.7 ± 1.0 (7)	-	-	7.0 ± 2.2 (5)	4.4 ± 1.8 (3)
	44	-	9.4 ± 2.5 (5)	-	-	5.5 ± 0.8 (4)	4.4 ± 1.4 (3)
	70	-	8.6 ± 2.5 (3)	-	-	6.3 ± 1.3 (3)	3.6 ± 0.9 (3)

Table 5.9 Normalized Mean Bond Strengths of Cement Plugs in Apache Leap Tuff Cylinders.--Continued
In parentheses are given the number of samples tests (130 push-out tests have been performed). L/D = cement plug length-to-diameter ratio.

Apache Leap Tuff Cylinder		Normalized Mean Average Shear Stress at Failure ± One Standard Deviation (MPa)					
	Curing and	Tuff Cylinder Inside Diameter (mm)					
Saturation Condition	Test Temp. (°C)	12.7 L/D = 1	25.4 L/D = 1	25.4 L/D = 2	25.4 L/D = 4	50.8 L/D = 1	101.6 L/D = 1
Relatively Dry	24 ± 2*	-	7.6 ± 0.1 (3)	-	-	6.9 ± 1.2 (3)	4.6 ± 0.3 (3)
	36	-	5.6 ± 1.2 (7)	-	-	5.5 ± 0.5 (3)	4.3 ± 0.2 (3)

*Cylinders cured at room conditions (i.e. not in environmental chamber) at 24 ± 2°C, 36 ± 2% relative humidity with a thin film of water remaining on the top boreholes.

Table 5.10 Normalized Mean Maximum Exponential Shear Stress at Failure along Cement-Rock Interface for Apache Leap Tuff Push-out Tests. In parentheses are given the number of tests. Data is for the 130 push-out tests performed. L/D = cement plug length-to-diameter ratio.

Apache Leap Tuff Cylinder		Normalized Mean Maximum Exponential Shear Stress at Failure ± One Standard Deviation (MPa)					
	Curing and	Tuff Cylinder Inside Diameter (mm)					
Saturation Condition	Test Temp. (°C)	12.7 L/D = 1	25.4 L/D = 1	25.4 L/D = 2	25.4 L/D = 4	50.8 L/D = 1	101.6 L/D = 1
Presaturated	24 ± 2	-	18.7 ± 2.6 (4)	-	-	14.4 ± 4.6 (3)	-
Highly Saturated	24 ± 2	35.2 ± 4.1 (14)	24.3 ± 3.1 (6)	40.3 ± 5.4 (5)	91.8 ± 1.7 (3)	17.6 ± 4.6 (3)	12.7 ± 1.7 (3)
	45	-	28.5 ± 2.7 (5)	-	-	17.2 ± 4.9 (3)	13.8 ± 1.3 (3)
	70	-	20.7 ± 3.7 (4)	-	-	16.4 ± 3.1 (3)	11.0 ± 3.0 (3)
	90	-	12.3 ± 2.6 (3)	-	-	7.8 ± 2.7 (4)	5.5 ± 1.6 (3)
Partially Saturated	24 ± 2	-	24.2 ± 4.1 (7)	-	-	19.9 ± 6.1 (5)	12.4 ± 5.1 (3)
	44	-	31.1 ± 6.8 (5)	-	-	15.2 ± 2.7 (4)	12.5 ± 4.2 (3)
	70	-	28.1 ± 7.4 (3)	-	-	18.2 ± 4.2 (3)	10.6 ± 1.7 (3)

Table 5.10 Normalized Mean Maximum Exponential Shear Stress at Failure along Cement-Rock Interface for Apache Leap Tuff Push-out Tests.--Continued In parentheses are given the number of tests. Data is for the 130 push-out tests performed. L/D = cement plug length-to-diameter ratio.

Apache Leap Tuff Cylinder		Normalized Mean Maximum Exponential Shear Stress at Failure ± One Standard Deviation (MPa)					
		Tuff Cylinder Inside Diameter (mm)					
Saturation Condition	Curing and Test Temp. (°C)	12.7 L/D = 1	25.4 L/D = 1	25.4 L/D = 2	25.4 L/D = 4	50.8 L/D = 1	101.6 L/D = 1
Relatively Dry	24 ± 2*	-	24.5 ± 0.2 (3)	-	-	19.8 ± 3.3 (3)	12.7 ± 0.8 (3)
	36	-	20.7 ± 1.2 (7)	-	-	17.2 ± 4.2 (3)	11.6 ± 1.5 (3)

*Cylinders cured at room conditions (i.e. not in environmental chamber) at 24 ± 2°C, 36 ± 2% relative humidity with a thin film of water remaining on the top boreholes.

bounds of this experimental data in Figure 5.8 (shaded data points) indicates that the experimental data compares well with the extrapolated (predicted) data (within ± 2.02 to 7.8%). Figure 5.9 gives the best fit of the upper, mean and lower bounds of the normalized axial stresses at failure vs. plug radii, including the data for the 6.35 mm radius plugs. Extrapolation of the lower bound of the axial stress at failure curve to a plug radius of 0.5 m gives an axial stress at failure of 4.61 MPa (which indicates that an in-situ plug in a highly saturated medium, with a radius of 0.5 m and plug length-to-radius ratio of 2, can withstand a water column of at least 470 m). An in-situ plug with a radius of 5 m can resist a water column of at least 148 m.

The axial stress at failure ± one standard deviation for the 12.7, 25.4, and 50.8 mm plug radius partially saturated samples cured at ambient conditions (24 ± 2°C, 80% r.h.) are 34.7 ± 6.4, 26.4 ± 8.1, and 11.9 ± 4.4 MPa, respectively (Table 4.1). The normalized axial stress at failure (i.e. normalized to a cylinder ratio of ∞) ± one standard deviation is 35.1 ± 6.5, 27.8 ± 8.6, and 14.0 ± 5.2 MPa, respectively. Figure 5.10 gives a best fit of the upper, mean and lower bounds of these normalized axial stresses at failure vs. plug radii for partially saturated, ambient (24 ± 2°C, 80% r.h.) conditions. The curves are extrapolated to plug radii of 6.35 and 120 mm. Extrapolation of the lower bound of these curves to plug radii of 0.5 and 5 m indicates that an in-situ plug emplaced in partially saturated tuff can withstand a water column of at least 138 and 19.6 m, respectively. Hence, borehole plugs emplaced in partially saturated tuff would have substantially lower strength (up to 87% lower) than those in highly saturated tuff.

The normalized axial strengths of the highly saturated, ambient push-out samples with plug radii of 12.7 mm increase with increased plug length (Table 5.8). Figure 5.11 gives the normalized axial strength of a 12.7 mm radius plug, cured and tested in highly saturated, ambient conditions, as a function of plug length-to-radius ratio. The equation for the best fit may be used for extrapolating the normalized strength to plug length-to-radius ratios (L/a) of more than 8.0 (experimental data is not available for plugs having L/a more than 8.0; Table 5.8). The axial strength of a borehole plug with L/a of 8 is more than seven times that of a borehole plug with L/a of 2 (Figure 5.11).

Figures 5.12 and 5.13 give the extrapolated normalized axial strengths for samples cured in highly saturated and partially saturated conditions, at ambient temperature, respectively. The plots are a function of larger plug radius (a) (i.e. a = 0.1, 0.5, 5.0 m) and for plug length-to-radius ratios. Figures 5.12 and 5.13 represent a combination of Figures 5.9 and 5.11 and Figures 5.10 and 5.11, respectively. The extrapolation suggests that borehole plugs emplaced in a highly saturated medium would have substantially higher strength that those in partially saturated tuff.

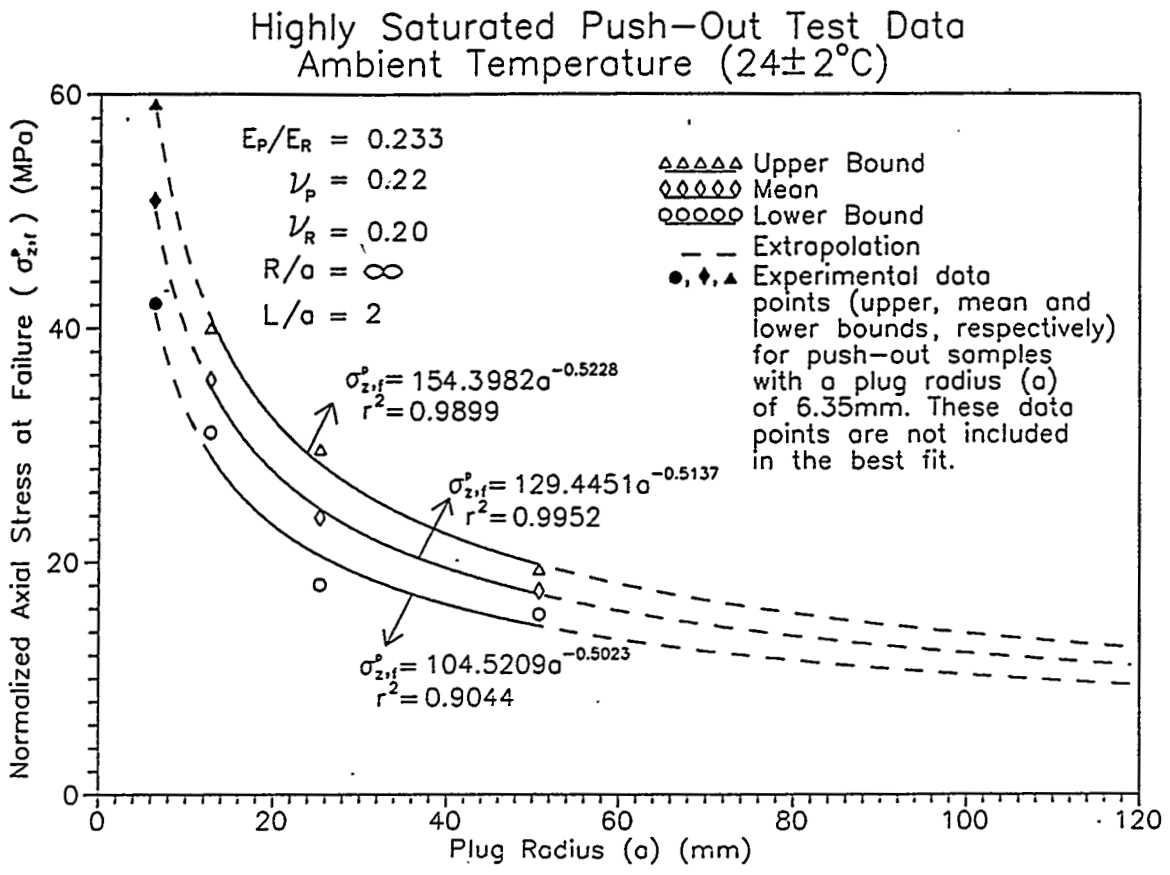

Figure 5.8 The upper, mean and lower bounds of the normalized axial stress at failure for highly saturated plugs cured under water and tested at ambient conditions (24 ± 2°C). The curves are extrapolated to plug radii of 6.35 and 120 mm by using a power fit. Plugs have length-to-diameter ratios of 1.0, in most cases. r^2 = coefficient of determination. Table 5.1 gives definition of all variables.

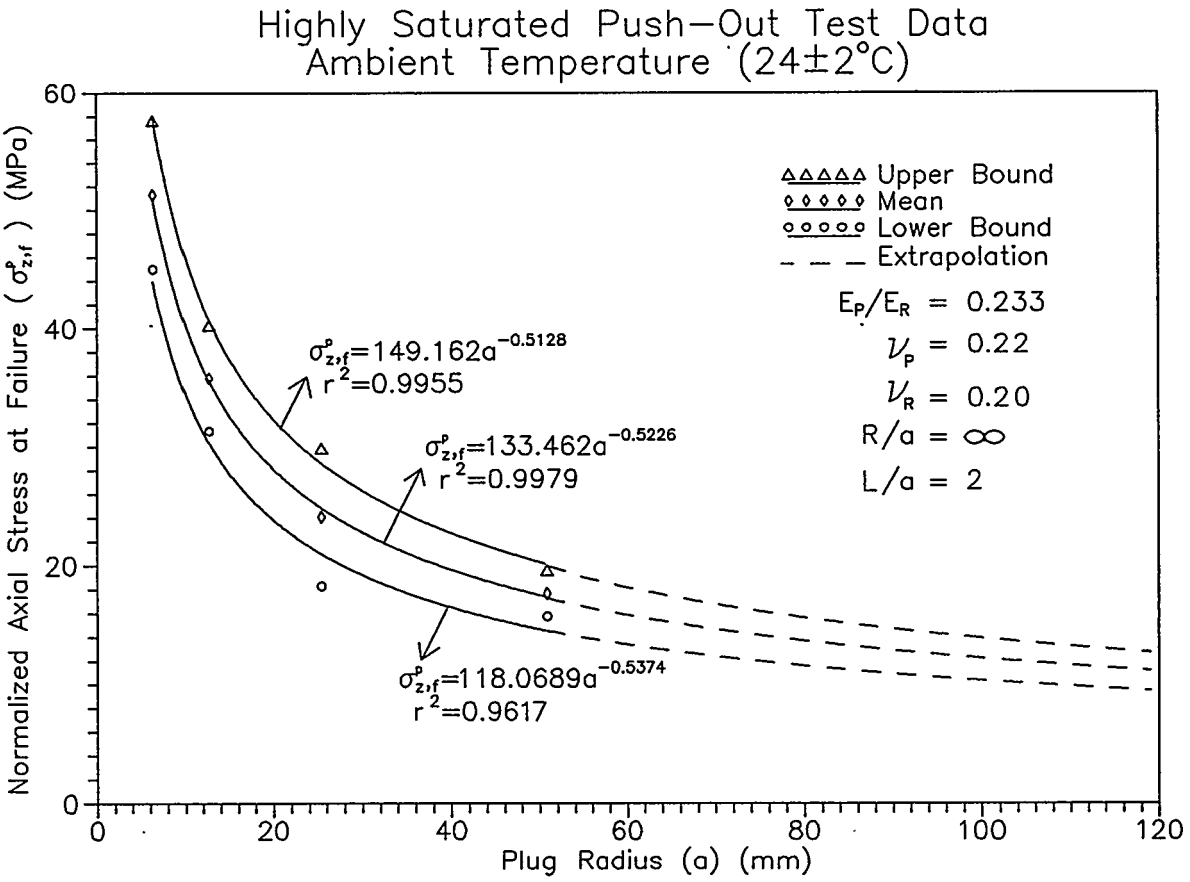

Figure 5.9 The upper, mean and lower bounds of the normalized axial stress at failure for highly saturated plugs cured under water and tested at ambient conditions (24 ± 2°C). The curves are extrapolated to plug radii of 120 mm by using a power fit. Plugs have length-to-diameter ratios of 1.0, in most cases. r^2 = coefficient of determination. Table 5.1 gives definition of all variables.

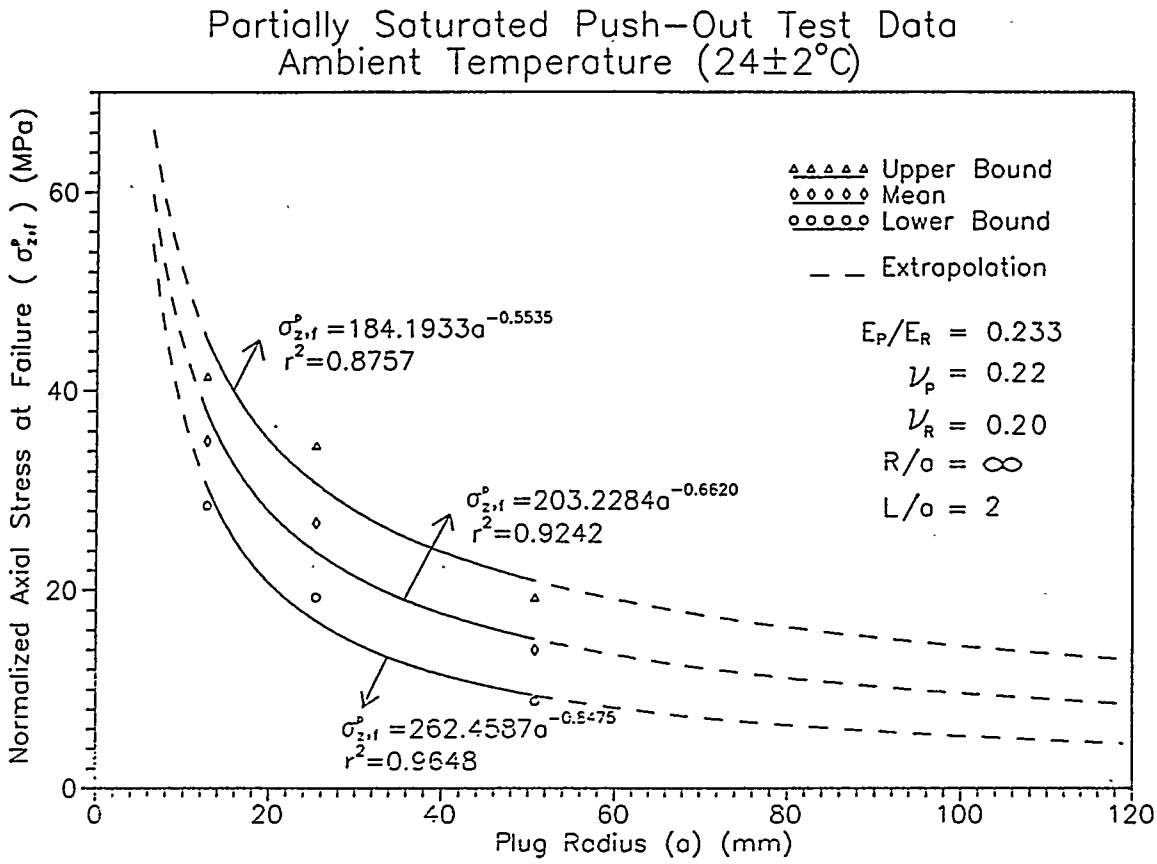

Figure 5.10 The upper, mean and lower bounds of the normalized axial stress at failure for partially saturated plugs cured and tested at ambient conditions (24 ± 2°C, 80% r.h.). The curves are extrapolated to plug radii of 6.35 and 120 mm by using a power fit. Plugs have length-to-diameter ratios of 1.0, in most cases. r^2 = coefficient of determination. Table 5.1 gives definition of all variables.

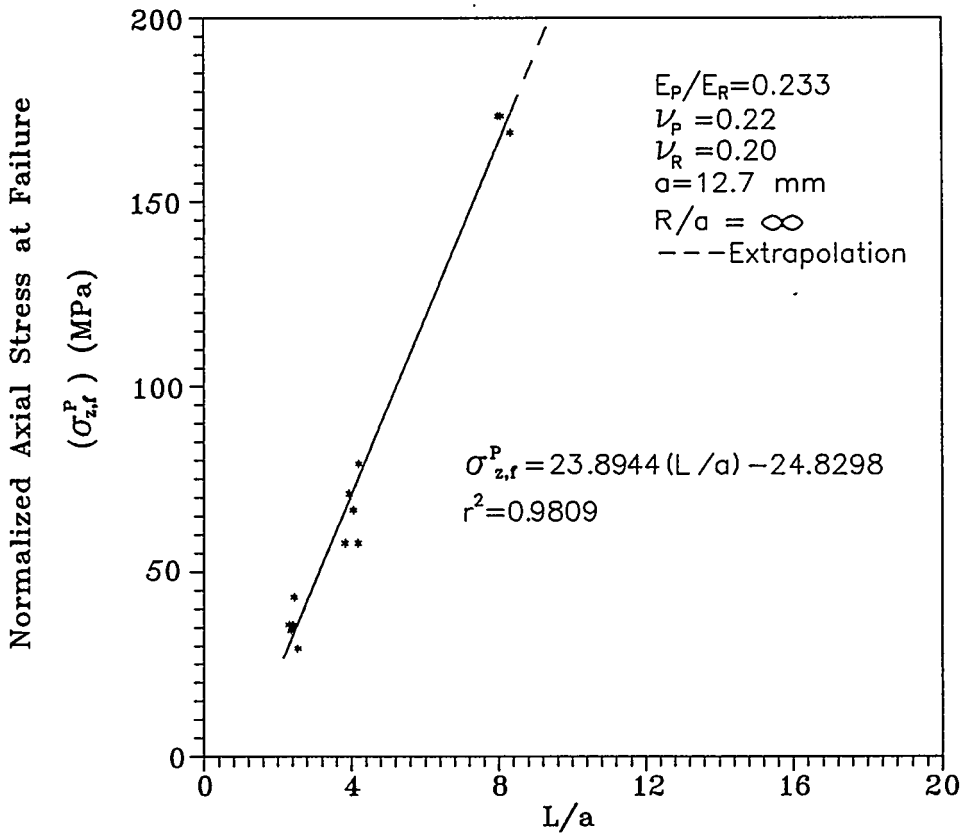

Figure 5.11 Normalized axial strength for highly saturated plugs cured under water and tested at ambient conditions. The plot is given as a function of plug length-to-radius ratio (L/a). Table 5.1 gives definition of all variables.

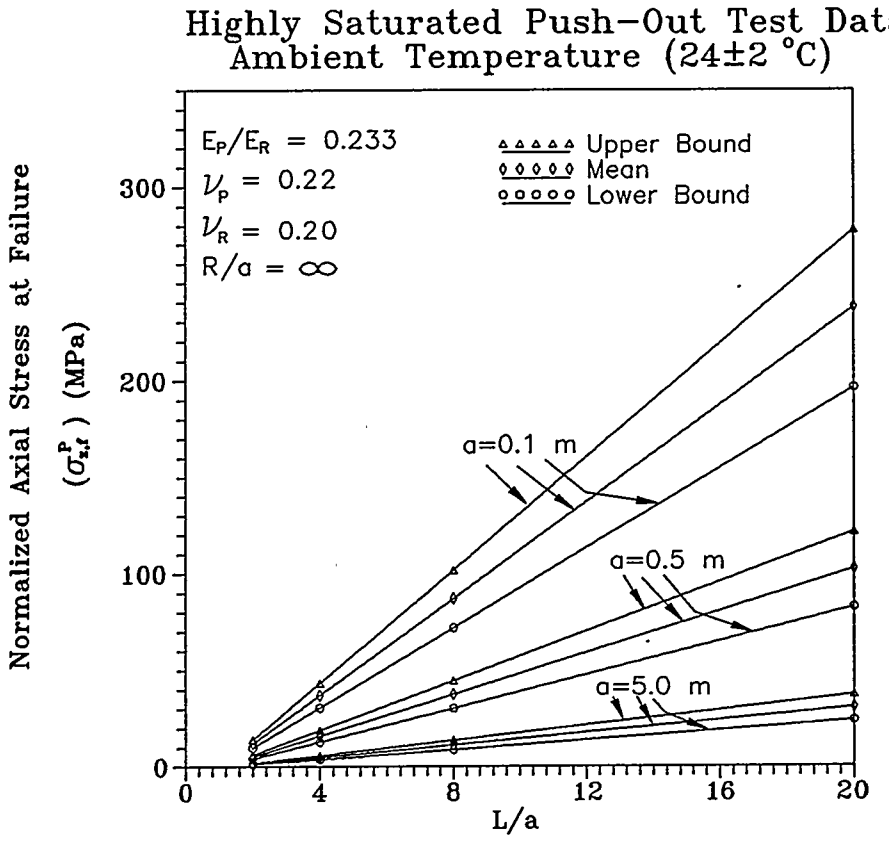

Figure 5.12 Extrapolated normalized axial strength for highly saturated plugs cured under water and tested at ambient conditions. The strength is an extrapolation of the normalized axial strength to larger plug radii (a = 0.1, 0.5, 5 m) and is given as a function of plug length-to-radius ratio (L/a). Table 5.1 gives definition of all variables.

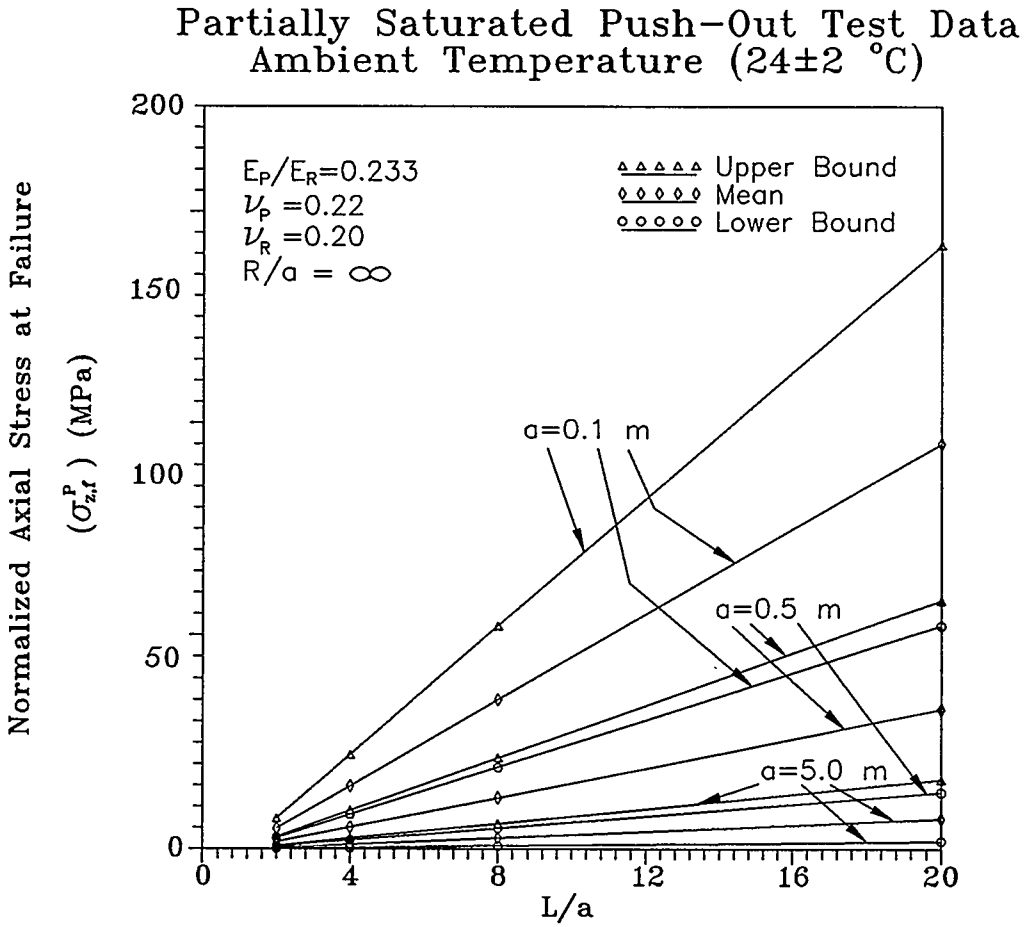

Figure 5.13 Extrapolated normalized axial strength for partially saturated samples cured at ambient conditions. The strength is given as a function of plug radius and plug length. Table 5.1 gives definition of all variables.

5.5.3 Discussion of the Results of Push-Out Tests

The push-out tests show a decrease in axial strength with increasing plug radius and with decreasing plug length (Tables 4.1-4.3; 5.8-5.10). The decrease in strength with decreasing plug length results from the increase in peak interfacial shear stresses at the loaded end of the plug with decreasing plug length (Eq. (2.48)).

The push-out tests show a decrease in axial strength with increasing plug radius due to the increasing peak shear stresses. The laboratory specimens with larger plug radii have smaller tuff cylinder radius ratios which leads to higher peak shear stresses at the loaded end of the plug/rock interface (Table 5.1). Normalization of the specimens to a common cylinder outside-to-inside radius ratio of infinity also shows a decrease in axial strength with increased plug radius (Table 5.8). A possible explanation for the size effects on normalized tuff cylinders follows from the size-strength studies performed on pillars (Tsur-Lavie and Denekamp, 1982; Farmer, 1983, pp. 189-191; 1985 pp. 51-53). When a fracture occurs in a cubic pillar with a linear dimension, L, an amount of strain energy (U) is required to satisfy the energy balance for each unit area of the fracture surface created. If the fracture results from brittle breakdown, and the strain energy per unit fracture area (U/L^2) is assumed to be constant, then the strength of the pillar (σ_{po}) is inversely proportional to one of the pillar linear dimensions (i.e. $\sigma_{po} \alpha 1/L$). The push-out samples fail through brittle (shear) failure (Appendix I) and lead to an inversely proportional relationship between axial strength and plug radius.

The curves of the best fit for the highly saturated samples, rock bridge specimens and for the upper bounds for the partially saturated samples obey the power law with exponents in the neighborhood of 0.5. According to Millard et al. (1955) (as quoted by Jaeger and Cook, 1979, p. 197), a power law curve with an exponent of 0.5 indicates that the lengths of Griffith cracks are proportional to the lengths of the sides of a cubic specimen (or the plug diameter in case of a push-out specimen). This is another finding of this study that might explain the inverse size-strength relationship which has implications in plug design. The extrapolated strengths of cement plugs emplaced in highly saturated host tuff are higher than those of the plugs in partially saturated tuff.

The average degree of saturation in the low, intermediate, presaturated and highly saturated push-out cylinders (prior to push-out testing) is 29, 43, 78 and 73%, respectively; and increases from specimens cured at relatively dry conditions to presaturated samples. There is no discernible difference between the strength measures of highly and partially saturated samples (Tables 4.1-4.3; 5.8-5.10). This most probably indicates that, as long as the cement plugs are not allowed to dry out, their performance will not degrade. The relatively dry samples cured and tested at 36°C show lower strength measures than the more saturated samples cured and tested at 44-45°C. This is because drying out of the cement plugs reduces the expansion of cement.

The push-out cylinders show moderate changes in all three strength measures from samples cured and tested at ambient temperature (24 ± 2°C) to 70°C (Tables 4.1-4.3; 5.8-5.10). A pronounced strength drop occurs at 90°C. These results agree well with those of Diederichs and Schneider (1982), Sager and Rostasy (1982), Hertz (1982), Morley and Royles (1983a), and Morley and Royles (1983b) who investigate the effect of uniform elevated temperatures on the bond between steel and concrete in reinforced concrete. They perform pull-out tests on steel bars embedded in concrete and also find that the bond strength decreases with increasing temperature. The steel-concrete bond strength does not show a significant decrease from 20 to 90°C (e.g. a decrease of not more then 10%). They attribute the decrease in bond strength at higher temperatures to the increased thermal shear stresses occurring due to the difference in the coefficients of thermal expansion of the reinforcing bar and concrete. The resultant maximum exponential interface shear stress at the top of the cement plug (i.e. at $z = 0$; Eq. (2.105)) does not change due to the contribution from the thermally induced shear stresses. Therefore, the attribution of the decrease in bond strength of the increasing shear stresses at the interface does not seem to be reasonable. Akaiwa and Sudoh (1966, p. 42), Lankard et al. (1971, p. 72), Nasser and Lohtia (1971, p. 183), Nasser and Marzouk (1979, p. 541), and Nasser and Chakraborty (1985, p. 130) perform uniaxial compressive strength tests on cylindrical cement/concrete samples cures at -11 to 260°C for periods up to 6 months. Their results agree well with those of the elevated temperature push-out tests. They conclude that curing temperatures of up to 71°C have a minor effect on the uniaxial compressive strength of cement/concrete cylinders. At temperatures higher than 71°C, they observe a reduction in strength. They attribute the decrease in strength with elevated temperatures to the weakening of cement. Whenever cement/concrete masses are subject to high temperatures, saturated steam pressure is induced, which leads to high pore pressures and deterioration in the structural properties of the cement gel. This seems to be a more likely explanation for the pronounced push-out strength drop at 90°C.

Table 4.5 gives the mean axial plug displacement per applied axial stress at failure. The closed-form solution (Eq. (2.47)) underestimates the axial plug displacements with a mean ± one standard deviation of 30 ± 8%, most probably due to the deformation of the test system.

5.6 Borehole Stability under Internal Pressure

A borehole plug emplaced in an underground opening may generate radial stresses on the walls of openings. Such radial stresses may be caused by axial load on the plug (e.g. due to water or gas pressures, by thermally induced deformation, or by plug swelling). Radial stresses may widen fractures or may lead to tensile fracturing, and cause preferential pathways around seals, e.g. for water flow or for gaseous radionuclides. This section studies the effect of tensile fracturing and cement swelling on borehole stability.

5.6.1 Effect of Tensile Fracturing on Borehole Stability

5.6.1.1 Experimental Results

Seven (out of 34) of the 50.8 mm samples and 17 (out of 27) of the 101.6 mm push-out samples split in tension during push-out testing. The tensile strengths of the 50.8 and 101.6 mm specimens ± one standard deviation (calculated from App. J, Eq. (J.2)) are 8.98 ± 1.7 MPa and 9.16 ± 1.2 MPa, respectively. Overall, the 24 samples show a mean tensile strength/axial stress at failure ± one standard deviation of 0.677 ± 0.344. None of the samples showing tensile splitting have fractures running through the cement plugs (i.e. the cement plugs do not split in tension). This suggests that the failure mechanism is different from that induced by cement swelling itself, e.g. as observed by Akgun and Daemen (1986, pp. 39-68).

Stormont and Daemen (1983, p. 117) perform push-out tests on basalt and granite cores plugged with cement. The geometry of their specimens is very similar to those tested in this study. They observe tensile splitting on 16 of the 100 push-out tests. The mean tensile strength ± one standard deviation is 11.5 ± 13.0 MPa. Fuenkajorn and Daemen (1990) report results of 50.8 mm diameter, 25.4 mm thick Brazilian tensile strength tests on Apache Leap tuff discs. The Brazilian tensile strength of these samples is 5.12 ● 1.20 MPa. The Brazilian tensile strength of 95.4 mm diameter, 50.8 mm thick discs is 6.51 ± 0.95 MPa. On the average, the tensile strength of the Apache Leap tuff push-out cylinders are 30 to 40% higher than those report by Fuenkajorn and Daemen (1990).

Figure 5.14 shows the bottom view of a tensile fractured 50.8 mm Apache Leap tuff push-out specimen AP3-6-2-AMB-FS-3-P01-SSII after testing. The fracture is not radial. For most splitting failures induced by push-out testing, nonradial fractures have been observed. The possibility exists that the illustrated fracture may be induced by nonuniform loading, resulting in bending. Given the occurrence of several other (not illustrated) fracture patterns, a more likely explanation is that the fracture patterns are strongly influenced by pre-existing weaknesses in the tuff, thus confirming the repeated observations about the complexity of the mechanical behavior of welded tuff (Fuenkajorn and Daemen, 1990). For the particular example illustrated, the tensile stress across the fracture is less than that calculated by Eq. J.2 (App. J), and hence the calculated strength underestimates the real strength.

5.6.1.2 Tensile Stresses in and near an Axially Loaded Borehole Plug

The determination of the tensile stress in rock hosting a plug is important. Tensile fracturing may cause preferential pathways around seals. The objective of this section is to analyze the tensile zone in the vicinity of an axially loaded borehole plug. The results of the finite element analysis is given in Chapter 3, Section 3.4.

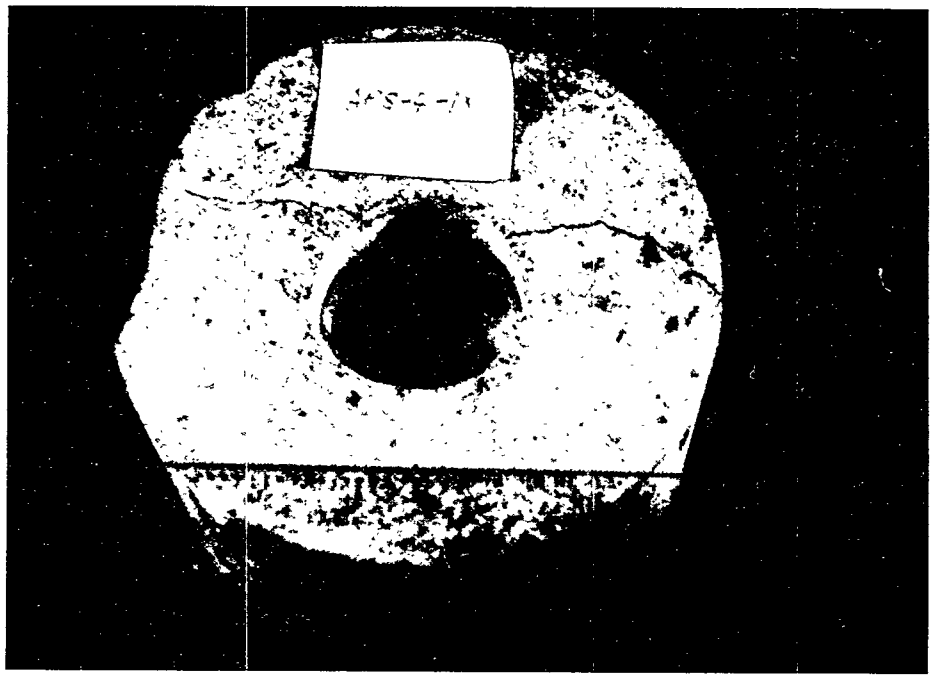

Figure 5.14 Bottom view of 50.8 mm Apache Leap tuff specimen AP3-6-2-amb-FS-3-PO1x-SSII showing partial tensile splitting during push-out testing. Note that the tensile fracture does not travel through the cement plug.

5.6.1.3 Summary and Discussion

The results of the finite element analysis presented in Section 3.4 shows that, for a borehole plug with a length-to-radius ratio of 2.0 and modulus ratio of 0.233, the most critical area within the plug is the top corner (Table 3.3). The tensile stress in this location is uniaxial. It reaches 74% of the applied axial stress and may lead to separation along the interface with the combined effect of the peak interfacial shear stresses. All 130 push-out tests show shear failure. Very little or no cement remains along the interface, suggesting that a tensile normal stress may exist along the interface. The magnitude of the tensile stresses at the top plug corner decreases with increased plug length-to-radius ratio and increased modulus ratio.

A modulus ratio of 10.0 leads to peak tensile stresses at the bottom center of the plug with a peak tensile stress up to 41% of the axial stress applied to the plug. The state of tensile stresses at the location is biaxial and the magnitude of the tensile stresses decrease with decreasing modulus ratio and increasing plug length. A plug with a modulus ratio of 10.0 suggests that tensile fracturing at the bottom center of the plug is very likely due to a biaxial tensile stressfield (Table 3.3).

The maximum tensile stresses in rock occur adjacent to the top plug corner and decrease with increased modulus ratio and increased plug length. A borehole plug with a length-to-radius ratio of 2.0 and modulus ratio of 0.233 shows the most severe maximum tensile stress of 80% of the applied axial stress at this location (Table 3.3).

The most likely axial stress on a borehole plug in rock is due to a water pressure across the plug. The maximum water pressure is estimated once the repository depth is known. If a borehole plug is emplaced 1000 m under the ground surface, and the top borehole fills up with water, this creates a water pressure (or axial stress applied to the plug) of 9.81 MPa on the borehole plug. This water pressure creates a maximum tensile stress of 6.74, 4.85, and 2.56 MPa at the most critical plug location (location B, Table 3.3) of borehole plugs having a modulus ratio of 0.233 and cement plug length-to-radius ratios of 2, 4 and 8, respectively.

The mean tensile strength of medium strength concrete is 2.95 MPa (Neville, 1981, pp. 549-552). Therefore, tensile failure of plugs with a modulus ratio of 0.233 and length-to-radius ratios of 2 and 4 is very likely. The tensile strength of plugs with length-to-radius ratios of 8 (2.95 MPa) exceeds the maximum tensile stresses developed at location B (2.56 MPa); hence, a borehole plug with a modulus ratio of 0.233 should have a length-to-radius ratio of at least 8 to avoid tensile fracturing.

The mean tensile strength of Apache Leap tuff is 9 MPa (Section 5.6.1.1). A water pressure of 9.81 MPa creates a maximum tensile stress of 7.49, 5.89 and 4.02 MPa at the most critical rock location (location C, Table 3.3) near borehole plugs having a modulus ratio of 0.233 and

cement plug length-to-radius ratios of 2, 4 and 8, respectively. Hence, no tensile fracturing of rock is expected (and has not been observed experimentally on 12.7 mm radius borehole plugs).

The results of the theoretical analysis shows that a borehole plug with a modulus ratio of 0.233 and plug length-to-radius ratio of 8 shows smaller maximum exponential shear stresses and shows little probability of tensile failure in the plug (when compared to shorter plugs). Hence, it provides an attractive borehole plug geometrical design criterion.

5.6.2 Effect of Cement Swelling Stress on Borehole Stability

This section studies the effect of cement swelling on borehole stability. Two hollow Apache Leap tuff cylinders with outside diameters of 187.3 mm (7.4 in), inside diameters of 101.6 mm (4 in) and with visible hairline fractures on one side of each sample are plugged with cement. The cement plugs have length-to-diameter ratios of approximately 1.0. Three points are marked along the dominant fractures to measure the increase of the aperture as a function of time (Figure 5.15). The fracture widths are measured by means of an engineering filler gage. Table 5.11 gives the results of the measurements for a period of 164 days. Sample AP122-1-1 shows a total fracture aperture growth of 0.91 mm after 164 days, sample AP20-1-1 0.58 mm. If plugs are installed in hole sections where joints are present and unfavorably oriented (as observed by Akgun and Daemen, 1986, p. 39), excessive cement swelling might be detrimental by enhancing flowpaths that allow bypassing of the plug. Neretnieks (1987) points out the additional potential influence of swelling, and the resulting change of stress state within the surrounding rock, on radionuclide retardation as a result of the influence of a change in stress state on radionuclide retardation through matrix diffusion.

Figure 5.15 Apache Leap tuff cylinder AP122-1-1 with an outside diamter of 187.3 mm (7.4 in), inside diameter of 101.6 mm (4 in), and with hairline fractures on one side of sample. The increase of the aperture along the dominant fracture (at points marked 1, 2 and 3) due to cement swelling is monitored as a function of time.

Table 5.11 Increase of the Aperture Along the Dominant Fractures of Samples AP122-1-1 and AP20-1-1 Due to Cement Swelling. The fracture widths are measured as a function of time at points 1, 2 and 3 along both fractures (locations of points shown in Figures 4.12 and 4.13) and indicated as e_1, e_2, and e_3, respectively)

	Sample AP122-1-1			Sample AP20-1-1		
Time (days)	e_1 (mm)	e_2 (mm)	e_3 (mm)	e_1 (mm)	e_2 (mm)	e_3 (mm)
0	0	0	0	0	0	0
7	0.12	0.08	0.20	0.05	0.02	0.05
14	0.16	0.09	0.25	0.07	0.04	0.08
28	0.32	0.10	0.28	0.13	0.09	0.18
56	0.59	0.25	0.36	0.30	0.18	0.42
77	0.77	0.28	0.45	0.35	0.25	0.48
91	0.79	0.31	0.51	0.38	0.27	0.56
119	0.84	0.53	0.60	0.38	0.32	0.56
164	0.91	0.60	0.70	0.40	0.32	0.58

REFERENCES

Adisoma, G., R. Armstrong, K. Fuenkajorn, and J.J.K. Daemen, 1987, "Surface Preparation and Strain Gage Installation," Geomechanics Laboratory, Dept. of Mining and Geological Engineering, Univ. of Arizona, Tucson.

Adisoma, G. and J.J.K. Daemen, 1988, "Experimental Assessment of the Influence of Dynamic Loading on the Permeability of Wet and of Dried Cement Borehole Seals," NUREG/CR-5129, prepared for the U.S. Nuclear Regulatory Commission, Office of Nuclear Regulatory Research, Division of Engineering, by the Department of Mining and Geological Engineering, University of Arizona, Tucson.

Akaiwa, S. and G. Sudoh, 1966, "Strength and Microstructure of Hardened Cement," Proc., Symp. on Structure of Portland Cement Paste and Concrete, Special Rpt. No. 90, Highway Traffic Board, Washington, DC, pp. 36-47.

Akgun, H. and J.J.K. Daemen, 1986, "Size Influence on the Sealing Performance of Cementitious Borehole Plugs," NUREG/CR-4738, prepared for the U.S. Nuclear Regulatory Commission, Office of Nuclear Regulatory Research, Division of Engineering Safety, by the Department of Mining and Geological Engineering, University of Arizona, Tucson.

Akgun, H. and J.J.K. Daemen, 1989, "Bond Strength of Cement Borehole Plugs in Salt," NUREG/CR-5401, prepared for the U.S. Nuclear Regulatory Commission, Office of Nuclear Regulatory Research, Division of Engineering, by the Department of Mining and Geological Engineering, University of Arizona, Tucson.

American Petroleum Institute, 1986, *Specifications for Materials and Testing for Well Cements*, 3rd Ed., Am. Petroleum Inst., Production Dept., Dallas.

Amir, J.M., 1986, *Piling in Rock*, A.A. Balkema, Rotterdam, Boston.

Arya, S.K. and G.A. Hegemier, 1982, "Finite Element Method for Interface Problems," J. of the Structural Div., Proc. of the ASCE, Vol. 108, No. ST2, pp. 327-342.

ASTM C39-86, "Standard Test Method for Compressive Strength of Cylindrical Concrete Specimens," *Annual Book of ASTM Standards*, Vol. 04.02, Am. Soc. for Testing and Materials, Philadelphia.

ASTM C192-81, "Standard Method of Making and Curing Concrete Test Specimens in the Laboratory," *Annual Book of ASTM Standards*, Vol. 04.02, Am. Soc. for Testing and Materials, Philadelphia.

ASTM C305-82, "Standard Method for Mechanical Mixing of Hydraulic Cement Pastes and Mortars of Plastic Consistency," *Annual Book of ASTM Standards*, Vol. 04.01, Am. Soc. for Testing and Materials, Philadelphia.

ASTM D1143-81, "Standard Method for Testing Piles Under Static Axial Compressive Load," *Annual Book of ASTM Standards*, Vol. 04.08, Am. Soc. for Testing and Materials, Philadelphia.

ASTM D2938-79, "Standard Test Method for Unconfined Compressive Strength of Intact Rock Core Specimens," *Annual Book of ASTM Standards*, Vol. 04.08, Am. Soc. for Testing and Materials, Philadelphia.

ASTM D3148-80, "Standard Method for Elastic Moduli of Intact Rock Core Specimens in Uniaxial Compression," *Annual Book of ASTM Standards*, Vol. 04.08, Am. Soc. for Testing and Materials, Philadelphia.

Baguelin, F. and R. Frank, 1979, "Theoretical Studies of Piles Using the Finite Element Method," Int. Conf. on Numerical Methods in Offshore Piling, ICE, London, pp. 33-91.

Bieniawski, Z.T., et al., 1978, "Suggested Methods for Determining the Uniaxial Compressive Strength and Deformability of Rock Materials," Inter. Soc. for Rock Mechanics, Comm. on Standardization of Laboratory and Field Tests, Committe on Lab. Tests, Sept. Published by Inter. J. of Rock Mechanics and Mining Sciences & Geomech. Abs., Vol 16, No. 2, pp. 135-140, 1979. Also in *Rock Characterization Testing and Monitoring*, ISRM Suggested Methods, E.T. Brown, ed., pp. 111-116. Pergamon Press, Oxford, 1981.

Binnall, E.P., S.M. Benson, L. Tsao, H.A. Wollenberg, T.K. Takunaga, and E.M. Didwall, 1987, "Critical Parameters for a High-Level Waste Repository, Vol. 2: Tuff," NUREG/CR-4161, prepared for the U.S. Nuclear Regulatory Commission, Division of Engineering, Office of Nuclear Regulatory Research, by the Lawrence Livermore National Laboratory, P.O. Box 808, Livermore, CA.

Bowles, J.E., 1977, *Foundation Analysis and Design*, McGraw-Hill Book Co., NY.

Buck, A.D. and J.P. Burkes, 1979, "Examination of Grout and Rock from Duval Mine, New Mexico," Misc. Paper SL-79-6, U.S. Army Engineer Waterways Experiment Station, Vicksburg, MS.

Buck, A.D. and K. Mather, 1982, "Grout Formulations for Nuclear Waste Isolation," ONWI-413, prepared by the Structures Laboratory, U.S. Army Engineer Waterways Experiment Station, for the Office of Nuclear Waste Isolation, Battelle Memorial Institute, Columbus, OH.

Burgreen, D., 1971, *Elements of Thermal Stress Analysis*, C.P. Press, Jamaica, NY.

Calvert, D.G., 1980, "Shrinkage-Compensating Cements in Oil Well Cementing," pp. 193-197, Paper SP 64-11, Cedric Wilson Symp. on Expansive Cement, Pub. SP-64, Am. Concrete Institute, Detroit.

Coates, D.F. and H.S. Yu, 1970, "Three Dimensional Stress Distribution around a Cylindrical Hole and Anchor," Proc. 2nd Cong. Int. Soc. Rock Mech., Belgrade, 3, pp. 175-182.

Cook, R.D., 1981, *Concepts and Applications of Finite Element Analysis*, 2nd Ed., John Wiley and Sons, NY.

Coons, W.E., D. Meyer, and P.C. Kelsall, 1982, "Evaluation of Polymer Concrete for Application to Repository Sealing," ONWI-410, prepared by D'Appolonia Consulting Engineers, Inc., for the Office of Nuclear Waste Isolation, Battelle Memorial Institute, Columbus, OH.

Cox, H.L., 1952, "The Elasticity and Strength of Paper and Other Fibrous Materials," British J. of Applied Physics, Vol. 3, March.

D'Appolonia Consulting Engineers, 1981, "Sealing Considerations for Repository Shafts in Bedded and Dome Salt," ONWI-255, prepared for the Office of Nuclear Waste Isolation, Battelle Memorial Institute, Columbus, OH.

Daemen, J.J.K., 1974, "Mechanics of Grouted Bolts," *Advances in Rock Mechanics*, Proc. of 3rd Congress of the International Society for Rock Mechanics, Denver, pp. 128-131.

Daemen, J.J.K., W.B. Greer, K. Fuenkajorn, A. Yazdandoost, H. Akgun, A. Schaffer, A.F. Kimbrell, T.S. Avery, J.R. Williams, B. Kousari, and R.O. Roko, 1986, "Experimental Assessment of Borehole Plug Performance, Annual Report, June 1, 1984 - May 31, 1985," NUREG/CR-4642, prepared for the U.S. Nuclear Regulatory Commission, Office of Nuclear Regulatory Research, by the Department of Mining and Geological Engineering, University of Arizona, Tucson.

Desai, C.S., 1974, "Numerical Design-Analysis of Piles in Sands," J. Geotech. Engg. Div., ASCE, 100, GT6, pp. 613-635.

Desai, C.S., 1977, "Soil-Structure Interaction and Simulation Problems," Ch. 7 in *Finite Elements in Geomechanics*, G. Gudehus (ed.), John Wiley and Sons, UK.

Desai, C.S., 1979, *Elementary Finite Element Method*, Prentice-Hall, Inc., Englewood Cliffs, NJ.

Desai, C.S. and J.F. Abel, 1972, *Introduction to the Finite Element Method - A Numerical Method for Engineering Analysis*, Van Nostrand Reinhold Co., New York.

Desai, C.S. and D.M. Holloway, 1972, "Load-Deformation Analysis of Deep Pile Foundations, " Proc. Symp. Appl. Finite Elem. Meth. Geotech. Engg., Vicksburg, MS.

Desai, C.S., M.M. Zaman, J.G. Lightner, and H.J. Siriwardane, 1984, "Thin Layer Element for Interfaces and Joints," Int. J. Num. and Anal. Meth. Geomech., Vol. 8, pp. 19-43.

Diederichs, U. and U. Schneider, 1981, "Bond Strength at High Temperature," Magazine of Concrete Research, Vol. 33, No. 115, June, pp. 75-84.

Drucker, D.C., 1967, *Introduction to the Mechanics of Deformable Solids*, McGraw Hill, New York.

Farmer, I.W., 1975, "Stress Distribution along a Resin Grouted Rock Anchor," Int. J. Rock Mechanis, Mining Sciences and Geomechanics Abstracts, Pergamon Press, Vol. 12, pp. 347-351.

Farmer, I.W., 1983, *Engineering Behaviour of Rocks*, Second Edition, Chapman and Hall, London.

Farmer, I.W., 1985, *Coal Mine Structures*, Chapman and Hall, London.

Fleming, W.G.K., A.J. Weltman, M.F. Randolph, and W.K. Elson, 1985, *Piling Engineering*, John Wiley and Sons, N.Y.

Fuenkajorn, K. and J.J.K. Daemen, 1991, "Mechanical Characterization of the Densely Welded Apache Leap Tuff," NUREG/CR-5668, Technical Report, prepared for the U.S. Nuclear Regulatory Commission, Office of Nuclear Regulatory Research, Division of Engineering, by the Department of Mining and Geological Engineering, University of Arizona, Tucson.

Garrett, W.S. and L.T. Campbell Pitt, 1961, "Design and Construction of Underground Bulkheads and Water Barriers," pp. 1283-1299, Discussion pp. 1300-1, Vol. III, Transactions of the Seventh Commonwealth Mining and Metallurgical Congress, South African Institute of Mining and Metallurgy, Johannesburg.

Gere, J.M. and S.P. Timoshenko, 1984, *Mechanics of Materials*, 2nd Ed., PWS Engineering, Boston, MA.

Goodman, R.E., R.L. Taylor, and T.L. Brekke, 1968, "A Model for the Mechanics of Jointed Rock," J. Soil Mech. Found. Div., ASCE, 94, SM3.

Greer, W.B. and J.J.K. Daemen, 1991, "In-Situ Tests of the Hydraulic Performance of Grout Borehole Seals," NUREG/CR-5684, Technical Report, prepared for the U.S. Nuclear Regulatory Commission, Office of Nuclear Regulatory Research, Division of Engineering, by the Department of Mining and Geological Engineering, University of Arizona, Tucson.

Greszczuk, L.B., 1979, "Theoretical Studies of the Mechanics of the Fiber-Matrix Interface in Composites," *Interfaces in Composites*, ASTM STP 452, American Society for Testing and Materials, pp. 42-58.

Gulick, C.W., Jr., J.A. Boa, Jr., and A.D. Buck, 1980a, "Bell Canyon Test - Cement Development Report," pp. 277-296, Proc. Workshop on Borehole and Shaft Plugging, jointly organized by the OECD Nuclear Energy Agency and U.S. Dept. of Energy, Columbus, OH, May.

Gulick, C.W., Jr., J.A. Boa, Jr., and A.D. Buck, 1980b, "Bell Canyon Test (BCT) Cement Grout Development Report," SAND80-1928, Sandia National Laboratories, Albuquerque, NM.

Hancox, N.L., 1981, "Introduction to Fibre Composite Hybrids," pp. 1-22 in *Fibre Composite Hybrid Materials*, N.L. Hancox, ed., Applied Science Pub., London.

Hearn, E.J., 1977, *Mechanics of Materials*, Pergamon Press, London.

Hertz, K., 1982, "The Anchorage Capacity of Reinforcing Bars at Normal and High Temperatures," Magazine of Concrete Research, Vol. 34, No. 121, Dec., pp. 213-220.

Holister, G.S. and C. Thomas, 1966, *Fibre Reinforced Materials*, Elsevier Pub. Co., Amsterdam, pp. 14-49.

Hollingshead, G.W., 1971, "Stress Distributions in Rock Anchors," Can. Geotech. J., Vol. 8, pp. 508-592.

Jaeger, J.C. and N.G.W. Cook, 1979, *Fundamentals of Rock Mechanics*, Third Edition, Chapman and Hall, London.

Jeffrey, R.G. and J.J.K. Daemen, 1981, "Shaft or Borehole Plug-Rock Mechanical Interaction," pp. 865-879, Vol. 2, Proc. of the Symp. on Waste Management, Tucson, AZ, Feb.

Jezierski, H., 1984, "Dam Construction in Salt Formations," pp. 261-7, Vol. 2, Waste Management '84, Tucson, AZ.

Kardestuncer, H., 1987, *Finite Element Handbook*, H. Kardestuncer, ed., McGraw-Hill, NY.

Katona, M.G., 1983, "A Simple Contact-Friction Interface Element with Aplciations to Buried Calverts," Int. J. Num. Anal. Meth. Geomech., Vol. 7, pp. 371-384.

Kelly, A., 1973, *Strong Solids*, 2nd Ed., Clarendon Press, Oxford.

Kelly, A. and N.H. Macmillan, 1986, *Strong Solids*, 3rd Ed., Clarendon Press, Oxford.

Kelsall, P.C., W.E. Coons, and D. Meyer, 1983, "Repository Sealing Program Plan: Repository in Salt," ONWI-414, prepared by D'Appolonia Consulting Engineers, Inc., for the Office of Nuclear Waste Isolation, Battelle Memorial Institute, Columbus, OH.

Kinstler, F.L., 1983, "Mackintoshand Murchison Dams - River Diversions," Civil Eng. Trans. I.E. Aust., Vol. 25, No. 1, Feb., pp. 51-56.

Konya, C.J., F. Otuonye, and D. Skidmore, 1982, "Airblast Reduction from Effective Blasthole Stemming," Proc. of 8th Conf. on Explosives and Blasting Technique, Soc. of Explosives Engineers, Annual Meeting, New Orleans, LA, pp. 145-156.

Lankard, D.R., D.L. Birkmeir, F.F. Fondreist, and M.J. Snyder, 1971, "Effects of Moisture Content on the Structural Properties of Portland Cement Concrete Exposed to Temperatures up to 500°F," Symp. On Effects of Temperature on Concrete, SP 25, ACI, Detroit, pp. 59-102.

Lappin, A.R., 1980, "Preliminary Thermal Expansion Screening Data for Tuffs," prepared by Sandia National Laboratories, for the U.S. Dept. of Energy, SAND 78-1147, March.

Loofbourow, R.L., 1973, "Ground Water and Ground-Water Control," Ch. 26, pp. 26-55, Vol. 2, *SME Mining Engineering Handbook*, Soc. of Mining Engineers of the Am. Institute of Mining, Metallurgical, and Petroleum Engineers, Inc., New York.

Malinowski, R., 1982, "Ancient Mortars and Concretes: Aspects of Their Durability," pp. 89-100, *History of Technology*, 7th Annual Vol., A.R. Hall and N. Smith, eds., Mansell Publishing Ltd., London.

Measurements Group, Inc., 1979, "Strain Gage Installations with M-Bond 43-B, 600 and 610 Adhesive Systems," Instruction Bulletin B-130-11, Measurements Group, Raleigh, NC.

Millard, D.J., P.C. Newman, and J.W. Phillips, 1955, "The Apparent Strength of Extensively Cracked Materials," Proc. Phys. Soc. London, B 68, pp. 723-728.

Mitchell, W.R., 1982, "Examples of Dewatering Considerations and Outlet Arrangements in H.E.C. Dams, Tasmania," ANCOLD Bulletin No. 61, May, pp. 26-28.

Moore, J.G., M.T. Morgan, E.W. McDaniel, H.B. Greene, and G.A. West, 1978, "Cement Technology for Plugging Boreholes in Radioactive Waste Repository Sites," Progress Report for the Period Oct. 1, 1977 to Sept. 30, 1978, ORNL-5524, Oak Ridge National Laboratory, Oak Ridge, TN.

Morley, P.D. and R. Royles, 1983a, "Response of the Bond in Reinforced Concrete to High Temperatures," Magazine of Concrete Research, Vol. 35, No. 123, June, pp. 67-74.

Morley, P.D. and R. Royles, 1983b, "Further Responses of the Bond in Reinforced Concrete to High Temperature," Magazine of Concrete Research, Vol. 35, No. 124, Sept., pp. 157-163.

Morley, P.D. and R. Royles, 1983c, "Use of Bond Stress-Slip Data for Studying the Effect of High Temperatures on the Bond in the Anchorage Zone of Reinforced Concrete Structures," Proc. Instn. Civ. Engrs., Part 2, Vol. 75, Dec., pp. 657-669.

Nasser, K.W. and R.P. Lohtia, 1971, "Mass Concrete Properties at High Temperatures," ACI Journal, Vol. 68, No. 3, March, pp. 180-186.

Nasser, K.W. and H.M. Marzouk, 1981, "Properties of Concrete Containing Fly Ash at Normal and High Temperatures," Proc., Second Australian Conf. on Engineering Materials, Univ. of New South Wales, Sydney, July, pp. 189-199.

Nasser, K.W. and M. Chakraborty, 1985, "Temperature Effects on Strength and Elasticity of Concrete Containing Admixtures," in *Temperature Effects on Concrete*, ASTM Special Technical Publication 858, T.R. Naik, ed., Philadelphia.

Neretnieks, I., 1987, "Some Coupled Processes Which May be Important for a Nuclear Waste Repository," Ch. 55, pp. 759-763, *Coupled Processes Associated with Nuclear Waste Repositories*, C.F. Tsang, ed., Academic Press, Inc., Orlando.

Neville, A.M., 1981, *Properties of Concrete*, Third Edition, Pitman, London.

Nitzsche, R.N. and C.J. Haas, 1976, "Installation Induced Stresses for Grouted Roof Bolts," Int. J. Rock. Mech. Min. Sci. & Geomech. Abstr., Vol. 13, pp. 17-24.

Organization for Economic Cooperation and Development, Nuclear Energy Agency, 1982, "Geological Disposal of Radioactive Waste Research in the OECD Area," May, OECD, 39, boulevad Suchet, Paris.

Otuonye, F., C.J. Konya, and D.R. Skidmore, 1983, "Effects of Stemming Size Distribution on Explosive Charge Confinement: A Laboratory Study," Mining Engineering, Vol. 35, No. 8, pp. 1205-8, Aug.

Pettman, E.R., 1984, "Tunnel Plugs in Recent H.E.C. Practice," 5th Australian Tunnelling Conf., Sydney, Oct., pp. 207-212.

Piggott, M.R., 1980, *Load-Bearing Fibre Composites*, Pergamon Press, Oxford.

Potts, D.M. and J.P. Martins, 1982, "The Shaft Resistance of Axially Loaded Piles in Clay," Geotechnique, Vol. 32, No. 4, pp. 369-386.

Randolph, M.F. and C.P. Wroth, 1978, "Analysis of Deformation of Vertically Loaded Piles," Journal of the Geotechnical Engineering Division, Proceedings of the ASCE, Vol. 104, No. GT12, Dec., pp. 1465-1488.

Rhoderick, J.E. and A.D. Buck, 1981, "Examination of Simulated Borehole Specimens," ONWI-247, prepared by Structures Laboratory, U.S. Army Engineer Waterways Experiment Station, for the Office of Nuclear Waste Isolation, Battelle Memorial Institute, Columbus, OH.

Rhoderick, J.E., 1981, "Examination of Sample of Grout after 63 Years Exposure Underground," ONWI-248, USAE-WES SL-81-6, prepared by the Structures Laboratory, U.S. Army Engineer Waterways Experiment Station, for the Office of Nuclear Waste Isolation, Battelle Memorial Institute, Columbus, OH.

Roy, D.M. and C.A. Langton, 1983, "Characterization of Cement-Based Ancient Building Materials in Support of Repository Seal Materials Studies," BMI/ONWI-523, prepared by the Materials Research Laboratory, The Pennsylvania State University, for the Office of Nuclear Waste Isolation, Battelle Memorial Institute, Columbus, OH.

Roy, D.M., M.W. Grutzeck, and P.H. Licastro, 1979, "Evaluation of Cement Borehole Longevity," ONWI-30, prepared by the Materials Research Laboratory, The Pennsylvania State University, for the Office of Nuclear Waste Isolation, Battelle Memorial Institute, Columbus, OH.

Roy, D.M., M.W. Grutzeck, and L.D. Wakeley, 1983, "Selection and Durability of Seal Materials for a Bedded Salt Repository: Preliminary Studies," ONWI-479, prepared by the Materials Research Laboratory, The Pennsylvania State University, and the Structures Laboratory, U.S. Army Engineer Waterways Experiment Station, for the Office of Nuclear Waste Isolation, Battelle Memorial Institute, Columbus, OH.

Roy, D.M., M.W. Grutzeck, and L.D. Wakeley, 1985, "Salt Repository Seal Materials: A Synopsis of Early Cementitious Materials Development," BMI/ONWI-536, prepared by the Materials Research Laboratory, The Pennsylvania State University, for the Office of Nuclear Waste Isolation, Battelle Memorial Institute, Columbus, OH.

Sager, H. and F.S. Rostasy, 1982, "The Effect of Elevated Temperatures on the Bond Behaviour of Embedded Reinforcing Bars," Bond in Concrete: Proc. of the Interntl. Conf., Paisley, June, P. Bartos, ed., Applied Science Publ., London, pp. 206-216.

Sandor, B.I., 1978, *Strength of Materials*, Prentice-Hall, London.

Scott, R.F., 1981, *Foundation Analysis*, Prentice-Hall, Inc., Englewood Cliffs, N.J.

Smith, D.K., 1976, *Cementing*, Soc. of Petroleum Engineers Monograph Series, Vol. 4, Dallas, 184 pp.

Smith, R.C. and D.G. Calvert, 1980, "The Use of Sea Water in Well Cementing," pp. 89-94, in *Well Completions*, Vol. 1, SPE Reprint Series No. 5a, pub. by Soc. of Petroleum Engineers, Dallas.

Sokolnikoff, I.S., 1956, *Mathematical Theory of Elasticity*, 2nd Ed., Krieger Pub. Co., Malabar, FL.

South, D.L. and J.J.K. Daemen, 1986, "Permeameter Studies of Water Flow Through Cement and Clay Borehole Seals in Granite, Basalt and Tuff," NUREG/CR-4748, prepared for the U.S. Nuclear Regulatory Commission, Office of Nuclear Regulatory Research, Division of Engineering Safety, by the Department of Mining and Geological Engineering, University of Arizona, Tucson.

Stormont, J.C. And J.J.K. Daemen, 1983, "Axial Strength of Cement Plugs in Granite and Basalt," NUREG/CR-3594, prepared for the U.S. Nuclear Regulatory Commission, Office of Nuclear Regulatory Research, Division of Health, Siting and Waste Management, by the Department of Mining and Geological Engineering, University of Arizona, Tucson.

Tadolini, S.C, 1986, "Anchorage Capacities in the Thick Coal Roofs," Bu. Mines, IC 9058, 13 pp.

Timoshenko, S.P., 1956, *Strength of Materials, Part II: Advanced Theory and Problems*, 3rd Ed., D. Van Nostrand Co., Inc., Princeton, NJ.

Timoshenko, S.P. and J.N. Goodier, 1970, *Theory of Elasticity*, 3rd Ed., McGraw-Hill Book Co., New York.

Tomlinson, M.J., 1971, "Some Effects of Pile Driving on Skin Friction," Proc. of ICE Conf., Behavior of Piles, London, pp. 107-114.

Tsur-Lavie, Y. and S.A. Denekamp, 1982, "Size and Shape Effect in Pillar Design," *In Strata Mechanics: Developments in Geotechnical Engineering*, I.W. Farmer, ed., Vol. 32, Elsevier, Amsterdam, pp. 245-248.

U.S. Nuclear Regulatory Commission, 1983, "Disposal of High-Level Radioactive Wastes in Geologic Repositories," Final Rule 10 CFR 60, Federal Register, Vol. 48, No. 120, June 30.

U.S. Nuclear Regulatory Commission, 1985, "Disposal of High-Level Radioactive Wastes in Geologic Repositories," Final Rule, Unsaturated Zone Amendment, Federal Register, Vol. 50, No. 140, pp. 29641-8, July 22.

Van Sambeek, L.L., 1987, "Thermal and Thermomechanical Analyses of WIPP Shaft Seals," RSI-0324, prepared by Sandia National Laboratories, Albuquerque, NM.

Vijayvergiya, V.N. and J.A. Focht, Jr., 1972, "A New Way to Predict Capacity of Piles in Clay, OTC Paper 1718, 4th Offshore Tech. Conf., Houston.

Wakeley, L.D. and D.M. Roy, 1985, "Cementitious Mixtures for Sealing Evaporite and Clastic Rocks in a Radioactive-Waste Repository," Misc. Paper SL-85-16, prepared by the Materials Research Laboratory, The Pennsylvania State University, and the Structures Laboratory, and by the U.S. Army Engineer Waterways Experiment Station, for the Office of Nuclear Waste Isolation, Battelle Memorial Institute, Columbus, OH, and for Sandia National Laboratories, Albuquerque, NM.

Wakeley, L.D. and D.M. Roy, 1986, "Nature of the Interficial Region Between Cementitious Mixtures and Rocks from the Palo Duro Basin and Other Seal Components," BMI/ONWI-580, prepared by the Materials Research Laboratory, The Pennsylvania State University, for the Office of Nuclear Waste Isolation, Battelle Memorial Institute, Columbus, OH.

Wakeley, L.D., D.M. Roy, and M.W. Grutzeck, 1981, "Experimental Studies of Seal Materials for Potential Use in a Los Medanos-Type Bedded Salt Repository," ONWI-325, prepared by the Materials Research Laboratory, The Pennsylvania State University, for the Office of Nuclear Waste Isolation, Battelle Memorial Institute, Columbus, OH.

Wakeley, L.D., D.M. Roy, and M.W. Grutzeck, 1985, "Cementitious Mixtures for Sealing Access Shafts/Boreholes through Evaporite and Clastic Rocks in a Radioactive-Waste Repository," pp. 951-958, Materials Research Soc. Symposia, Procs., Vol. 44, C.M. Jantzen, J.A. Stone and R.C. Ewing, eds., in *Scientific Basis for Nuclear Waste Management VIII*, Materials Research Soc.

Wakeley, L.D. D.M. Walley, and A.D. Buck, 1986 "Development of a Freshwater Grout Subsequent to the Bell Canyon Tests (BCT)," Misc. Paper SL-85-2, prepared by the Structures Laboratory, U.S. Army Engineer Waterways Experiment Station, for Sandia National Laboratories, Albuquerque, NM.

Winograd, I.J., 1986, "Potential Contributions of Archaeology to Evaluation of Thick Unsaturated Zones of Arid Regions for Toxic Waste Disposal," U.S. Geol. Survey Open-File Report 86-0136, Reston, VA.

Yap, L.P. and A.A. Rodger, 1984, "A Study of the Behaviour of Vertical Rock Anchors Using the Finite Elemet Method," Int. J. Rock Mech. Min. Sci. & Geomech. Abstr., Vol. 21, No. 2, pp. 47-61.

Zienkiewicz, O.C., 1977, *The Finite Element Method*, 3rd Ed., McGraw-Hill, London.

Zienkiewicz, O.C., S. Valliappan, C. Dullage, and K.G. Stagg, 1970, "Analysis of Nonlinear Problems in Rock Mechanics with Particular Reference to Jointed Rock Systems," Proc., 2nd Congress, Intl. Soc. for Rock Mech., Belgrade, 3.

APPENDIX A

SHEAR STRESS DISTRIBUTION ALONG AN AXIALLY LOADED RIGID PLUG

The shear stress distribution along an elastic plug in an elastic medium is given by Eq. (2.48):

$$\frac{\tau_{rz,i}}{\sigma_{po}} = \frac{\alpha a}{2} \frac{\cosh[\alpha(L-z)]}{\sinh(\alpha L)} \qquad (A.1)$$

where

$$\alpha = \left[\frac{1-2\nu_p(VSF)}{(E_p/E_R)(1+\nu_R)a^2 \ln(r_m/a)} \right]^{1/2}$$

σ_{po} = axial stress applied to the plug
L = plug length
z = distance from initial location of loaded end of plug
a = plug radius
r_m = critical radius
R = rock cylinder radius
E_R = Young's modulus of rock
ν_R = Poisson's ratio of rock
E_p = Young's modulus of plug
ν_p = Poisson's ratio of plug

VSF =

$$\frac{\nu_p(1-(a/R)^2)}{(1-\nu_p)(1-(a/R)^2)+(E_p/E_R)(1+\nu_R)[(1-2\nu_R)(a/R)^2+1]}$$

for a plane strain configuration.

The limiting case for a rigid plug in an elastic medium can be calculated by taking the limit of Eq. (A.1) when the Young's modulus (E_p) of the plug tends to infinity. This leads to 0/0 as lim α = 0 and lim VSF = 0. Applying L'Hospital's rule to Eq. (A.1) when α tends to zero yields:

$$\lim_{\alpha\to 0}\frac{\tau_{rz,i}}{\sigma_{po}} = \lim_{\alpha\to 0}\frac{\alpha a}{2\sinh(\alpha L)} \quad \lim_{\alpha\to 0}\cosh[\alpha(L-z)]$$

$$= \lim_{\alpha\to 0}\frac{\alpha a}{2\sinh(\alpha L)}$$

$$= \frac{\frac{d}{d\alpha}\alpha a}{\frac{d}{d\alpha}2\sinh(\alpha L)}$$

$$= \frac{a}{2[\cosh(\alpha L)]L}$$

$$\frac{\tau_{rz,i}^{av}}{\sigma_{po}} = \frac{a}{2L} \qquad (A.2)$$

This result is identical to Eq. (2.115).

APPENDIX B

FINITE ELEMENT MESHES AND STRESS DISTRIBUTIONS

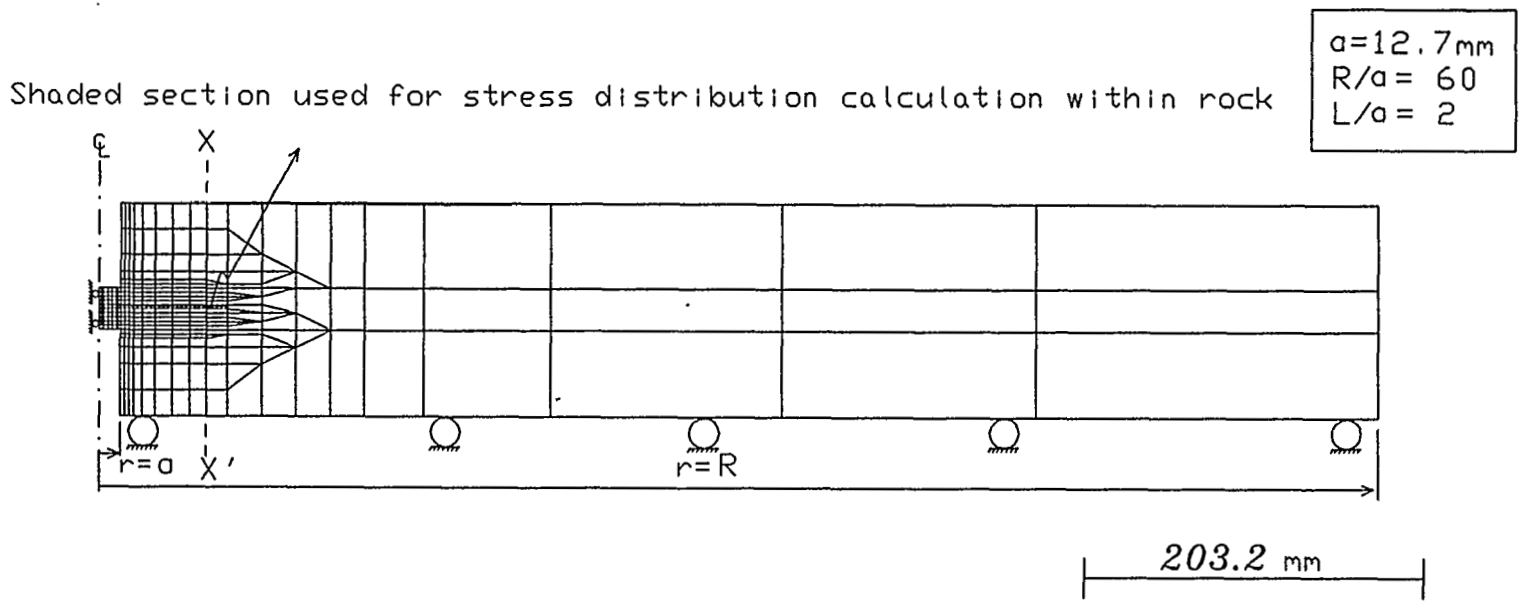

Figure B.1 Finite element mesh and boundary conditions for a push-out specimen with a plug radius of 12.7 mm, cylinder length of 127 mm, cylinder outside-to-inside radius ratio of 60, and plug length-to-radius ratio of 2. The mesh consists of 313 elements and 342 nodal points. An enlargement of a portion of the mesh, from center line to section XX', is given in Figure 3.1 (Chapter 3).

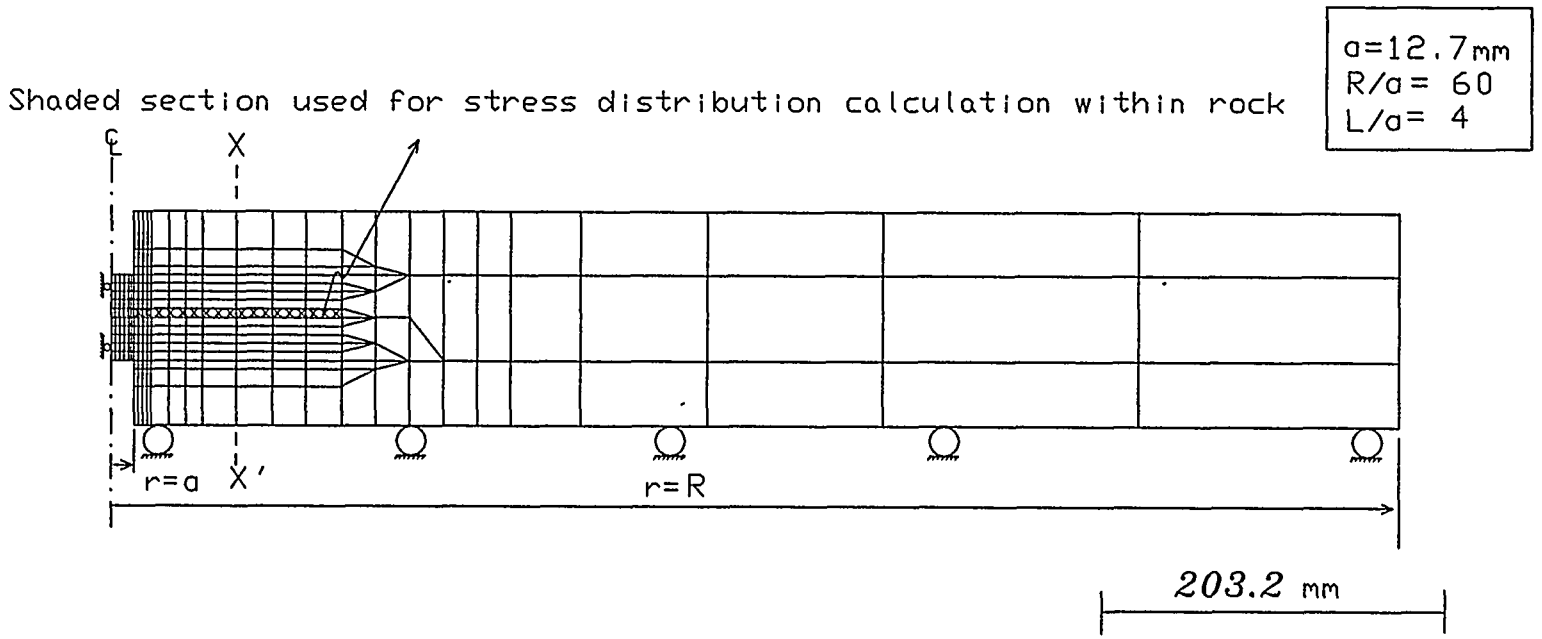

Figure B.2 Finite element mesh and boundary conditions for a push-out specimen with a plug radius of 12.7 mm, cylinder length of 127 mm, cylinder outside-to-inside radius ratio of 60, and plug length-to-radius ratio of 4. The mesh consists of 298 elements and 329 nodal points.

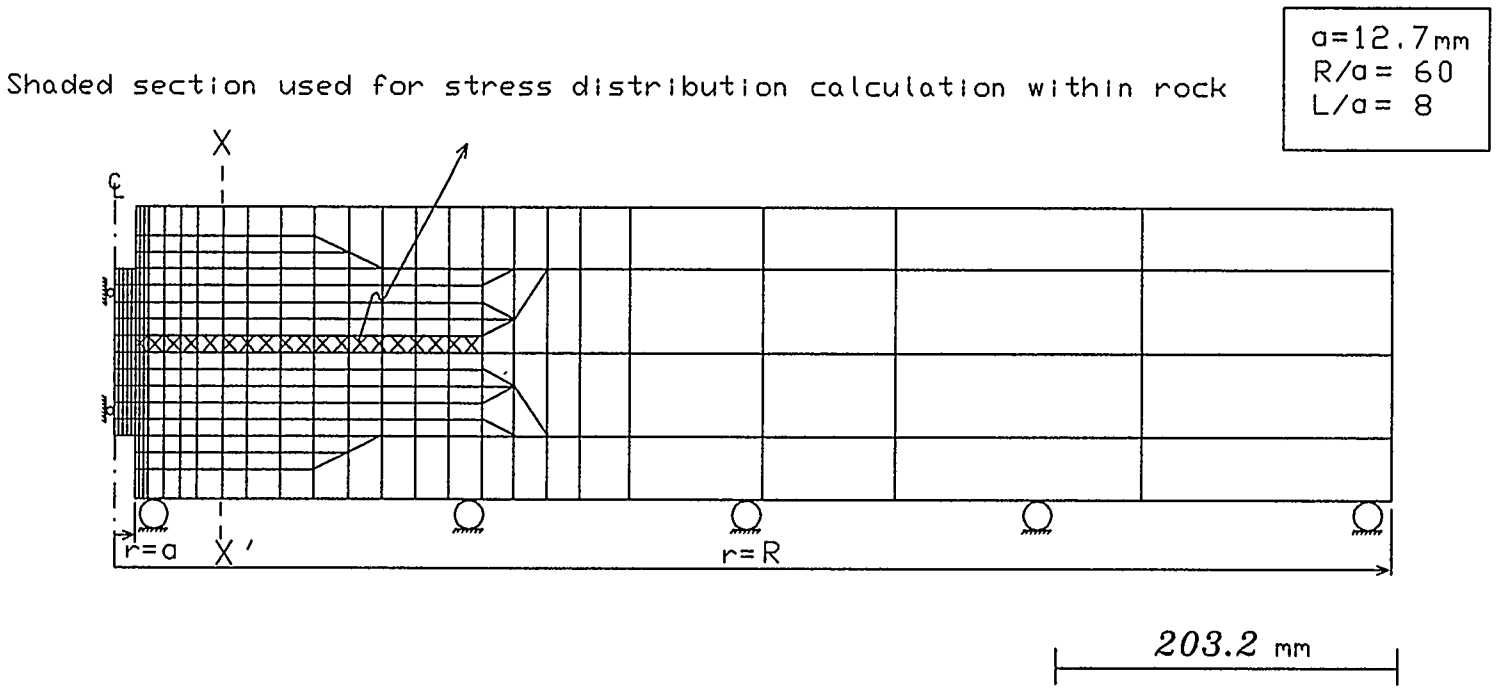

Figure B.3 Finite element mesh and boundary conditions for a push-out specimen with a plug radius of 12.7 mm, cylinder length of 177.8 mm, cylinder outside-to-inside radius ratio of 60, and plug length-to-radius ratio of 8. The mesh consists of 318 elements and 351 nodal points.

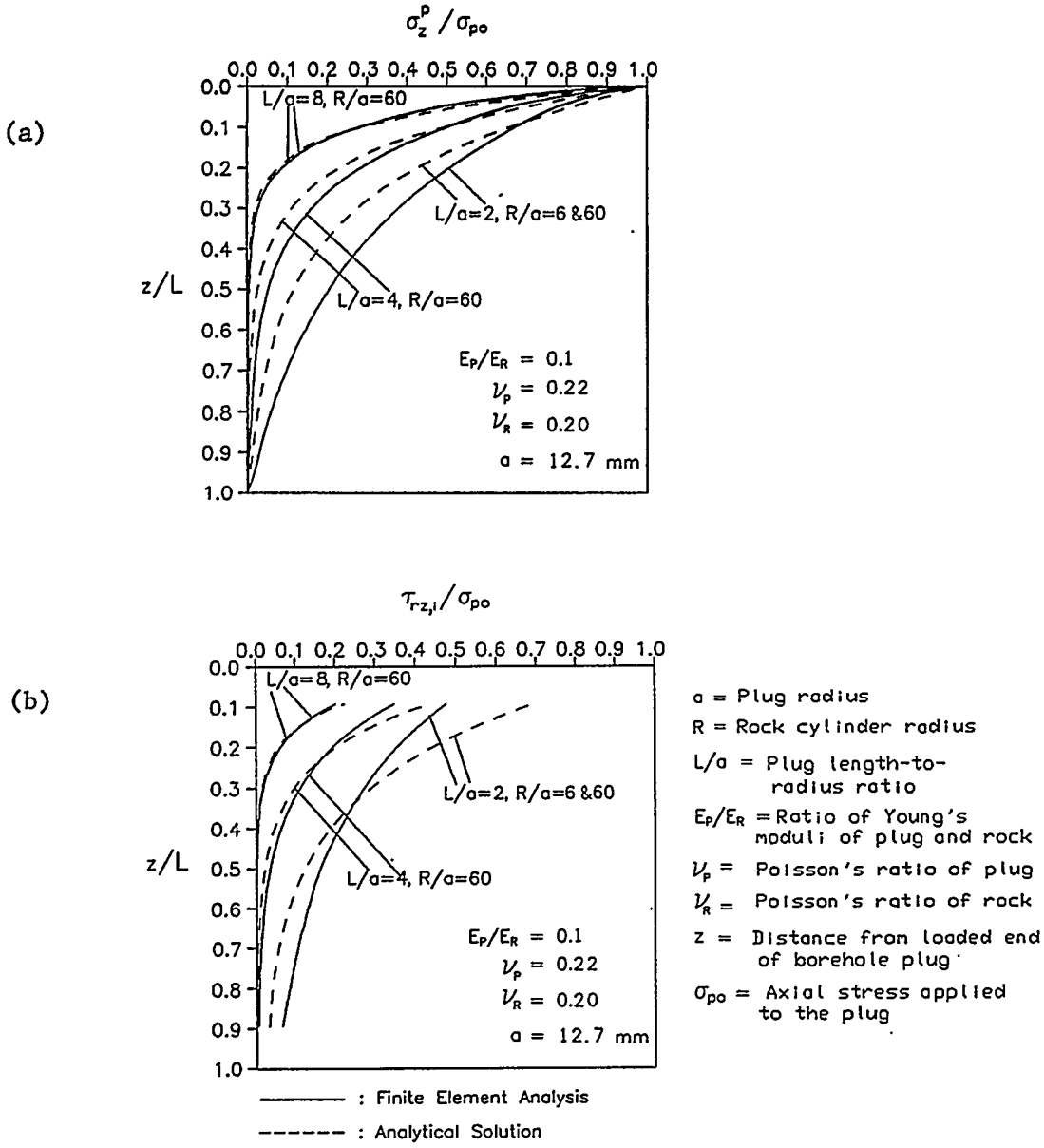

Figure B.4 (a) Axial stress distribution along a plug (σ_z^p/σ_{po}), and (b) shear stress distribution along the plug/rock interface ($\tau_{rz,i}/\sigma_{po}$) for a modulus ratio (E_p/E_R) of 0.1.

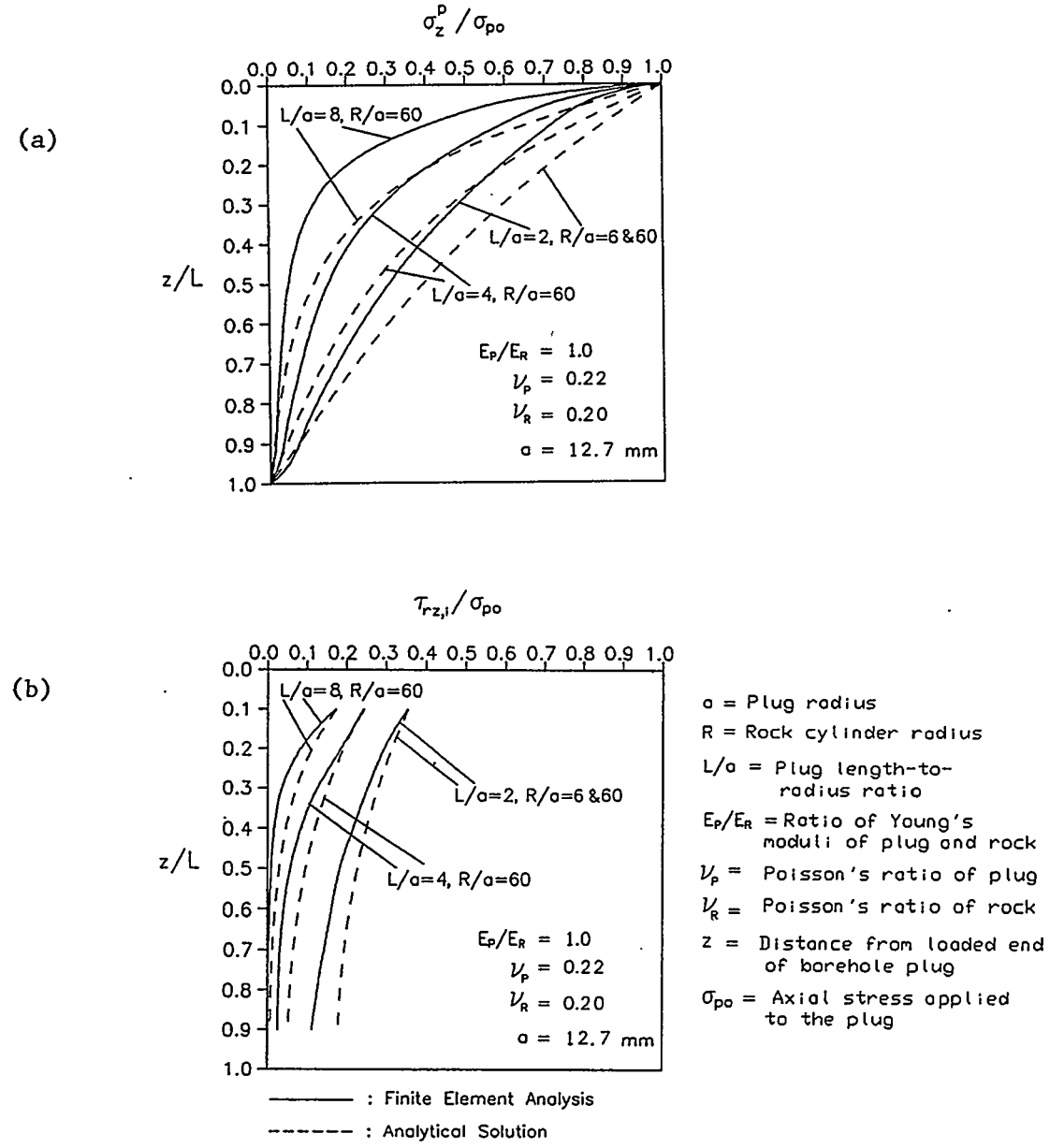

Figure B.5 (a) Axial stress distribution along a plug (σ_z^p/σ_{po}), and (b) shear stress distribution along the plug/rock interface ($\tau_{rz,i}/\sigma_{po}$) for a modulus ratio (E_p/E_R) of 1.0.

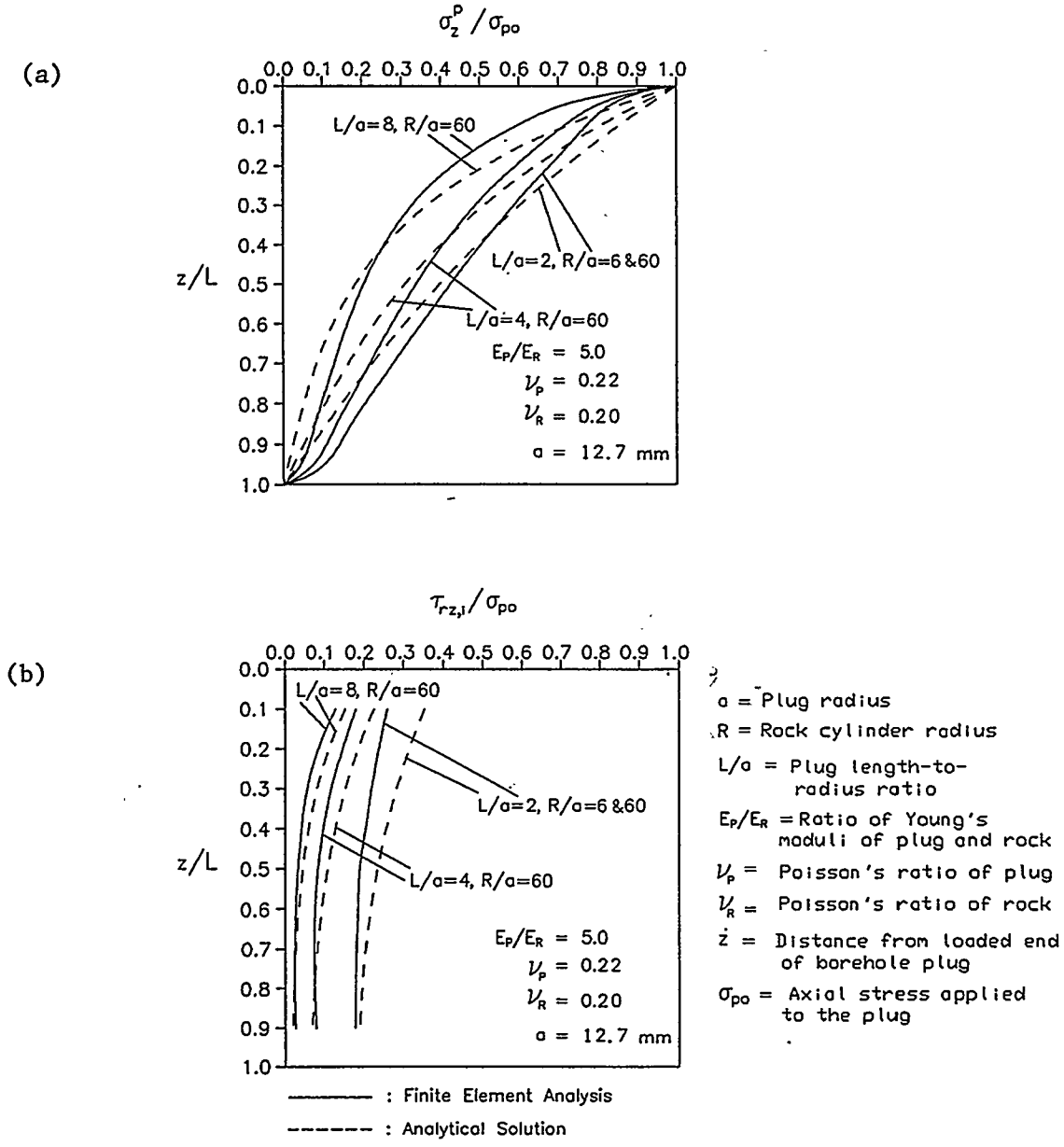

Figure B.6 (a) Axial stress distribution along a plug (σ_z^p/σ_{po}), and (b) shear stress distribution along the plug/rock interface ($\tau_{rz,i}/\sigma_{po}$) for a modulus ratio (E_p/E_R) of 5.0.

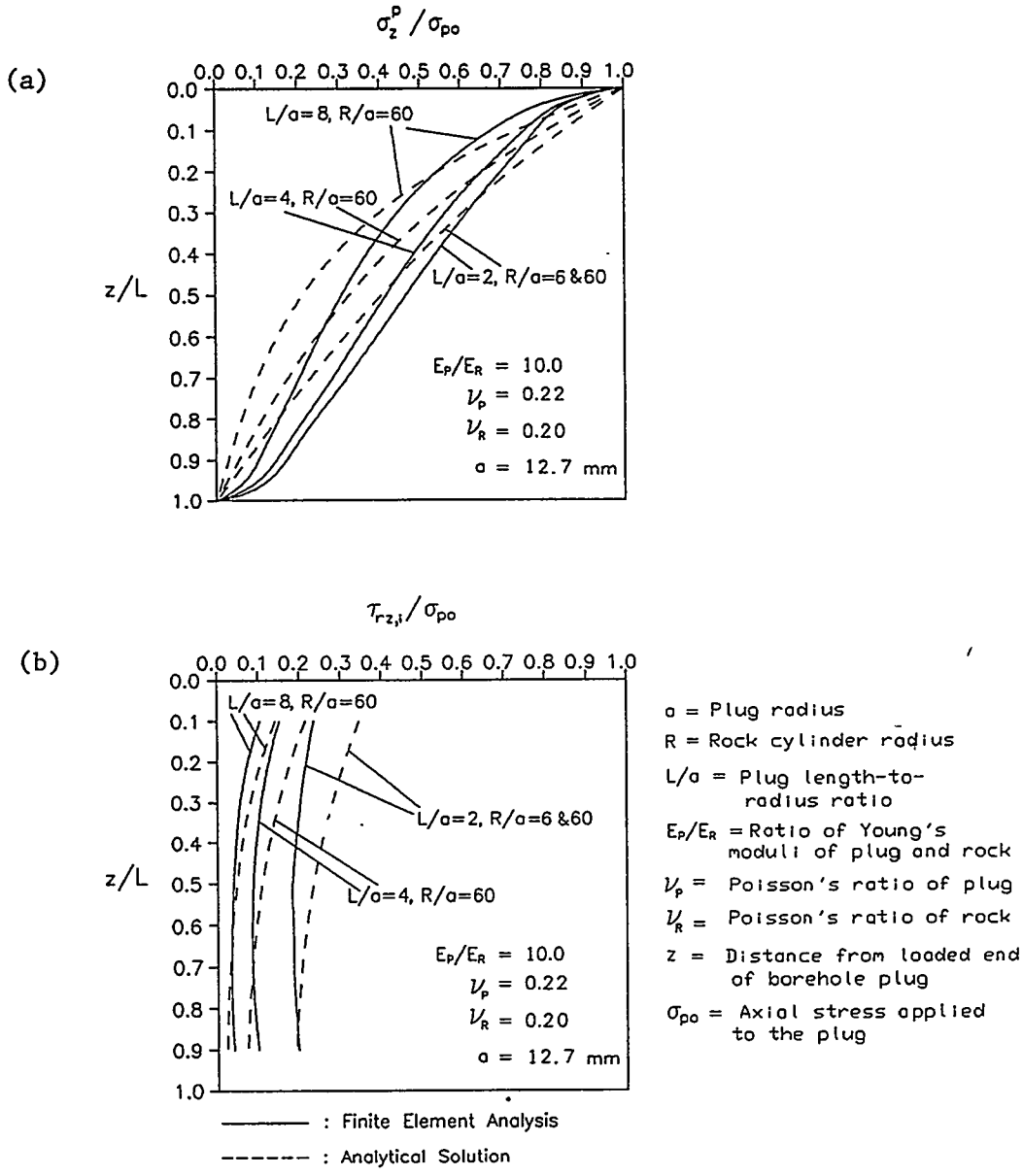

Figure B.7 (a) Axial stress distribution along a plug (σ_z^p/σ_{po}), and (b) shear stress distribution along the plug/rock interface ($\tau_{rz,i}/\sigma_{po}$) for a modulus ratio (E_p/E_R) of 10.0.

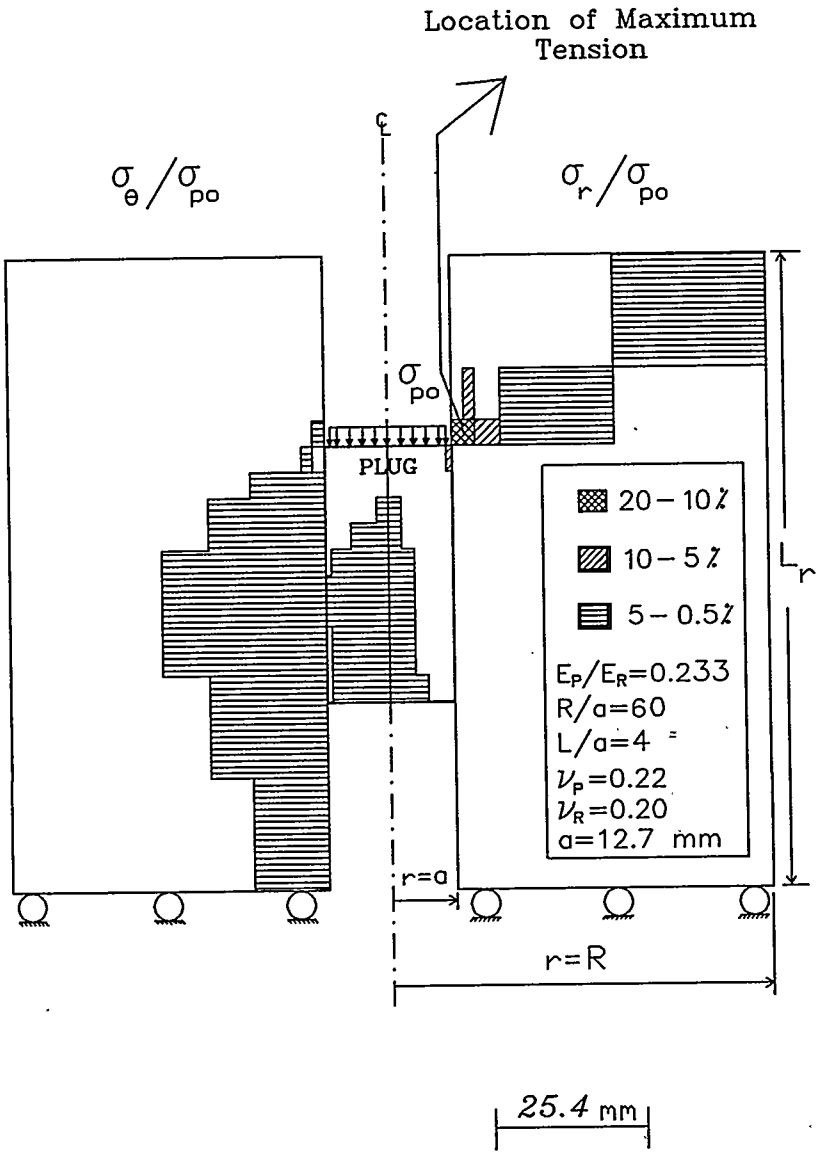

Figure B.8 Percentage normalized tensile radial stress (σ_r/σ_{po}; right) and tensile tangential stress ($\sigma_\theta/\sigma_{po}$; left) contours for an axially loaded borehole plug in rock. Modulus ratio of 0.233 and plug length-to-radius ratio of 4. A portion of the mesh, from centerline to Section XX', is given in Figure B.2.

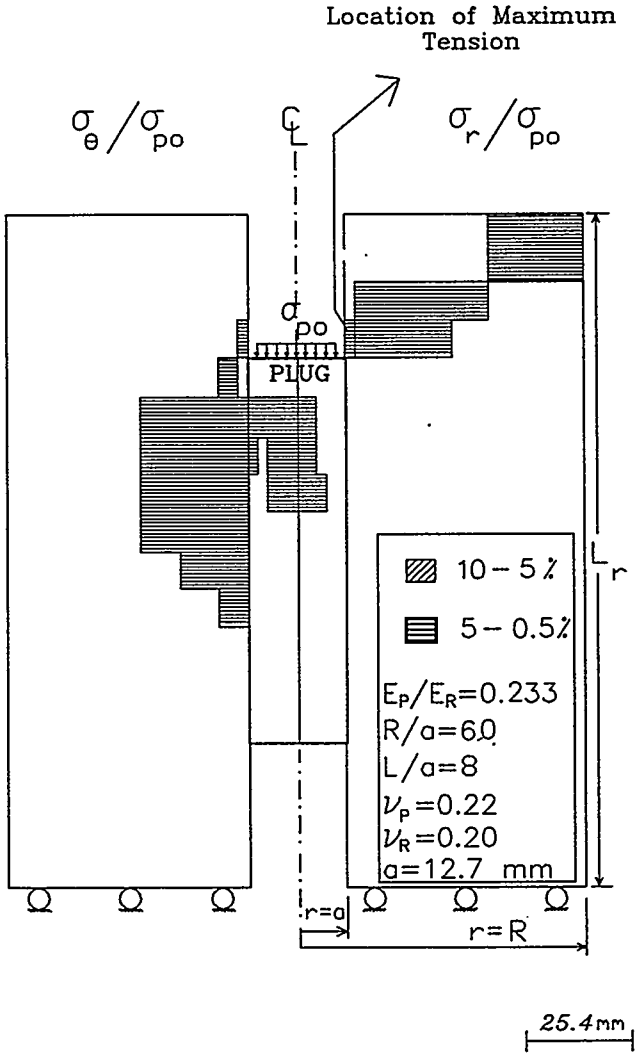

Figure B.9 Percentage normalized tensile radial stress (σ_r/σ_{po}; right) and tensile tangential stress ($\sigma_\theta/\sigma_{po}$; left) contours for an axially loaded borehole plug in rock. Modulus ratio of 0.233 and plug length-to-radius ratio of 8. A portion of the mesh, from centerline to Section XX', is given in Figure B.3.

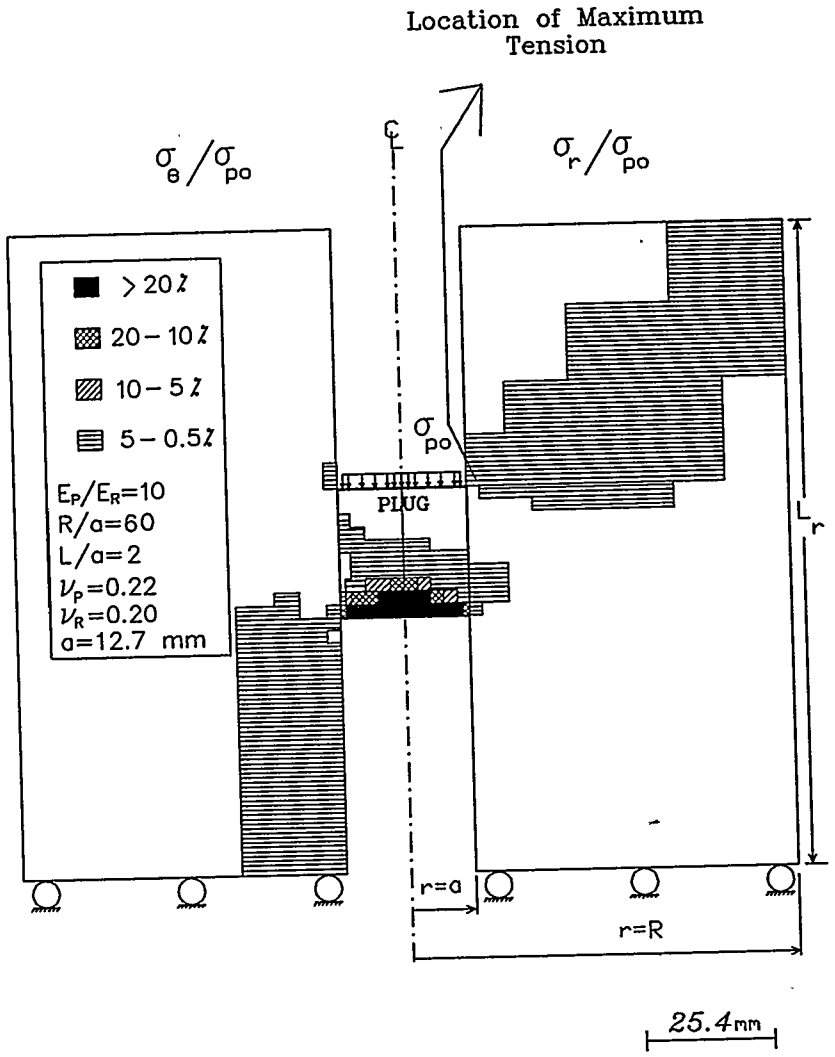

Figure B.10 Percentage normalized tensile radial stress (σ_r/σ_{po}; right) and tensile tangential stress ($\sigma_\theta/\sigma_{po}$; left) contours for an axially loaded borehole plug in rock. Modulus ratio of 10 and plug length-to-radius ratio of 2. A portion of the mesh, from centerline to Section XX', is given in Figure B.1.

APPENDIX C

PROCEDURE FOR PREPARING SELF-STRESS II (SSII) CEMENT BOREHOLE PLUGS

C.1 Introduction

The cement mixing for the borehole plugs is performed according to the API Specification No. 10 (American Petroleum Institute, 1986, pp. 14-19). The type of cement used (provided by Dowell Schlumberger) is Ideal Type I/II cement, and will be referred to as Self-Stress II.

Self-Stress II cement is composed of Ideal Type I/II Portland cement (from Tijeras Canyon, New Mexico), mixed with 50% distilled water, 10% D53 (an expansive agent), and 1% D65 (a dispersant). All percentages are weight percent with respect to cement.

Mix preparation parameters involved in cement plug performance are: 1) cement mixing time and temperature, 2) cement viscosity, 3) time between cement mixing and pouring, 4) cement weight/volume control, and 5) curing conditions (i.e. moisture protection on cement, ambient temperature, relative room humidity, curing period and atmospheric pressure).

C.2 Apparatus

1) Plastic scoop, spatula
2) Ohaus heavy-duty solution balance (capacity of 20 kg (45 lb), readable to 1 g)
3) Waring Blendor (Model 31BL42) (7-speed); the mixing container has a volume of 1182.8 ml (0.3125 U.S. gal).
4) Fann 35A/SR 12 Viscometer (Part No. 30166).
5) Rubber stopper
6) Funnel and plastic tube
7) Silicone grease
8) Digital thermometer (Omega type JTC, Omega Engineering Co., Stamford, Connecticut).
9) Cement stirrer (Model R-4554-00 manufactured by Cole Parmer, Inc.) with a speed range of 300-5000 rpm
10) Nalgene tank (7 U.S. gallon capacity)
11) Hydrometer (Cole Parmer Model J-8291-50) with a specific gravity range from 1.000 to 2.000.

C.3 Procedure for Preparing Self-Stress II Cement Borehole Plugs

1. Prepare the cement slurry at an ambient room temperature of 27 ± 6°C (80 ± 10°F) (API, 1986) and a relative room humidity not less than 50% (ASTM, C305-82, Section 4). Make certain that the temperature of water prior to mixing is 27 ± 3°C (80 ● 5°F). Record the room temperature, relative humidity and atmospheric pressure. If the room temperature falls outside the above range, bring cement and mix water to the desired temperature in a water bath.

2. Weigh 333 g of cement and 150 g of distilled water. Pour the distilled water into the mixing container. Add the cement to the water in not more than 15 seconds (while the mixer speed is on 2). After all the cement is added, mix at speed 6 for an additional 35 seconds.[1] During this mixing, scrape down any paste that collects on the sides of the mixing container with a spatula.

3. Place a rubber stopper into the inner borehole of the tuff sample at the level where a cement plug is to be located. Pour the cement slurry onto the rubber stopper with minimum time lag (i.e. in less than 30 seconds), yet sufficiently slow to avoid violent turbulence. Pour cement through a funnel and plastic tube (Figure C.1). Submerge the bottom end of the plastic tube in the slurry. Raise the funnel and tube as the cement slurry level increases. Minimize turbulence as much as possible during pouring. Stop pouring when the desired plug length is obtained. Measure and write down pouring time. Pour a thin layer of water on top of the cement plug 15 minutes after cement mixing (in order to prevent cement drying). Record the volume of water poured. Place the cement plugs in tuff samples under water or in the environmental chamber 1 hour after cement mixing.

4. Make certain that the sample cup of the Fann 35A/SR12 Viscometer is in the room for a sufficient time to maintain a steady temperature (± 2°C, ± 5°F). Immediately pour the rest of the cement slurry into the

---

1 ASTM C305-82 (Section 4) differs from API Specification No. 10, 1986 (with respect to mixing cement) in the following regards: 1) Pour the distilled water into the mixing container, 2) add the cement to the water and allow 30 seconds for the absorption of water, 3) start the mixer and mix at slow speed (140 ± 5 rpm) for 30 seconds, 4) stop the mixer for 15 seconds, and during this time scrape down into the batch any paste that may have collected on the sides of the bowl, and 5) start the mixer at medium speed (280 ± 10 rpm) and mix for 1 minute.

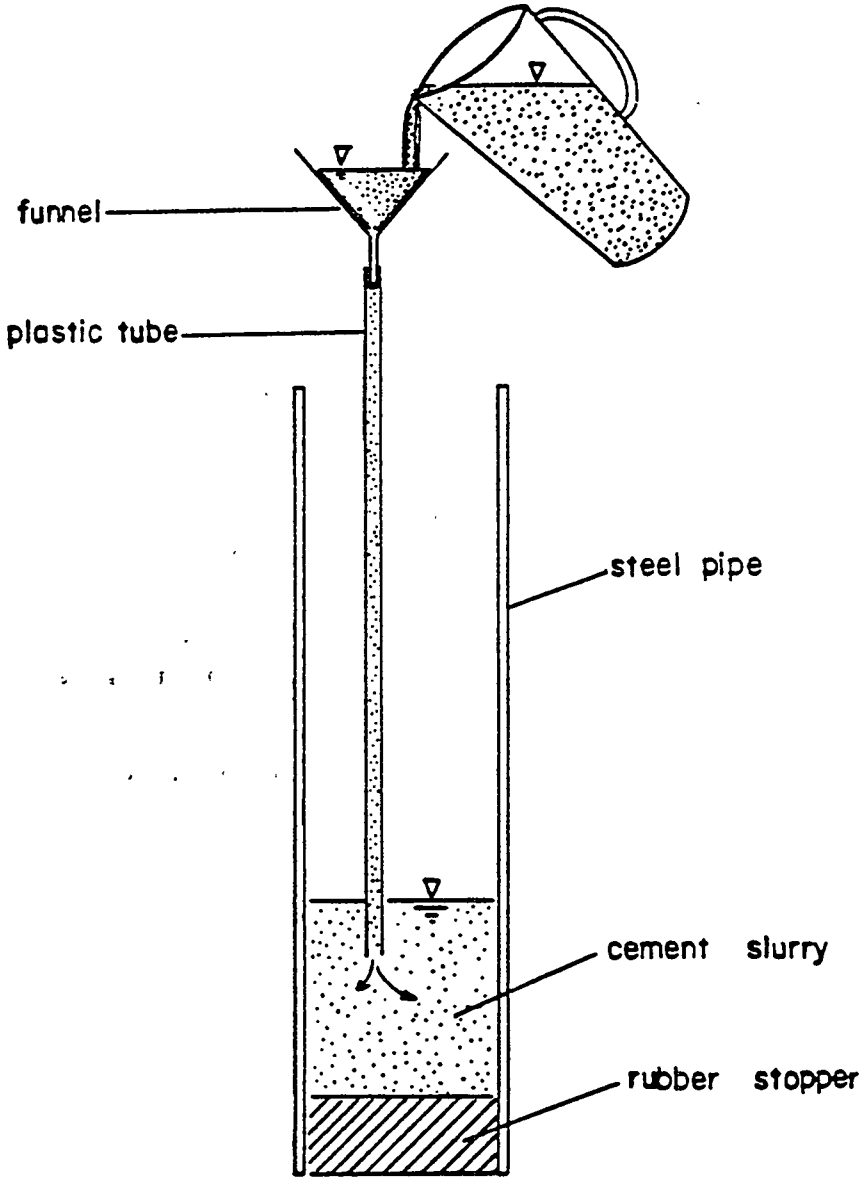

Figure C.1 Installation of cement plug. Cement slurry is poured into the steel pipe or rock cylinder using funnel and plastic tube to minimize turbulence and trapped air voids.

Viscometer sample cup.[2] Stir the cement slurry with the cement stirrer (Model R-4554-00) at speed 1.5 (approximately 300 rpm) for 20 minutes.[3]

5. Place the sample cup in the Fann 35A/SR12 Viscometer for determination of the cement rheological properties. With the rotor not turning, raise the cup until the liquid level is at the inscribed line on the sleeve. Perform this operation as quickly as possible. Immediately take instrument readings in descending order. Do not rotate the instrument at 600 rpm, either to take a reading or at any time. Such high speed rotation causes centrifugation and erroneous results.

6. Immediately before taking the readings, record the temperature (T_1) of the slurry in the viscometer cup. Take the initial reading at 300 rpm, 60 seconds after continuous rotation at that speed. Record dial readings at 200, 100, 6 and 3 rpm in descending order. Shift the rotor speed to the succeeding lower speed at 20 second intervals. Take each dial reading just before shifting to the next lower speed. Record the slurry temperature (T_2) at the end of this portion of the test. Report the slurry rheological properties at the average of the temperatures T_1 and T_2.

7. Clean the plastic scoop, balance, mixing container, viscometer cup, funnel, plastic tube and cement stirrer thoroughly with distilled water.

8. Cure the cement plugs in tuff specimens under water or in the environmental chamber for 8 days,[4] prior to initiating testing. Appendix D, Section D.3, describes the curing conditions (i.e. curing temperature ranges, degree of saturation). Record the total volume of water poured on cement plugs during curing, for partially saturated and for relatively dry samples.

---

2 Procedure deviates from API, 1986, due to the lack of an atmospheric consistometer.

3 Personal communication with Mr. P. Parcevaux, Dowell-Schlumberger, October 1987. Procedure deviates from API, 1986, which requires stirring of the cement slurry in an atmospheric consistometer for 20 minutes.

4 Procedure deviates from API Spec. No. 10 (1986, p. 18) which requires an 8 hour curing period for Class G cement prior to testing.

APPENDIX D

PUSH-OUT TEST PROCEDURE

D.1 Sample Preparation Procedure

The objective of this procedure is to prepare cylindrical push-out test specimens with 25.4 mm (1 in), 50.8 mm (2 in) and 101.6 mm (4 in) diameter holes perpendicular to the bottom sample surfaces.

(1) Core 76.2 mm (3 in), 152.4 mm (6 in), or 187.3 mm (7.375 in) diameter cylinders from welded tuff blocks. Sketch the tuff block in a laboratory notebook. Write down the tuff block number, core number and source location. Mark the top and bottom of the cylinders (the direction of coring is towards the bottom of the cylindrical samples). Cut the cylinders with a diamond saw to a length between 101.6 mm (4 in) and 177.8 mm (7 in). Number the cut cylinders, starting from the top towards the bottom of the core. Mark the top and bottom of the cut cylinders.

(2) Place each cylinder, with the bottom surface up, on the drill table. Clamp the "center locator"[1] onto the bottom surface of each cut cylindrical sample. Check the horizontality of the clamped bottom surface every 90° by means of a level (from the center towards the outside surface). If the bottom sample surface is not horizontal, shim the interface between the sample bottom and drill table until horizontal. Core a 12.7 mm (0.5 in) or 25.4 mm (1 in) or 50.8 mm (2 in) or 101.6 mm (4 in) central hole along the axis of each cylinder.[2]

---

1 Center locator is a square steel plate (203.2 x 203.2 x 12.7 mm (8 x 8 x 0.5 in)) with an adjustable central hole of 12.7 mm (0.5 in), 25.4 mm (1 in), 50.8 mm (2 in) and 101.6 mm (4 in) in diameter. It helps in drilling concentric (axial) holes through cylindrical samples.

2 A 12.7 mm (0.5 in) diameter central hole is cored in push-out samples with an outside diameter (OD) of 76.2 mm (3 in). A 25.4 mm (1 in) or 50.8 mm (2 in) diameter central hole is cored in push-out samples with an outside diameter (OD) of 152.4 mm (6 in). 101.6 mm (4 in) diameter central holes are cored in samples with a 187.3 mm (7.375 in) OD.

The specimen bottom end should not depart more than 0.25 degree from perpendicularity to the central hole. Measure the perpendicularity with a straight-edge.[3]

(3) Place the push-out samples in the oven. Keep the samples in the oven for a week at 100-105°C; remove and let cool for approximately 4 hours. For low saturated, intermediately saturated and highly saturated sample preparation, go to step (4). Prepare the presaturated samples by isolating the coaxial holes with packers and injecting water through one of the packers. Use a water injection pressure of 0.35 MPa (50 psi) after submerging the samples in water. Weigh the samples every day until the desired degree of saturation is obtained. The total weight of the samples (W_T) can be calculated as a function of the desired degree of saturation (S) as follows:

$$W_T = W_s[1 - (S/G_s)] + S\gamma_w V_T \qquad (D.1)$$

where W_s = weight of the dry tuff solids (weight of the push-out sample after it has been taken out of the oven)
G_s = specific gravity of tuff solids
V_T = total volume of the tuff core.

Calculate the total weight of water (W_w) in the sample as:

$$W_w = W_T - W_s \qquad (D.2)$$

Equation (D.1) gives the total weight of the tuff core (W_T) required to obtain the desired degree of saturation (S = 40, 60, 80 or 100%). For a degree of saturation of 100% (fully saturated specimen), equation (D.1) leads to:

$$W_T = (W_s/G_s)(G_s - 1) + \gamma_w V_T \qquad (D.3)$$

The degree of saturation (S) of the tuff samples can be calculated as:

$$S = \frac{G_s W_w}{(V_T \gamma_s - W_s)} \qquad (D.4)$$

---

3 Deviates from the ASTM standard (D2938-79, Section 4) for preparing samples for uniaxial compressive strength testing. This standard requires that the sample ends shall be ground flat to 0.025 mm (0.001 in) and shall not depart from perpendicularity to the axis of the specimen by more than 0.025 degree [approximately 0.25 mm (0.01 in) in 51 mm (2 in)].

Weigh the tuff samples every day and put them back into the saturation tank. Record the total weight (W_T) and calculate S from Eq. (D.4). When the desired degree of saturation (S) is reached, take the samples out of the saturation tank and go to the next step.

(4) Place a rubber stopper into the borehole at a level where a centered cement plug is to be located. Pour the Self-Stress II cement slurry onto the rubber stopper with minimum time lag (i.e. in less than 30 seconds), yet sufficiently slow and through a funnel and plastic tube to avoid violent turbulence. Appendix C gives the procedure for preparing Self-Stress II (SS II) cement borehole plugs. Stop pouring when the desired plug length is obtained. Measure and write down pouring time. Pour a thin film of water on top of the cement plugs 15 minutes after pouring the cement. Record the volume of water poured. Place the push-out specimens into the environmental chamber or underwater one hour after cement pouring.

(5)(a) Cure the cement plugs of the highly saturated and presaturated push-out specimens under water at the desired temperature for 8 days. Two stainless steel (SS 304) water tanks are available for preparing highly saturated samples. The first cylindrical water tank has a diameter and length of 317.5 mm (12.5 in). It holds four push-out cores 152.4 mm (6 in) in diameter and 101.6 mm (4 in) in length. The water is heated by means of a Cole Parmer water circulator (Model 1253-00 with a temperature range of 20°C to 104°C). The second water tank has dimensions (L x D x W) of 711.2 x 508 x 406.4 mm (28 x 20 x 16 in) and holds up to 6 push-out specimens. Its heating unit includes six heating elements (four actives and two spares), a temperature controller and a centrifugal pump. The temperature controller is constructed by the University of Arizona Electronics Shop. A special feature of the apparatus is the control on the rate of heating needed, 1°C/minute, up to 125°C. The temperature of the water is controlled by a temperature probe (LM 235A, manufactured by National Semiconductor, Inc.) connected to the heater controller. Four heating elements heat the water in the lower part of the tank. As hot water convects upward, the exhaust port of the electrical pump (centrifugal) redirects it to the bottom of the tank where the pumped water is reheated. Twelve thermocouple probes (Type J, Omega Engineering, Inc.) sense the temperatures at various locations in the water tank.

(b) Cure the cement plugs of the intermediately saturated push-out samples in an environmental chamber at desired temperature, airflow and 80% relative humidity (rh) for 8 days. The environmental chamber, manufactured by American Scientific Products (Type J1685-1) controls humidity from 20-98% and temperature from room temperature to 77°C. The desired condition is reached within 20 minutes. The unit's airflow can be adjusted from 0 to 150 cfm. An inverted Pyrex glass jar forms a 406.4 mm (16 in) diameter x 355.6 mm (14 in) height visible chamber for storing 4 push-out specimens.

(c) Cure the cement plugs of the low saturated push-out samples in the environmental chamber at the desired temperature, airflow and 45% relative humidity (the lower limit of the environmental chamber) for 8 days.

(d) Use curing temperatures of ambient (24 + 2°C), 44 to 45°C, 65 to 70°C, or 90°C for highly saturated samples (curing temperatures of 90 C can not be used for intermediately or low saturated samples, as the temperature of the environmental chamber can only be taken up to a maximum of 77°C).

(6) Number the push-out specimens as follows:

AP3	-	3	- 1/2	-	AMB	-	FS	- 1	- PO2	- SSII
		6	1		45°C		PS			
		8	2		70°C		RD			
			4		90°C		FSS			

The first column refers to the type of tuff and to the tuff block number (i.e. AP3: Apache Leap tuff - block number 3. The second and third columns give the outside diameters and inside diameters in inches, respectively. The fourth and fifth columns give the curing and test temperatures (i.e. ambient, 45°C, 70°C or 90°C) and specimen saturation condition (i.e. FS: highly saturated; PS: intermediately saturated; RD: low saturated; FSS: presaturated), respectively. The sixth, seventh and last columns refer to the core number, sample number and type of cement used (SSII: Self-Stress II cement), respectively.

(7) On the seventh day of cement curing, grind the top end of the cement plug with a blind bit. Put the sample back into its curing environment. The next day, remove the rubber stopper from the bottom end of the cement plug. Drill a 1.27 mm (0.05 in) diameter and a 2.54 mm (0.1 in) long central hole into the cement from its bottom end. Screw the bottom vertical bar (using a plastic anchor to increase rigidity) into this hole (Figures 4.1 and 4.2 (Ch. 4) give the push-out test set-up). Install a linear variable differential transformer (LVDT) and a dial gage on the horizontal arm of the bottom vertical bar to measure the bottom cement plug displacement during push-out testing.

D.2 Experimental Apparatus and Sample Loading

An HP data acquisition system (HP-3497A) is used to record the applied load, cement plug top and bottom axial displacement, and ambient room temperature. Two dial gages are used to measure the top and bottom cement plug displacements manually, thus providing a check on the automatically recorded data.

The top and bottom displacements of the borehole plug are measured with two LVDT's (manufactured by Schaevitz Engineering) (Figures 4.1 and 4.2 (Ch. 4)). These produce an electrical output differential voltage proportional to the displacement of a separate movable core. They have a resolution of a thousandth of an inch (0.0254 mm). The linearity, a measure of instrument error, is about 0.25% of the full range of ± 25.4 mm (1 in). Axial load is measured with a Terrametrics compression load cell with a capacity of 44,480 N (10,000 lbf) (Figures 4.1 and 4.2). Combined instrument error (nonlinearity and hysteresis) is 2 to 7%[4] of the full range. The top plug displacement is measured manually with a Starrett dial gage with a resolution of 0.0254 mm (0.001 in) and with a total travel of 50.8 mm (2 in). The bottom plug displacement is measured manually with a SoilTest dial gage with a similar resolution and total travel. A SoilTest compression machine with a dial indicator applies the load. The machine has a capacity of 266,860 N (60,000 lbf) with a resolution of 445 N (100 lbf).

The push-out test heating unit consists of a heater controller, heating tape, thermocouples at the top and at the bottom of the cement plug and a digital thermometer (Figures 4.1 and 4.2).

The heater controller probe (LM 235A, manufactured by National Semiconductor, Inc.) is attached to the top of the push-out specimen (about 12.7 mm (0.5 in) inside from the outside of the sample) in order to keep the sample at constant temperature. The liquid crystal display (LCD) on the heater controller provides an easy control for setting and maintaining desired constant temperatures up to 125°C. The specimen is heated by wrapping a grounded heating tape (Part No. H1890-8, manufactured by Electrothermal, Inc.) around it. The heating tape is connected to the heater controller for applying controlled heat to the push-out sample. Because the heating tape can only be applied to metallic surfaces, a steel pipe is placed loosely between the push-out specimen and heating tape. During push-out testing, the temperature at the top and at the bottom of the cement plug is monitored through thermocouple sensors (Type J, manufactured by Omega Engineering, Inc.). The thermocouple sensors are connected to a digital thermometer (Type JTC, manufactured by Omega Engineering, Inc.) for temperature readout.

For the push-out experiments, center a cylindrical steel plate with a 304.8 mm (12 in) diameter and a 12.7 mm (0.5 in) thickness on the bottom bearing plate of the SoilTest compression machine (Figures 4.1 and 4.2). The plate has six equally spaced holes 9.53 mm (0.375 in) in diameter, each located 25.4 mm (1 in) from the circumference. Three steel rods, 7.94 mm (0.3125 in) in diameter and 508 mm (20 in) in length, threaded up to 127 mm (5 in) on one end are bolted vertically to three neighboring holes of the plate. They are also clamped to each other to increase stability. Four horizontal arms are clamped to the vertical steel rods.

---

4 Procedure deviates from ASTM D1143-81, Section 4, p. 241, which requires an instrument error less than 2% of the applied load.

The bottom LVDT and dial gage for measuring the bottom plug displacement are clamped to the two lower-most horizontal arms. The upper horizontal arms (machined flat on their upper surfaces) support the top LVDT and dial gage which measure the top plug displacement. A circular steel platen with an outside diameter of 152.4 mm (6 in), a central hole with diameter of 50.8 mm (2 in), and a thickness of 50.8 mm (2 in) is centered on the 304.8 mm (12 in) diameter bottom plate. The platen has a 25.4 mm (1 in) wide slit on one side to allow the downward movement of the horizontal arm of the bottom displacement monitoring rod. The horizontal arm is machined flat on the upper surface to support the bottom LVDT and dial gage. A 12.7 mm (0.5 in) thick, 203.2 mm (8 in) square platen with a central hole with a diameter of 50.8 mm (2 in) is centered on the circular steel platen with a slit.

A tuff cylinder with a centered borehole plug or rock bridge is placed centrally on the square steel platen (Figures 4.1 and 4.2 (Ch. 4)). A steel disc 6.35 mm (0.25 in) thick, and 12.0 mm (0.47 in), 24.1 mm (0.95 in), or 48.3 mm (1.90 in) or 99.1 mm (3.90 in) in diameter, depending on the plug diameter, is centered on top of the cement plug (with care taken so that it does not touch the inner borehole, in order to prevent friction). A cylindrical steel rod 127 mm (5 in) in length, and 20.32 mm (0.8 in), or 41.66 mm (1.64 in) or 85.60 mm (3.37 in) in diameter, depending on the hole diameter, centered on the thinner disc, transmits the load to the plug in push-out experiments. The reason for placing a relatively larger diameter and thinner steel disc in between the loading rod and the plug is to distribute the load uniformly on the plug and to prevent as much as possible any friction between the steel and the borehole sidewalls.

Two circular jackets with horizontal arms are clamped around the loading rod to install the top LVDT and top dial gage (Figures 4.1 and 4.2 (Ch. 4)). The applied load is measured by the load cell in between the cylindrical axial bar and the loading platen.

D.3 Testing Procedure

(1) Turn on the SoilTest compression machine and HP-3497A. Let them warm up for at least one hour.

(2) Calibrate the load cell at loads of 0, 8896, 17,792, 26,688, 35, 584, and 44,480 N (0, 2000, 4000, 6000, 8000, and 10,000 lbf). Record the corresponding direct current voltages (DCV's) with the HP-3497A. Repeat this procedure three times. Calculate the average values of the DCV readings at corresponding loads. Enter load (y-axis) vs. the corresponding average DCV (x-axis) into the HP-3497A. This provides the linear relationship $y = mx + b$ (where y = load, x = DCV), so that the HP-3497A can convert the DCV reading into load.

(3) Calibrate the LVDT's with a precision displacement dial indicator at displacements of 0, 2.54, 5.08, 7.62, ..., up to 25.4 mm (0, 0.1, 0.2, 0.3, ..., 1 in), with displacement increments of 2.54 mm (0.1 in). Obtain the corresponding DCV's with the HP-3497A. Repeat this procedure three times and calculate the average values of the DCV readings at corresponding displacements. Enter displacement (y-axis) vs. the corresponding average DCV (x-axis) into the HP-3497A. Find the linear relationship $y = mx + b$ (where y = displacement, x = DCV) to convert the DCV reading into displacement.

(4) Set up the push-out test as shown in Figures 4.1 and 4.2 (Ch. 4). It is very important to center the load cell, steel platens, rock sample, and cylindrical steel bar around the loading axis (y-axis). Follow the procedure given in Appendix E to obtain the degree of saturation, water content, void ratio, porosity and density of the push-out sample prior to and following push-out testing.

(5) Push-Out Testing:

Zero the readings of the SoilTest compression tester gage and the top and bottom displacement gages. Record the room temperature, relative humidity, and temperature at the top and bottom of the cement plug. Program the HP-3497A to collect data every 10 seconds. Start the HP. Load the sample initially to 4448 N (1000 lbf)[5] and try to keep the load constant by adjusting the loading knob. Write down the load, top and bottom plug displacements at 30 second intervals for 2 minutes. Repeat the procedure by adding load increments of 4448 N (1000 lbf) until the sample fails. Upon failure, record the load and displacements every 15 seconds. Change the time increment in the HP-3497 to collect data every second. Record the room temperature, relative humidity, and temperature at the top and bottom of the cement plug at the end of the push-out test.

---

5 Procedure agrees with ASTM D1143-81, Section 4, p. 244, which requires loading piles to 100% of the anticipated design load in increments of 25%.

APPENDIX E

DETERMINATION OF PUSH-OUT SAMPLE WATER CONTENT (w) DEGREE OF SATURATION (S), VOID RADIO (e), POROSITY (n), and DENSITY (ρ)

Procedure and Worksheet

1. Number the tuff sample: e.g., AP3 - 3 - 1/2 - AMB - FS - 1 - PO2 - SSII

6	1	45°	PS	
8	2	70°	RD	
	4	90°	FSS	

In the above push-out test specimen numbering scheme, the first column refers to the type of tuff and to the tuff block number (i.e. AP3: Apache Leap tuff - block number 3). The second and third columns give the outside diameters and inside diameters in inches, respectively. The fourth and fifth columns give the curing and test temperatures (i.e. ambient, 45°C, 70°C or 90°C) and specimen saturation condition (i.e. FS: highly saturated; PS: intermediately saturated; RD: low saturated; FSS: presaturated), respectively. The sixth, seventh and last columns refer to the core number, sample number and type of cement used (i.e. SSII: Self-Stress II cement), respectively.

2. Weigh the rubber stopper (W_2): g

3. Weigh the dry sample (after it has been left in oven for at least a week at 100-105°) (W_3): g

4. Wait for about 4 hours after weighing dry, hot tuff sample, for it to cool down.[1]

5. Measure the volume of tuff core (V_T).

5a. Measure outside diameter (in inches) in 3 directions at 120°: D_1 = D_2 = D_3 =
Average outside diameter (AOD) = in = cm.

5b. Measure specimen length (in inches) at 6 locations (in) at 60°: L_1 = L_2 = L_3 =
L_4 = L_5 = L_6 =
Average length (AL) = in = cm.

5c. Measure inside diameter with calipers (at the top, middle and bottom of inner borehole) ID_1 = ID_2 = ID_3 =
Average inside diameter (AID) = in = cm.

5d. Calculate total volume of tuff specimen (TVT) (cc) = $[(AOD)^2 - (AID)^2][\pi/4][AL]$ = cc.

6.a) For low saturated, partially saturated, and highly saturated sample preparation, go to step 7.

b) For presaturated sample preparation, weigh the samples daily, at the same time, and put them back into the saturation tank. Record the total weight (W_T). Calculate the degree of saturation (S) by:

$$S = \frac{G_s W_w}{(TVT)\gamma_s - W_3} \times 100 \qquad \text{(E.1)}$$

---

1 Step 4 requires a dessicator to keep the sample dry and to bring the temperature down. Due to the lack of a dessicator, sample is left at room conditions (24 ± 2°C, 42-46% rh) for 4 hours to cool down.

Use the following table for determination of the degree of saturation (S):

γ_s = g/cc
W_3 = g
G_s =

Date	Time	W_T	W_W*	S** (%)

*$W_w = W_T - W_3$
**S calculated from Eq. (E.1).

When the desired degree of saturation (S) is reached, go to the next step.

7. Put rubber stopper in sample. Weigh specimen + rubber stopper + any moisture absorbed during cooling (W_6): g

8. Mix cement according to the cement mixing procedure given in Appendix C. Note:

   8a. Day, time:
   8b. Room temperature: °C
   8c. Relative Room humidity: % rh

9. For 12.7 or 25.4 mm I.D. push-out samples having cement plug length-to-diameter ratios (L/D) of 1.0, measure 5 or 15 cc of cement slurry into syringe tube. For 50.8 or 101.6 mm I.D. samples with L/D = 1.0, measure 103 or 824 cc of cement slurry in a graduated cylinder. Pour the cement slurry into the borehole (according to the procedure in Appendix C).

10. Measure the weight of the sample + rubber stopper + cement slurry (W_9): g.

11. Calculate the cement slurry weight = $W_9 - W_6 = W_{CT}$ = g.

12. Pour distilled water on cement plugs 15 minutes after cement pouring; record the volume of water poured (V_W): cc.

13. a) Place specimens into the environmental chamber or under water after an hour of cement pouring, as described in Appendix D, Section D.1. (Waiting for an hour will allow the cement to set.)

    b) For highly saturated and presaturated samples, keep the samples under water at desired temperature for 8 days.

    c) For intermediately saturated samples, keep the sample in the environmental chamber for 8 days at desired temperature, airflow and 80% relative humidity (rh).

    d) For low saturated samples, keep the sample in environmental chamber for 8 days at desired temperature, airflow and 45% rh (the lower limit of the environmental chamber).

    e) Use curing temperatures of ambient (24 ± 2°C), 44 to 45°C, 65 to 70°C; or 90°C for highly saturated samples. (Curing temperatures of 90°C can not be used for intermediately saturated or low saturated samples as the temperature of the environmental chamber can be taken up to a maximum of only 77°C)

14. Weigh specimens each day, starting on the third day after cement pouring (in order not to disturb the cement plugs) for 6 days. Dry surfaces of samples prior to weighing. For highly saturated samples, try to determine the time when the weight of the sample becomes essentially constant.

14a. Day 3:	Date:	Time:	Room Temp.:	°C	Humidity:	% rh	W_{14a} =	g
14b. Day 4:	Date:	Time:	Room Temp.:	°C	Humidity:	% rh	W_{14b} =	g
14c. Day 5:	Date:	Time:	Room Temp.:	°C	Humidity:	% rh	W_{14c} =	g
14d. Day 6:	Date:	Time:	Room Temp.:	°C	Humidity:	% rh	W_{14d} =	g
14e. Day 7:	Date:	Time:	Room Temp.:	°C	Humidity:	% rh	W_{14e} =	g
14f. Day 8: (prior to push-out test)	Date:	Time:	Room Temp.:	°C	Humidity:	% rh	W_{14f} =	g

15. On day 8, shortly before the push-out test, first measure the height of the water column (h_W) remaining above the cement plug (h_W = cm). This step is necessary only for low saturated or intermediately saturated samples (the fully saturated samples are submerged in water). Measure the top hole and bottom hole lengths:

    Top hole length (THL) = in = cm. Bottom hole length (BHL) = in = cm.
    Volume of water column above the cement plug (V_{hw}) = $(\pi/4)(AID)^2$ x h_W = cc.

16. Set up push-out test as described in Appendix D.

17. Before initiating push-out testing, record:

    Temperature at top of plug = TC1 = °C; Temperature at bottom of plug = TC2 = °C

    Keep the time interval between steps #14 and 17 as short as possible to avoid moisture loss from samples.

18. Following push-out testing, record:

    18a. TC1 = °C; TC2 = °C
    18b. Measure total weight of specimen; W_{18} = g.

19. Determine the water content (w) of specimen:

    Each batch of cement mixture consists of 333 g of cement and 150 g of water (W_w). Out of 333 g of cement, 300 g is dry cement solids (W_{cs}), 30 g is D53 additive, and 3 g is D65 additive.

    The net cement slurry weight is (W_{CT}, step 11) = weight of cement solids (W_{cs}) + weight of water in cement batch (W_w) + weight of additives (W_{AD}).

    Thus, W_{AD}/W_{cs} = 33/300 = 0.11. Therefore, W_{AD} = 0.11 W_{cs}.
    W_w/W_{cs} = 150/300 = 0.5. Therefore, W_w = 0.5 W_{cs}.
    $W_{CT} = W_{cs} + 0.5\ W_{cs} + 0.11\ W_{cs}$
    $W_{cs} = W_{CT}/1.61$
    $W_w = 0.5\ W_{cs}$
    $W_{AD} = 0.11\ W_{cs}$

The total volume of the cement slurry (TVS), excluding the volume of air, equals the volume of cement solids (V_{cs}) plus the volume of cement water (V_w) and the volume of cement additives (V_{AD}). This approximation is used to determine the volume of the cement additives.

The average cement slurry density is 1.855 g/cc. Therefore,

$TVS = W_{CT}/1.855$
$V_{cs} = W_{cs}/\rho_{cs}$ (density of cement solids = 3.15 g/cc, according to Dowell-Schlumberger)
$V_w = W_w/\rho_w$ (density of water)

The volume of additives, V_{AD}, is:

$V_{AD} = TVS - V_{cs} - V_w = W_{CT}/1.855 - W_{cs}/\rho_{cs} - W_w/\rho_w$

Total weight of solids in each plugged tuff cylinder = W_{SF} = W_3 [step 3] + W_{cs} = g.

Total weight of water prior to push-out test in each tuff specimen = W_{WP} = W_{14f} [step 14] - W_2 [step 2] - W_{SF} + $V_w\gamma_w$ [step 12] - V_{hw} - W_{AD} = g.
Total weight of water in each tuff specimen following push-out test = W_{WF} = W_{18} [step 18] - W_{SF} + $V_w\gamma_w$ [step 12] - V_{hw} - W_{AD} = g.

Water content of tuff core prior to push-out test = $w_p = W_{WP}/W_{SF}$ x 100 (%) = %
Water content of tuff core following push-out test = $w_f = W_{WF}/W_{SF}$ x 100 (%) = %

20. Calculate the total specimen volume (V_T) = TVT [Step 5d] + TVS = cc.

21. Determine the degree of saturation (S) of tuff sample:

Volume of cement solids = $V_{cs} = W_{cs}$ [step 19]/ρ_{cs} (ρ_{cs} = density of cement solids) = cc
Volume of tuff solids = $V_{ts} = W_3$ [step 3]/ρ_{ts} (ρ_{ts} = density of tuff solids) = cc

Total volume of solids in each tuff specimen = $V_{ST} = V_{cs} + V_{ts}$ = cc.

Degree of saturation (S) of tuff core = S =
V_w (volume of water in tuff core)/V_V (volume of voids in tuff core) x 100 = %

Volume of water in tuff core prior to push-out test = $V_{WP} = W_{WP}$ [step 19]$/\rho_w$ (ρ_w = density of water) = cc.

Volume of water in tuff core following push-out test = $V_{WF} = W_{WF}$ [step 19]$/\rho_w$ = cc.

Total volume of specimen (V_T, step 20) = $V_{ST} + V_w + V_a$ (volume of air in sample) + V_{AD} (volume of additives, step 19).

Total volume of air in sample prior to push-out test (V_{AP}) = $V_T - V_{ST} - V_{WP} - V_{AD}$ = cc.

Total volume of voids in sample prior to push-out test (V_{VP}) = $V_{AP} + V_{WP}$ = cc.

Degree of saturation of tuff core prior to push-out test = $S_P = V_{WP}/V_{VP} \times 100$ = %.

Total volume of specimen following push-out test = $V_{TF} = V_T - [(AID)^2(\pi/4)\delta_p] - V_{AD}$ [step 19], where δ_p is the plug compression (cm) following push-out test = cc.

Total volume of air in sample following push-out test (V_{AF}) = $V_{TF} - V_{ST} - V_{WF}$ = cc.

Total volume of voids in sample following push-out test (V_{VF}) = $V_{AF} + V_{WF}$ = cc.

Degree of saturation of tuff core following push-out test = $S_f = V_{WF}/V_{VF} \times 100$ = %.

22. Void ratio of sample prior to push-out test (e_p) = V_{VP}/V_{ST} =

    Void ratio of sample following push-out test (e_f) = V_{VF}/V_{ST} =

23. Porosity of sample prior to push-out test (n_p) = $V_{VP}/V_{TP} \times 100$ = %

    Porosity of sample following push-out test (n_f) = $V_{VF}/V_{TF} \times 100$ = %

24. Sample density prior to push-out test (ρ_p) = $(W_{14f} - W_{AD})/(V_T - V_{AD})$ = g/cc

    Sample density following push-out test (ρ_f) = $(W_{20} - W_{AD})/V_{TF}$ = g/cc

Worksheet (without text) for Determination of Push-Out Sample Water Content (w), Degree of Saturation (S), Void Ratio (e), Porosity (n), and Density (ρ)

1. Sample number: e.g., AP3 - 6 - 1 - AMB - FS - 1 - PO2 - SSII

2. Weight of rubber stopper (W_2): g

3. Weight of dry sample (W_3): g

4. 4a. Outside diameter in 3 directions (in) at 120°: D_1 = D_2 = D_3 =
   Average outside diameter (AOD) = in = cm.

   4b. Specimen length at 3 locations (in) at 120°: L_1 = L_2 = L_3 =
   L_4 = L_5 = L_6 =
   Average length (AL) = in = cm.

   4c. Inside diameter (measured with calipers) at the top, middle and bottom of inner borehole (in):
   ID_1 = ID_2 = ID_3 =
   Average inside diameter (AID) = in = cm.

   4d. Total volume of tuff specimen (TVT) (cc) = $[(AOD)^2 - (AID)^2][\pi/4][AL]$ = cc.

5. 5a. For the preparation of low saturated, partially saturated and highly saturated samples, go to step 6.

   5b. For the preparation of presaturated samples, use the following table:

   W_3 = g
   γ_s = g/cc
   G_s =

Date	Time	W_T (g)	$W_w = W_T - W_3$ (g)	$S = \frac{G_S W_w}{(TVT)\gamma_S - W_3} \times 100$ (%)

When the desired degree of saturation (S) is reached, go to the next step.

6. Weight of specimen + rubber stopper (W_6): g

7. 7a. Date, time of mixing cement:
   7b. Room temperature: C
   7c. Relative Room humidity: % rh

8. Weight of the sample + rubber stopper + cement slurry (W_8): g.

9. Cement slurry weight = $W_{CT} = W_8 - W_6$ = g.

10. Volume of distilled water poured on cement slurry 15 minutes after cement pouring (V_W): cc.

11. Wait for an hour (following cement pouring) to put the specimens into environmental chamber or under water.

12. Weight of specimens each day (starting from the third day of cement pouring):

12a. Day 3: Date: Time: Room Temp.: °C Humidity: % rh W_{12a} = g
12b. Day 4: Date: Time: Room Temp.: °C Humidity: % rh W_{12b} = g
12c. Day 5: Date: Time: Room Temp.: °C Humidity: % rh W_{12c} = g
12d. Day 6: Date: Time: Room Temp.: °C Humidity: % rh W_{12d} = g
12e. Day 7: Date: Time: Room Temp.: °C Humidity: % rh W_{12e} = g
12f. Day 8: Date: Time: Room Temp.: °C Humidity: % rh W_{12f} = g
(prior to push-out test)

13. Height of water column (h_W) remaining above the cement plug prior to push-out test (h_W = cm). NOTE: This step is necessary only for low or intermediately saturated samples.

14. a) Top hole length (THL) = in = cm.
b) Bottom hole length (BHL) = in = cm.
c) Volume of water column above the cement plug (V_{hw}) = $(\pi/4)(AID)^2$ x h_W = cc.

15. Before initiation of push-out testing,

a) Temperature at top of plug = TC1 = °C;
b) Temperature at bottom of plug = TC2 = °C

16. Following push-out testing:

a) TC1 = °C;
b) TC2 = °C
c) Weight of specimen; W_{16} = g.

17. Determine the water content of specimen prior to push-out test (w_p):

a) $W_{SF} = W_3$ [step 3] + W_{CT} [step 9]/1.61
b) $W_{WP} = W_{12f}$ [step 12f] - W_2 [step 2] - W_{SF} + $V_w\gamma_w$ [step 10] - 0.068323 W_{CT} [step 9] - V_{hw} [step 14c]

c) $w_p = W_{WP}/W_{SF} \times 100 =$

18. Determine water content of specimen following push-out test (w_f):
    a) $W_{WF} = W_{16}$ [step 16] - $W_{SF} + V_w\gamma_w$ [step 10] - 0.068323 W_{CT} [step 9] - V_{hw} [step 14c]
    b) $w_f = W_{WF}/W_{SF} \times 100 =$ %

19. Calculate the total specimen volume (V_T) = TVT [step 4d] + 0.5078 W_{CT} [step 9] = cc.

20. Determine the degree of saturation of specimen prior to push-out test (S_p):

    a) $V_{VP} = V_T$ [step 19] - 0.2285 W_{CT} [step 9] - W_3 (step 3)/2.70 = cc
    b) $S_p = W_{WP}$ [step 17b]/$V_{VP} \times 100 =$ %

21. Determine the degree of saturation of specimen following push-out test (S_f):

    a) $V_{VF} = V_{VP}$ [step 20a] - $[(AID)^2(\pi/4)\delta_p]$, where δ_p = total plug compression following push-out test (cm)
    b) $S_f = W_{WF}$ [step 18a]/$V_{VF} \times 100 =$ %

22. Determine void ratio of sample prior to push-out test (e_p):

    a) $V_{ST} = 0.6211\ W_{CT}$ [step 9] + W_3 [step 3]/2.70
    b) $e_p = V_{VP}$ [step 20a]/$V_{ST} =$

23. Determine void ratio of sample following push-out test (e_f):

    a) $e_f = V_{VF}$ [step 21a]/$V_{ST} =$

24. Calculate the porosity of sample prior to push-out test (n_p):

    a) $V_{TP} = V_T$ [step 19] - 0.0313442 W_{CT} [step 9]
    b) $n_p = V_{VP}$ [step 20a]/$V_{TP} \times 100 =$ %

25. Calculate the porosity of sample following push-out test (n_f):

    a) $V_{TF} = V_{TP} - [(AID)^2(\pi/4)\delta_p]$, where δ_p = total plug compression

b) $n_f = V_{VF}$ [step 21a]$/V_{TF}$ x 100 = %

26. Determine the sample density prior to push-out test (ρ_p):

a) $\rho = (W_{12f}$ - 0.0683 W_{CT} [step 9]$)/V_{TP}$ [step 24a] = g/cc

27. Determine the sample density following push-out test (ρ_f):

a) $\rho_f = (W_{16}$ [step 16] - 0.0683 W_{CT} [step 9]$)/V_{TF}$ [step 25a] = g/cc

NOTES:

APPENDIX F

DIMENSIONS AND MECHANICAL PROPERTIES OF PUSH-OUT CYLINDERS

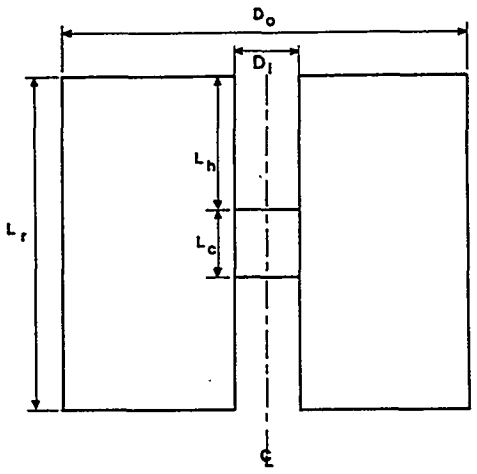

D_i = inside hole diameter
D_o = outside cylinder diam.
L_h = top hole length
L_c = cement plug length
L_r = cylinder length

Not to scale.

Apache Leap Tuff Cylinder	L_r (mm)	L_h (mm)	L_c (mm)
AP3-6-1-AMB-PS-4-PO2-SSII[a]	120.9	63.9	25.5
AP3-6-1-AMB-PS-2-PO1-SSII[a]	111.9	35.9	25.4
AP3-6-1-AMB-FS-3-PO1-SSII[a]	105.3	30.2	31.0
AP3-6-1-AMB-FS-4-PO1-SSII[a]	115.1	33.5	30.7
AP3-6-1-AMB-FS-1-PO1-SSII[a]	82.0	24.6	32.2
AP3-6-1-45-FS-1-PO2-SSII[a]	87.6	31.5	29.7
AP8-6-1-45-FS-1-PO1-SSII[a]	102.9	29.8	32.4
AP8-6-1-45-FS-4-PO1-SSII[a]	106.8	36.1	28.1
AP8-6-2-AMB-FS-3-PO1-SSII[b]	129.6	38.3	49.1
AP8-6-1-45-FS-1-PO2-SSII[a]	102.3	31.4	30.8
AP8-6-1-45-FS-2-PO1-SSII[a]	100.9	26.0	31.6
AP8-6-1-70-FS-2-PO2-SSII[a]	103.7	34.3	28.4
AP5-6-1-70-FS-1-PO1-SSII[a]	95.7	34.5	28.3
AP5-6-1-70-FS-2-PO2-SSII[a]	99.4	38.3	28.0
AP3-6-2-AMB-FS-3-PO1-SSII[b]	102.9	15.3	43.6
AP3-6-2-AMB-FS-4-PO1-SSII[b]	114.6	34.4	46.5

Figure F.1 Dimensions of the Apache Leap tuff cylinders used for push-out tests.

Apache Leap Tuff Cylinder	L_r (mm)	L_h (mm)	L_c (mm)
AP8-6-2-45-FS-1-PO1-SSII[b]	102.1	25.3	41.2
AP8-6-2-45-FS-4-PO1-SSII[b]	105.4	25.0	42.1
AP8-6-2-45-FS-4-PO2-SSII[b]	101.9	25.4	45.7
AP3-6-2-70-FS-2-PO1-SSII[b]	109.5	18.6	46.2
AP5-6-1-44-PS-3-PO2-SSII[a]	98.0	32.3	30.1
AP5-6-1-44-PS-4-PO1-SSII[a]	99.2	34.5	30.5
AP5-6-1-70-FS-3-PO4-SSII[a]	82.3	28.2	29.6
AP5-6-1-44-PS-2-PO3-SSII[a]	95.1	35.2	28.7
AP5-6-1-AMB-FS-1-PO2-SSII[a]	100.1	33.5	30.1
AP5-6-1-AMB-FS-3-PO1-SSII[a]	87.1	28.8	29.8
AP5-6-1-AMB-FS-2-PO3-SSII[a]	99.0	27.9	29.3
AP5-6-1-90-FS-2-PO1-SSII[a]	86.6	31.3	30.8
AP5-6-1-90-FS-4-PO2-SSII[a]	136.8	44.4	27.6
AP8-6-2-90-FS-2-PO2-SSII[b]	103.1	9.2	51.2
AP8-6-2-90-FS-2-PO1-SSII[b]	100.5	27.5	46.6
AP5-6-2-90-FS-2-PO2-SSII[b]	100.1	14.5	47.1
AP5-6-2-90-FS-3-PO2-SSII[b]	98.0	19.4	48.8
AP5-6-2-44-PS-2-PO3-SSII[b]	98.5	25.2	43.5
AP5-6-2-44-PS-4-PO2-SSII[b]	136.9	43.7	51.4
AP5-6-2-44-PS-1-PO2-SSII[b]	100.1	20.1	49.2
AP113-8-4-AMB-FS-1-PO1-SSII[c]	186.9	45.8	101.2
AP121-8-4-AMB-FS-1-PO1-SSII[c]	206.4	64.2	102.2
AP22-6-1-44-PS-1-PO1-SSII[a]	140.6	68.9	31.5
AP122-6-1-44-PS-2-PO1-SSII[a]	158.0	62.4	35.6
AP5-6-2-44-PS-3-PO2-SSII[b]	95.2	12.0	51.4
AP114-8-4-AMB-FS-2-PO1-SSII[c]	133.3	6.3	87.6
AP920-8-4-44-PS-1-PO1-SSII[c]	160.2	18.8	100.5
AP114-8-4-45-FS-1-PO1-SSII[c]	137.6	8.6	89.4
APB-8-4-44-PS-1-PO1-SSII[c]	173.2	33.8	99.0

Figure F.1 Dimensions of the Apache Leap tuff cylinders used for push-out tests.--Continued

Apache Leap Tuff Cylinder	L_r (mm)	L_h (mm)	L_c (mm)
APG-8-4-70-FS-1-PO1-SSII[c]	200.6	57.6	102.7
APC-8-4-AMB-PS-1-PO1-SSII[c]	183.3	39.4	101.9
AP927-6-1-AMB-PS-1-PO1-SSII[a]	151.4	95.9	30.3
AP22-6-1-AMB-PS-2-PO1-SSII[a]	128.5	44.7	29.1
APE-6-1-AMB-PS-1-PO1-SSII[a]	170.5	83.1	32.5
APG-6-1-AMB-PS-2-PO1-SSII[a]	132.6	58.4	31.3
APE-6-1-AMB-PS-2-PO1-SSII[a]	172.0	82.5	29.0
AP122-6-2-AMB-PS-2-PO1-SSII[b]	157.9	57.4	52.6
AP22-6-2-AMB-PS-1-PO1-SSII[b]	141.4	61.3	49.9
APE-6-2-AMB-PS-1-PO1-SSII[b]	171.2	65.2	50.3
APE-6-2-AMB-PS-2-PO1-SSII[b]	172.1	61.1	49.7
AP22-6-2-AMB-PS-2-PO1-SSII[b]	127.9	49.4	51.7
AP77-6-1-36-RD-1-PO1-SSII[a]	163.6	67.2	30.2
AP921-6-1-36-RD-1-PO1-SSII[a]	110.5	45.7	28.6
APG-6-1-36-RD-1-PO2-SSII[a]	135.2	57.5	31.3
AP927-6-1-36-RD-2-PO1-SSII[a]	116.2	43.2	31.8
AP3-6-1-36-RD-2-PO1-SSII[a]	161.4	54.3	37.4
AP1-6-1-36-RD-1-PO1-SSII[a]	140.4	46.3	26.5
APA4-6-1-36-RD-1-PO1-SSII[a]	155.0	70.1	29.4
APG-6-2-70-FS-1-PO1-SSII[b]	135.1	56.3	50.3
APG-6-2-70-FS-2-PO1-SSII[b]	132.8	31.1	51.8
APE-8-4-70-FS-4-PO1-SSII[c]	186.4	25.8	94.4
APG-8-4-70-FS-4-PO2-SSII[c]	160.2	17.6	102.7
AP3-8-4-45-FS-1-PO1-SSII[c]	143.7	7.2	96.0
APD-6-1-70-PS-3-PO1-SSII[a]	161.1	70.4	35.2
APA3-6-1-70-PS-3-PO1-SSII[a]	113.8	37.7	25.6
APA4-6-1-70-PS-3-PO1-SSII[a]	144.3	47.9	33.0
APA3-6-2-70-PS-2-PO1-SSII[b]	157.7	53.6	48.5

Figure F.1 Dimensions of the Apache Leap tuff cylinders used for push-out tests.--Continued

Apache Leap Tuff Cylinder	L_r (mm)	L_h (mm)	L_c (mm)
AP927-6-2-AMB-RD-2-P01-SSII[b]	116.1	32.7	51.7
AP5-6-2-AMB-RD-4-P01-SSII[b]	98.7	19.9	49.5
APA3-6-1-90-FS-3-P03-SSII[a]	102.5	32.9	32.2
AP1-6-2-AMB-RD-1-P01-SSII[b]	140.2	46.4	51.2
APH-8-4-45-FS-1-P05-SSII[c]	146.3	22.2	102.2
APB-8-4-90-FS-2-P01-SSII[c]	117.4	8.1	86.5
APH-8-4-90-FS-1-P01-SSII[c]	135.9	10.0	105.0
APD-6-2-70-PS-3-P01-SSII[b]	161.0	64.4	51.0
APA3-6-2-70-PS-3-P04-SSII[b]	113.8	37.8	53.9
APE-8-4-AMB-RD-8-P01-SSII[c]	181.1	18.5	99.9
APE-8-4-70-PS-5-P01-SSII[c]	205.5	83.0	101.1
AP8-8-4-90-FS-3-P01-SSII[c]	170.5	24.0	105.3
APA5-6-1-AMB-RD-3-P02-SSII[a]	139.5	66.5	29.7
APA2-6-1-AMB-RD-1-P01-SSII[a]	132.5	63.8	30.2
APD-6-1-AMB-RD-1-P03-SSII[a]	129.8	53.9	30.3
APJ-8-4-AMB-RD-4-P01-SSII[c]	131.5	13.6	93.9
APA5-6-2-36-RD-4-P03-SSII[b]	113.0	25.2	50.2
AP113-6-2-36-RD-2-P01-SSII[b]	130.3	41.5	47.0
APD-6-2-36-RD-2-P01-SSII[b]	106.7	19.8	53.6
APA6-8-4-36-RD-1-P02-SSII[c]	118.3	11.3	80.7
API-8-4-36-RD-1-P01-SSII[c]	168.8	27.2	102.0
APM-8-4-AMB-RD-2-P01-SSII[c]	170.1	15.8	93.6
APJ-8-4-AMB-PS-3-P01-SSII[c]	159.0	16.5	99.1
APM-8-4-AMB-PS-6-P01-SSII[c]	213.2	92.0	97.9
APM-8-4-36-RD-1-P01-SSII[c]	199.0	42.6	97.5
APA-8-4-70-PS-4-P01-SSII[c]	210.7	40.5	129.5
APM-8-4-70-PS-5-P01-SSII[c]	198.5	56.3	101.5
APA-8-4-44-PS-5-P01-SSII[c]	228.9	57.4	103.6

Figure F.1 Dimensions of the Apache Leap tuff cylinders used for push-out tests.--Continued

Apache Leap Tuff Cylinder	L_r (mm)	L_h (mm)	L_c (mm)
APA5-6-1-AMB-FSS-1-P01-SSII[a]	134.1	50.4	29.2
AP1-6-1-AMB-FSS-2-P01-SSII[a]	128.9	64.5	25.7
APA3-6-1-AMB-FSS-4-P02-SSII[a]	115.6	51.1	26.7
APA2-6-1-AMB-FSS-4-P01-SSII[a]	119.3	53.1	28.5
APA2-6-2-AMB-FSS-1-P01-SSII[b]	132.4	37.1	50.8
AP77-6-2-AMB-FSS-1-P01-SSII[b]	163.4	44.8	49.8
APA4-6-2-AMB-FSS-1-P01-SSII[b]	158.7	61.5	53.4
AP41-3-1/2-AMB-FS-7-P01-SSII[d]	77.0	31.4	14.5
AP41-3-1/2-AMB-FS-10-P01-SSII[d]	77.3	34.1	14.2
AP41-3-1/2-AMB-FS-11-P01-SSII[d]	83.3	40.7	15.4
AP41-3-1/2-AMB-FS-7-P02-SSII[d]	79.1	34.2	13.7
AP852-3-1/2-AMB-FS-7-P02-SSII[d]	74.9	21.7	15.6
AP41-3-1/2-AMB-FS-11-P03-SSII[d]	75.3	35.4	13.4
AP41-3-1/2-AMB-FS-11-P02-SSII[d]	80.1	36.0	14.5
AP852-3-1/2-AMB-FS-5-P01-SSII[d]	77.9	34.2	15.3
AP852-3-1/2-AMB-FS-5-P02-SSII[d]	73.7	27.3	15.5
AP41-3-1/2-AMB-FS-8-P01-SSII[d]	71.5	21.2	13.5
AP852-3-1/2-AMB-FS-7-P01-SSII[d]	74.7	26.7	16.3
AP41-3-1/2-AMB-FS-11-P01-SSII[d]	73.7	23.9	16.3
AP41-3-1/2-AMB-FS-9-P01-SSII[d]	76.7	33.8	12.8
AP852-3-1/2-AMB-FS-8-P01-SSII[d]	91.7	44.0	15.3
AP566-6-1-2-AMB-FS-8-P01-SSII[a]	145.6	20.1	53.3
AP631-6-1-2-AMB-FS-1-P02-SSII[a]	137.4	75.0	48.6
APG-6-1-2-AMB-FS-3-P01-SSII[a]	119.2	40.3	53.1
AP566-6-1-2-AMB-FS-7-P01-SSII[a]	134.0	31.5	51.4
APA3-6-1-2-AMB-FS-3-P04-SSII[a]	102.9	30.8	50.0
APH-6-1-4-AMB-FS-7-P01-SSII[a]	173.8	24.9	101.4

Figure F.1 Dimensions of the Apache Leap tuff cylinders used for push-out tests.--Continued

Apache Leap Tuff Cylinder	L_r (mm)	L_h (mm)	L_c (mm)
AP566-6-1-4-AMB-FS-3-PO2-SSII[a]	199.2	17.8	102.2
AP56A-6-1-4-AMB-FS-1-PO1-SSII[a]	176.7	10.1	105.6

NOTES:

[a]Samples with inside diameters (D_i) of 25.4 mm (1 in) and outside diameters (D_o) of 152.4 mm (6 in).

[b]Samples with inside diameters (D_i) of 50.8 mm (2 in) and outside diameters (D_o) of 152.4 mm (6 in).

[c]Samples with inside diameters (D_i) of 101.6 mm (4 in) and outside diameters (D_o) of 187.3 mm (7.375 in).

[d]Samples with inside diameters (D_i) of 12.7 mm (0.5 in) and outside diameters (D_o) of 76.2 mm (3 in).

Figure F.1 Dimensions of the Apache Leap tuff cylinders used for push-out tests.--Continued

Table F.1 Axial Stress at Failure ($\sigma^{p}_{z,f}$), Plug Length (L_c), Average ($\tau^{av}_{rz,i}$) and Exponential Extreme Shear Stresses ($\tau^{max}_{rz,i}$, $\tau^{min}_{rz,i}$), Top (w_t) and Bottom (w_b) Axial Plug Displacements at Failure. The maximum exponential shear stress is calculated at the loaded end of the plug (i.e. at z = 0), the minimum at the bottom (i.e. at z = L_c) of the plug.

Apache Leap Tuff Cylinder	$\sigma^{p}_{z,f}$ (MPa)	L_c (mm)	$\tau^{av}_{rz,i}$ * (MPa)	$\tau^{max}_{rz,i}$ ** (MPa)	$\tau^{min}_{rz,i}$ ** (MPa)	w_t (mm) x 10^2	w_b (mm) x 10^2
AP3-6-1-AMB-PS-4-PO2-SSII	32.1	25.5	7.99	22.96	2.64	8.9	4.8
AP3-6-1-AMB-PS-2-PO1-SSII	29.7	25.4	7.42	21.23	2.47	3.8	0.1
AP3-6-1-AMB-FS-3-PO1-SSII	42.7	31.0	8.74	28.98	2.12	15.5	5.1
AP3-6-1-AMB-FS-4-PO1-SSII	35.2	30.7	7.29	23.95	1.81	15.2	1.3
AP3-6-1-AMB-FS-1-PO2-SSII	29.0	32.2	5.71	19.58	1.28	18.8	3.8
AP3-6-1-45-FS-1-PO2-SSII	35.4	29.7	7.57	24.09	1.98	23.1	5.2
AP8-6-1-45-FS-1-PO1-SSII	43.9	32.4	8.59	29.67	1.90	17.3	7.4
AP8-6-1-45-FS-4-PO1-SSII	44.2	28.1	9.99	30.75	2.85	15.6	3.3
AP8-6-2-AMB-FS-3-PO1-SSII	17.6	49.1	4.54	15.19	1.08	30.7	12.6

Table F.1 Axial Stress at Failure ($\sigma^{p}_{z,f}$), Plug Length (L_c), Average ($\tau^{av}_{rz,l}$) and Exponential Extreme Shear Stresses ($\tau^{max}_{rz,l}$, $\tau^{min}_{rz,l}$), Top (w_t) and Bottom (w_b) Axial Plug Displacements at Failure.--Continued

Apache Leap Tuff Cylinder	$\sigma^{p}_{z,f}$ (MPa)	L_c (mm)	$\tau^{av}_{rz,l}$ * (MPa)	$\tau^{max}_{rz,l}$ ** (MPa)	$\tau^{min}_{rz,l}$ ** (MPa)	w_t (mm) x 10^2	w_b (mm) x 10^2
AP8-6-1-45-FS-1-PO2-SSII	38.9	30.8	8.02	26.46	1.97	19.3	6.6
AP8-6-1-45-FS-2-PO1-SII	44.1	31.6	8.86	29.80	2.05	11.7	4.8
AP8-6-1-70-FS-2-PO2-SSII	35.1	28.5	7.82	24.36	2.19	19.6	2.5
AP5-6-1-70-FS-1-PO1-SSII	26.7	28.3	5.98	18.55	1.69	24.9	2.8
AP3-6-1-70-FS-2-PO2-SSII	32.3	28.0	7.33	22.52	2.11	21.1	3.3
AP3-6-2-AMB-FS-3-PO1-SSII	28.5	43.6	8.31	24.76	2.55	21.3	8.9
AP3-6-2-AMB-FS-4-PO1-SSII	22.0	46.5	5.99	19.01	1.61	14.2	1.3
AP8-6-2-45-FS-1-PO1-SSII	28.5	41.2	8.80	24.81	3.01	26.9	9.8
AP8-6-2-45-FS-4-PO1-SSII	19.1	42.1	5.75	16.59	1.89	23.9	8.5
AP8-6-2-45-FS-4-PO2-SSII	17.6	45.7	4.88	15.21	1.36	22.4	11.0

Table F.1 Axial Stress at Failure ($\sigma^{p}_{z,f}$), Plug Length (L_c), Average ($\tau^{av}_{rz,l}$) and Exponential Extreme Shear Stresses ($\tau^{max}_{rz,l}$, $\tau^{min}_{rz,l}$), Top (w_t) and Bottom (w_b) Axial Plug Displacements at Failure.--Continued

Apache Leap Tuff Cylinder	$\sigma^{p}_{z,f}$ (MPa)	L_c (mm)	$\tau^{av}_{rz,l}$ * (MPa)	$\tau^{max}_{rz,l}$ ** (MPa)	$\tau^{min}_{rz,l}$ ** (MPa)	w_t (mm) x 10^2	w_b (mm) x 10^2
AP3-6-2-70-FS-2-P01-SSII	17.7	46.2	4.85	15.29	1.32	14.0	6.0
AP5-6-1-44-PS-3-P02-SSII	43.9	30.1	9.27	30.03	2.36	17.3	5.6
AP5-6-1-44-PS-4-P01-SSII	51.8	30.5	10.78	35.32	2.69	18.9	3.8
AP5-6-1-70-[a]-FS-3-P04-SSII	23.9	29.6	5.12	16.41	1.35	22.6	4.8
AP5-6-1-44-PS-2-P03-SSII	56.2	28.7	12.43	38.91	3.44	19.4	16.8
AP5-6-1-AMB-FS-1-P02-SSII	35.1	30.1	7.40	24.03	1.89	6.4	3.8
AP5-6-1-AMB-FS-3-P01-SSII	33.7	29.9	7.17	23.10	1.85	16.0	4.1
AP5-6-1-AMB-FS-2-P03-SSII	35.3	29.3	7.64	24.31	2.04	16.5	1.3
AP5-6-1-90-FS-2-P01-SSII	22.0	30.8	4.53	14.93	1.11	16.5	9.4
AP5-6-1-90-FS-4-P02-SSII	15.3	27.6	3.51	10.69	1.03	16.6	1.0

Table F.1 Axial Stress at Failure ($\sigma^{p}_{z,f}$), Plug Length (L_c), Average ($\tau^{av}_{rz,t}$) and Exponential Extreme Shear Stresses ($\tau^{max}_{rz,t}$, $\tau^{min}_{rz,t}$), Top (w_t) and Bottom (w_b) Axial Plug Displacements at Failure.--Continued

Apache Leap Tuff Cylinder	$\sigma^{p}_{z,f}$ (MPa)	L_c (mm)	$\tau^{av}_{rz,t}$ * (MPa)	$\tau^{max}_{rz,t}$ ** (MPa)	$\tau^{min}_{rz,t}$ ** (MPa)	w_t (mm) x 10^2	w_b (mm) x 10^2
AP8-6-2-90-FS-2-PO2-SSII	8.6	51.2	2.12	7.40	0.46	15.0	8.9
AP8-6-2-90-[b] FS-2-PO1-SSII	15.1	46.6	4.13	13.12	1.10	19.1	10.2
AP5-6-2-90-[b] FS-2-PO2-SSII	9.7	47.1	2.60	8.36	0.68	23.9	9.7
AP5-6-2-90-[b] FS-3-PO2-SSII	7.4	48.8	1.91	6.36	0.46	38.1	10.4
AP5-6-2-44-[c] PS-2-PO3-SSII	15.4	43.5	4.48	13.33	1.38	26.7	10.4
AP5-6-2-44-g PS-4-PO2-SSII	20.0	51.4	4.93	17.27	1.05	43.4	19.6
AP5-6-2-44-PS-1-PO2-SSII	19.9	49.2	5.13	17.20	1.21	26.4	6.9
AP113-8-4-g AMB-FS-1-PO1-SSII	15.4	101.6	3.84	17.85	0.34	20.5	20.2
AP121-8-4-[c,d] AMB-FS-1-PO1-SSII	13.0	102.2	3.23	15.11	0.28	24.9	1.7

Table F.1 Axial Stress at Failure ($\sigma^{p}_{z,f}$), Plug Length (L_c), Average ($\tau^{av}_{rz,l}$) and Exponential Extreme Shear Stresses ($\tau^{max}_{rz,l}$, $\tau^{min}_{rz,l}$), Top (w_t) and Bottom (w_b) Axial Plug Displacements at Failure.--Continued

Apache Leap Tuff Cylinder	$\sigma^{p}_{z,f}$ (MPa)	L_c (mm)	$\tau^{av}_{rz,l}$ * (MPa)	$\tau^{max}_{rz,l}$ ** (MPa)	$\tau^{min}_{rz,l}$ ** (MPa)	w_t (mm) x 10^2	w_b (mm) x 10^2
AP22-6-1-44-PS-I-PO1-SSII	31.8	31.8	6.35	21.49	1.46	33.2	0.8
AP122-6-1-44-PS-2-PO1-SSII	42.6	35.6	7.59	28.75	1.31	32.8	5.2
AP5-6-2-e,f,g 44-PS-3-PO2-SSII	25.0	51.4	6.18	21.63	1.31	56.1	18.5
AP114-8-4-AMB-FS-2-PO1-SSII	16.2	87.6	4.69	18.82	0.68	14.7	10.7
AP920-8-4-44-d PS-1-PO1-SSII	13.1	100.5	3.32	15.24	0.31	11.7	10.7
AP114-8-4-45-FS-1-PO1-SSII	17.6	89.4	4.99	20.41	0.68	29.2	25.2
APB-8-4-44-c,d PS-1-PO1-SSII	10.8	99.0	2.77	12.56	0.27	32.4	29.6
APG-8-4-70-d FS-1-PO1-SSII	17.3	102.7	4.27	20.08	0.37	21.6	17.8
APC-8-4-AMB-d PS-1-PO1-SSII	8.0	101.9	1.98	9.25	0.17	27.2	25.7
AP927-6-1-AMB-PS-1-PO1-SSII	34.7	30.3	7.28	23.69	1.83	25.4	9.4

Table F.1 Axial Stress at Failure ($\sigma^{p}_{z,f}$), Plug Length (L_c), Average ($\tau^{av}_{rz,i}$) and Exponential Extreme Shear Stresses ($\tau^{max}_{rz,i}$, $\tau^{min}_{rz,i}$), Top (w_t) and Bottom (w_b) Axial Plug Displacements at Failure.--Continued

Apache Leap Tuff Cylinder	$\sigma^{p}_{z,f}$ (MPa)	L_c (mm)	$\tau^{av}_{rz,i}$ * (MPa)	$\tau^{max}_{rz,i}$ ** (MPa)	$\tau^{min}_{rz,i}$ ** (MPa)	w_t (mm) x 10^2	w_b (mm) x 10^2
AP22-6-1-AMB-[a] PS-2-P01-SSII	32.1	29.1	7.01	22.17	1.90	12.7	8.4
APE-6-1-AMB-PS-1-P01-SSII	48.6	32.5	9.51	32.87	2.08	27.2	4.1
APG-6-1-AMB-PS-2-P01-SSII	30.7	31.3	6.24	20.82	1.49	17.8	4.8
APE-6-1-AMB-PS-2-P01-SSII	34.6	29.0	7.58	23.89	2.06	13.0	4.1
AP122-6-2-AMB-PS-2-P01-SSII	33.4	52.6	8.06	28.84	1.62	11.6	11.1
AP22-6-2-AMB-[g] PS-1-P01-SSII	31.6	49.9	8.04	27.34	1.84	22.9	17.3
APE-6-2-AMB-PS-1-P01-SSII	24.1	50.3	6.10	20.88	1.37	26.7	7.6
APE-6-2-AMB-PS-2-P01-SSII	29.6	49.7	7.57	25.63	1.75	29.1	13.4
AP22-6-2-[e,g] AMB-PS-2-P01-SSII	13.3	51.7	3.26	11.46	0.68	17.0	6.6
AP77-6-1-36-RD-1-P01-SSII	22.1	30.2	4.66	15.12	1.18	12.7	5.1

Table F.1 Axial Stress at Failure ($\sigma^{p}_{z,f}$), Plug Length (L_c), Average ($\tau^{av}_{rz,t}$) and Exponential Extreme Shear Stresses ($\tau^{max}_{rz,t}$, $\tau^{min}_{rz,t}$), Top (w_t) and Bottom (w_b) Axial Plug Displacements at Failure.--Continued

Apache Leap Tuff Cylinder	$\sigma^{p}_{z,f}$ (MPa)	L_c (mm)	$\tau^{av}_{rz,t}$ * (MPa)	$\tau^{max}_{rz,t}$ ** (MPa)	$\tau^{min}_{rz,t}$ ** (MPa)	w_t (mm) x 10^2	w_b (mm) x 10^2
AP921-6-1-36-RD-1-P01-SSII	31.3	28.6	6.94	21.65	1.93	20.1	4.1
APG-6-1-36-RD-1-P02-SSII	21.4	31.3	4.35	14.51	1.04	14.2	7.4
AP927-6-1-36-RD-2-P01-SSII	34.2	31.8	6.84	23.15	1.58	6.1	3.1
AP3-6-1-36-RD-2-P01-SSII	29.7	37.4	5.04	20.03	0.75	25.4	3.8
AP1-6-1-36-RD-1-P01-SSII	16.7	26.5	3.99	11.80	1.25	12.7	4.8
APA4-6-1-36-RD-1-P01-SSII	22.1	29.4	4.78	15.23	1.27	21.3	4.8
APG-6-2-70-g FS-1-P01-SSII	26.1	50.3	6.59	22.59	1.48	23.1	13.0
APG-6-2-70-c FS-2-P01-SSII	21.3	51.8	5.22	18.42	1.09	10.7	4.3
APE-8-4-70-FS-4-P01-SSII	11.0	94.4	2.95	12.75	0.34	13.0	6.9
APG-8-4-70-g FS-4-P02-SSII	11.0	102.7	2.71	12.75	0.23	30.5	29.7

Table F.1 Axial Stress at Failure ($\sigma^{p}_{z,f}$), Plug Length (L_c), Average ($\tau^{av}_{rz,l}$) and Exponential Extreme Shear Stresses ($\tau^{max}_{rz,l}$, $\tau^{min}_{rz,l}$), Top (w_t) and Bottom (w_b) Axial Plug Displacements at Failure.--Continued

Apache Leap Tuff Cylinder	$\sigma^{p}_{z,f}$ (MPa)	L_c (mm)	$\tau^{av}_{rz,l}$ * (MPa)	$\tau^{max}_{rz,l}$ ** (MPa)	$\tau^{min}_{rz,l}$ ** (MPa)	w_t (mm) x 10^2	w_b (mm) x 10^2
AP3-8-4-45-[d] FS-1-P01-SSII	15.4	96.0	4.07	17.86	0.44	9.4	6.3
APD-6-1-70- PS-3-P01-SSII	31.3	35.2	5.64	21.10	1.00	15.2	5.3
APA3-6-1-70- PS-3-P01-SSII	38.6	25.6	9.58	27.58	3.15	19.8	3.8
APA4-6-1-70- PS-3-P01-SSII	52.7	33.0	10.13	35.59	2.14	7.0	1.1
APA3-6-2-70- PS-2-P01-SSII	17.7	48.5	4.62	15.27	1.13	34.5	5.1
AP927-6-2-[d,f] RD-2-P01-SSII	22.0	51.7	5.39	18.98	1.13	18.0	3.1
AP5-6-2-AMB- RD-4-P01-SSII	26.3	49.5	6.75	22.78	1.57	7.6	4.8
APA3-6-1-90- FS-3-P03-SSII	16.0	32.2	3.15	10.80	0.71	12.7	7.6
AP1-6-2-AMB-[g] RD-1-P01-SSII	30.7	51.2	7.62	26.57	1.64	14.5	12.2
APH-8-4-45-[g] FS-1-P05-SSII	15.5	102.2	3.85	17.98	0.34	16.3	8.1

Table F.1 Axial Stress at Failure ($\sigma^{p}_{z,f}$), Plug Length (L_c), Average ($\tau^{av}_{rz,i}$) and Exponential Extreme Shear Stresses ($\tau^{max}_{rz,i}$, $\tau^{min}_{rz,i}$), Top (w_t) and Bottom (w_b) Axial Plug Displacements at Failure.--Continued

Apache Leap Tuff Cylinder	$\sigma^{p}_{z,f}$ (MPa)	L_c (mm)	$\tau^{av}_{rz,i}$ * (MPa)	$\tau^{max}_{rz,i}$ ** (MPa)	$\tau^{min}_{rz,i}$ ** (MPa)	w_t (mm) x 10^2	w_b (mm) x 10^2
APB-8-4-90-[d] FS-2-PO1-SSII	4.4	86.5	1.29	5.10	0.20	7.6	4.8
APH-8-4-90-g FS-1-PO1-SSII	6.6	103.5	1.61	7.61	0.13	21.3	0.5
APD-6-2-70-PS-3-PO1-SSII	26.3	51.0	6.56	22.77	1.42	25.7	8.4
APA3-6-2-70-PS-3-PO4-SSII	29.0	53.9	6.82	25.04	1.28	35.6	5.6
APE-8-4-AMB-RD-8-PO1-SSII	15.5	99.9	3.93	17.98	0.37	27.2	20.1
APE-8-4-70-PS-5-PO1-SSII	14.3	101.1	3.58	16.58	0.33	36.6	13.6
AP8-8-4-90-FS-3-PO1-SSII	8.5	105.3	2.05	9.88	0.16	12.7	3.3
APA5-6-1-AMB-RD-3-PO2-SSII	35.5	29.7	7.57	24.35	1.98	16.0	5.6
APA2-6-1-AMB-RD-1-PO1-SSII	35.1	30.2	7.38	24.01	1.87	21.6	2.8
APD-6-1-AMB-RD-1-PO3-SSII	35.6	30.3	7.47	24.35	1.89	20.3	3.6

Table F.1 Axial Stress at Failure ($\sigma^{p}_{z,f}$), Plug Length (L_c), Average ($\tau^{av}_{rz,t}$) and Exponential Extreme Shear Stresses ($\tau^{max}_{rz,t}$, $\tau^{min}_{rz,t}$), Top (w_t) and Bottom (w_b) Axial Plug Displacements at Failure.--Continued

Apache Leap Tuff Cylinder	$\sigma^{p}_{z,f}$ (MPa)	L_c (mm)	$\tau^{av}_{rz,t}$ * (MPa)	$\tau^{max}_{rz,t}$ ** (MPa)	$\tau^{min}_{rz,t}$ ** (MPa)	w_t (mm) x 10^2	w_b (mm) x 10^2
APJ-8-4-AMB-d RD-4-P01-SSII	15.5	93.9	4.19	17.98	0.49	34.3	23.9
APA5-6-2-36-RD-4-P03-SSII	24.4	50.2	6.16	21.07	1.39	18.5	9.9
AP113-6-2-36-RD-2-P01-SSII	22.0	47.0	5.95	19.08	1.56	9.4	8.9
APD-6-2-36-RD-2-P01-SSII	21.8	53.6	5.16	18.85	0.99	12.4	4.6
APA6-8-4-36-g RD-1-P02-SSII	11.0	80.7	3.45	12.77	0.64	11.7	1.5
API-8-4-36-d RD-1-P01-SSII	15.1	102.0	3.76	17.53	0.33	26.2	17.8
APM-8-4-AMB-d RD-2-P01-SSII	13.7	93.6	3.72	15.94	0.44	40.6	16.0
APJ-8-4-AMB-PS-3-P01-SSII	19.2	99.1	4.92	22.32	0.48	26.2	5.8
APM-8-4-AMB-PS-6-P01-SSII	16.7	97.9	4.34	19.45	0.44	27.9	8.9
APM-8-4-36-RD-1-P01-SSII	14.5	97.5	3.79	16.90	0.39	34.8	32.2

Table F.1 Axial Stress at Failure ($\sigma^{p}_{z,f}$), Plug Length (L_c), Average ($\tau^{av}_{rz,l}$) and Exponential Extreme Shear Stresses ($\tau^{max}_{rz,l}$, $\tau^{min}_{rz,l}$), Top (w_t) and Bottom (w_b) Axial Plug Displacements at Failure.--Continued

Apache Leap Tuff Cylinder	$\sigma^{p}_{z,f}$ (MPa)	L_c (mm)	$\tau^{av}_{rz,l}$ * (MPa)	$\tau^{max}_{rz,l}$ ** (MPa)	$\tau^{min}_{rz,l}$ ** (MPa)	w_t (mm) x 10^2	w_b (mm) x 10^2
APA-8-4-70-[d] PS-4-PO1-SSII	11.0	129.5	2.15	12.75	0.07	10.2	5.1
APM-8-4-70- PS-5-PO1-SSII	13.3	101.5	3.32	15.34	0.30	17.8	7.6
APA-8-4-44-[d] PS-5-PO1-SSII	20.6	103.6	5.05	23.91	0.42	25.9	25.1
APA5-6-1-AMB- FSS-1-PO1-SSII	29.0	29.2	6.29	19.97	1.69	17.8	5.8
AP1-6-1-AMB- FSS-2-PO1-SSII	20.7	25.7	5.12	14.78	1.67	11.9	2.0
APA3-6-1-AMB- FSS-4-PO2-SSII	29.0	26.7	6.88	20.43	2.11	17.8	7.6
APA2-6-1-AMB- FSS-4-PO2-SSII	26.9	28.5	5.98	18.64	1.67	16.6	5.3
APA2-6-2-AMB- FSS-1-PO1-SSII	25.0	50.8	6.25	21.64	1.37	14.0	3.1
APA77-6-2-AMB- FSS-1-PO1-SSII	12.8	49.8	3.26	11.05	0.75	23.9	7.9
APA4-6-2-AMB- FSS-1-PO1-SSII	20.0	53.4	4.75	17.26	0.92	26.7	5.1

Table F.1 Axial Stress at Failure ($\sigma^{p}_{z,f}$), Plug Length (L_c), Average ($\tau^{av}_{rz,i}$) and Exponential Extreme Shear Stresses ($\tau^{max}_{rz,i}$, $\tau^{min}_{rz,i}$), Top (w_t) and Bottom (w_b) Axial Plug Displacements at Failure.--Continued

Apache Leap Tuff Cylinder	$\sigma^{p}_{z,f}$ (MPa)	L_c (mm)	$\tau^{av}_{rz,i}$ * (MPa)	$\tau^{max}_{rz,i}$ ** (MPa)	$\tau^{min}_{rz,i}$ ** (MPa)	w_t (mm) x 10^2	w_b (mm) x 10^2
AP41-3-1/2-AMB-FS-7-PO1-SSII	43.4	14.5	9.50	29.95	2.58	13.2	N/A[h]
AP41-3-1/2-AMB-FS-10-PO1-SSII	43.4	14.2	9.70	30.11	2.73	10.2	N/A
AP41-3-1/2-AMB-FS-11-PO1-SSII	45.5	15.4	9.38	30.96	2.30	11.4	N/A
AP41-3-1/2-AMB-FS-7-PO2-SSII	43.4	13.7	10.05	30.40	2.99	10.2	N/A
AP852-3-1/2-AMB-FS-7-PO2-SSII	56.4	15.6	11.47	38.22	2.75	12.2	N/A
AP41-3-1/2-AMB-FS-11-PO2-SSII	43.4	13.4	10.28	30.58	3.16	11.4	N/A
AP41-3-1/2-AMB-FS-11-PO2-SSII	46.8	14.5	10.25	32.33	2.79	10.2	N/A
AP852-3-1/2-AMB-FS-5-PO1-SSII	53.8	15.3	11.16	36.63	2.77	17.8	N/A

Table F.1 Axial Stress at Failure ($\sigma^{p}_{z,f}$), Plug Length (L_c), Average ($\tau^{av}_{rz,l}$) and Exponential Extreme Shear Stresses ($\tau^{max}_{rz,l}$, $\tau^{min}_{rz,l}$), Top (w_t) and Bottom (w_b) Axial Plug Displacements at Failure.--Continued

Apache Leap Tuff Cylinder	$\sigma^{p}_{z,f}$ (MPa)	L_c (mm)	$\tau^{av}_{rz,l}$ * (MPa)	$\tau^{max}_{rz,l}$ ** (MPa)	$\tau^{min}_{rz,l}$ ** (MPa)	w_t (mm) x 10^2	w_b (mm) x 10^2
AP852-3-1/2-AMB-FS-5-PO2-SSII	52.9	15.5	10.87	35.92	2.63	18.0	N/A
AP41-3-1/2-AMB-FS-8-PO1-SSII	56.4	13.5	13.25	39.66	4.03	15.0	N/A
AP852-3-1/2-AMB-FS-7-PO1-SSII	53.8	16.3	10.47	36.33	2.28	14.0	N/A
AP41-3-1/2-AMB-FS-11-PO1-SSII	55.5	16.3	10.81	37.50	2.35	14.0	N/A
AP41-3-1/2-AMB-FS-9-PO1-SSII	50.3	12.8	12.47	35.90	4.10	11.2	N/A
AP852-3-1/2-AMB-FS-8-PO1-SSII	62.4	15.3	12.96	42.54	3.22	15.2	N/A
AP566-6-1-2-AMB-FS-8-PO1-SSII	78.1	53.3	9.31	52.70	0.37	25.4	N/A
AP631-6-1-2-AMB-FS-1-PO2-SSII	57.1	48.6	7.46	38.49	0.44	27.9	N/A

Table F.1 Axial Stress at Failure ($\sigma^{p}_{z,f}$), Plug Length (L_c), Average ($\tau^{av}_{rz,l}$) and Exponential Extreme Shear Stresses ($\tau^{max}_{rz,l}$, $\tau^{min}_{rz,l}$), Top (w_t) and Bottom (w_b) Axial Plug Displacements at Failure.--Continued

Apache Leap Tuff Cylinder	$\sigma^{p}_{z,f}$ (MPa)	L_c (mm)	$\tau^{av}_{rz,l}$ * (MPa)	$\tau^{max}_{rz,l}$ ** (MPa)	$\tau^{min}_{rz,l}$ ** (MPa)	w_t (mm) x 10^2	w_b (mm) x 10^2
APG-6-1-2-AMB-FS-3-PO1-SSII	57.1	53.1	6.83	38.49	0.27	22.9	N/A
AP566-6-1-2-AMB-FS-7-PO1-SSII	65.8	51.4	8.14	44.41	0.38	33.0	N/A
APA3-6-1-2-AMB-FS-3-PO4-SSII	70.2	50.0	8.91	47.37	0.47	30.5	N/A
APH-6-1-4-AMB-FS-7-PO1-SSII	171.2	101.4	10.72	115.46	0.00	83.3	N/A
AP566-6-1-4-AMB-FS-3-PO2-SSII	171.2	102.2	10.64	115.47	0.00	71.9	N/A
AP56A-6-1-4-AMB-FS-1-PO1-SSII	166.8	105.6	10.03	112.50	0.00	81.8	N/A

NOTES:

*Calculated from Eq. (2.54).

**Calculated from Eq. (2.48). The α parameter is obtained from Eq. (2.43a)

Table F.1 NOTES--Continued

[a]Vertical fracture in the top borehole of sample (prior to push-out testing).

[b]Plug accidentally drilled all the way through when drilling the hole to install the bottom arm; hole has a diameter of 1.59 mm.

[c]Vertical fracture on one side of inside borehole (prior to push-out testing).

[d]Sample shows tensile fracturing (a tensile fracture on one side of the tuff cylinder during push-out testing).

[e]Vertical fracture on both sides of inside borehole (prior to push-out testing).

[f]Horizontal fracture not going through the inside borehole (prior to push-out testing).

[g]Sample shows tensile splitting (a tensile fracture on both sides of the tuff cylinder during push-out testing).

[h]Data for bottom plug displacement not available.

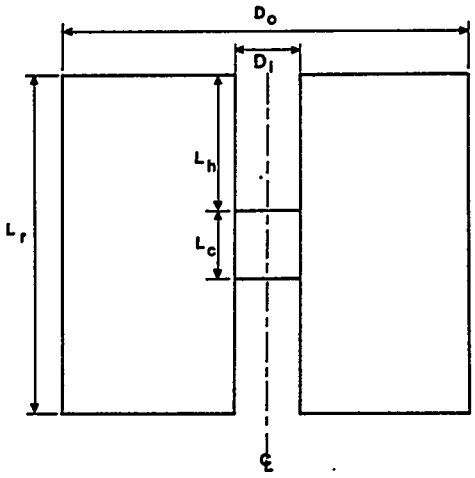

D_i = inside hole diameter
D_o = outside cylinder diam.
L_h = top hole length
L_c = rock bridge length
L_r = cylinder length

Not to scale.

Apache Leap Tuff Cylinder with Rock Bridge	L_r (mm)	L_h (mm)	L_c (mm)
AP31-6-1-AMB-RB-1-PO1[a]	99.6	36.4	25.8
AP46-6-1-AMB-RB-1-PO1[a]	143.1	62.8	26.2
AP31-6-1-AMB-RB-1-PO1[a]	111.6	41.9	31.8
APA5-6-1-AMB-RB-5-PO1[a]	92.9	28.8	35.7
AP56-6-1-AMB-RB-5-PO2[a]	87.6	26.4	21.1
AP566-6-2-AMB-RB-7-PO2[b]	119.0	35.8	45.5
APH-6-2-AMB-RB-6-PO2[b]	124.2	36.9	50.4
AP57-6-2-AMB-RB-2-PO2[b]	121.5	37.0	48.4
AP57-8-4-AMB-RB-1-PO1[c]	152.4	21.8	105.3
AP63-8-4-AMB-RB-2-PO2[c]	149.2	21.1	104.9
AP57-8-4-AMB-RB-1-PO1[c]	190.5	38.2	111.5

Figure F.2 Dimensions of the Apache Leap tuff cylinders with rock bridges.

Figure F.2 -- NOTES

NOTES:

[a]Samples with inside diameters (D_i) of 25.4 mm (1 in) and outside diameters (D_o) of 152.4 mm (6 in).

[b]Samples with inside diameters (D_i) of 50.8 mm (2 in) and outside diameters (D_o) of 152.4 mm (6 in).

[c]Samples with inside diameters (D_i) of 101.6 mm (4 in) and outside diameters (D_o) of 187.3 mm (7.375 in).

Table F.2 Axial Stress at Failure ($\sigma^{p}_{z,f}$), Rock Bridge Length (L_c), Average ($\tau^{av}_{rz,l}$ and Exponential Extreme Shear Stresses ($\tau^{max}_{rz,l}$, $\tau^{min}_{rz,l}$) at Failure for Apache Leap Tuff Cylinders with Rock Bridges. The maximum exponential shear stress occurs at the loaded end of the rock bridge (i.e. at z = 0); the minimum exponential shear stress occurs at the bottom (i.e. at z = L_c) of the rock bridge.

Apache Leap Tuff Cylinder with Rock Bridge	$\sigma^{p}_{z,f}$ (MPa)	L_c (mm)	$\tau^{av}_{rz,l}$* (MPa)	$\tau^{max}_{rz,l}$ (MPa)	$\tau^{min}_{rz,l}$ (MPa)
AP31-6-1-AMB-RB-1-P01	298.5	25.8	73.51	212.68	23.93
AP46-6-1-AMB-RB-1-P01	162.4	26.2	39.34	115.20	12.50
AP31-6-1-AMB-RB-1-P01	122.9	31.8	24.52	83.09	5.65
APA5-6-1-AMB-RB-5-P01	408.2	35.7	72.68	275.61	12.47
AP56-6-1-AMB-RB-5-P02	368.7	21.1	111.18	278.80	46.73
AP566-6-2-AMB-RB-7-P02	279.8	45.5	78.16	242.49	22.03
APH-6-2-AMB-[a,c] RB-6-P01	114.1	50.4	28.76	98.70	6.42
AP57-6-2-AMB-[a,c] RB-2-P02	104.2	48.4	27.37	90.22	6.74
AP57-8-4-AMB-[b] RB-1-P01	79.0	105.3	19.06	91.84	1.48
AP63-8-4-AMB-RB-2-P02	238.7	104.9	57.79	277.42	4.57
AP57-8-4-AMB-RB-1-P01	142.1	111.5	32.38	165.17	2.01

*Calculated from Eq. (2.54).
**Calculated from Eq. (2.48).
[a]Vertical fracture running through the center of the specimen prior to push-out testing.
[b]Sample shows tensile fracturing (a tensile fracture on one side of the push-out cylinder).
[c]Sample shows tensile splitting (a tensile fracture on both sides of the push-out cylinder).

APPENDIX G

WEIGHT PARAMETERS OF APACHE LEAP TUFF CYLINDERS PRIOR TO AND FOLLOWING PUSH-OUT TESTING

Weight Parameters of Apache Leap Tuff Cylinders Prior to and Following Push-Out Testing. The parameters are used to determine the degree of saturation, water content, void ratio, porosity, and density of push-out cylinders. Detailed procedure for the determination of the degree of saturation, void ratio, etc., is given in Appendix E.

Apache Leap Tuff Cylinder	W_3[a] (g)	W_6[b] (g)	W_9[c] (g)	W_{14f}[d] (g)	W_{18}[e] (g)
AP3-6-1-AMB-PS-4-PO2-SSII	4950.5	4968.0	4998.0	5021.4	5005.0
AP3-6-1-AMB-PS-2-PO1-SSII	4541.0	4558.5	4558.5	4666.2	4646.0
AP3-6-1-AMB-FS-3-PO1-SSII	4293.0	4316.0	4347.0	4485.0	4460.5
AP3-6-1-AMB-FS-4-PO1-SSII	4719.0	4743.5	4773.5	4920.0	4900.5
AP3-6-1-AMB-FS-1-PO1-SSII	3349.5	3367.1	3400.0	3505.0	3485.0
AP3-6-1-45-FS-1-PO2-SSII	3579.0	3595.0	3625.0	3728.5	3706.0
AP8-6-1-45-FS-1-PO1-SSII	4192.5	4211.5	4241.8	4374.0	4343.5
AP8-6-1-45-FS-4-PO1-SSII	4367.5	4386.5	4416.5	4543.5	4511.0
AP8-6-2-AMB-FS-3-PO1-SSII	4771.5	4846.5	5043.0	5213.5	5139.5
AP8-6-1-45-FS-1-PO2-SSII	4147.5	4164.0	4193.0	4339.5	4308.5
AP8-6-1-45-FS-2-PO1-SSII	4117.0	4136.5	4166.5	4300.0	4268.0
AP8-6-1-70-FS-2-PO2-SSII	4222.5	4240.0	4268.3	4406.0	4364.0
AP5-6-1-70-FS-1-PO1-SSII	3905.5	3922.0	3951.0	4086.0	4040.0
AP5-6-1-70-FS-2-PO2-SSII	4094.5	4110.0	4139.5	4270.0	4226.0
AP3-6-2-AMB-FS-3-PO1-SSII	3904.5	3972.5	4176.8	4302.0	4213.0
AP3-6-2-AMB-FS-4-PO1-SSII	4299.0	4368.0	4564.0	4684.0	4602.0
AP8-6-2-45-FS-1-PO1-SSII	3805.0	3865.0	4062.0	4196.0	4104.0
AP8-6-2-45-FS-4-PO1-SSII	3964.0	4035.0	4227.0	4367.0	4259.0
AP8-6-2-45-FS-4-PO2-SSII	3765.0	3838.0	4032.0	4167.0	4071.0
AP3-6-2-70-FS-2-PO1-SSII	4123.0	4196.0	4389.0	4521.0	4418.0
AP5-6-1-44-PS-3-PO2-SSII	4028.0	4045.0	4076.0	4109.0	4090.0
AP5-6-1-44-PS-4-PO1-SSII	4048.0	4066.0	4097.0	4139.0	4112.0
AP5-6-1-70-FS-3-PO4-SSII	3353.0	3373.0	3404.0	3516.0	3481.0
AP5-6-1-44-PS-2-PO3-SSII	3904.0	3922.0	3951.0	3987.0	3968.0
AP5-6-1-AMB-FS-1-PO2-SSII	4097.0	4115.0	4146.0	4294.0	4271.0
AP5-6-1-AMB-FS-3-PO1-SSII	3561.0	3578.0	3608.0	3735.0	3713.0

Weight Parameters of Apache Leap Tuff Cylinders--Continued

Apache Leap Tuff Cylinder	W_3[a] (g)	W_6[b] (g)	W_9[c] (g)	W_{14f}[d] (g)	W_{18}[e] (g)
AP5-6-1-AMB-FS-2-PO3-SSII	4047.0	4064.0	4094.0	4242.0	4220.0
AP5-6-1-90-FS-2-PO1-SSII	3548.5	3565.0	3597.0	3713.0	3670.0
AP5-6-1-90-FS-4-PO2-SSII	5569.0	5587.0	5616.0	5814.0	5750.0
AP8-6-2-90-FS-2-PO2-SSII	3818.0	3894.0	4090.0	4223.0	4144.0
AP8-6-2-90-FS-2-PO1-SSII	3721.0	3797.0	3991.0	4121.0	3999.0
AP5-6-2-90-FS-2-PO2-SSII	3704.0	3780.0	3975.0	4101.0	3996.0
AP5-6-2-90-FS-3-PO2-SSII	3648.0	3725.0	3918.0	4038.0	3921.0
AP5-6-2-44-PS-2-PO3-SSII	3667.0	3744.0	3937.0	4006.0	3927.0
AP5-6-2-44-PS-4-PO2-SSII	5082.0	5158.0	5352.0	5423.0	5341.0
AP5-6-2-44-PS-1-PO2-SSII	3716.0	3792.0	3990.0	4039.0	3957.0
AP113-8-4-AMB-FS-1-PO1-SSII	8657.0	9069.0	10661.0	10841.0	10419.0
AP121-8-4-AMB-FS-1-PO1-SSII	9438.0	9867.0	11460.0	11691.0	11248.0
AP22-6-1-44-PS-1-PO1-SSII	5661.0	5678.0	5708.0	5775.0	5752.0
AP122-6-1-44-PS-2-PO1-SSII	6546.0	6564.0	6599.0	6635.0	6617.0
AP5-6-2-44-PS-3-PO2-SSII	3540.0	3613.0	3809.0	3848.0	3771.0
AP114-8-4-AMB-FS-2-PO1-SSII	6133.0	6563.0	7938.0	8068.0	7630.0
AP920-8-4-44-PS-1-PO1-SSII	7337.0	7769.0	9351.0	9475.0	9031.0
AP114-8-4-45-FS-1-PO1-SSII	6372.0	6799.0	8304.0	8355.0	7903.0
APB-8-4-44-PS-1-PO1-SSII	7746.0	8174.0	9731.0	9897.0	9452.0
APG-8-4-70-FS-1-PO1-SSII	9316.0	9753.0	11338.0	11519.0	11049.0
APC-8-4-AMB-PS-1-PO1-SSII	8089.0	8515.0	10100.0	10309.0	9876.0
AP927-6-1-AMB-PS-1-PO1-SSII	5987.0	6006.0	6036.0	6132.0	6113.0
AP22-6-1-AMB-PS-2-PO1-SSII	5150.0	5169.0	5199.0	5253.0	5233.0
APE-6-1-AMB-PS-1-PO1-SSII	6927.0	6946.0	6978.0	7032.0	7009.0
APG-6-1-AMB-PS-2-PO1-SSII	5302.0	5318.0	5348.0	5414.0	5395.0
APE-6-1-AMB-PS-2-PO1-SSII	7007.0	7025.0	7054.0	7110.0	7090.0
AP122-6-2-AMB-PS-2-PO1-SSII	5920.0	5994.0	6197.0	6243.0	6166.0
AP22-6-2-AMB-PS-1-PO1-SSII	5117.0	5193.0	5392.0	5464.0	5385.0
APE-6-2-AMB-PS-1-PO1-SSII	6290.0	6364.0	6562.0	6633.0	6556.0

Weight Parameters of Apache Leap Tuff Cylinders--Continued

Apache Leap Tuff Cylinder	W_3[a] (g)	W_6[b] (g)	W_9[c] (g)	W_{14f}[d] (g)	W_{18}[e] (g)
APE-6-2-AMB-PS-2-P01-SSII	6341.0	6415.0	6608.0	6681.0	6604.0
AP22-6-2-AMB-PS-2-P01-SSII	4668.0	4744.0	4951.0	5037.0	4959.0
AP77-6-1-36-RD-1-P01-SSII	6441.0	6463.0	6490.0	6531.0	6512.0
AP921-6-1-36-RD-1-P01-SSII	4428.0	4448.0	4478.0	4496.0	4479.0
APG-6-1-36-RD-1-P02-SSII	5374.0	5390.0	5420.0	5448.0	5430.0
AP927-6-1-36-RD-2-P01-SSII	4522.0	4542.0	4574.0	4598.0	4583.0
AP3-6-1-36-RD-2-P01-SSII	6761.0	6778.0	6808.0	6826.0	6809.0
AP1-6-1-36-RD-1-P01-SSII	5592.0	5609.0	5634.0	5666.0	5648.0
APA4-6-1-36-RD-1-P01-SSII	6540.0	6557.0	6585.0	6597.0	6580.0
APG-6-2-70-FS-1-P01-SSIIX	4870.0	4949.0	5145.0	5329.0	5208.0
APG-6-2-70-FS-2-P01-SSIIX	4807.0	4886.0	5093.0	5271.0	5160.0
APE-8-4-70-FS-4-P01-SSII	8395.0	8832.0	10341.0	10622.0	10137.0
APG-8-4-70-FS-4-P02-SSII	7055.0	7477.0	9004.0	9182.0	8737.0
AP3-8-4-45-FS-1-P01-SSII	6529.0	6943.0	8443.0	8593.0	8169.0
APD-6-1-70-PS-3-P01-SSII	6473.0	6489.0	6522.0	6579.0	6559.0
APA3-6-1-70-PS-3-P01-SSII	4790.0	4800.0	4835.0	4883.0	4858.0
APA4-6-1-70-PS-3-P01-SSII	6059.0	6076.0	6107.0	6152.0	6132.0
APA3-6-2-70-PS-2-P01-SSII	6098.0	6175.0	6378.0	6458.0	6349.0
AP927-6-2-AMB-RD-2-P01-SSII	4103.0	4168.0	4366.0	4391.0	4326.0
AP5-6-2-AMB-RD-4-P01-SSII	3667.0	3741.0	3939.0	3947.0	3874.0
APA3-6-1-90-FS-3-P03-SSII	4292.0	4307.0	4337.0	4442.0	4405.0
AP1-6-2-AMB-RD-1-P01-SSII	5079.0	5147.0	5342.0	5361.0	5294.0
APH-8-4-45-FS-1-P05-SSII	6735.0	6976.0	8567.0	8771.0	8510.0
APB-8-4-90-FS-2-P01-SSII	5218.0	5450.0	6842.0	7032.0	6738.0
APH-8-4-90-FS-1-P01-SSII	6257.0	6504.0	8068.0	8256.0	7904.0
APD-6-2-70-PS-3-P01-SSII	5886.00	5952.0	6143.0	6221.0	6143.0
APA3-6-2-70-PS-3-P04-SSII	4360.0	4427.0	4630.0	4673.0	4598.0
APE-8-4-AMB-RD-8-P01-SSII	8156.0	8577.0	10142.0	10207.0	9785.0
APE-8-4-70-PS-5-P01-SSII	9188.0	9449.0	11024.0	11182.0	10919.0

Weight Parameters of Apache Leap Tuff Cylinders--Continued

Apache Leap Tuff Cylinder	W_3[a] (g)	W_6[b] (g)	W_9[c] (g)	W_{14f}[d] (g)	W_{18}[e] (g)
AP8-8-4-90-FS-3-PO1-SSII	7757	8185	9820	10020	9520
APA5-6-1-AMB-RD-3-PO2-SSII	5828	5844	5873	5881	5865
APA2-6-1-AMB-RD-1-PO1-SSII	5624	5640	5669	5679	5662
APD-6-1-AMB-RD-1-PO3-SSII	5166	5183	5212	5224	5209
APJ-8-4-AMB-RD-4-PO1-SSII	5668	5910	7386	7348	7105
APA5-6-2-36-RD-4-PO3-SSII	4289	4364	4557	4576	4501
AP113-6-2-36-RD-2-PO1-SSII	4953	5028	5208	5211	5134
APD-6-2-36-RD-2-PO1-SSII	3833	3906	4104	4210	4044
APA6-8-4-36-RD-1-PO2-SSII	4922	5172	6496	6448	6196
API-8-4-36-RD-1-PO1-SSII	7916	8343	9944	9900	9473
APM-8-4-AMB-RD-2-PO1-SSII	7334	7762	9250	9244	8815
APJ-8-4-AMB-PS-3-PO1-SSII	6883	7309	8858	8927	8499
APM-8-4-AMB-PS-6-PO1-SSII	9168	9414	10948	11048	10803
APM-8-4-36-RD-1-PO1-SSII	8524	8952	10513	10512	10085
APA-8-4-70-PS-4-PO1-SSII	8671	9095	10750	10898	10453
APM-8-4-70-PS-5-PO1-SSII	8540	8961	10558	10654	10229
APA-8-4-44-PS-5-PO1-SSII	9553	9978	11613	11753	11325
APA5-6-1-AMB-FSS-1-PO1-SSII	5576	5727	5753	5755	5733
AP1-6-1-AMB-FSS-2-PO1-SSII	5159	5407	5431	5433	5414
APA3-6-1-AMB-FSS-4-PO2-SSII	4883	5024	5050	5051	5031
APA2-6-1-AMB-FSS-4-PO1-SSII	5089	5234	5262	5263	5244
APA2-6-2-AMB-FSS-1-PO1-SSII	5105	5306	5500	5509	5433
AP77-6-2-AMB-FSS-1-PO1-SSII	5840	6191	6388	6396	6327
APA4-6-2-AMB-FSS-1-PO1-SSII	5908	6132	6324	6331	6262
AP41-3-1/2-AMB-FS-7-PO1-SSII	767	772	775	804	797
AP41-3-1/2-AMB-FS-10-PO1-SSII	778	782	785	813	808
AP41-3-1/2-AMB-FS-11-PO1-SSII	836	841	844	876	871
AP41-3-1/2-AMB-FS-7-PO2-SSII	789	794	798	826	820
AP852-3-1/2-AMB-FS-7-PO2-SSII	801	806	810	827	820

APA3-6-1-90-FS-3-P03-SSII

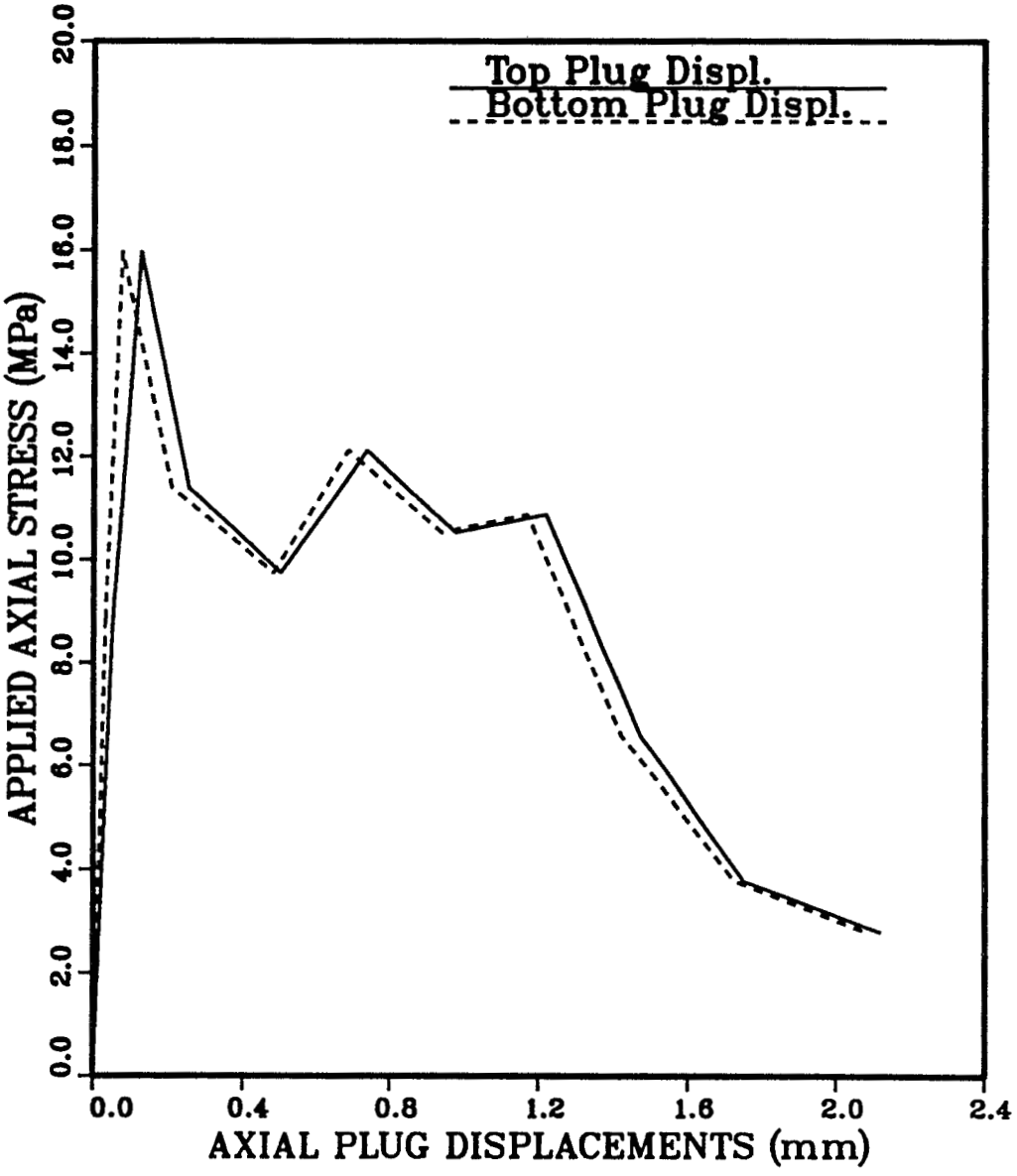

AP1-6-2-AMB-RD-1-P01-SSII

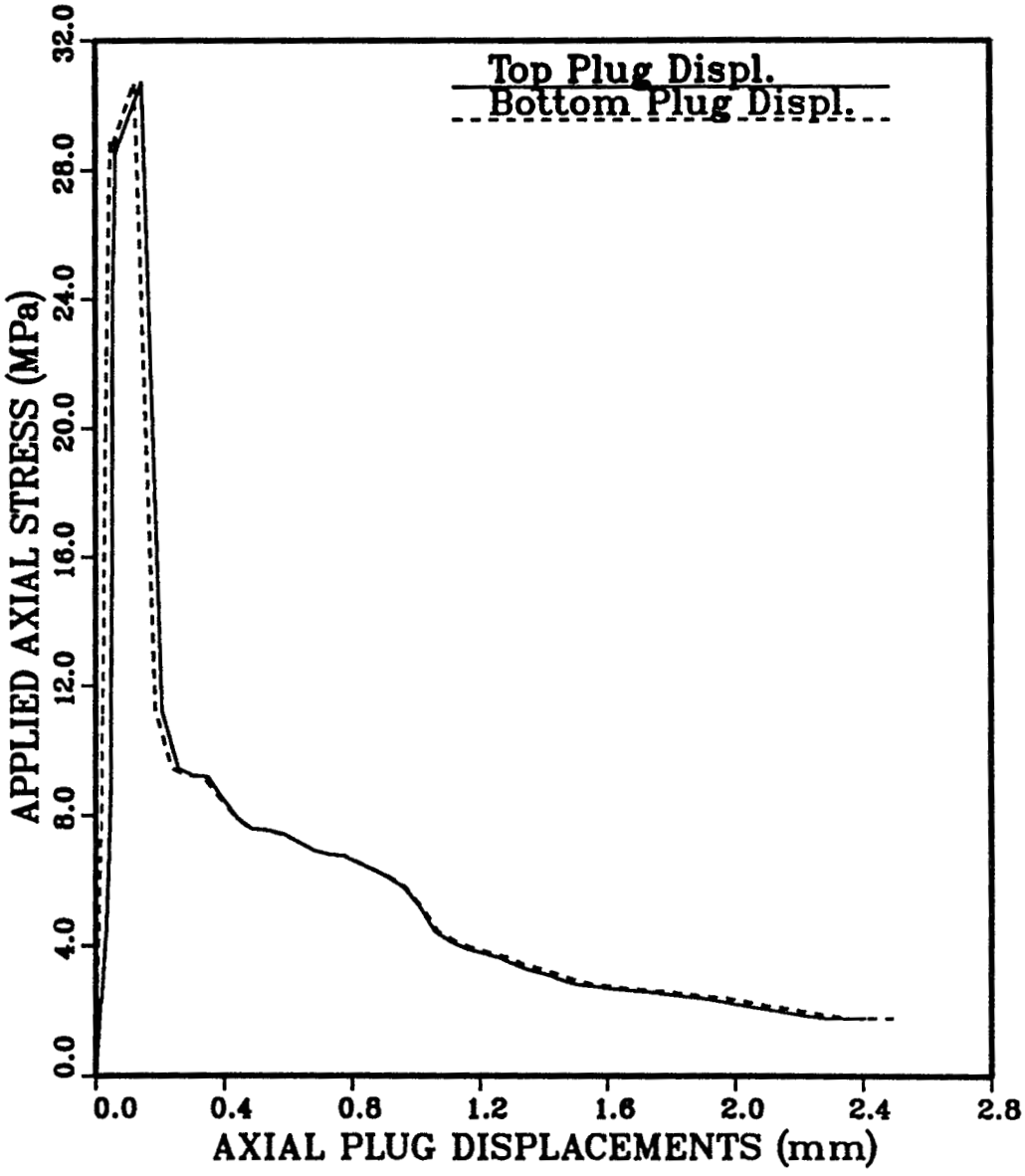

Weight Parameters of Apache Leap Tuff Cylinders--Continued

Apache Leap Tuff Cylinder	W_3[a] (g)	W_6[b] (g)	W_9[c] (g)	W_{14f}[d] (g)	W_{18}[e] (g)
AP41-3-1/2-AMB-FS-11-PO3-SSII	752	757	761	789	783
AP41-3-1/2-AMB-FS-11-PO2-SSII	801	806	810	842	836
AP852-3-1/2-AMB-FS-5-PO1-SSII	825	830	834	855	849
AP852-3-1/2-AMB-FS-5-PO2-SSII	784	789	793	812	807
AP41-3-1/2-AMB-FS-8-PO1-SSII	716	721	725	751	745
AP852-3-1/2-AMB-FS-7-PO1-SSII	794	799	804	822	817
AP41-3-1/2-AMB-FS-11-PO1-SSII	736	740	745	775	770
AP41-3-1/2-AMB-FS-9-PO1-SSII	766	771	775	800	795
AP852-3-1/2-AMB-FS-8-PO1-SSII	980	985	989	1009	1004
AP566-6-1-2-AMB-FS-8-PO1-SSII	6090	6107	6162	6248	6223
AP631-6-1-2-AMB-FS-1-PO2-SSII	5561	5571	5623	5833	5814
APG-6-1-2-AMB-FS-3-PO1-SSII	4696	4714	4763	4941	4921
AP566-6-1-2-AMB-FS-7-PO1-SSII	5598	5614	5666	5763	5744
APA3-6-1-2-AMB-FS-3-PO4-SSII	4290	4317	4366	4416	4396
APH-6-1-4-AMB-FS-7-PO1-SSII	7221	7241	7344	7495	7474
AP566-6-1-4-AMB-FS-3-PO2-SSII	8346	8363	8464	8588	8572
AP56A-6-1-4-AMB-FS-1-PO1-SSII	7348	7384	7490	7602	7580

NOTES:

[a]W_3 = weight of the dry tuff cylinder (g)

[b]W_6 = weight of the dry tuff cylinder + rubber stopper + any moisture absorbed during cooling (g)

[c]W_9 = w6 + weight of the cement slurry (g)

[d]W_{14f} = weight of the plugged tuff cylinder after it has been left underwater or in the environmental chamber (at desired temperature and relative humidity) or at room conditions (24 ± 2°C, 36 ± 2% r.h.) for 8 days.

[e]W_{18} = weight of the plugged tuff cylinder following push-out testing.

APPENDIX H

THE DEGREE OF SATURATION, WATER CONTENT, VOID RATIO, POROSITY, AND DENSITY OF APACHE LEAP TUFF CYLINDERS PRIOR TO AND FOLLOWING PUSH-OUT TESTING

The Degree of Saturation, Water Content, Void Ratio, Porosity, and Density of Apache Leap Tuff Cylinders Prior to and Following Push-Out Testing. Detailed procedure for the determination of the degree of saturation, water content, etc., is given in Appendix E.

Apache Leap Tuff Cylinder	S_p[1] (%)	S_f[1] (%)	w_p[2] (%)	w_f[2] (%)	e_p[3]	e_f[3]	n_p[4] (%)	n_f[4] (%)	ρ_p[5] (g/cc)	ρ_f[5] (g/cc)
AP3-6-1-AMB-PS-4-PO2-SSII	12.73	12.75	0.68	0.68	0.14	0.14	12.6	12.6	2.38	2.38
AP3-6-1-AMB-PS-2-PO1-SSII	34.71	33.36	1.94	1.85	0.15	0.15	13.1	13.0	2.40	2.39
AP3-6-1-AMB-FS-3-PO1-SSII	68.72	65.23	3.57	3.39	0.14	0.14	12.3	12.3	2.46	2.45
AP3-6-1-AMB-FS-4-PO1-SSII	65.63	64.33	3.47	3.39	0.14	0.14	12.5	12.5	2.45	2.44
AP3-6-1-AMB-FS-1-PO1-SSII	61.84	60.14	3.45	3.35	0.15	0.15	13.1	13.1	2.44	2.43
AP3-6-1-45-FS-1-PO2-SSII	96.68	91.51	3.14	2.96	0.09	0.09	8.1	8.0	2.57	2.56
AP8-6-1-45-FS-1-PO1-SSII	59.27	53.18	3.43	3.09	0.16	0.16	13.5	13.6	2.43	2.41
AP8-6-1-45-FS-4-PO1-SSII	98.51	89.15	3.16	2.80	0.09	0.08	8.0	7.8	2.57	2.56
AP8-6-2-AMB-FS-3-PO1-SSII	73.99	71.65	4.95	4.75	0.18	0.18	15.3	15.2	2.44	2.41
AP8-6-1-45-FS-1-PO2-SSII	64.22	58.14	3.75	3.39	0.16	0.16	13.6	13.6	2.43	2.41
AP8-6-1-45-FS-2-PO1-SSII	63.40	56.51	3.54	3.15	0.15	0.15	13.1	13.1	2.44	2.42
AP8-6-1-70-FS-2-PO2-SSII	62.60	51.74	3.49	2.88	0.15	0.15	13.1	13.1	2.44	2.42
AP5-6-1-70-FS-1-PO1-SSII	72.71	57.91	3.68	2.92	0.14	0.14	12.0	12.0	2.47	2.45
AP5-6-1-70-FS-2-PO2-SSII	90.75	72.38	3.38	2.70	0.10	0.10	9.2	9.2	2.55	2.52
AP3-6-2-AMB-FS-3-PO1-SSII	82.90	73.09	4.72	4.16	0.15	0.15	13.4	13.4	2.50	2.45
AP3-6-2-AMB-FS-4-PO1-SSII	71.05	65.22	4.17	3.80	0.16	0.16	13.7	13.6	2.47	2.43
AP8-6-2-45-FS-1-PO1-SSII	76.37	64.06	5.02	4.15	0.18	0.18	15.1	15.0	2.45	2.40
AP8-6-2-45-FS-4-PO1-SSII	99.15	86.69	4.89	3.98	0.13	0.12	11.8	11.1	2.55	2.51
AP8-6-2-45-FS-4-PO2-SSII	75.06	66.56	5.08	4.43	0.18	0.18	15.5	15.3	2.45	2.40
AP3-6-2-70-FS-2-PO1-SSII	89.97	76.94	4.55	3.82	0.14	0.13	12.1	11.9	2.53	2.48
AP5-6-1-44-PS-3-PO2-SSII	32.76	32.07	1.67	1.62	0.14	0.14	12.1	12.0	2.41	2.40
AP5-6-1-44-PS-4-PO1-SSII	36.43	31.47	1.96	1.69	0.15	0.14	12.7	12.6	2.40	2.38
AP5-6-1-70-FS-3-PO4-SSII	66.48	56.56	3.73	3.16	0.15	0.15	13.2	13.1	2.45	2.42
AP5-6-1-44-PS-2-PO3-SSII	44.71	43.74	1.63	1.58	0.10	0.10	9.0	8.9	2.50	2.49
AP5-6-1-AMB-FS-1-PO2-SSII	74.98	72.57	3.85	3.71	0.14	0.14	12.2	12.1	2.47	2.46
AP5-6-1-AMB-FS-3-PO1-SSII	70.41	68.07	3.81	3.67	0.15	0.15	12.7	12.7	2.46	2.45
AP5-6-1-AMB-FS-2-PO3-SSII	97.85	94.71	3.89	3.75	0.11	0.11	9.7	9.7	2.54	2.53

The Degree of Saturation, Water Content, Void Ratio, Porosity, and Density of Apache Leap Tuff Push-Out Cylinders--Continued

Apache Leap Tuff Cylinder	S_p[1] (%)	S_f[1] (%)	w_p[2] (%)	w_f[2] (%)	e_p[3]	e_f[3]	n_p[4] (%)	n_f[4] (%)	ρ_p[5] (g/cc)	ρ_f[5] (g/cc)
AP5-6-1-90-FS-2-PO1-SSII	67.31	53.51	3.52	2.79	0.14	0.14	12.4	12.3	2.46	2.43
AP5-6-1-90-FS-4-PO2-SSII	68.60	52.86	3.72	2.88	0.15	0.15	12.8	12.8	2.45	2.42
AP8-6-2-90-FS-2-PO2-SSII	77.59	75.18	5.00	4.84	0.17	0.17	14.9	14.9	2.47	2.42
AP8-6-2-90-FS-2-PO1-SSII	76.06	57.63	5.00	3.76	0.18	0.18	15.1	15.0	2.46	2.39
AP5-6-2-90-FS-2-PO2-SSII	74.23	62.45	4.96	4.12	0.18	0.18	15.3	15.2	2.45	2.40
AP5-6-2-90-FS-3-PO2-SSII	75.09	58.92	4.86	3.71	0.18	0.17	14.9	14.6	2.46	2.40
AP5-6-2-44-PS-2-PO3-SSII	64.08	63.60	3.48	3.35	0.15	0.14	12.9	12.5	2.49	2.45
AP5-6-2-44-PS-4-PO2-SSII	40.70	38.84	2.56	2.41	0.17	0.17	14.6	14.4	2.41	2.38
AP5-6-2-44-PS-1-PO2-SSII	45.53	43.05	2.93	2.72	0.17	0.17	14.9	14.6	2.42	2.38
AP113-8-4-AMB-FS-1-PO1-SSII	64.40	63.27	7.01	6.89	0.30	0.30	23.0	23.0	2.35	2.26
AP121-8-4-AMB-FS-1-PO1-SSII	83.83	81.11	6.98	6.83	0.23	0.23	18.6	18.7	2.48	2.38
AP22-6-1-44-PS-1-PO1-SSII	31.82	29.22	1.36	1.24	0.12	0.11	10.4	10.3	2.46	2.45
AP122-6-1-44-PS-2-PO1-SSII	18.91	17.86	0.76	0.71	0.11	0.11	9.8	9.7	2.46	2.46
AP5-6-2-44-PS-3-PO2-SSII	55.88	55.44	2.75	2.62	0.13	0.13	11.8	11.4	2.51	2.47
AP114-8-4-AMB-FS-2-PO1-SSII	84.32	82.25	8.02	7.86	0.26	0.26	20.7	20.8	2.49	2.35
AP920-8-4-44-PS-1-PO1-SSII	78.50	76.80	7.42	7.25	0.26	0.26	20.6	20.6	2.45	2.34
AP114-8-4-45-FS-1-PO1-SSII	95.85	91.61	7.11	6.75	0.20	0.20	16.9	16.9	2.58	2.44
APB-8-4-44-PS-1-PO1-SSII	87.72	85.16	7.50	7.26	0.23	0.23	19.0	19.0	2.50	2.38
APG-8-4-70-FS-1-PO1-SSII	84.77	80.02	6.58	6.22	0.21	0.21	17.5	17.5	2.50	2.40
APC-8-4-AMB-PS-1-PO1-SSII	73.60	73.44	7.74	7.65	0.29	0.29	22.4	22.2	2.39	2.30
AP927-6-1-AMB-PS-1-PO1-SSII	29.51	28.76	1.80	1.75	0.17	0.16	14.2	14.1	2.37	2.36
AP22-6-1-AMB-PS-2-PO1-SSII	22.99	21.93	1.26	1.21	0.15	0.15	12.9	12.9	2.39	2.38
APE-6-1-AMB-PS-1-PO1-SSII	18.86	17.21	0.95	0.86	0.14	0.14	12.0	11.9	2.41	2.40
APG-6-1-AMB-PS-2-PO1-SSII	25.81	24.49	1.43	1.36	0.15	0.15	13.1	13.0	2.39	2.38
APE-6-1-AMB-PS-2-PO1-SSII	25.44	24.31	0.94	0.90	0.10	0.10	9.1	9.1	2.48	2.48
AP122-6-2-AMB-PS-2-PO1-SSII	44.81	42.93	1.82	1.75	0.11	0.11	9.9	10.0	2.51	2.48
AP22-6-2-AMB-PS-1-PO1-SSII	46.57	44.53	2.59	2.50	0.15	0.15	13.1	13.2	2.45	2.41
APE-6-2-AMB-PS-1-PO1-SSII	34.32	33.49	2.08	2.02	0.16	0.16	14.1	14.0	2.40	2.37

The Degree of Saturation, Water Content, Void Ratio, Porosity, and Density of Apache Leap Tuff Push-Out Cylinders--Continued

Apache Leap Tuff Cylinder	S_p[1] (%)	S_f[1] (%)	w_p[2] (%)	w_f[2] (%)	e_p[3]	e_f[3]	n_p[4] (%)	n_f[4] (%)	ρ_p[5] (g/cc)	ρ_f[5] (g/cc)
APE-6-2-AMB-PS-2-P01-SSII	54.84	54.11	2.07	2.01	0.10	0.10	9.3	9.1	2.53	2.51
AP22-6-2-AMB-PS-2-P01-SSII	50.58	49.64	3.17	3.09	0.17	0.17	14.5	14.4	2.43	2.39
AP77-6-1-36-RD-1-P01-SSII	12.35	11.91	0.84	0.81	0.18	0.18	15.6	15.5	2.31	2.30
AP921-6-1-36-RD-1-P01-SSII	13.45	13.05	0.70	0.68	0.14	0.14	12.4	12.4	2.39	2.38
APG-6-1-36-RD-1-P02-SSII	11.49	10.87	0.69	0.65	0.16	0.16	14.0	14.0	2.35	2.34
AP927-6-1-36-RD-2-P01-SSII	12.95	13.31	0.84	0.86	0.17	0.17	14.8	14.8	2.33	2.32
AP3-6-1-36-RD-2-P01-SSII	10.82	10.47	0.42	0.40	0.10	0.10	9.4	9.4	2.46	2.46
AP1-6-1-36-RD-1-P01-SSII	11.64	11.12	0.73	0.69	0.17	0.17	14.4	14.4	2.33	2.33
APA4-6-1-36-RD-1-P01-SSII	9.38	8.97	0.33	0.32	0.10	0.10	8.7	8.7	2.48	2.47
APG-6-2-70-FS-1-P01-SSII	65.25	52.80	5.05	4.06	0.20	0.20	16.9	16.8	2.32	2.27
APG-6-2-70-FS-2-P01-SSII	66.02	56.10	5.03	4.26	0.20	0.20	16.7	16.6	2.33	2.28
APE-8-4-70-FS-4-P01-SSII	86.53	80.24	8.14	7.52	0.25	0.25	20.0	19.9	2.40	2.29
APG-8-4-70-FS-4-P02-SSII	73.72	70.95	8.17	7.86	0.30	0.30	22.8	22.8	2.33	2.22
AP3-8-4-45-FS-1-P01-SSII	81.43	79.98	8.29	8.12	0.27	0.27	21.4	21.3	2.39	2.27
APD-6-1-70-PS-3-P01-SSII	17.66	16.36	1.05	0.97	0.16	0.16	13.5	13.5	2.29	2.28
APA3-6-1-70-PS-3-P01-SSII	26.66	22.56	1.08	0.91	0.11	0.11	9.6	9.5	2.40	2.38
APA4-6-1-70-PS-3-P01-SSII	22.86	20.87	0.93	0.85	0.11	0.11	9.6	9.6	2.39	2.38
APA3-6-2-70-PS-2-P01-SSII	51.38	39.07	2.35	1.78	0.12	0.12	10.7	10.7	2.42	2.38
AP927-6-2-AMB-RD-2-P01-SSII	23.79	23.41	2.09	2.05	0.23	0.23	18.8	18.7	2.21	2.18
AP5-6-2-AMB-RD-4-P01-SSII	27.87	27.70	1.89	1.86	0.18	0.18	15.1	15.0	2.31	2.27
APA3-6-1-90-FS-3-P03-SSII	62.33	50.39	2.65	2.14	0.11	0.11	10.0	10.0	2.42	2.40
AP1-6-2-AMB-RD-1-P01-SSII	21.32	20.71	1.59	1.55	0.20	0.20	16.3	16.3	2.25	2.22
APH-8-4-45-FS-1-P05-SSII	92.28	90.16	9.06	8.78	0.26	0.26	20.8	20.6	2.37	2.30
APB-8-4-90-FS-2-P01-SSII	85.90	78.90	10.12	9.21	0.32	0.31	24.0	23.8	2.32	2.23
APH-8-4-90-FS-1-P01-SSII	92.47	77.71	9.36	7.87	0.27	0.27	21.3	21.3	2.37	2.27
APD-6-2-70-PS-3-P01-SSII	33.37	30.46	2.30	2.09	0.18	0.18	15.3	15.2	2.29	2.27
APA3-6-2-70-PS-3-P04-SSII	45.73	42.22	2.43	2.19	0.14	0.14	12.2	12.0	2.39	2.36

The Degree of Saturation, Water Content, Void Ratio, Porosity, and Density of Apache Leap Tuff Push-Out Cylinders--Continued

Apache Leap Tuff Cylinder	S_p[1] (%)	S_f[1] (%)	w_p[2] (%)	w_f[2] (%)	e_p[3]	e_f[3]	n_p[4] (%)	n_f[4] (%)	ρ_p[5] (g/cc)	ρ_f[5] (g/cc)
APE-8-4-AMB-RD-8-PO1-SSII	63.33	62.49	6.04	6.03	0.26	0.26	20.5	20.4	2.34	2.24
APE-8-4-70-PS-5-PO1-SSII	69.29	67.72	6.59	6.35	0.25	0.25	20.2	19.9	2.31	2.26
AP8-8-4-90-FS-3-PO1-SSII	83.68	75.79	8.11	7.25	0.26	0.25	20.5	20.3	2.39	2.28
APA5-6-1-AMB-RD-3-PO2-SSII	6.78	6.78	0.29	0.29	0.11	0.11	10.1	10.1	2.36	2.36
APA2-6-1-AMB-RD-1-PO1-SSII	9.35	8.85	0.34	0.32	0.09	0.09	8.6	8.6	2.40	2.39
APD-6-1-AMB-RD-1-PO3-SSII	6.95	6.95	0.44	0.44	0.17	0.17	14.3	14.3	2.25	2.25
APJ-8-4-AMB-RD-4-PO1-SSII	49.83	49.59	6.40	6.37	0.34	0.34	25.6	25.6	2.19	2.12
APA5-6-2-36-RD-4-PO3-SSII	31.65	31.65	1.79	1.79	0.15	0.15	12.9	12.9	2.36	2.32
AP113-6-2-36-RD-2-PO1-SSII	22.14	21.03	1.18	1.12	0.14	0.14	12.3	12.3	2.36	2.32
APD-6-2-36-RD-2-PO1-SSII	23.98	23.06	1.96	1.88	0.21	0.21	17.6	17.6	2.24	2.20
APA6-8-4-36-RD-1-PO2-SSII	44.14	43.65	6.36	6.29	0.39	0.39	27.8	27.8	2.14	2.05
API-8-4-36-RD-1-PO1-SSII	60.99	60.58	5.12	5.09	0.22	0.22	18.3	18.3	2.39	2.29
APM-8-4-AMB-RD-2-PO1-SSII	47.43	47.33	5.52	5.51	0.31	0.31	23.7	23.7	2.25	2.14
APJ-8-4-AMB-PS-3-PO1-SSII	58.78	58.46	7.02	6.99	0.32	0.32	24.2	24.2	2.27	2.16
APM-8-4-AMB-PS-6-PO1-SSII	52.46	52.01	5.75	5.71	0.29	0.29	22.5	22.5	2.22	2.17
APM-8-4-36-RD-1-PO1-SSII	44.67	44.49	5.13	5.11	0.30	0.30	23.4	23.4	2.23	2.14
APA-8-4-70-PS-4-PO1-SSII	51.34	49.64	6.84	6.61	0.35	0.35	26.1	26.1	2.18	2.09
APM-8-4-70-PS-5-PO1-SSII	56.30	55.83	6.22	6.17	0.29	0.29	22.7	22.7	2.27	2.18
APA-8-4-44-PS-5-PO1-SSII	49.93	49.62	6.14	6.10	0.33	0.33	24.6	24.6	2.20	2.12
APA5-6-1-AMB-FSS-1-PO1-SSII STP* = 68.50	58.21	55.87	2.59	2.49	0.12	0.12	10.4	10.4	2.41	2.40
AP1-6-1-AMB-FSS-2-PO1-SSII STP* = 88.80	76.40	75.70	4.67	4.61	0.16	0.16	13.8	13.7	2.36	2.36
APA3-6-1-AMB-FSS-4-PO2-SSII STP* = 81.14	71.26	69.39	2.74	2.66	0.10	0.10	9.1	9.1	2.45	2.44
APA2-6-1-AMB-FSS-4-PO1-SSII STP* = 91.27	79.59	78.07	2.72	2.66	0.09	0.09	8.2	8.2	2.47	2.46

The Degree of Saturation, Water Content, Void Ratio, Porosity, and Density of Apache Leap Tuff Push-Out Cylinders--Continued

Apache Leap Tuff Cylinder	S_p[1] (%)	S_f[1] (%)	w_p[2] (%)	w_f[2] (%)	e_p[3]	e_f[3]	n_p[4] (%)	n_f[4] (%)	ρ_p[5] (g/cc)	ρ_f[5] (g/cc)
APA2-6-2-AMB-FSS-1-PO1-SSII STP* = 93.72	79.02	78.36	3.79	3.72	0.13	0.12	11.2	11.1	2.45	2.42
AP77-6-2-AMB-FSS-1-PO1-SSII STP* = 82.82	75.50	74.72	5.99	5.89	0.21	0.21	17.2	17.1	2.32	2.30
APA4-6-2-AMB-FSS-1-PO1-SSII STP* = 91.24	61.30	60.29	3.76	3.68	0.16	0.16	13.8	13.8	2.37	2.34
AP41-3-1/2-AMB-FS-7-PO1-SSII	73.27	68.38	3.89	3.63	0.14	0.14	12.2	12.2	2.40	2.38
AP41-3-1/2-AMB-FS-10-PO1-SSII	74.56	71.99	3.71	3.58	0.13	0.13	11.5	11.5	2.41	2.39
AP41-3-1/2-AMB-FS-11-PO1-SSII	69.64	67.59	4.05	3.93	0.15	0.15	13.2	13.2	2.37	2.36
AP41-3-1/2-AMB-FS-7-PO2-SSII	83.35	80.50	3.69	3.57	0.12	0.12	10.4	10.4	2.44	2.42
AP852-3-1/2-AMB-FS-7-PO2-SSII	94.18	83.85	2.27	2.02	0.06	0.06	5.9	5.9	2.53	2.51
AP41-3-1/2-AMB-FS-11-PO3-SSII	74.84	72.28	3.88	3.74	0.14	0.14	11.9	11.9	2.40	2.39
AP41-3-1/2-AMB-FS-11-PO2-SSII	82.86	80.37	4.14	4.01	0.13	0.13	11.5	11.5	2.42	2.40
AP852-3-1/2-AMB-FS-5-PO1-SSII	89.50	85.48	2.69	2.57	0.08	0.08	7.3	7.3	2.50	2.48
AP852-3-1/2-AMB-FS-5-PO2-SSII	91.98	91.98	2.57	2.57	0.07	0.07	6.8	6.8	2.51	2.50
AP41-3-1/2-AMB-FS-8-PO1-SSII	73.57	70.87	3.79	3.65	0.13	0.13	11.9	11.9	2.41	2.39
AP852-3-1/2-AMB-FS-7-PO1-SSII	86.45	86.45	2.45	2.45	0.07	0.07	6.9	6.9	2.51	2.49

The Degree of Saturation, Water Content, Void Ratio, Porosity, and Density of Apache Leap Tuff Push-Out Cylinders--Continued

Apache Leap Tuff Cylinder	S_p[1] (%)	S_f[1] (%)	w_p[2] (%)	w_f[2] (%)	e_p[3]	e_f[3]	n_p[4] (%)	n_f[4] (%)	ρ_p[5] (g/cc)	ρ_f[5] (g/cc)
AP41-3-1/2-AMB-FS-11-PO1-SSII	82.41	82.41	4.13	4.13	0.13	0.13	11.6	11.6	2.42	2.40
AP41-3-1/2-AMB-FS-9-PO1-SSII	64.85	64.85	3.41	3.41	0.14	0.14	12.1	12.1	2.39	2.37
AP852-3-1/2-AMB-FS-8-PO1-SSII	90.70	90.70	2.16	2.16	0.06	0.06	5.9	5.9	2.52	2.51
AP566-6-1-2-AMB-FS-8-PO1-SSII	54.21	49.42	1.72	1.55	0.08	0.08	7.6	7.6	2.46	2.45
AP631-6-1-2-AMB-FS-1-PO2-SSII	95.61	91.80	4.06	3.88	0.11	0.11	10.0	9.9	2.45	2.44
APG-6-1-2-AMB-FS-3-PO1-SSII	76.02	74.38	4.15	4.05	0.14	0.14	12.5	12.4	2.39	2.38
AP566-6-1-2-AMB-FS-7-PO1-SSII	69.57	67.67	2.03	1.96	0.08	0.08	7.1	7.0	2.48	2.48
APA3-6-1-2-AMB-FS-3-PO4-SSII	48.12	45.97	1.76	1.67	0.10	0.10	8.7	8.7	2.44	2.43
APH-6-1-4-AMB-FS-7-PO1-SSII	75.45	73.43	2.57	2.50	0.09	0.09	8.2	8.2	2.47	2.46
AP566-6-1-4-AMB-FS-3-PO2-SSII	60.64	60.26	1.87	1.86	0.08	0.08	7.5	7.5	2.47	2.46
AP56A-6-1-4-AMB-FS-1-PO1-SSII	57.80	55.41	1.95	1.87	0.09	0.09	8.1	8.1	2.45	2.45

NOTES:

*STP: degree of saturation of tuff cylinder prior to cement plug emplacement

[1] S_p and S_f: degree of saturation of push-out cylinder prior to and following push-out test, respectively.

NOTES--Continued

[2] w_p and w_f: water content of push-out cylinder prior to and following push-out test, respectively.

[3] e_p and e_f: void ratio of push-out cylinder prior to and following push-out test, respectively.

[4] n_p and n_f: porosity of push-out cylinder prior to and following push-out test, respectively.

[5] ρ_p and ρ_f: density of push-out cylinder prior to and following push-out test, respectively.

APPENDIX I

AXIAL STRESS VS. TOP AND BOTTOM AXIAL PLUG DISPLACEMENT FOR PUSH-OUT TESTS

Figure F.1 (Appendix F) gives specimen dimensions. The specimen numbers are included with each plot.

AP8-6-1-45-FS-1-P02-SSII

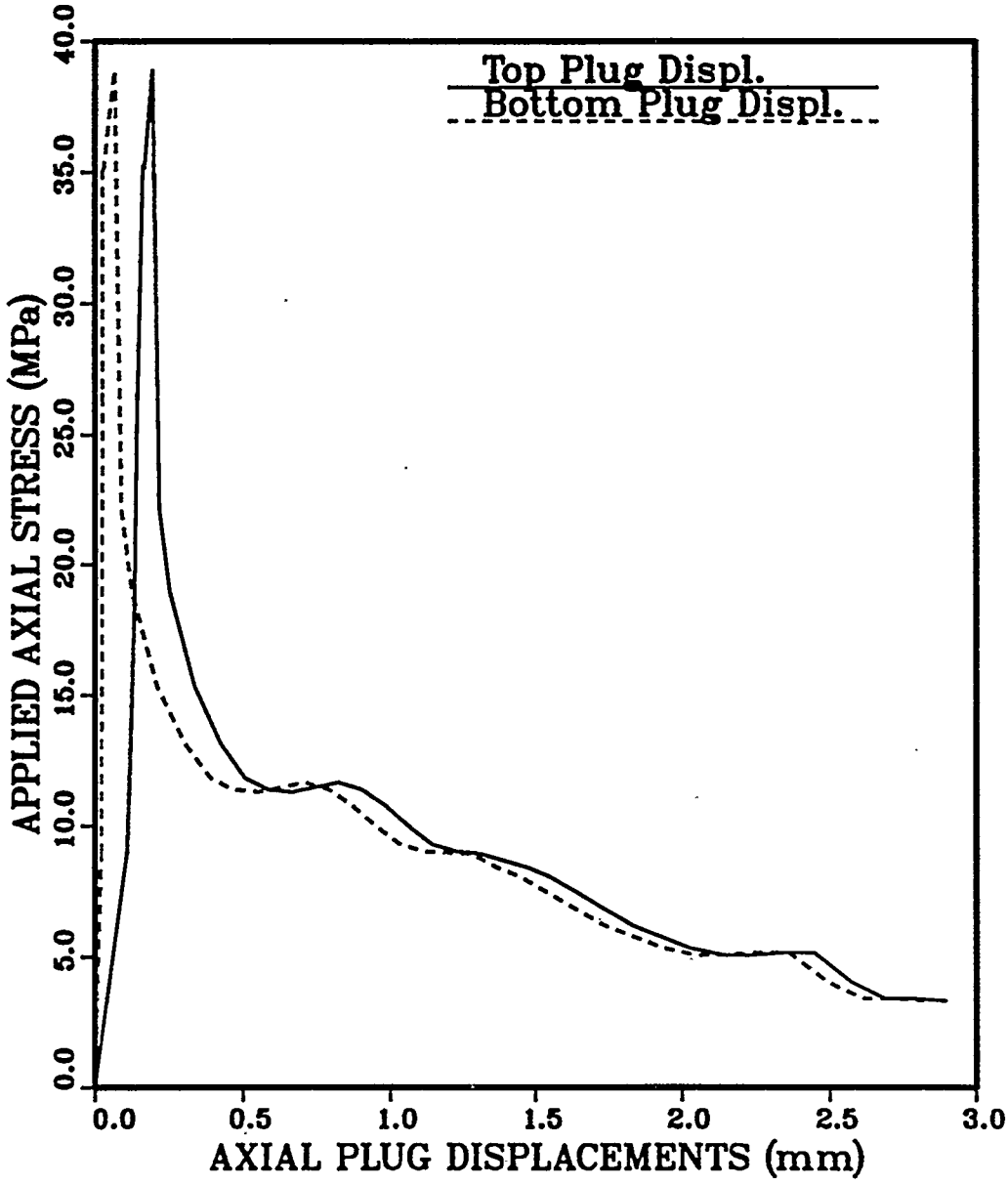

AP8-6-1-70-FS-2-P02-SSII

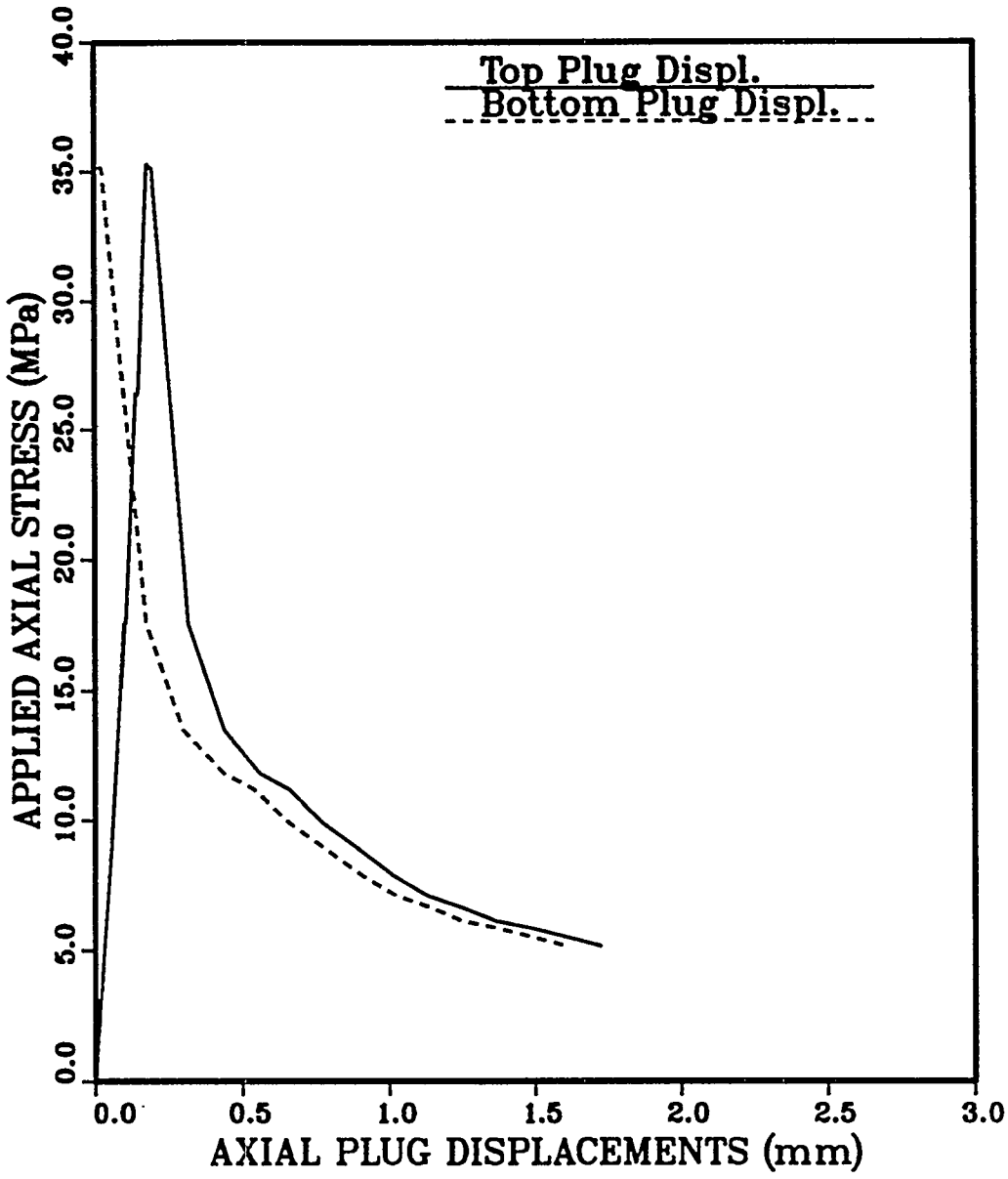

AP5-6-1-70-FS-1-P01-SSII

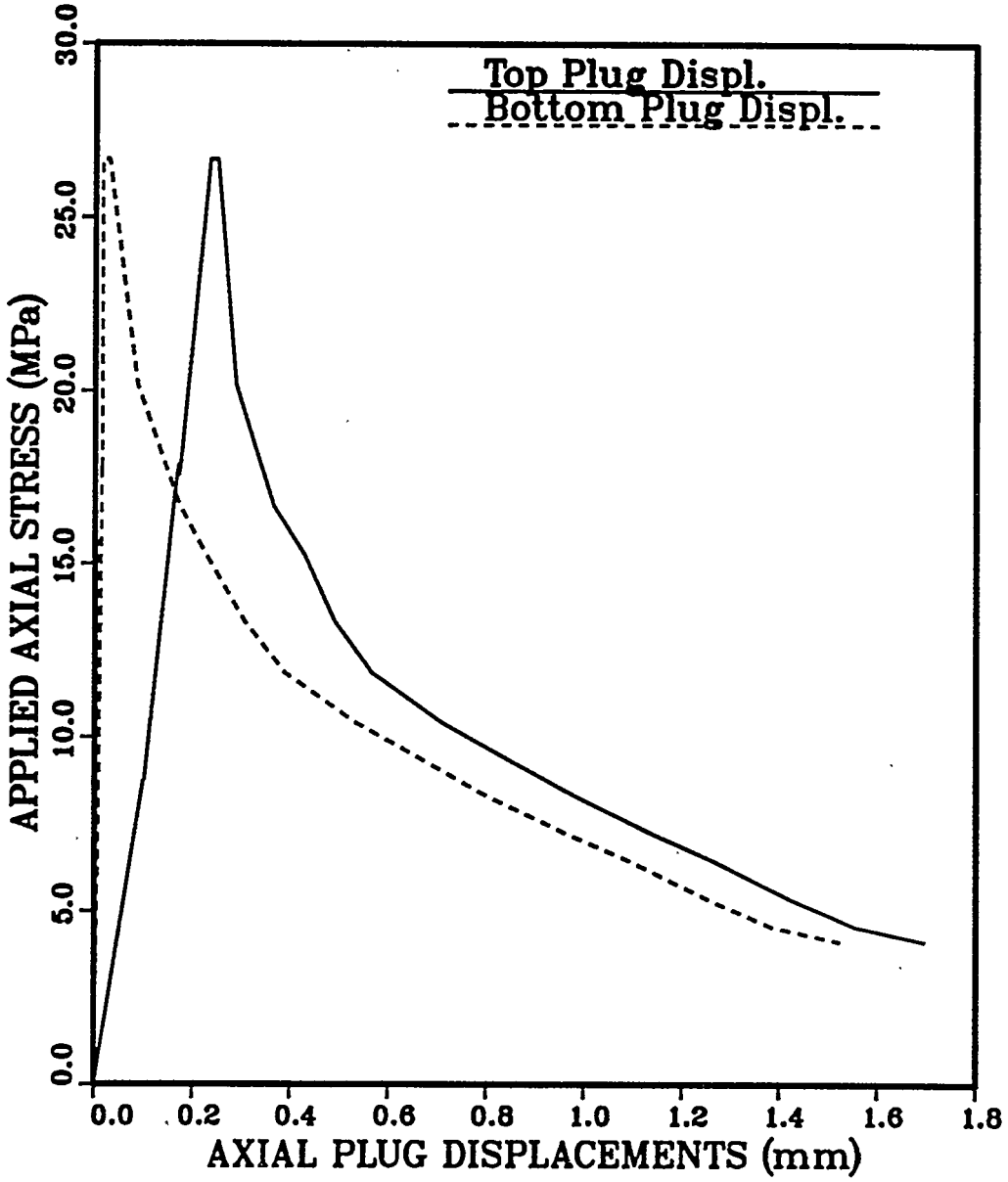

AP3-6-2-AMB-FS-4-P01-SSII

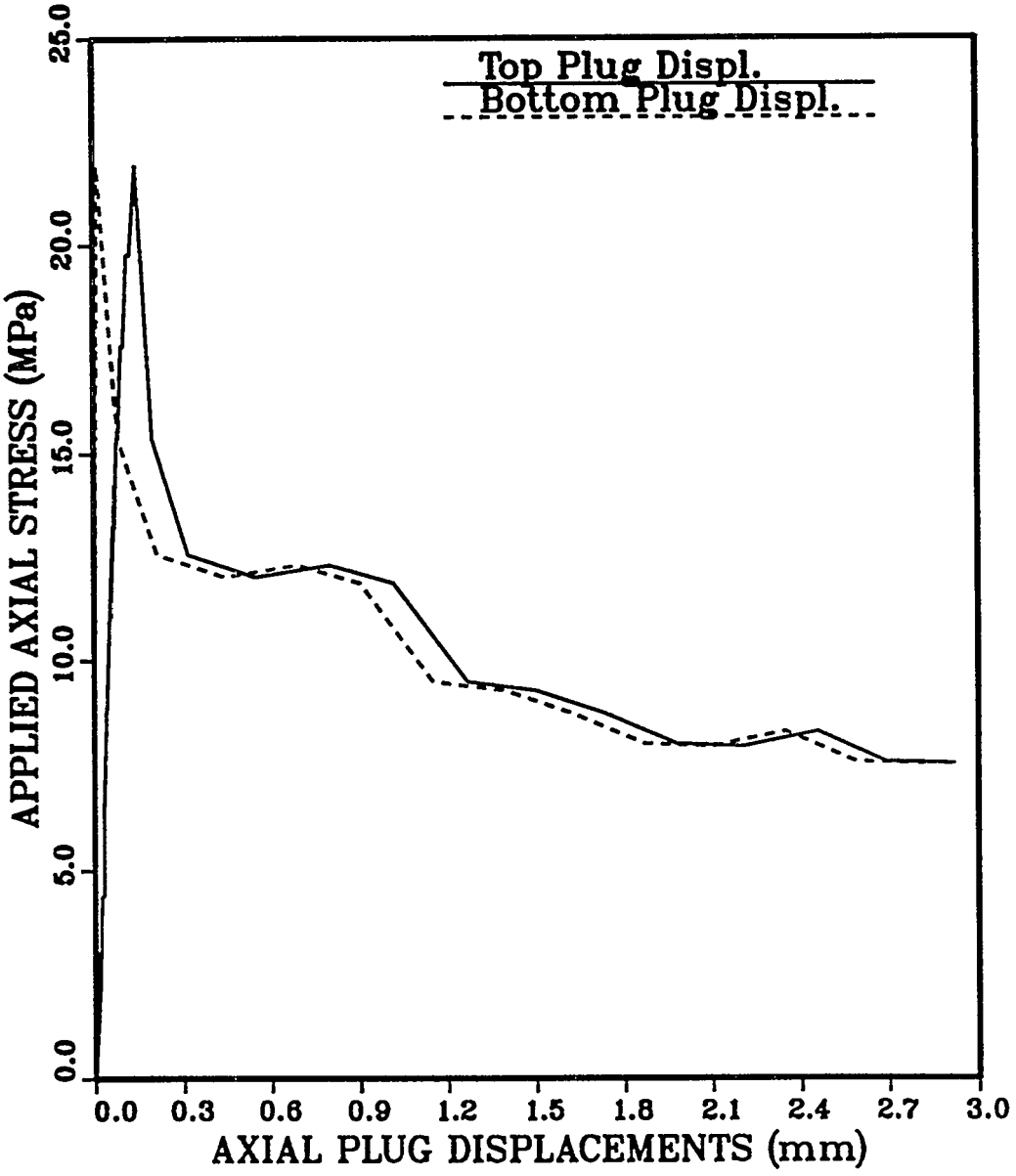

AP3-6-2-70-FS-2-P01-SSII

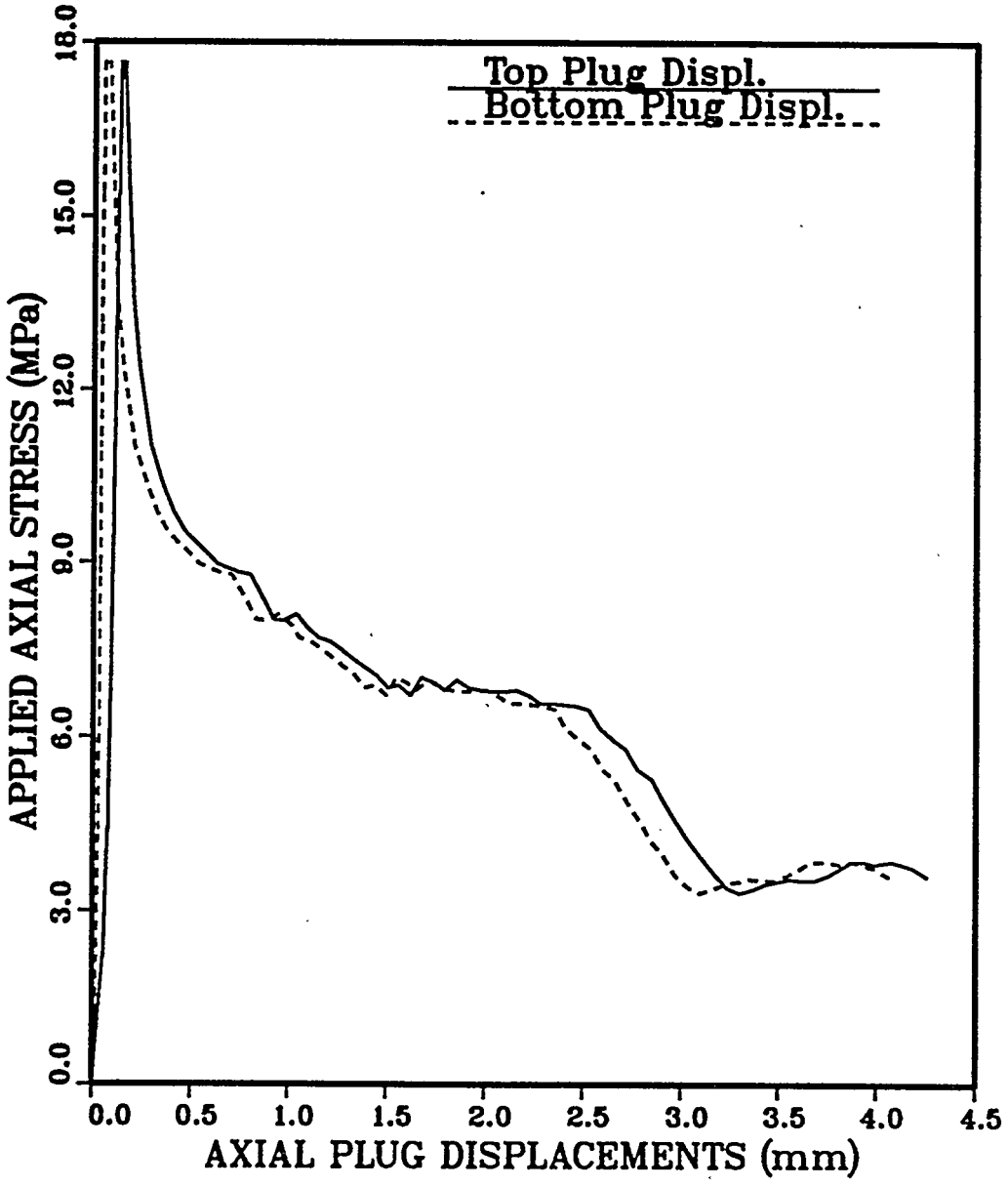

AP5-6-1-44-PS-3-P02-SSII

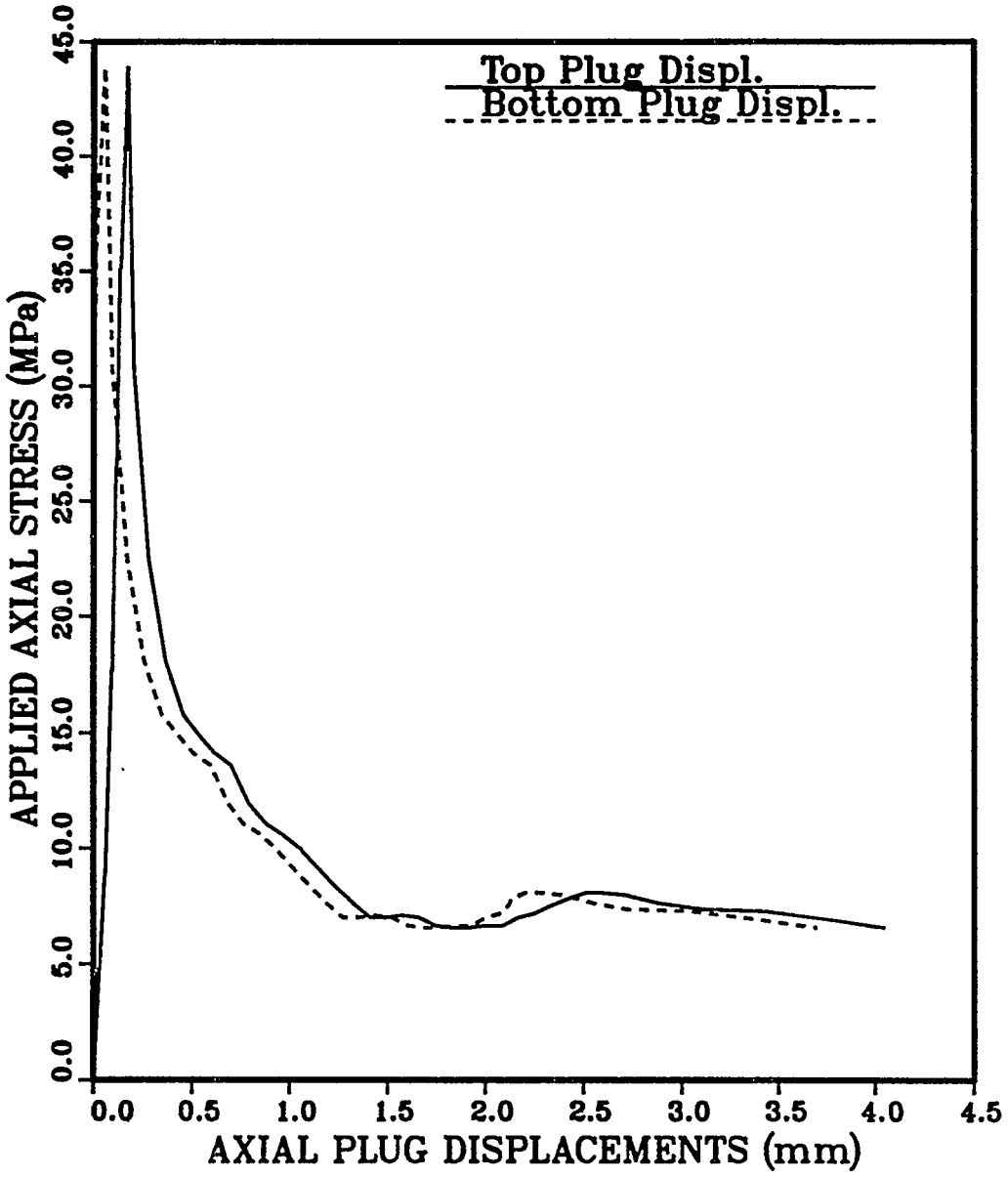

AP5-6-1-44-PS-2-P03-SSII

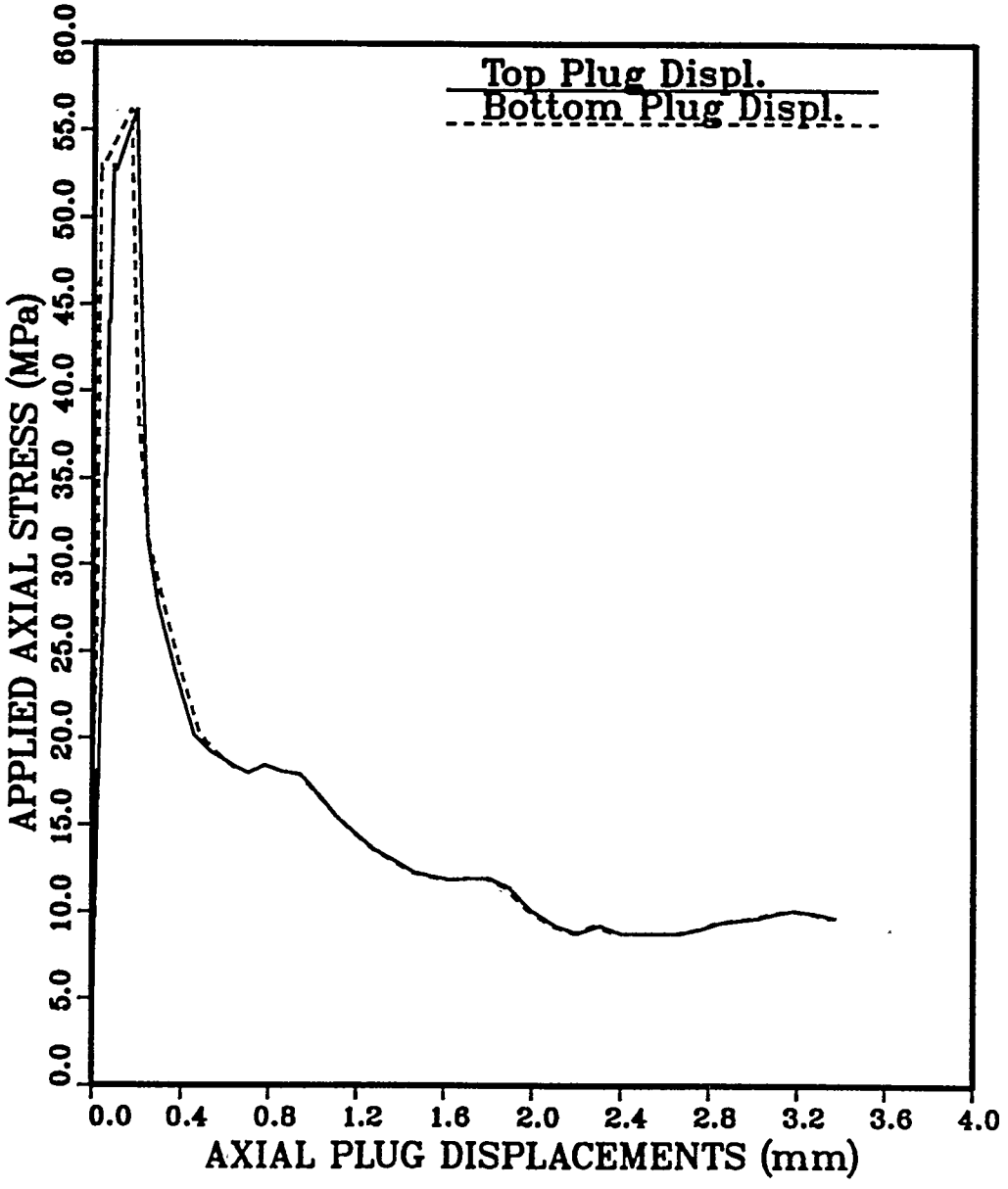

APC-8-4-AMB-PS-1-P01-SSII

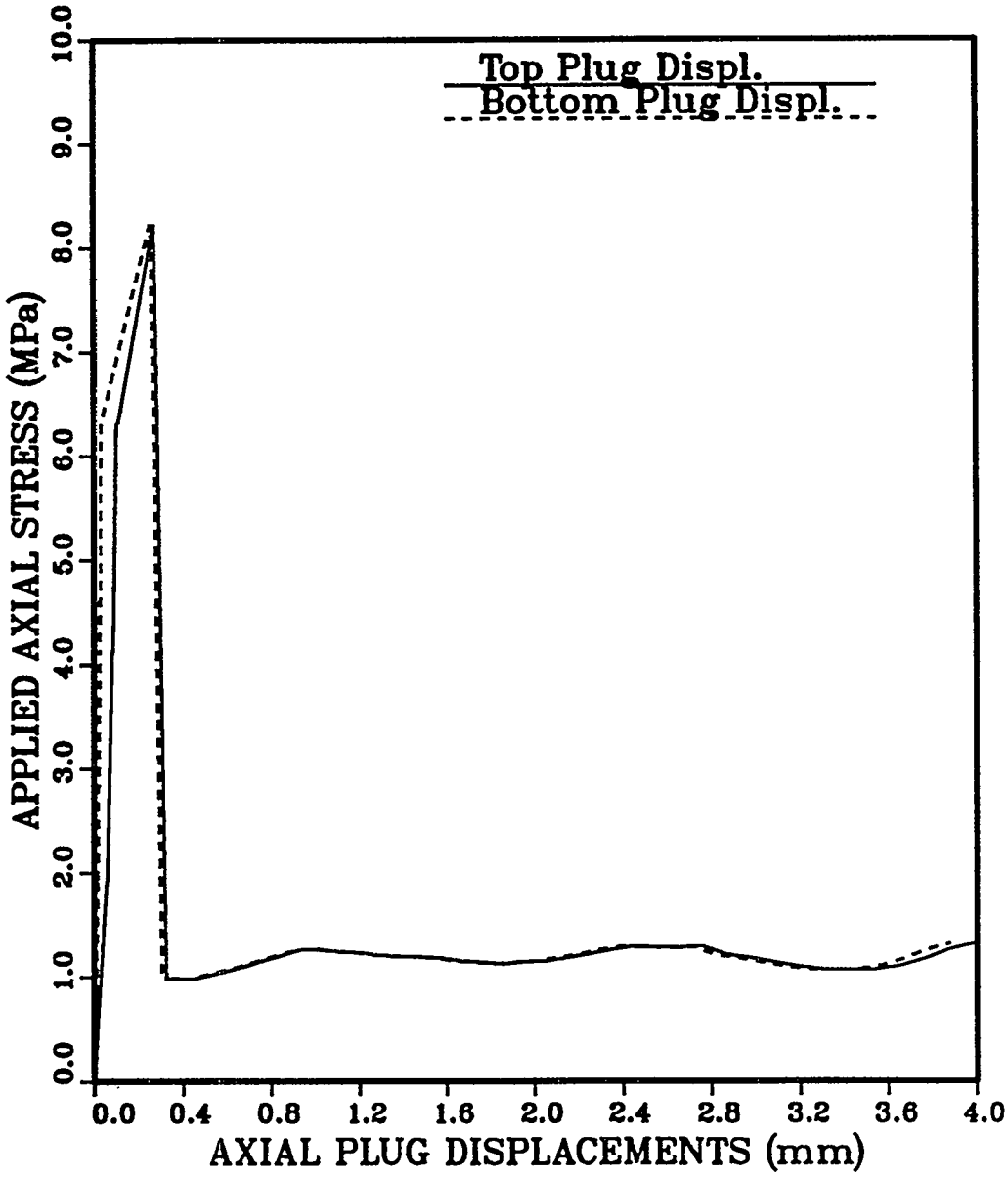

AP77-6-1-36-RD-1-P01-SSII

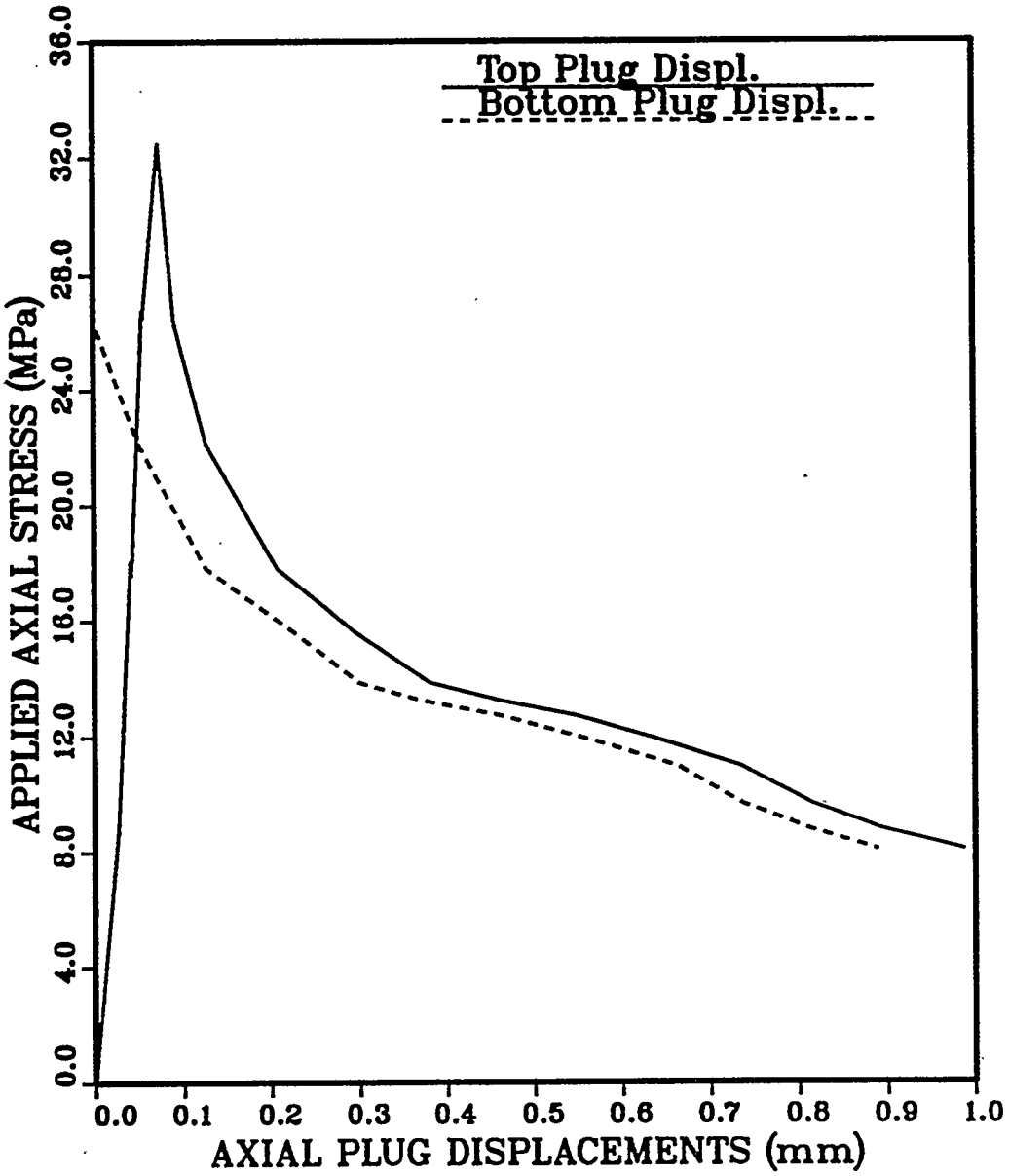

AP1-6-1-36-RD-1-P01-SSII

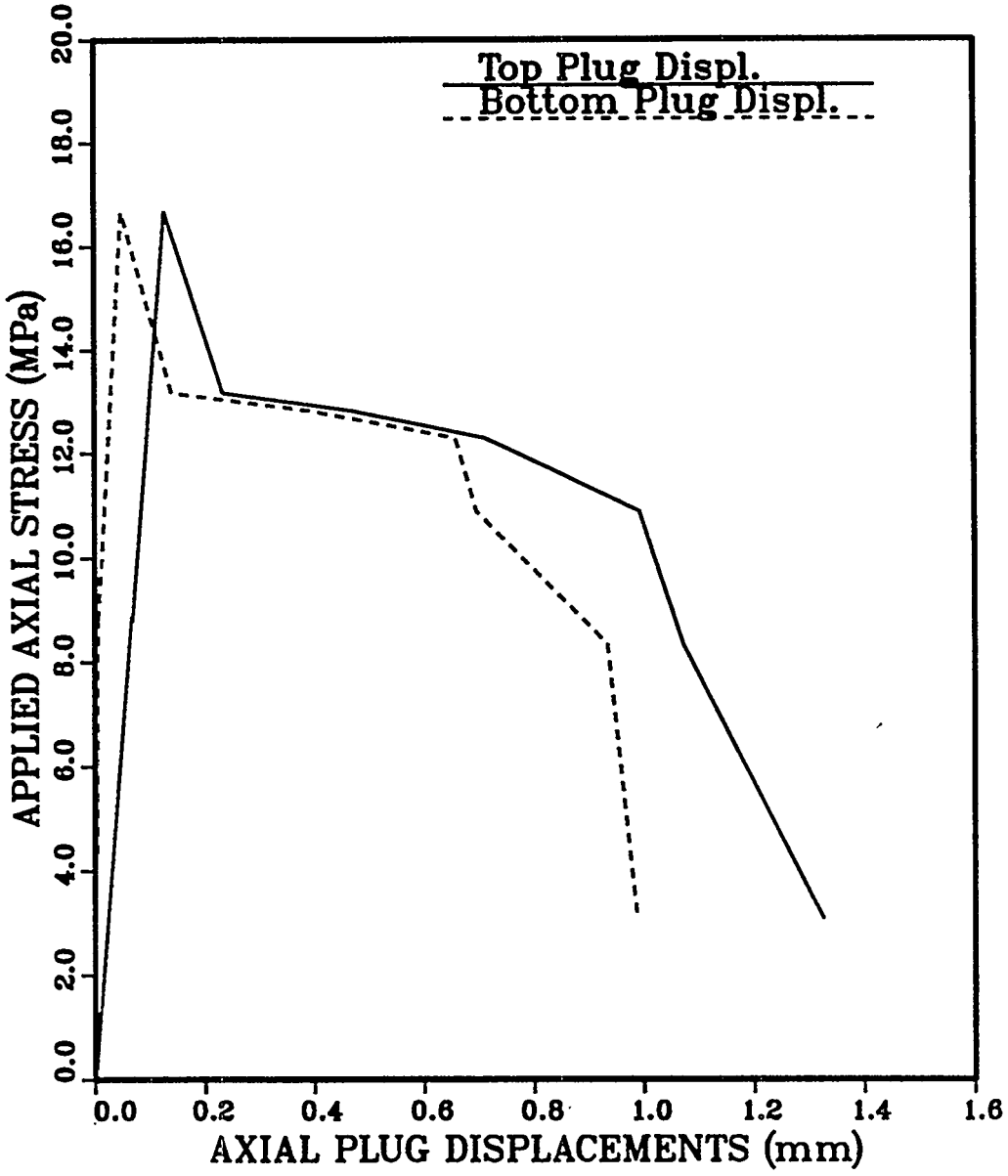

APA3-6-2-70-PS-2-P01-SSII

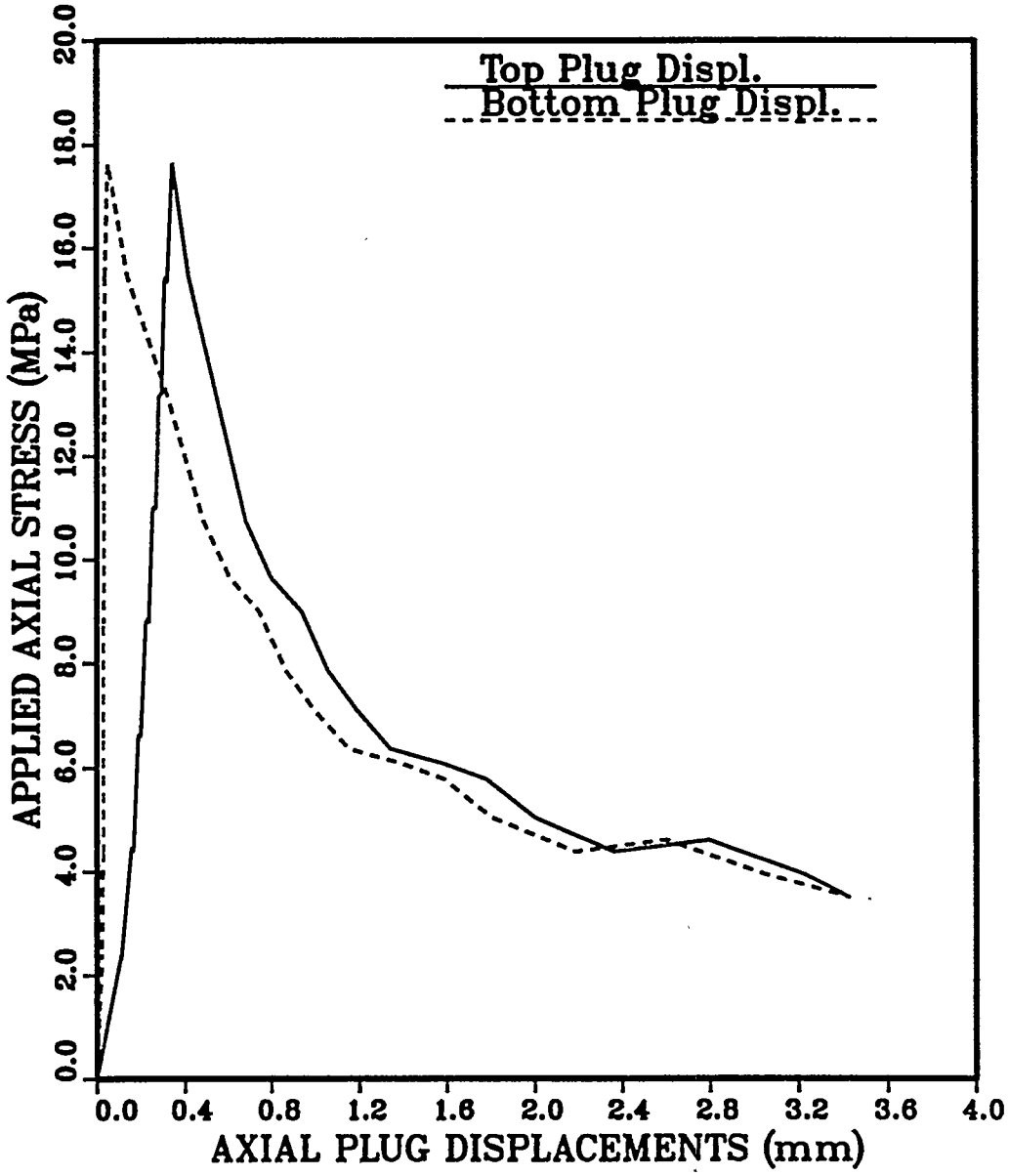

AP927-6-2-AMB-RD-2-P01-SSII

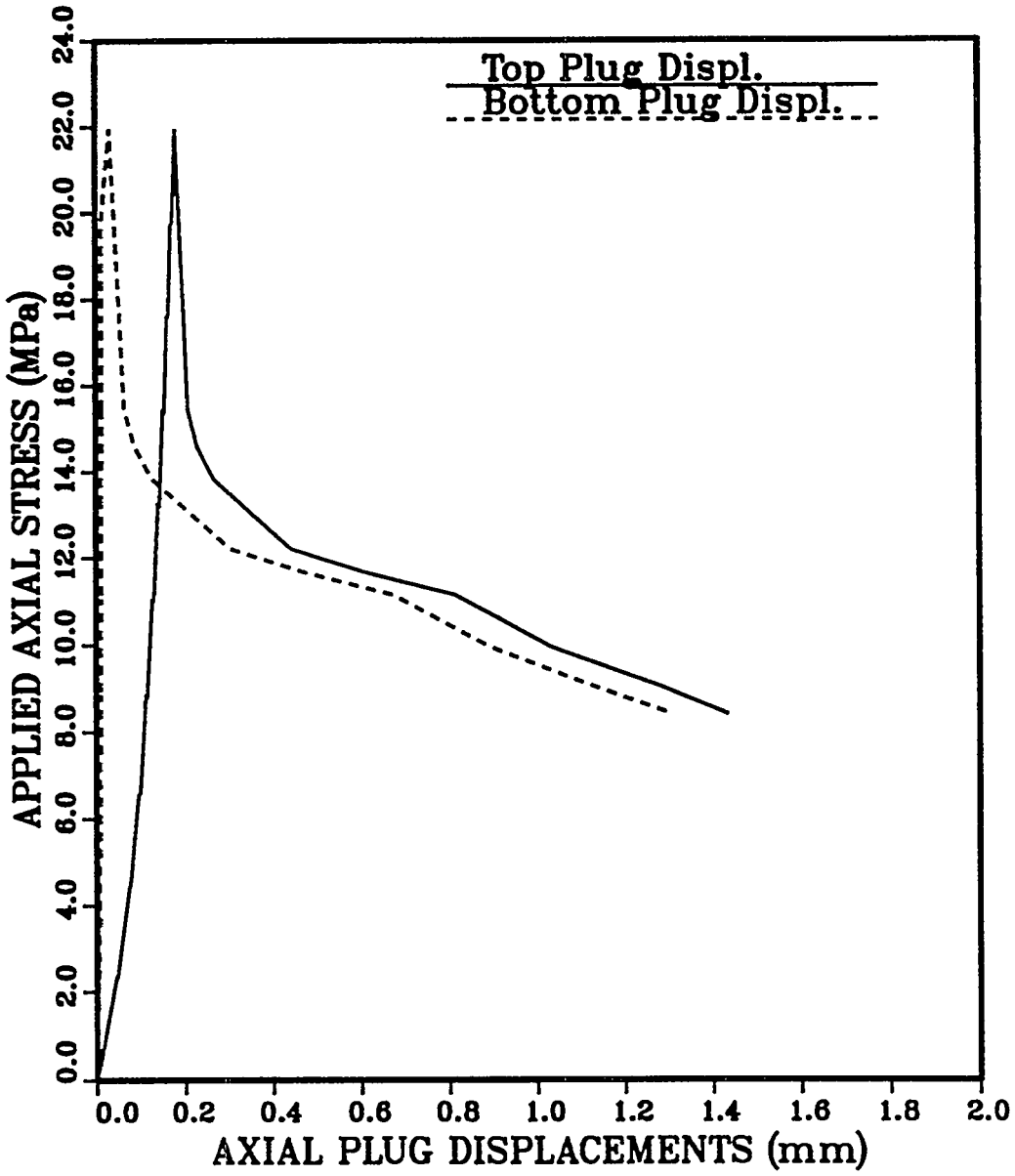

AP5-6-2-AMB-RD-4-P01-SSII

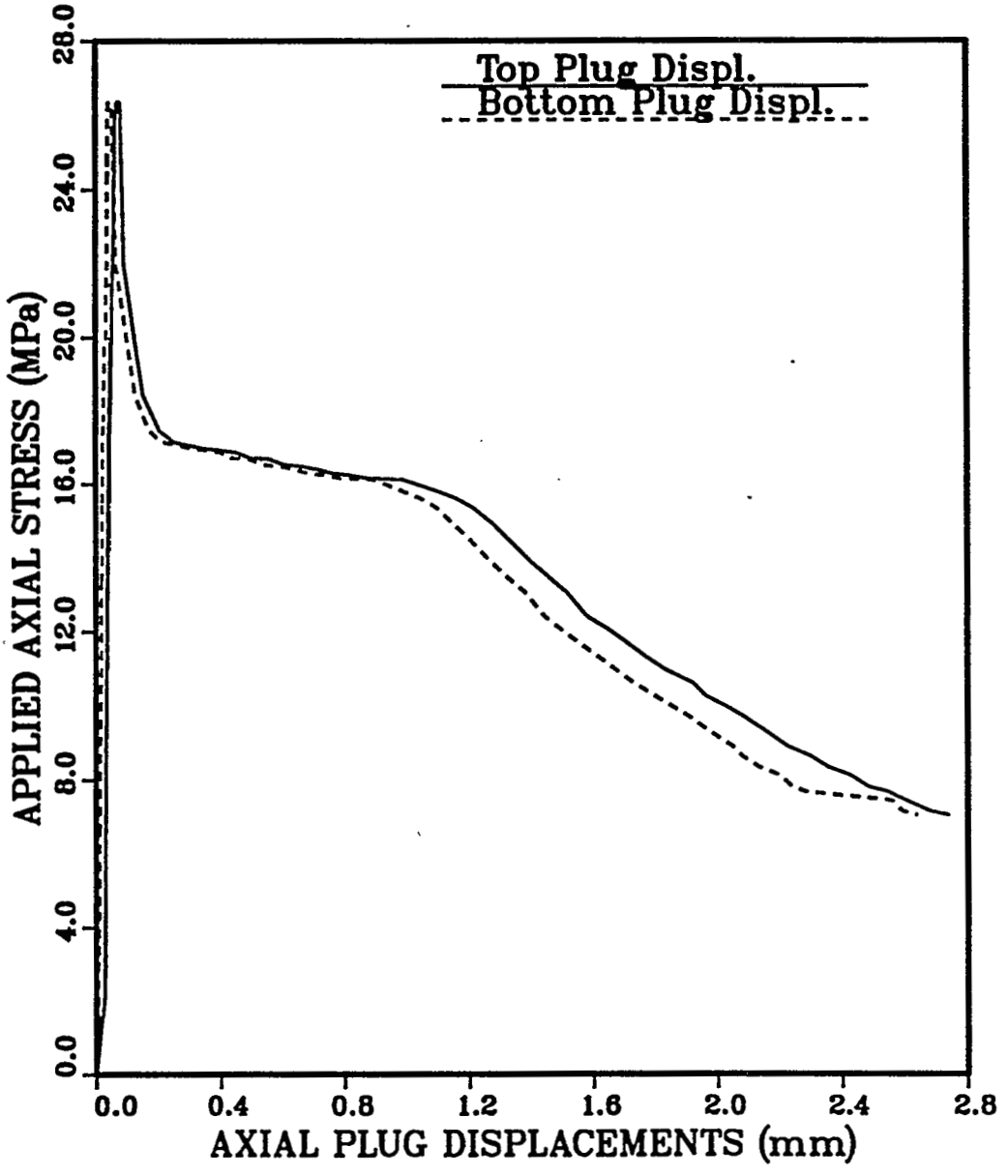

APA3-6-1-90-FS-3-P03-SSII

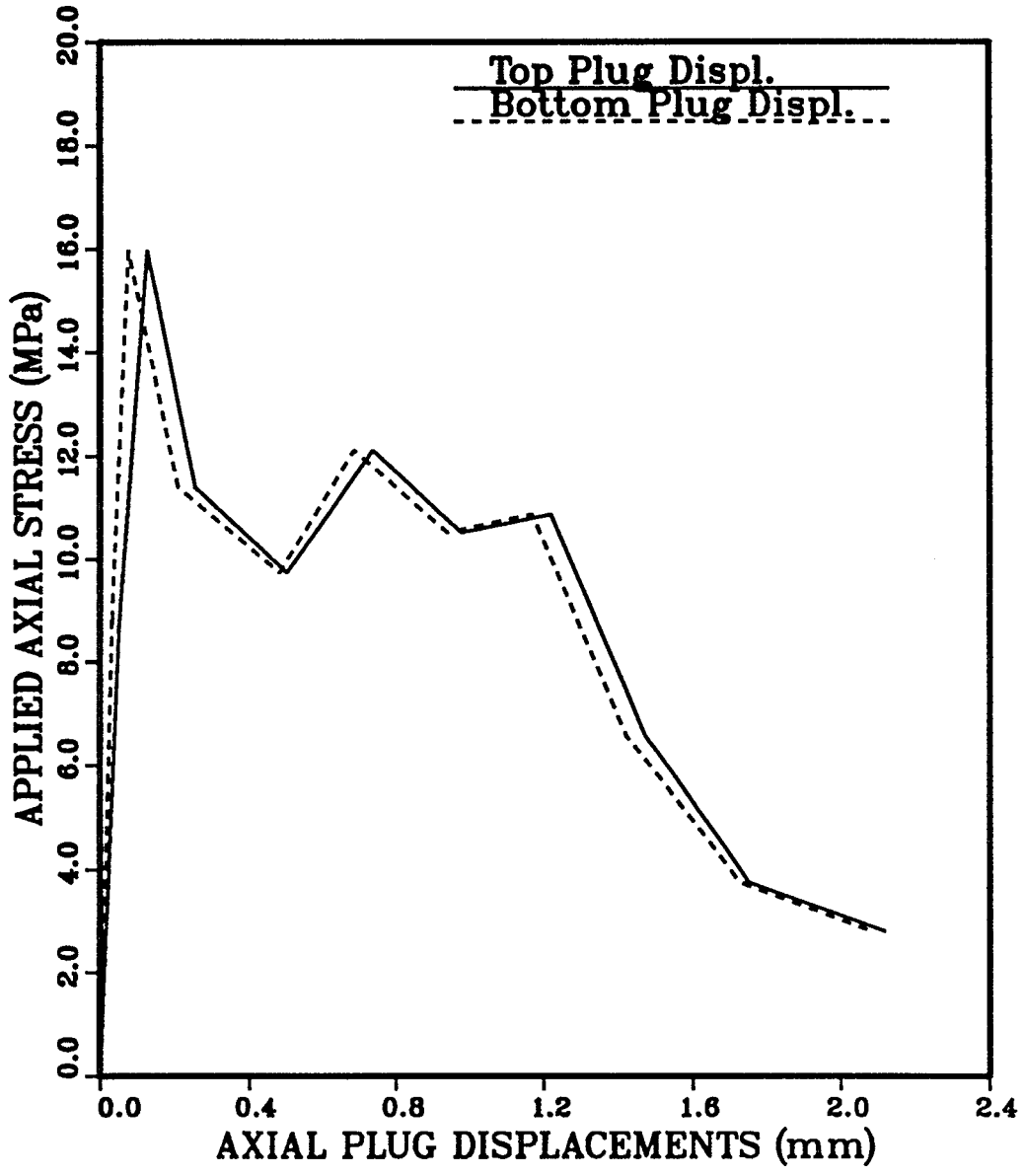

AP1-6-2-AMB-RD-1-P01-SSII

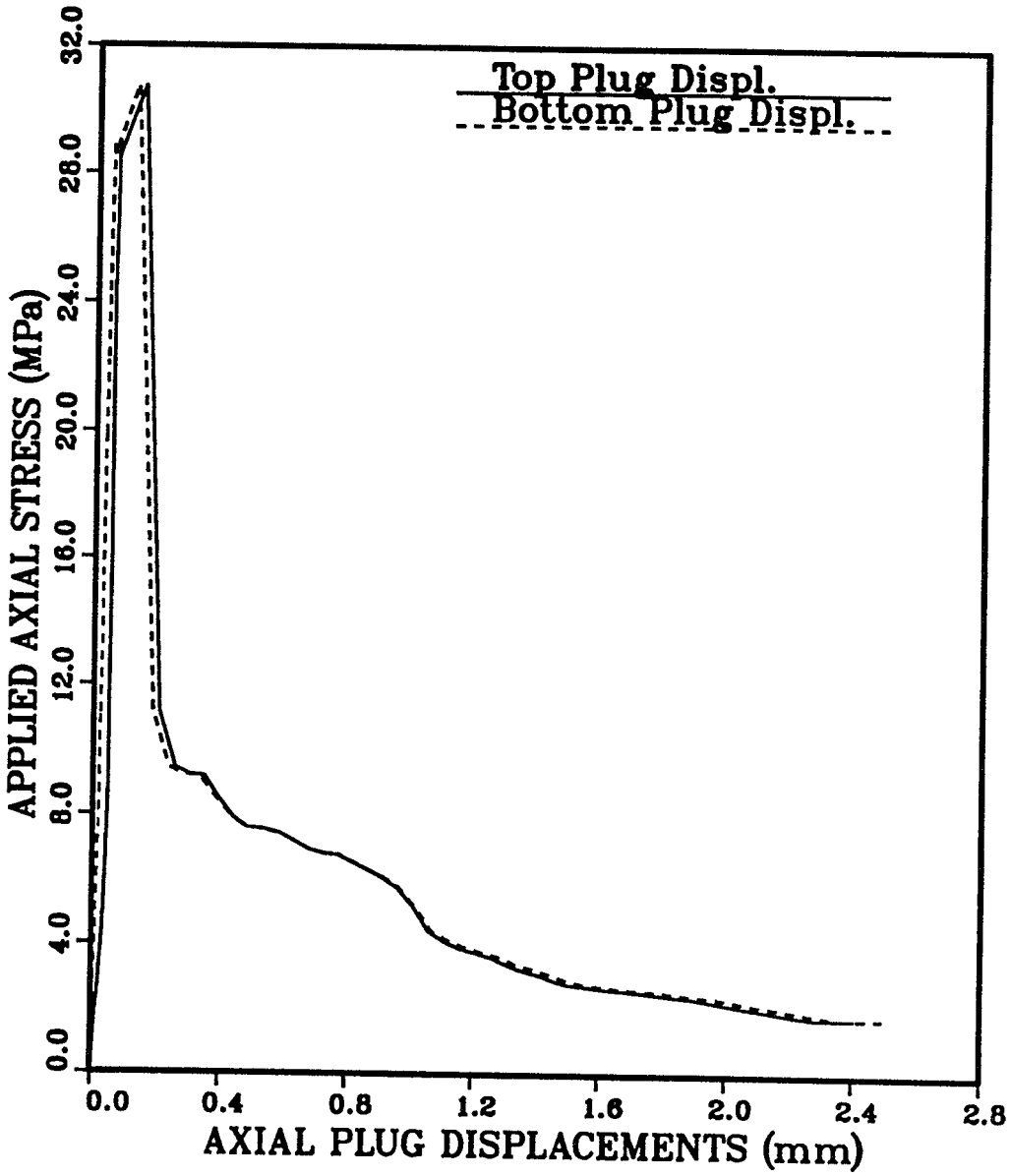

APH-8-4-45-FS-1-P05-SSII

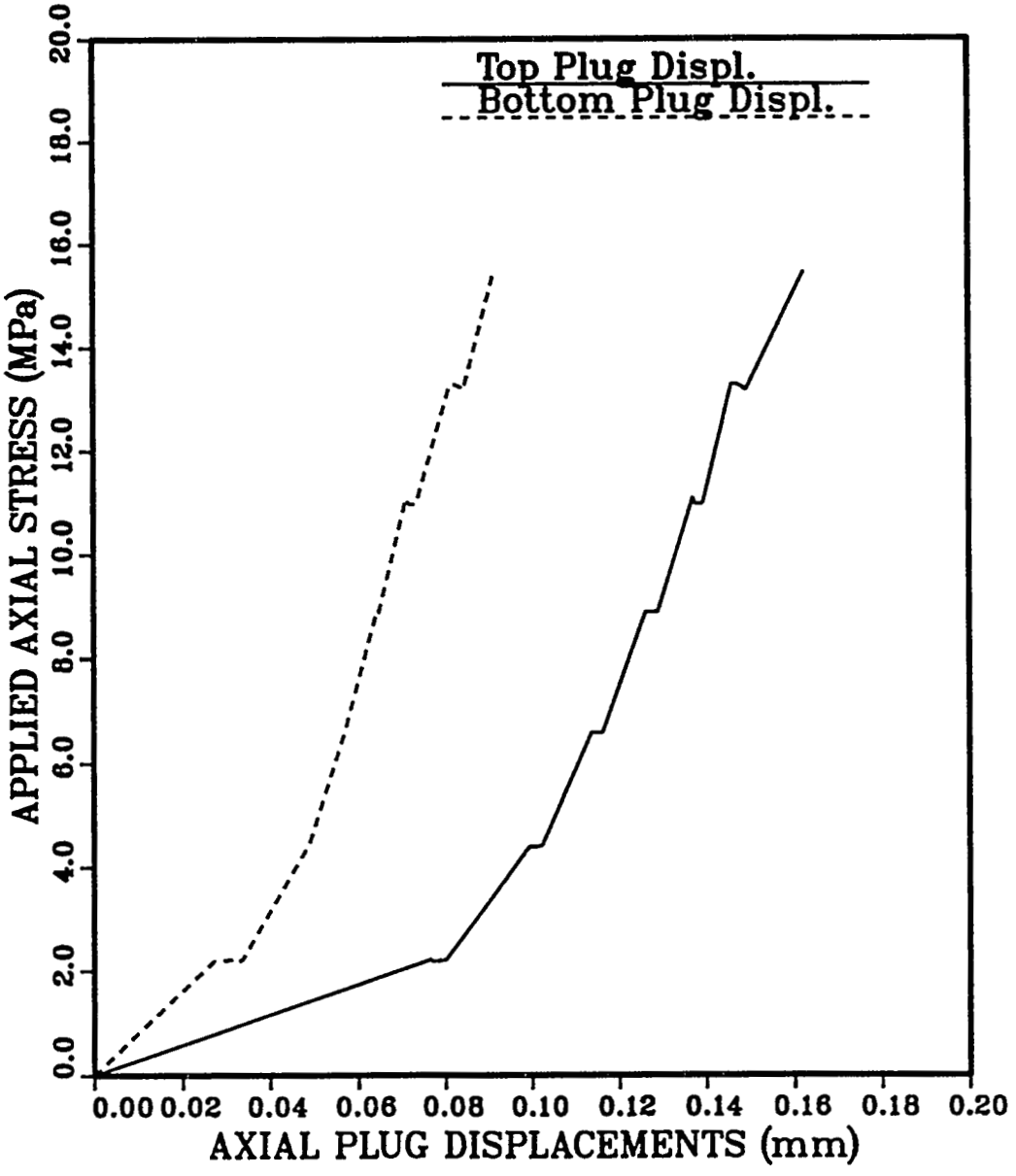

APB-8-4-90-FS-2-P01-SSII

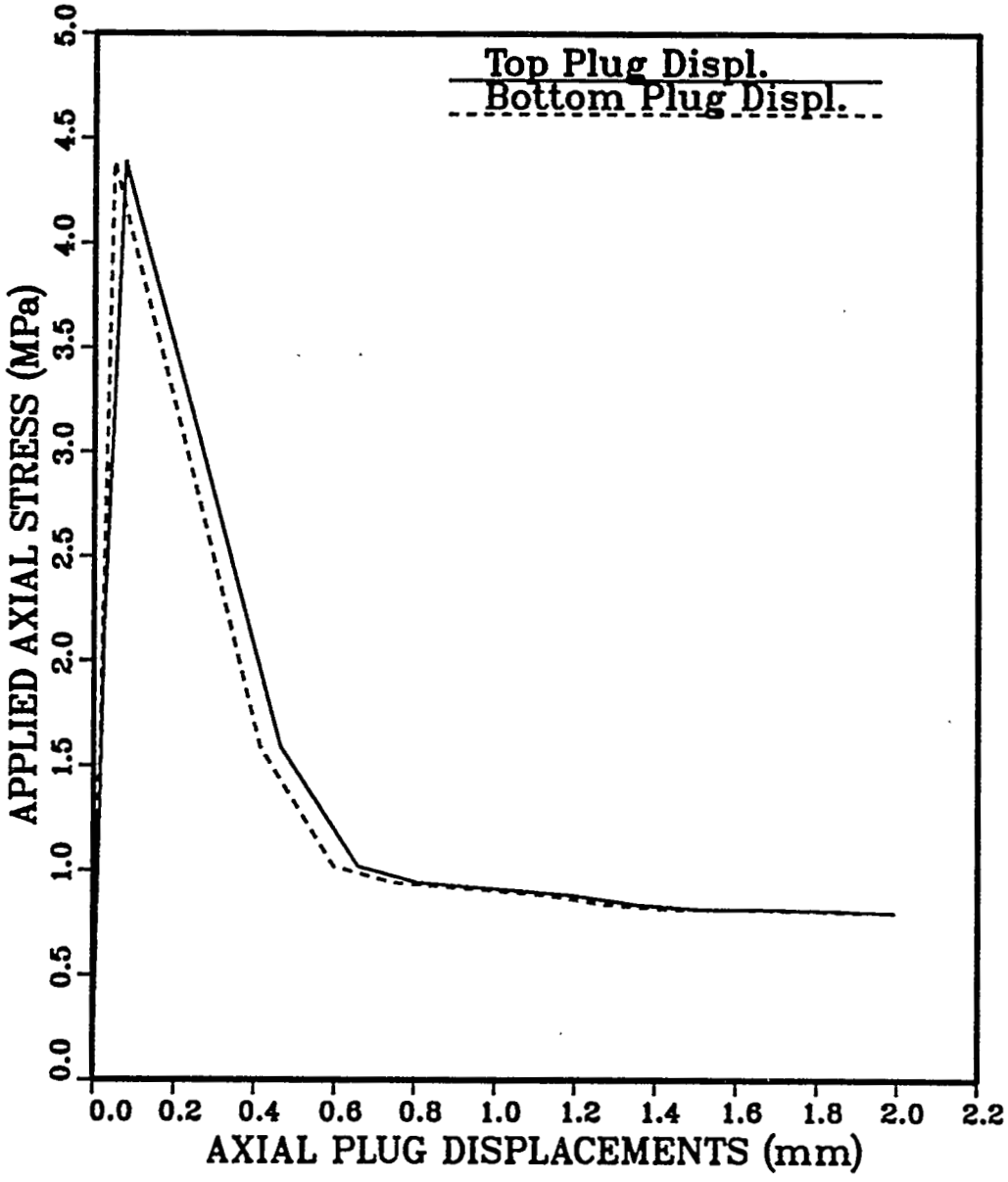

APE-8-4-AMB-RD-8-P01-SSII

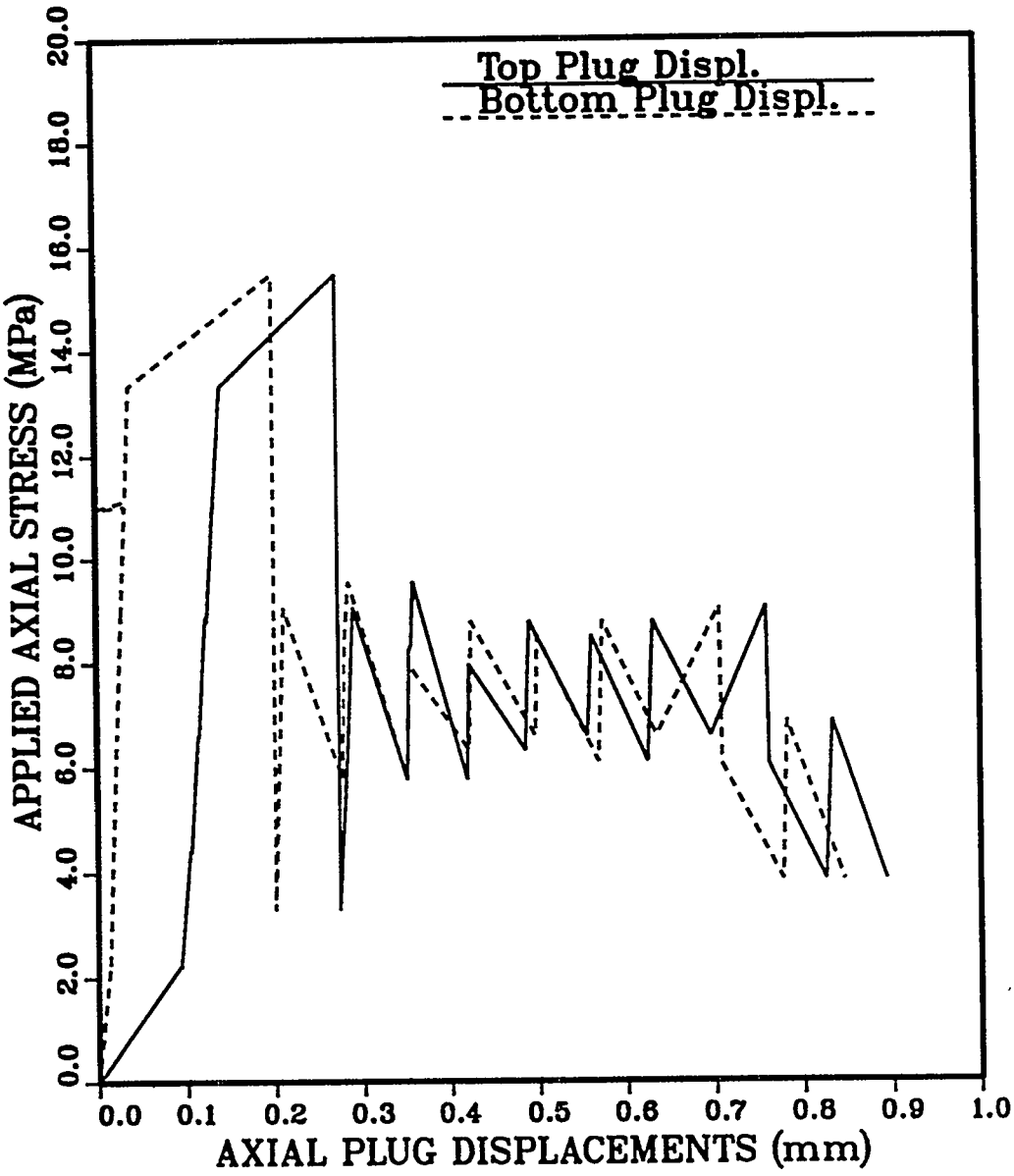

APE-8-4-70-PS-5-P01-SSII

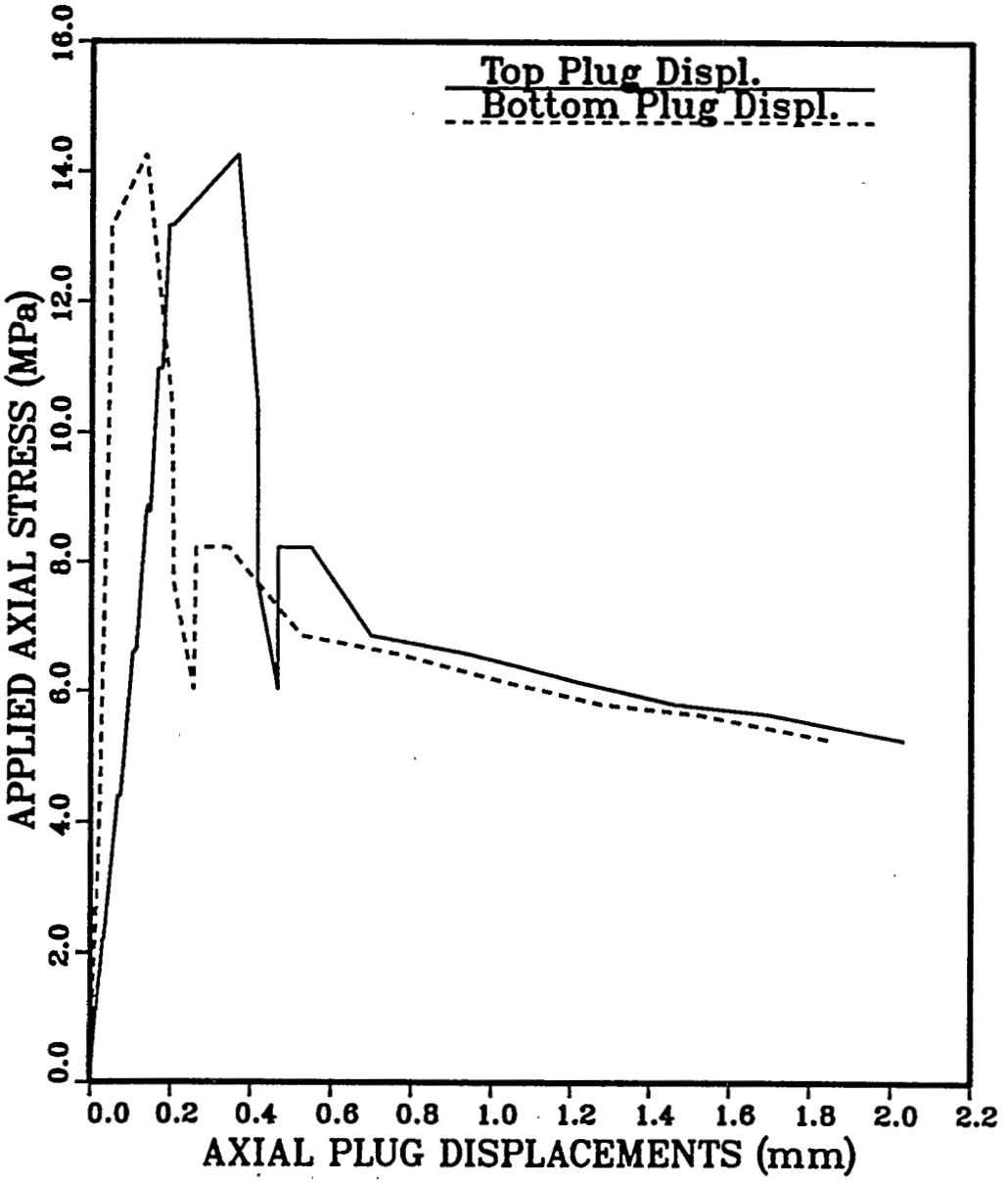

AP8-8-4-90-FS-3-P01-SSII

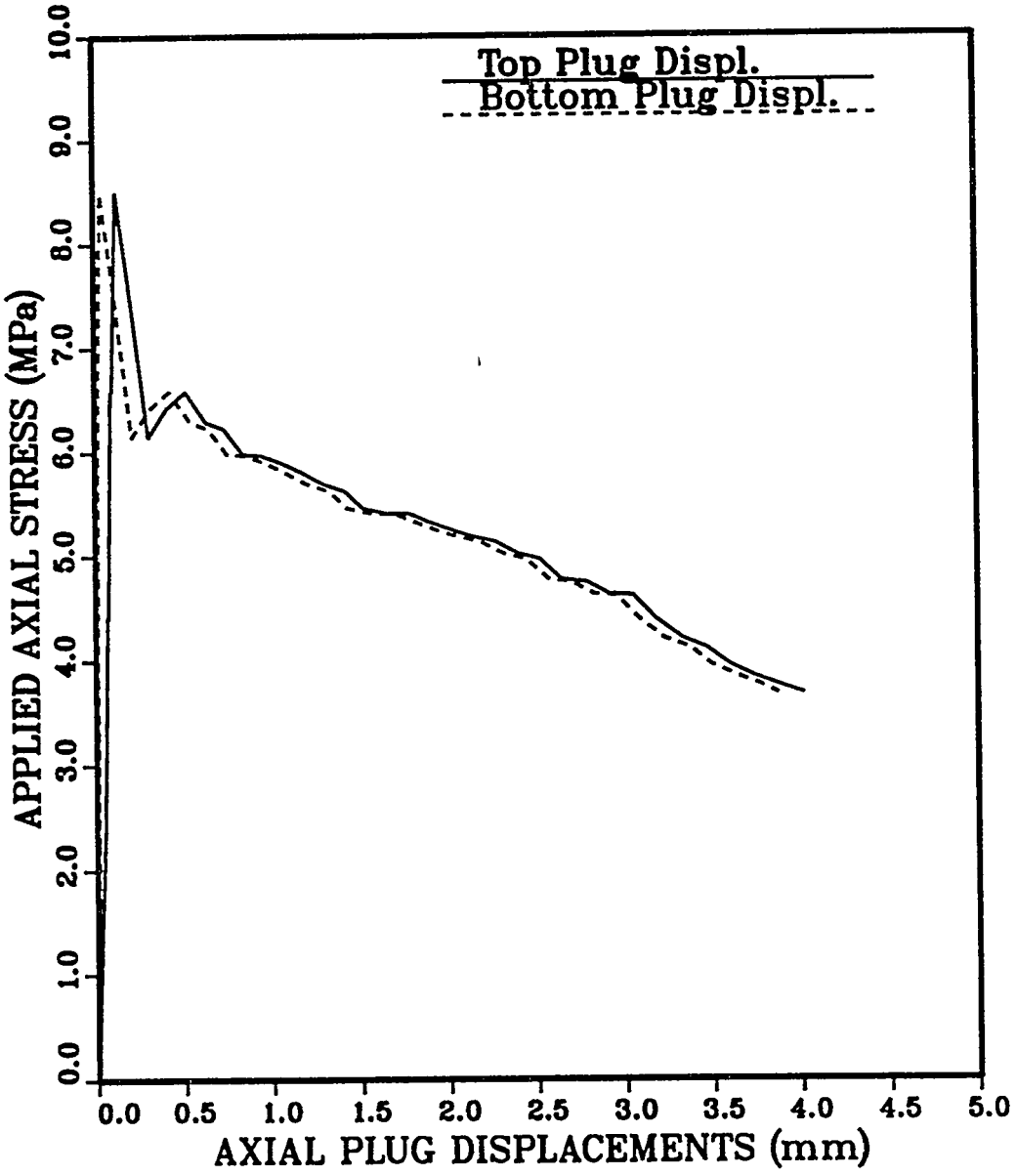

APA5-6-1-AMB-RD-3-P02-SSII

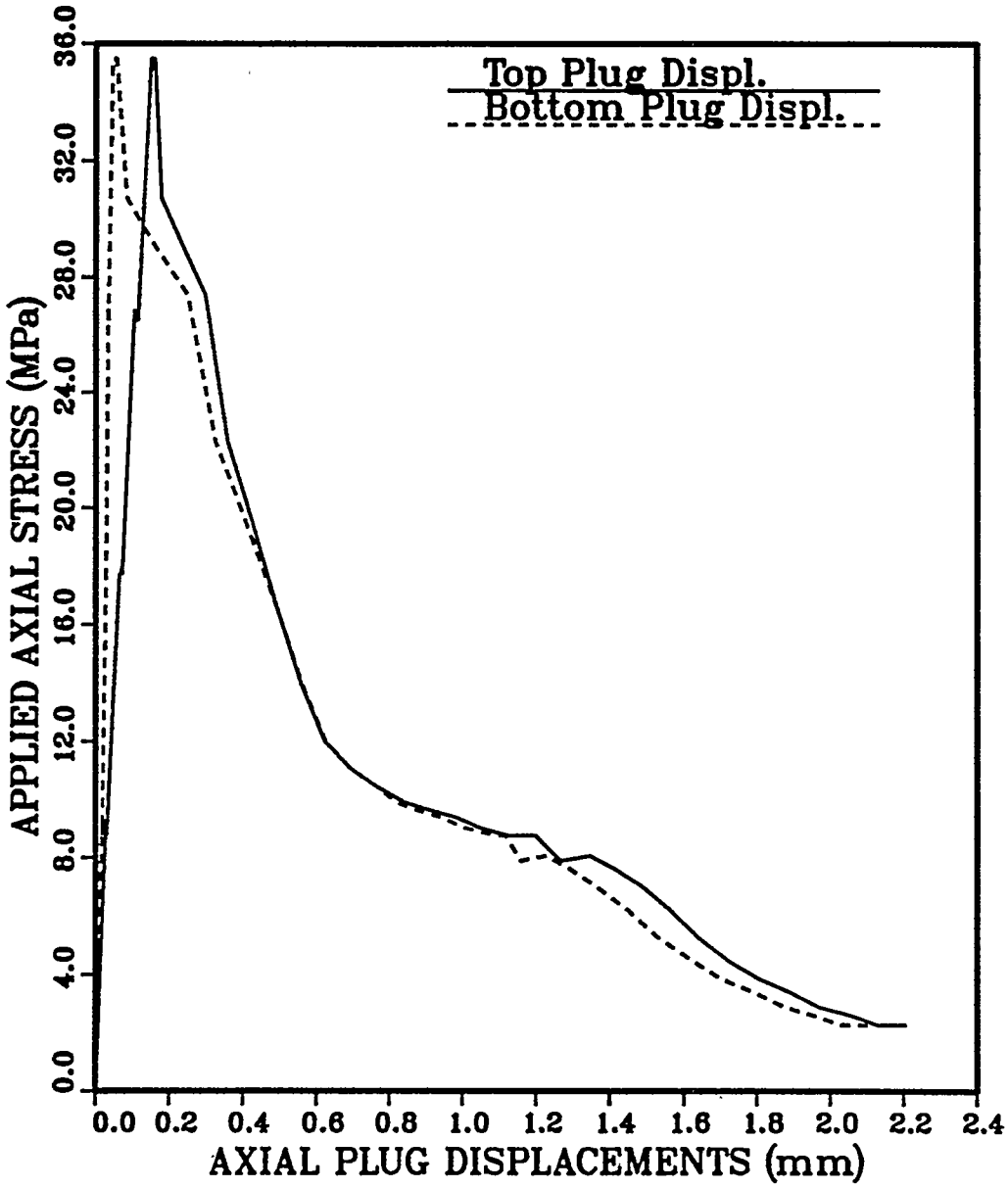

APA2-6-1-AMB-RD-1-P01-SSII

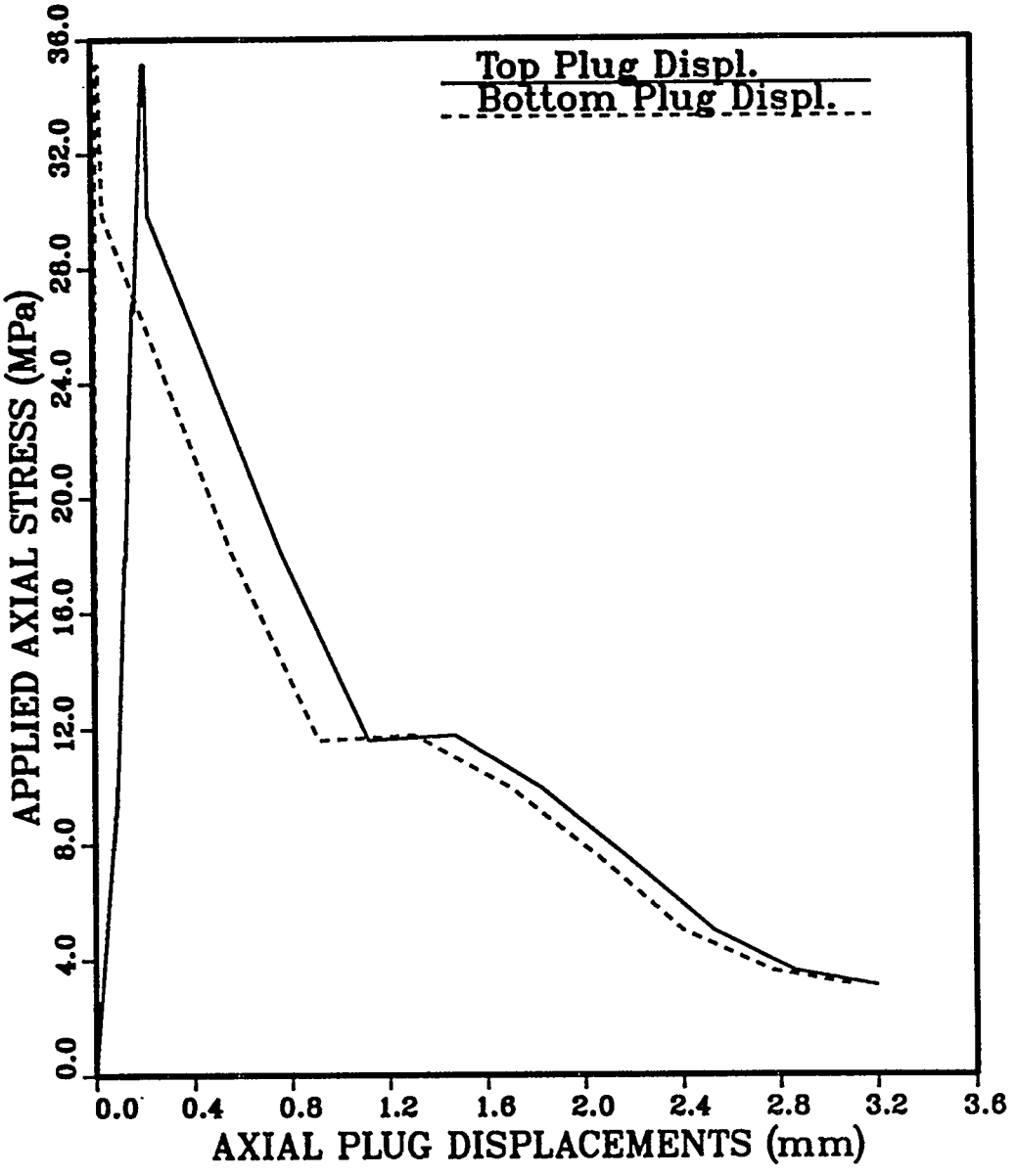

APD-6-1-AMB-RD-1-P03-SSII

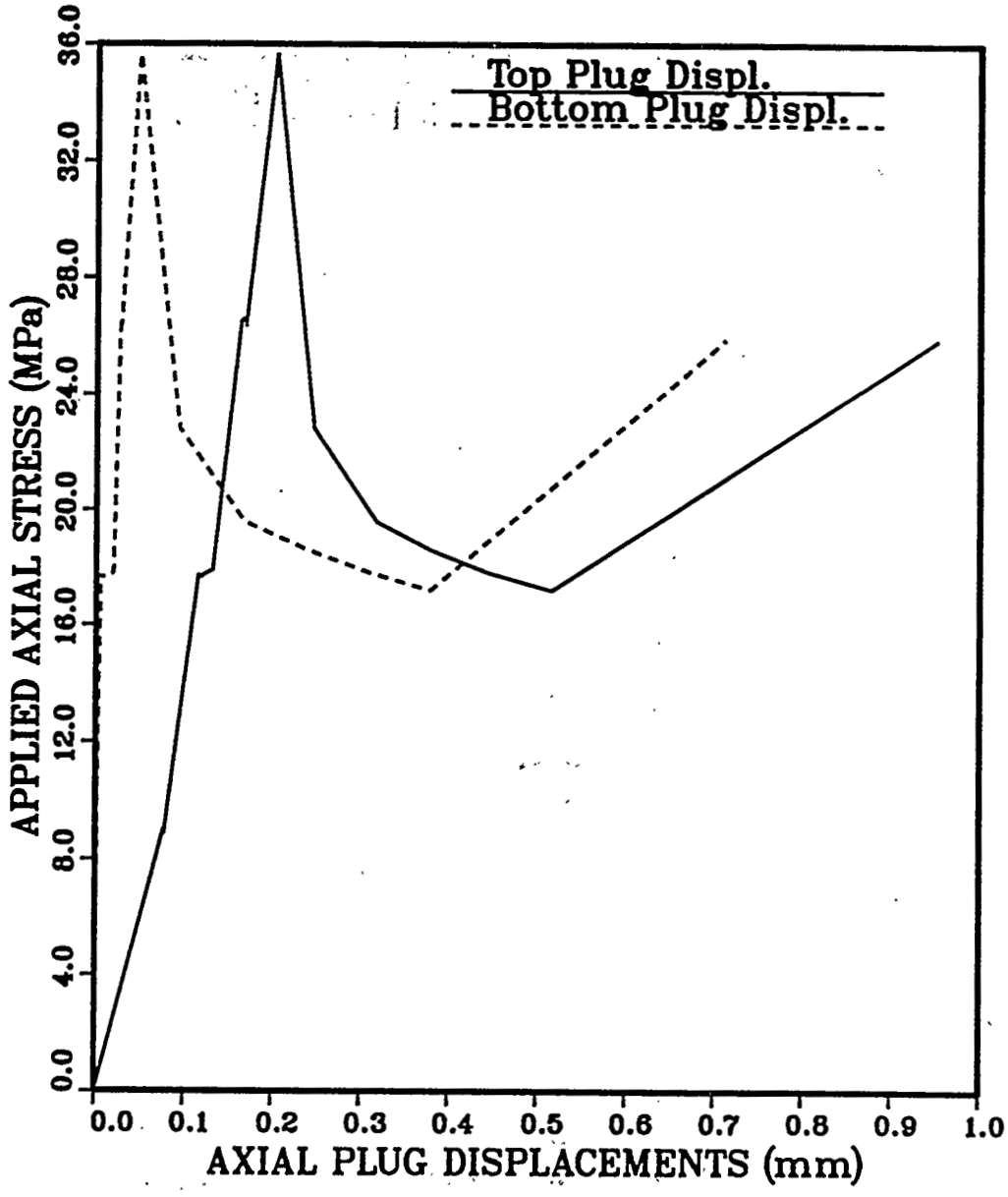

APJ-8-4-AMB-RD-4-P01-SSII

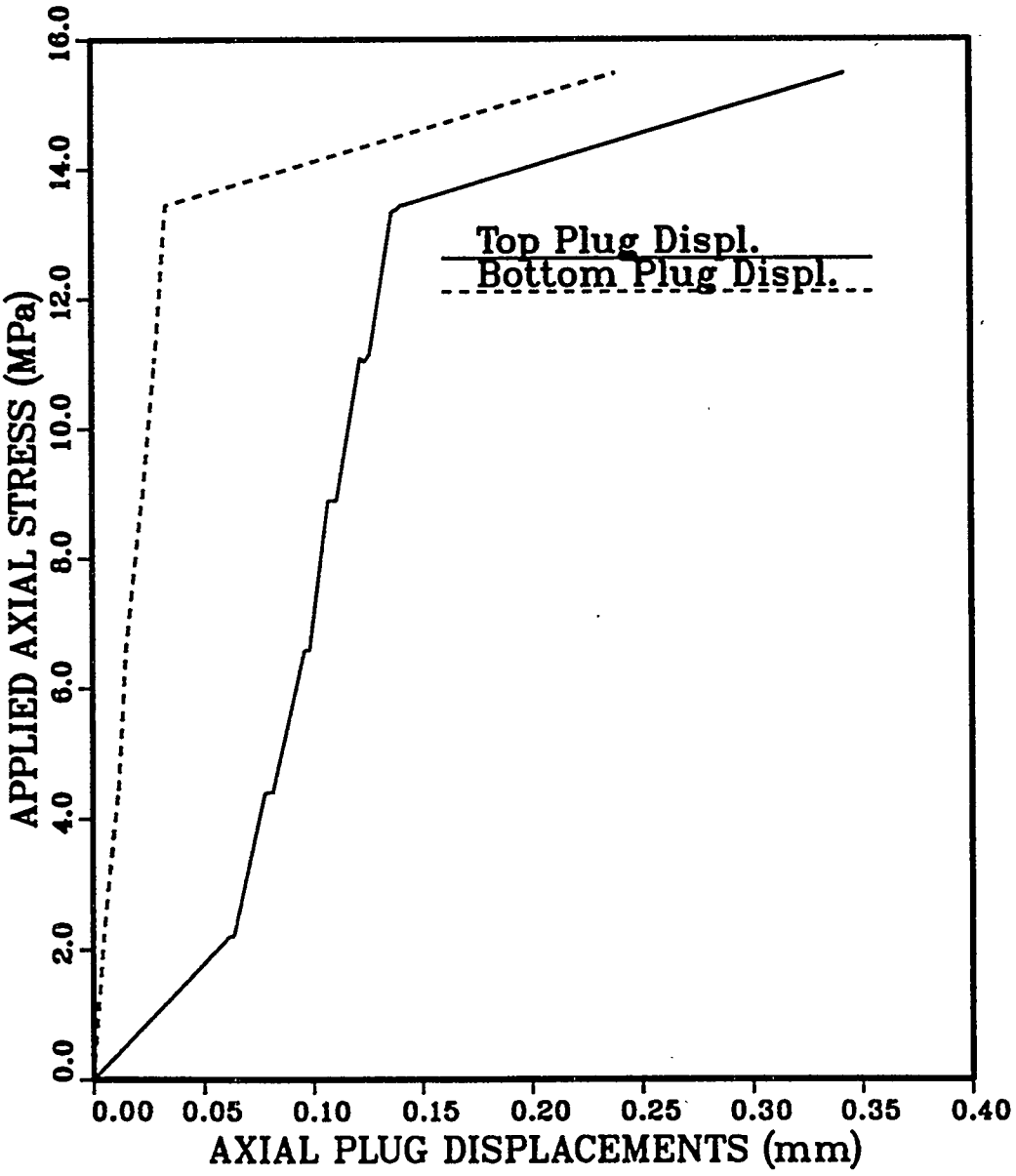

APA5-6-2-36-RD-4-P03-SSII

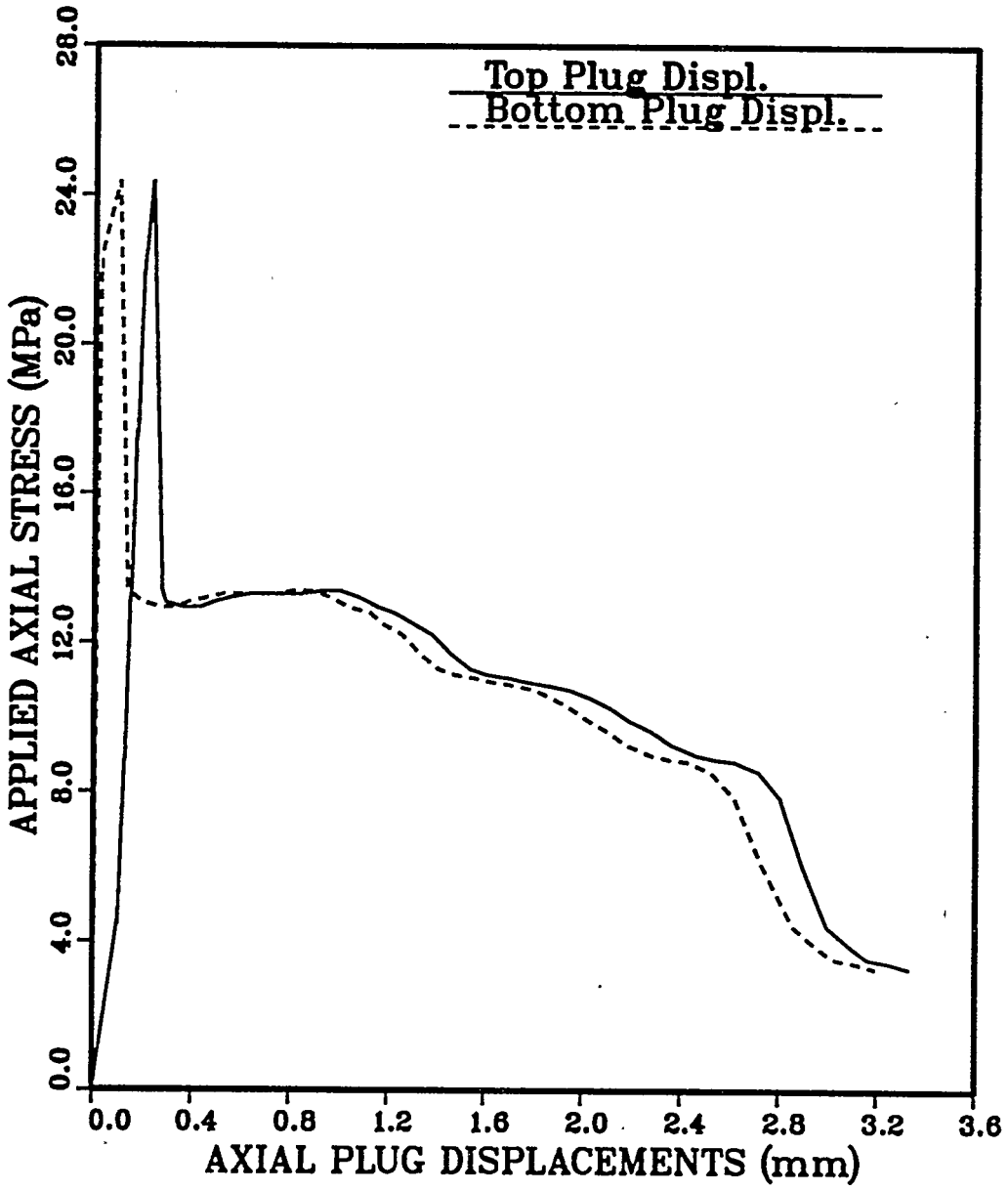

AP113-6-2-36-RD-2-P01-SSII

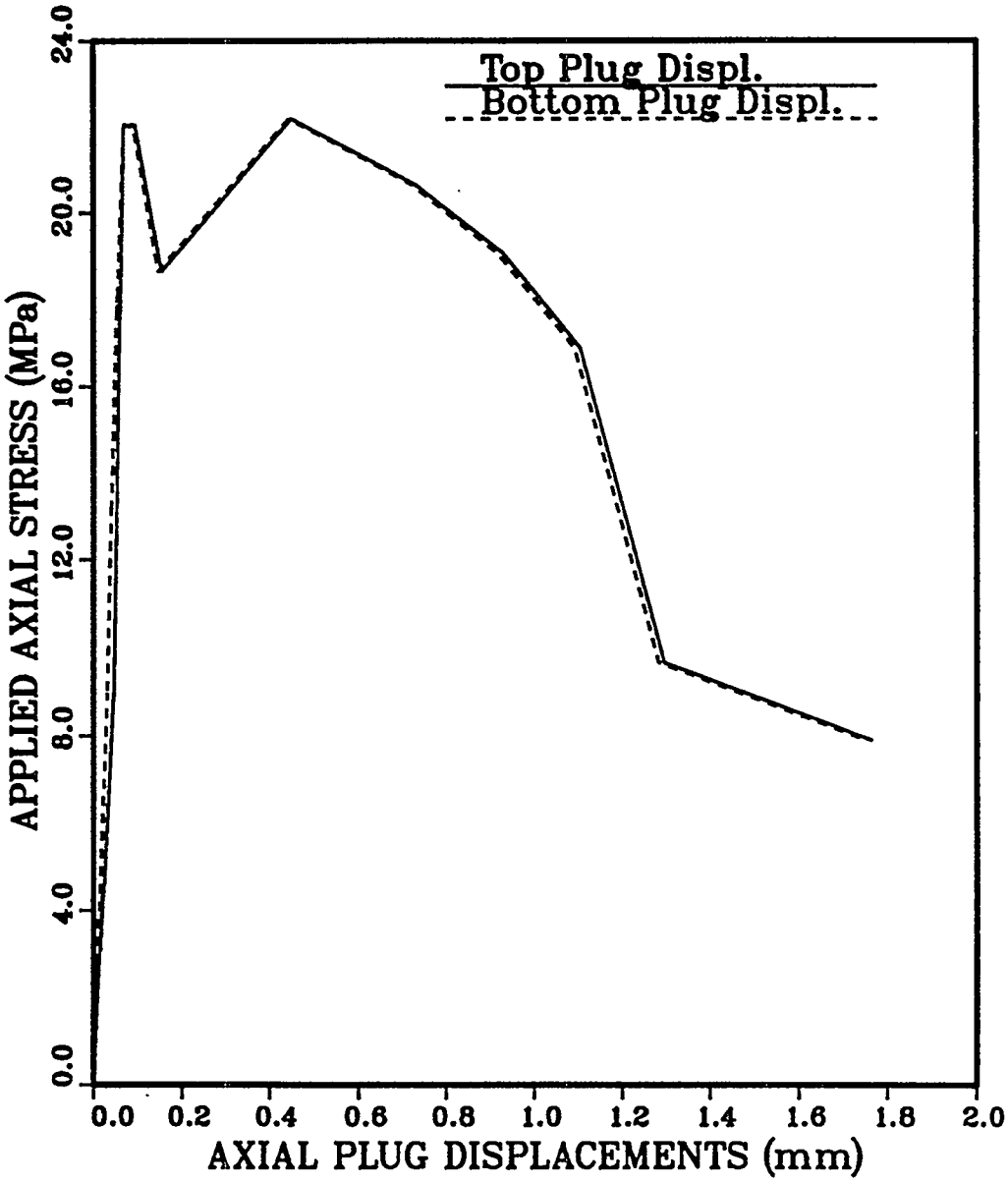

APA6-8-4-36-RD-1-P02-SSII

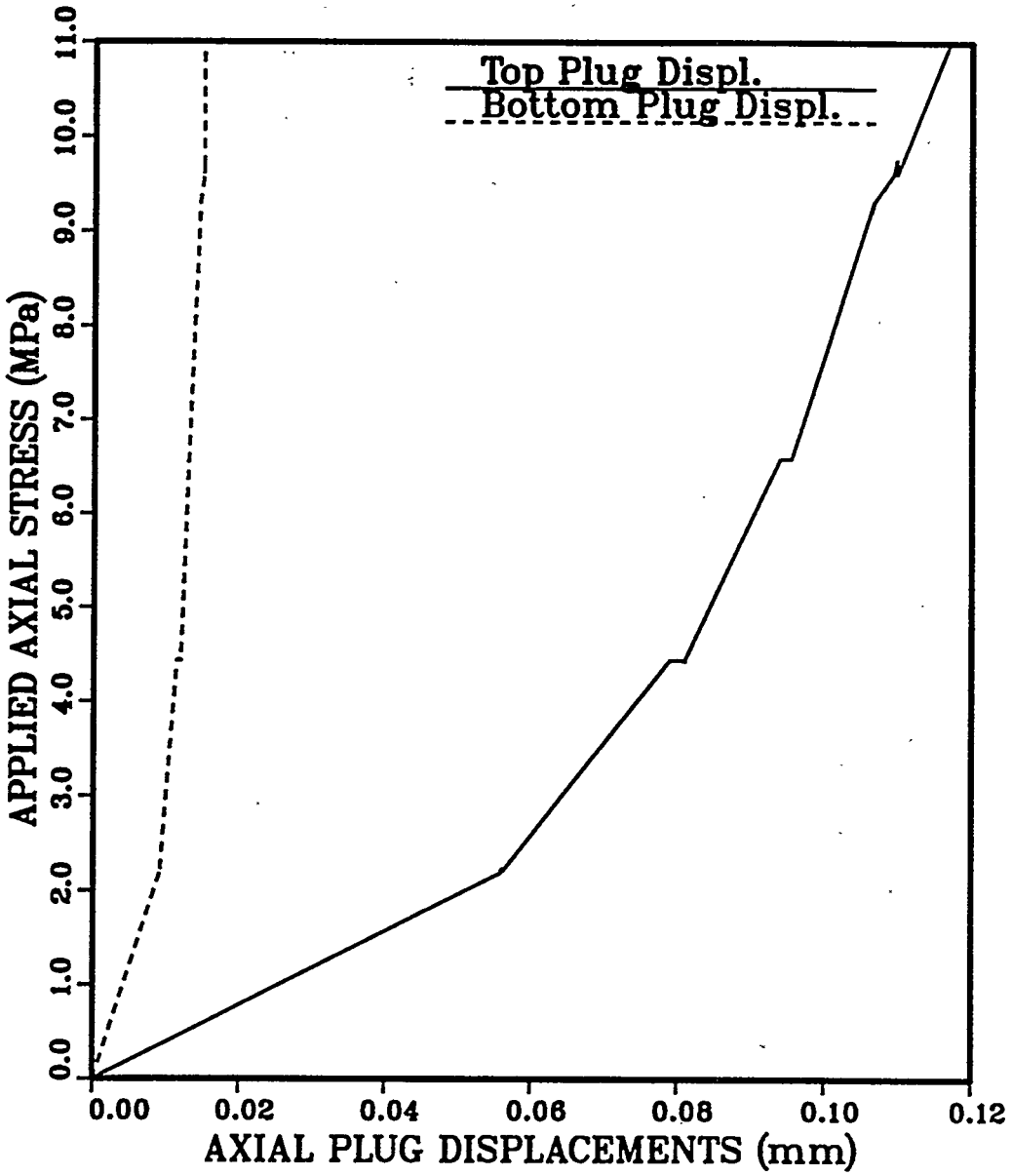

APD-6-2-36-RD-2-P01-SSII

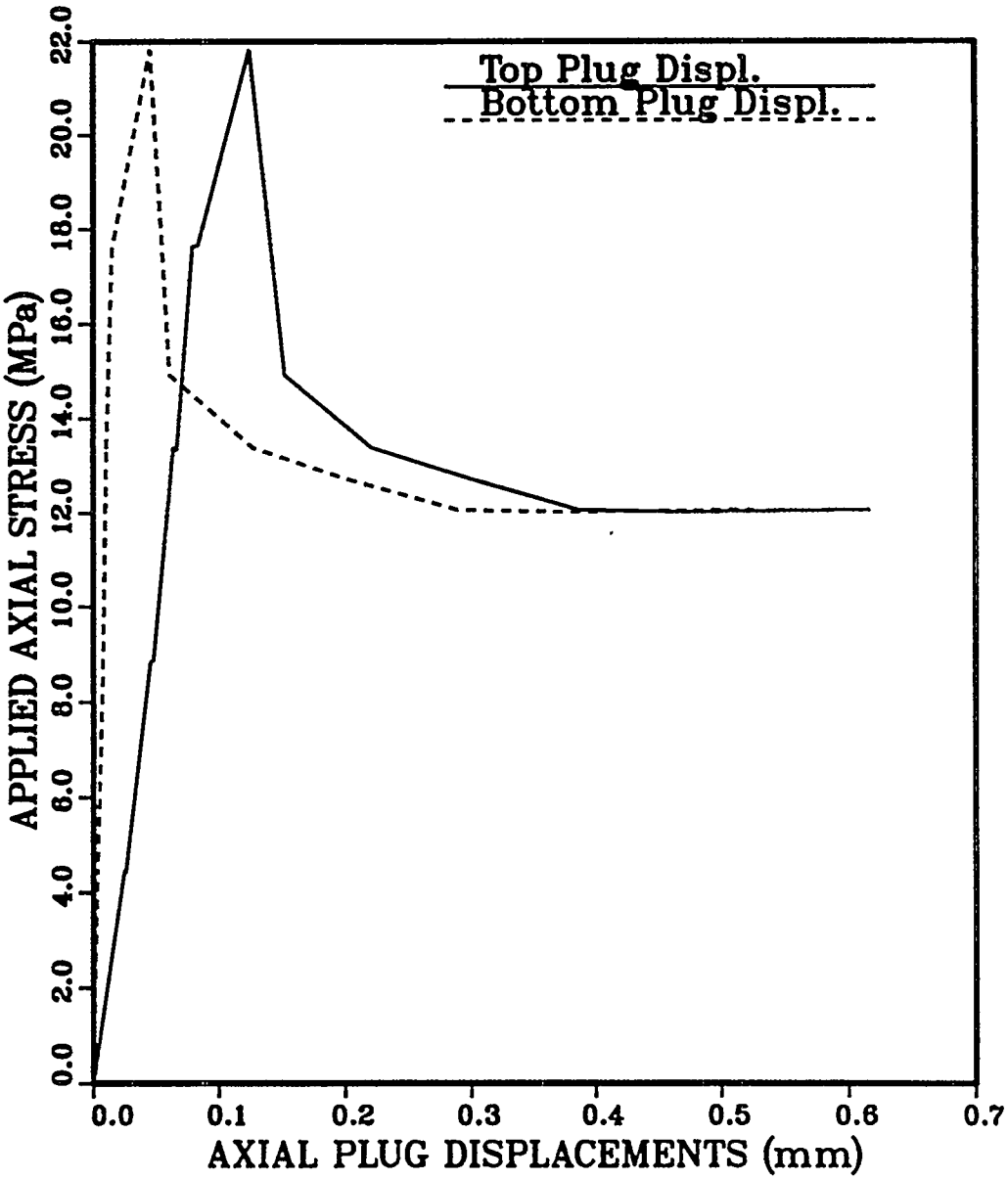

APPENDIX J

TENSILE STRENGTH OF PUSH-OUT CYLINDERS

The tensile stress in a hollow cylinder developed due to an internal radial stress is given by Jaeger and Cook (1979, p. 137):

$$\sigma_\theta \doteq -\frac{\sigma_n}{(R/a)^2-1}(1+(R/r)^2) \qquad (J.1)$$

where σ_θ = tensile stress in cylinder
σ_n = internal radial (normal) stress
R = radius of rock cylinder
a = radius of plug
r = radial distance from center.

The radial stress along the interface is the sum of the radial stress due to the axial stress applied to the plug, the thermal stress, and the cement swelling stress. The thermal radial stress and the cement swelling stress are assumed to be constant over the length of the plug.

The maximum tensile stress in the rock develops at r = a. The peak normal stress across the interface (Eq. (2.114)) occurs at the loaded end of the plug (i.e. z = 0). Substituting for σ_n and r = α into Eq. (J.1) gives the tensile strength of rock (σ_t):

$$\sigma_t = [\sigma_{po}(VSF)+\sigma_s+\sigma^P_{r,\Delta t}]\frac{[1+(R/a)^2]}{[1-(R/a)^2]} \qquad (J.2)$$

where σ_{po} = axial stress applied to the plug
VSF = vertical stress function (Eq. (2.39))
σ_s = cement swelling stress
$\sigma^P_{r,\Delta t}$ = thermal radial stress due to a temperature increase (Eq. (2.103))
R = radius of rock cylinder
a = radius of plug.

APPENDIX K

PROCEDURE FOR MECHANICAL CHARACTERIZATION OF SELF-STRESS II (SS II) CEMENT

K.1 Introduction

This section gives the procedure for the mechanical characterization of Self-Stress II (SSII) cement plugs. Testing provides the uniaxial compressive strength (σ_c), Young's modulus (E), and Poisson's ratio (ν) of Self-Stress II cement.

K.2 Sample Preparation and Testing Procedure for Compressive Strength Tests

50.8 mm diameter cylindrical cement specimens with length to diameter ratios ranging from 2.00 to 2.50 are prepared and tested according to standard practice (ASTM C39-86, Section 4; ASTM C192-81, Section 4; API Spec 10, 1986). For other sample diameters, the procedures are modified accordingly.

K.2.1 Apparatus

(1) Molds: all molds are acrylic tubes with 6.35 mm wall thickness, 25.4, 50.8 or 101.6 mm inside diameter and a length of 76 mm to 177.8 mm.

(2) Acrylic plate: 304.8 x 254 x 6.35 mm acrylic plate. Molds are glued on to the plate.

(3) Puddling rod: a glass or noncorroding metal rod.

(4) Funnel and plastic tube.

(5) Digital thermometer (Type JTC, Omega Engineering Co., Stamford, CT).

(6) Methylene chloride (PVC-cement)

K.2.2 Sample Preparation Procedure

K.2.2.1 Preparation of Molds

The molds are checked for any plastic residue from cutting. Use distilled water to remove any residue. Glue the bottom ends of the

cylindrical molds to the acrylic plate with methylene chloride (PVC-cement).

K.2.2.2 Preparation of the Cement Mixture

Mix the Self-Stress II (SSII) cement according to the API Specification No. 10 (American Petroleum Institute, 1986, pp. 14-19). Cement mixing procedure is given in Appendix C.

K.2.2.3 Placement of the Cement Mixture

Place the cement mixture in plastic molds in a layer equal to at least one-third of the mold length, using a funnel and plastic tube to avoid violent turbulence. Puddle 25 times with the puddling rod to eliminate cement segregation. Fill the molds with distilled water.[1,2] Three samples are prepared. Check the water level in the molds (above cement plugs) periodically to prevent drying out of the cement samples.

K.2.2.4 Curing Periods

The curing period is the time elapsed from pouring water on top of the cement in the molds to the time of testing. The curing period for all compressive strength tests is 8 days.[3] Molds are cured under atmospheric pressure, at room temperature (24 to 27°C) and at a monitored and reported relative room humidity.[3] Room temperature and relative humidity are monitored intermittently during curing.

K.2.2.5 Specimen Preparation

All cement cores are taken out of their molds after a curing period of 8 days.[4] The specimen ends are ground flat and parallel to 3 mm in 300 mm.[5] The diameter and length of the test specimen is determined to the

---

1 Procedure deviates from ASTM C192-81, Section 4, p. 149, which requires covering of molds with a plastic sheet to avoid evaporation.

2 Procedure deviates from API Spec No. 10 (1986, p. 18), which requires immersion of molds in a water bath maintained at the curing temperature (curing of test samples at 100% relative humidity).

3 Procedure deviates from API Spec No. 10 (1986, p. 18), which requires an 8 hr curing period for Class G cement prior to testing.

4 Procedure deviates from ASTM C192-81, Section 4, p. 149, which requires the removal of specimens from their molds in not less than 20 nor more than 48 h after casting.

5 Procedure according to ASTM C39-86, Section 4, p. 27.

nearest 0.25 mm by averaging three diameters and three lengths measured at 60° to one another. The diameter is determined at specimen ends and at about mid-height of the specimen.[6]

K.2.3 Testing

Test the moist-cured specimens after 8 days ± 7 hours (as soon as possible after removal from molds). Clean the bearing faces of the upper and lower bearing plates of the SoilTest compression test machine. Place the deformation jacket (Part No. DJC, manufactured by Structural Behavior Engineering Laboratories) around the cement sample to obtain lateral and axial specimen displacement during compressive strength testing. (The deformation jacket has an inside diameter of 50.8 mm and can not be used with samples with 25.4 or 101.6 mm diameters.) Place the test specimen on the lower bearing (moving) plate and carefully align the axis of the specimen with the center of thrust of the spherically seated block. As the spherically seated block is brought to bear on the specimen, rock its movable portion gently by hand so that uniform seating is obtained (Figure K.1). Apply the load continuously and without a shock using a loading rate of 252 N/s (0.12 MPa/s).[7] Make no adjustment in the rate of movement of the lower plate at any time while specimen is yielding rapidly. Measure the axial and lateral displacements at every load increment of 4448 ± 90 N (1000 ± 20 lbf), up to a load of 26688 ± 90 N (6000 ● 20 lbf). Following this, unload the sample, remove the deformation jacket (in order to prevent any damage to the jacket), and load the cement cylinder to failure.

K.2.4 Calculation of Uniaxial Compressive Strength, Young's Modulus and Poisson's Ratio of Cement Specimens

Calculate the compressive strength (σ_c) of the specimen at failure by dividing the maximum load carried by the specimen during the test by the initial cross-section area (to the nearest 0.069 MPa).[8] If applicable, calculate the axial strain (ϵ_{ax})[9] (at failure) in mm/mm, and the lateral

---

6 Procedure deviates from ASTM C39-86, Section 4, p. 27, which requires the determination of the diameter by averaging two diameters measured at right angles to each other at about mid-height of the specimen and the determination of the length to the nearest 0.05 diameter.

7 Procedure deviates from ASTM C39-86, Section 4, p. 28, which requires a loading rate of 0.14 to 0.34 MPa/s, and from API, Spec 10, p. 18, which requires a loading rate of 0.46 MPa/s.

8 Procedure deviates from ASTM C39-86, Section 4, p. 28, which requires the use of the average cross-sectional area (i.e. the area before and after failure). The area after failure can not be measured as all samples show splitting failure.

9 $$\epsilon_{ax} = \frac{\text{(initial specimen length) - (final specimen length)}}{\text{(initial specimen length)}}$$

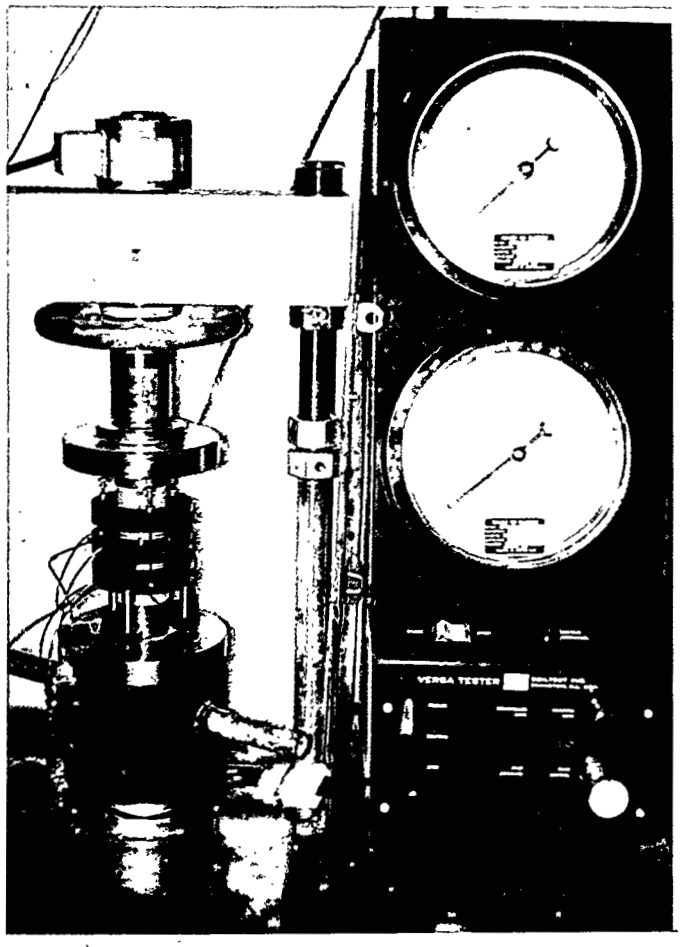

Figure K.1 Deformation jacket around cement paste cylinder measures the axial and lateral displacement during loading in SoilTest compression test machine.

strain (ϵ_{lat})[10] (at failure) in mm/mm. Calculate the Young's modulus and Poisson's ratio of the cement cylinder from the secant of the stress-strain curve at 50% of the strength (ISRM Suggested Methods, Bieniawski et al., 1978; ASTM D3148-80).

[10] $\epsilon_{lat} = \frac{\text{(initial specimen diameter) - (final specimen diameter)}}{\text{(initial specimen diameter)}}$

APPENDIX L

MECHANICAL PROPERTIES OF SELF-STRESS II CEMENT

Table L.1 Viscosity and Slurry Density of Self-Stress II Cement. Measurements made at a room temperature of 27°C and at 39 ± 1% relative humidity

Rotor Speed (rpm)	Time after Mixing Cement (sec)	Viscosity (kg/m·sec x 10^{-3})			
		Sample 1[a]	Sample 2[b]	Sample 3[c]	Sample 4[d]
300	60	35.5	35.0	35.5	32.0
200	80	37.5	36.8	37.5	33.0
100	100	42.0	42.0	42.0	37.5
6	120	112.5	112.5	112.5	112.5
3	140	200.0	200.0	200.0	200.0

[a]Cement slurry density of Sample 1 = 1.87 g/cc.
[b]Cement slurry density of Sample 2 = 1.85 g/cc.
[c]Cement slurry density of Sample 3 = 1.84 g/cc.
[d]Cement slurry density of Sample 4 = 1.86 g/cc.

Table L.2 Uniaxial Compressive Strengths of Self-Stress II Cement Paste Cylinders. The specimens have a nominal diameter of 50.8 mm (2 in).

Sample Number	Specimen Length-to-Diameter Ratio	Uniaxial Compressive Strength (MPa)
B-4	2.45	18.8
B-5	2.45	18.3
B-6	2.44	18.0
B-8	2.38	17.8
B-13	2.42	17.7
B-18	2.40	17.5
B-20*	2.44	20.1
B-21	2.39	19.7
B-23	2.50	20.1
B-24*	2.40	19.2
B-26*	2.50	19.4
Mean ± One Standard Deviation:		18.8 ± 0.97

*Tests with deformation jacket.

Table L.3 Results of the Cement-on-Rock Small-Scale Direct Shear Tests. Rock and cement discs have a nominal diameter of 50.8 mm (2 in).

Sample Number	Friction Angle (°) Peak (ϕ_p)	Friction Angle (°) Residual (ϕ_r)	Cohesion (MPa) Peak (c_p)	Cohesion (MPa) Residual (c_r)
APD-6(H1)	30	29	0.0303	0.02
APD-6(H2)	26	25	0.058	0.042
APD-6(H4)	20	19	0.063	0.053
Mean ± One Standard Deviation:	25 ± 5	24 ± 5	0.05 ± 0.018	0.038 ± 0.017

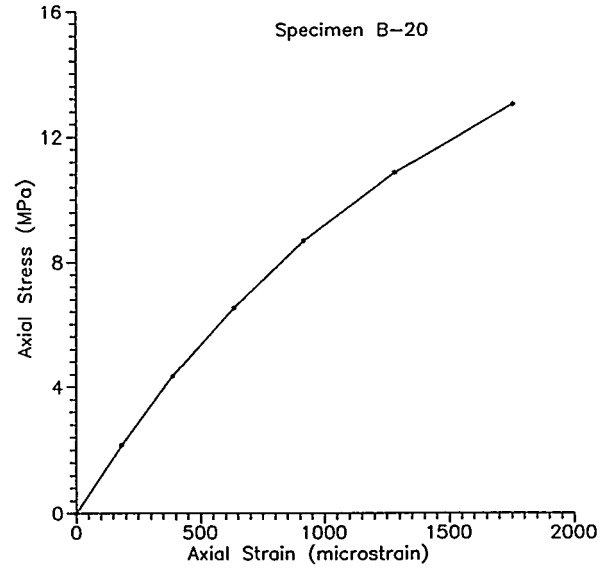

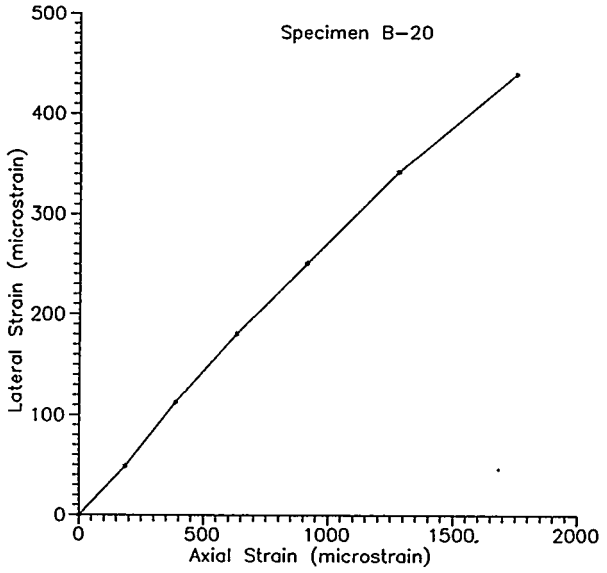

Figure L.1 Top: axial stress vs. axial strain. Bottom: lateral strain vs. axial strain.

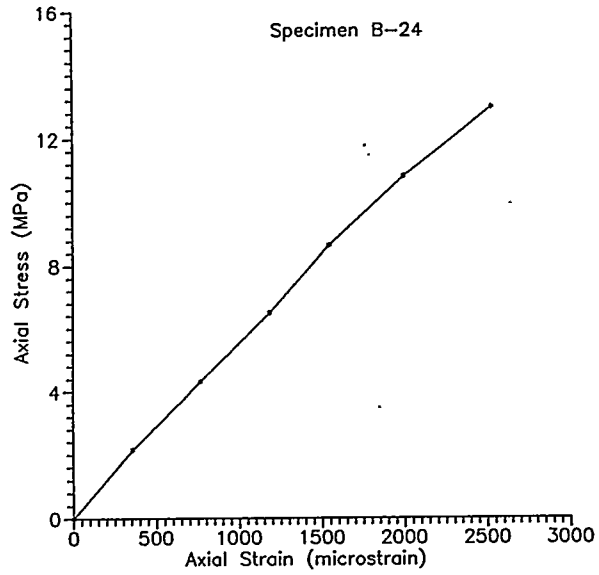

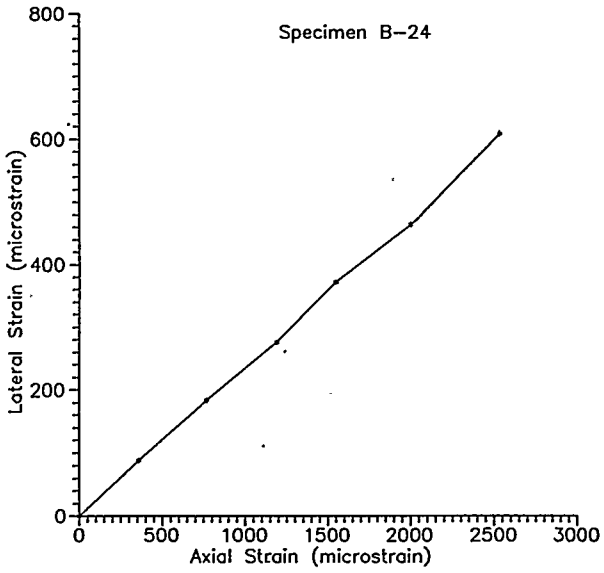

Figure L.2 Top: axial stress vs. axial strain. Bottom: lateral strain vs. axial strain.

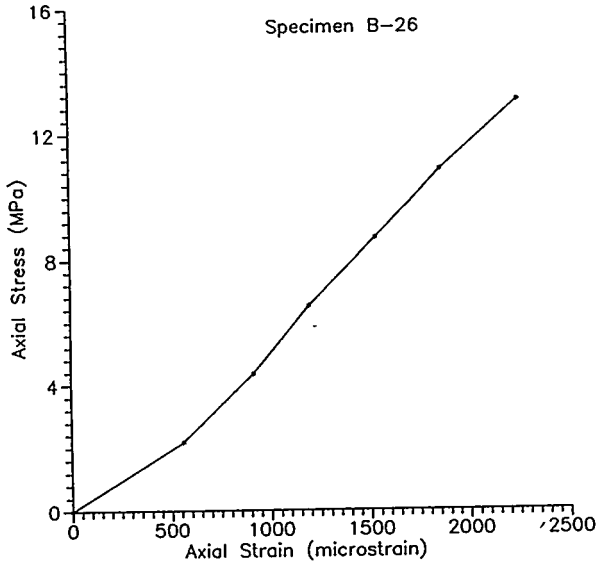

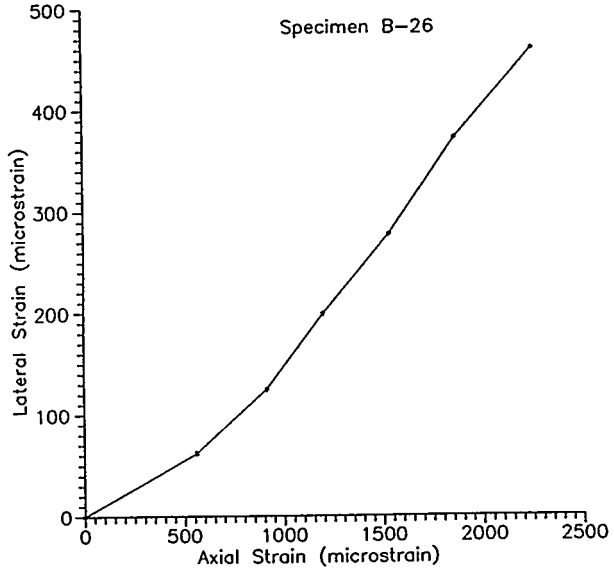

Figure L.3 Top: axial stress vs. axial strain. Bottom: lateral strain vs. axial strain.

CEMENT SWELLING TEST RESULTS

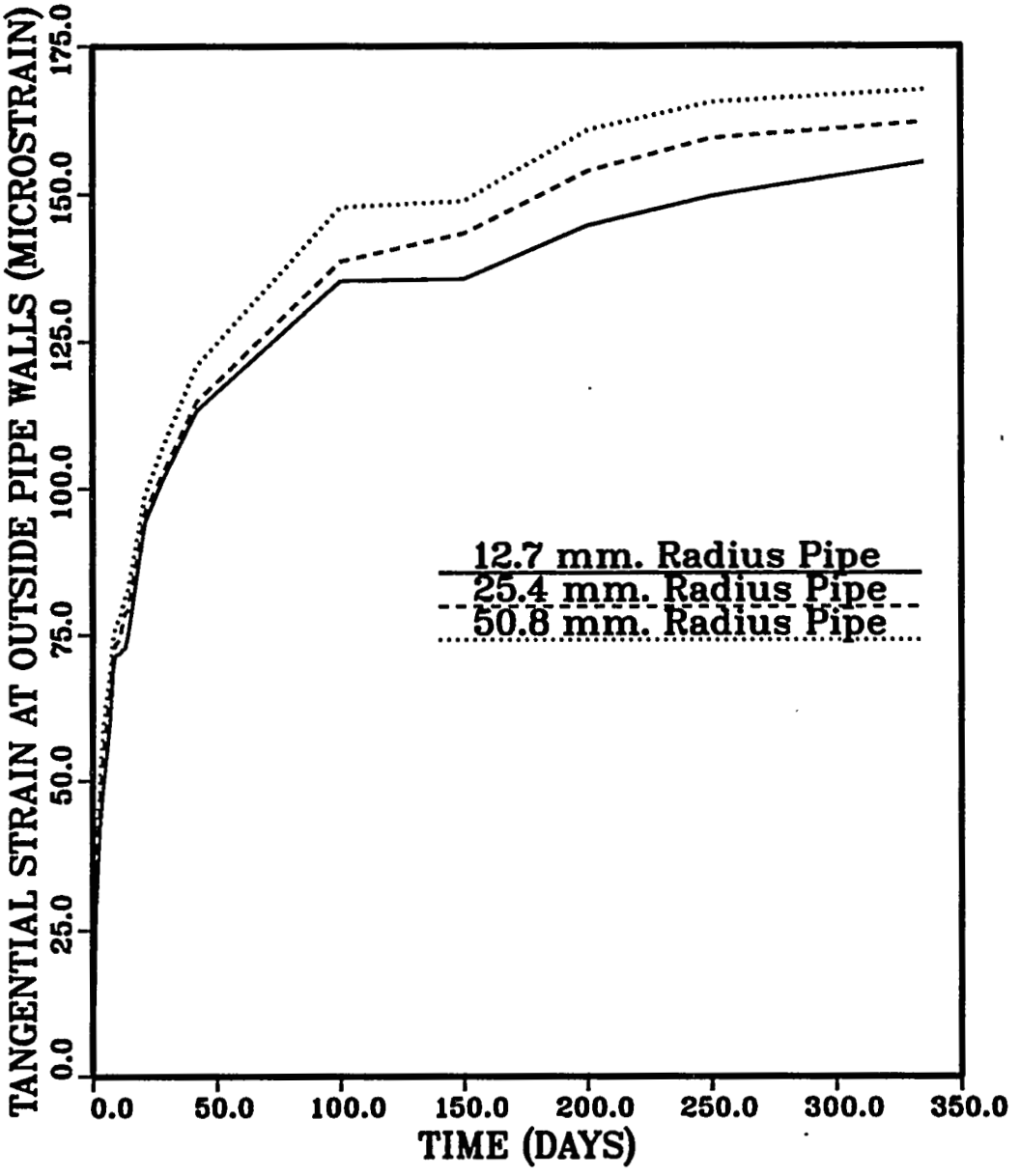

Figure L.4 Mean tangential strain on the steel pipe outside walls vs. curing time. The inside pipe diameters are identified in the legend. Time measured since emplacing cement.

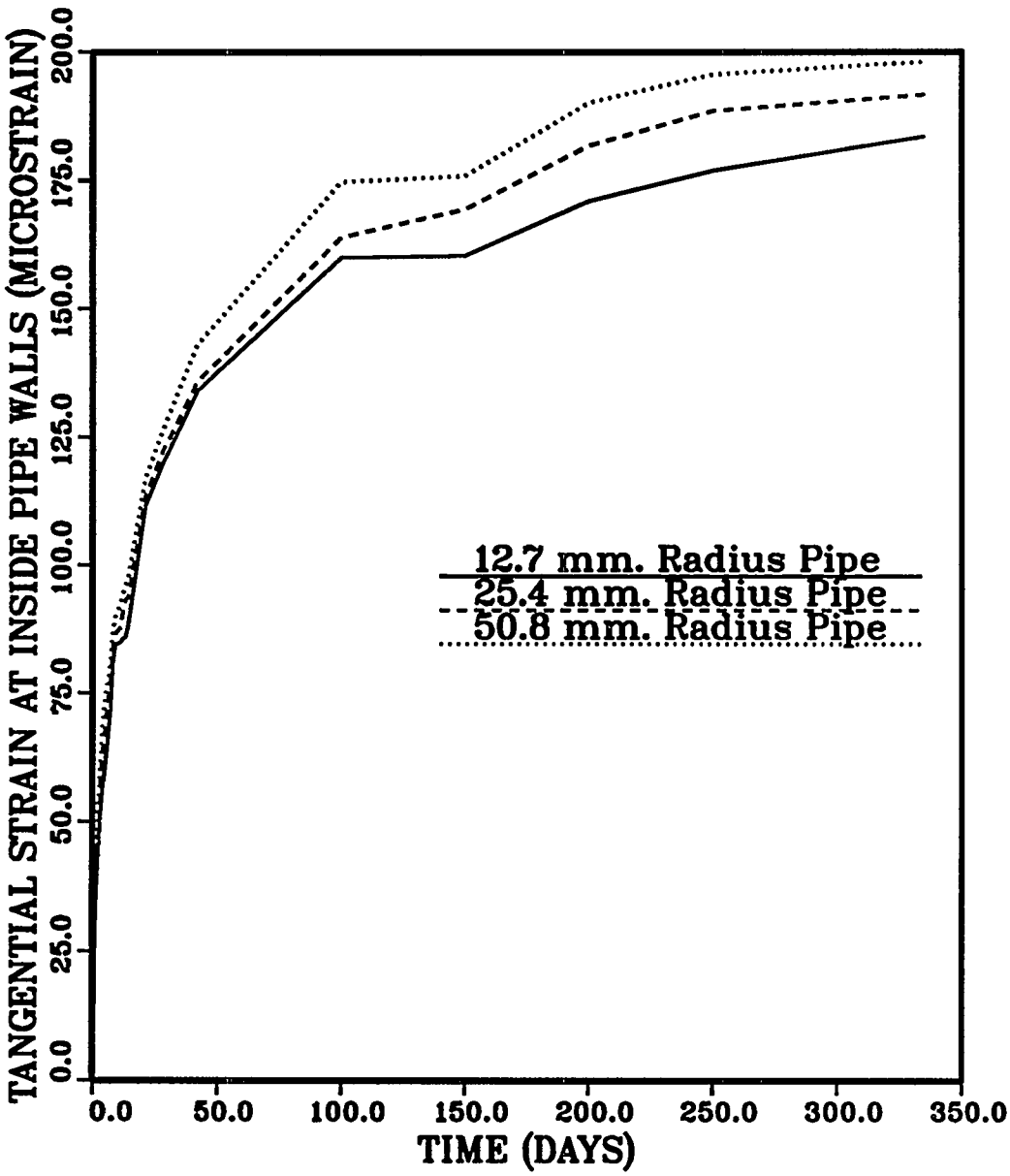

Figure L.5 Mean tangential strain on the steel pipe inside walls vs. curing time. Time measured since emplacing cement. The tangential strain on the steel pipe inside walls is calculated from Eq. (M.7) (Appendix M).

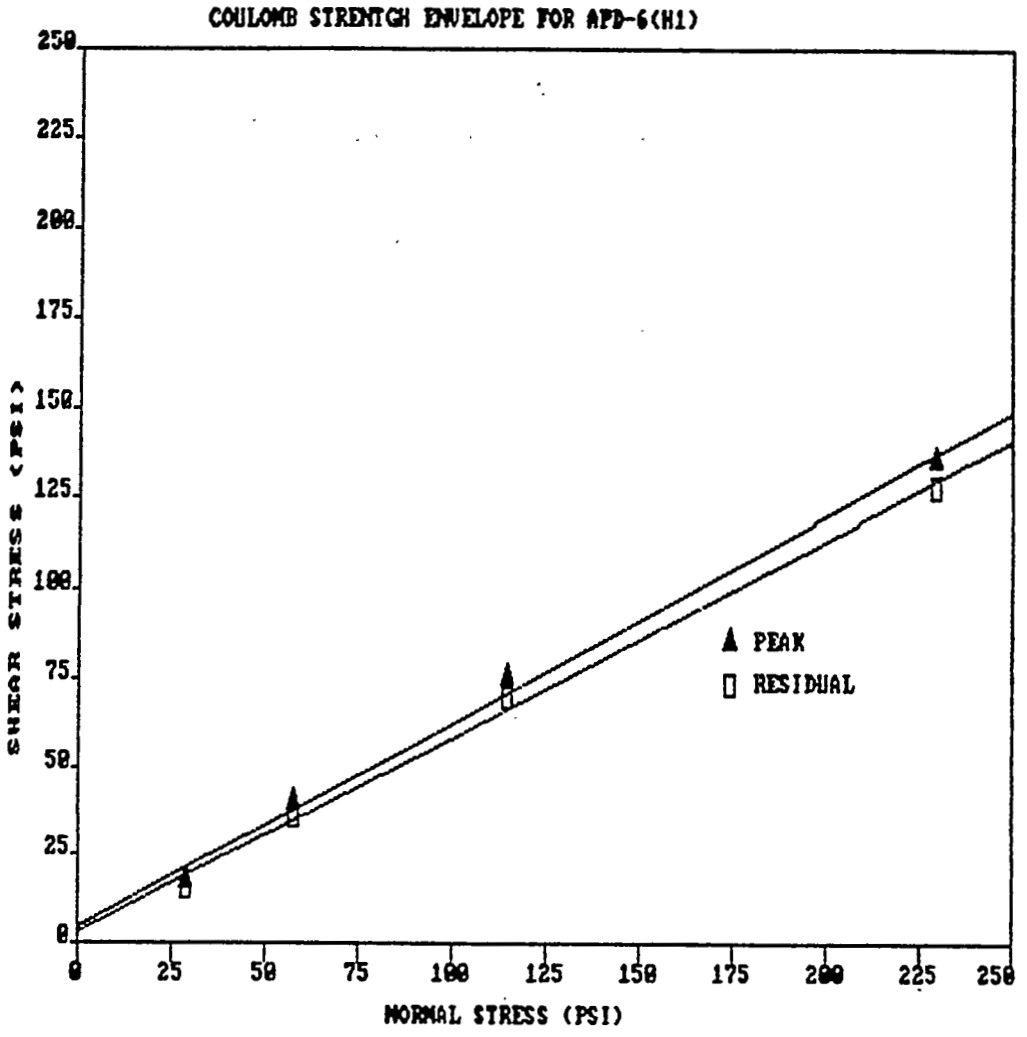

Figure L.6 Mohr-Coulomb strength envelope for cement-on-rock direct shear testing of sample APD-6(H1). Linear regression fit for the peak and residual envelopes.

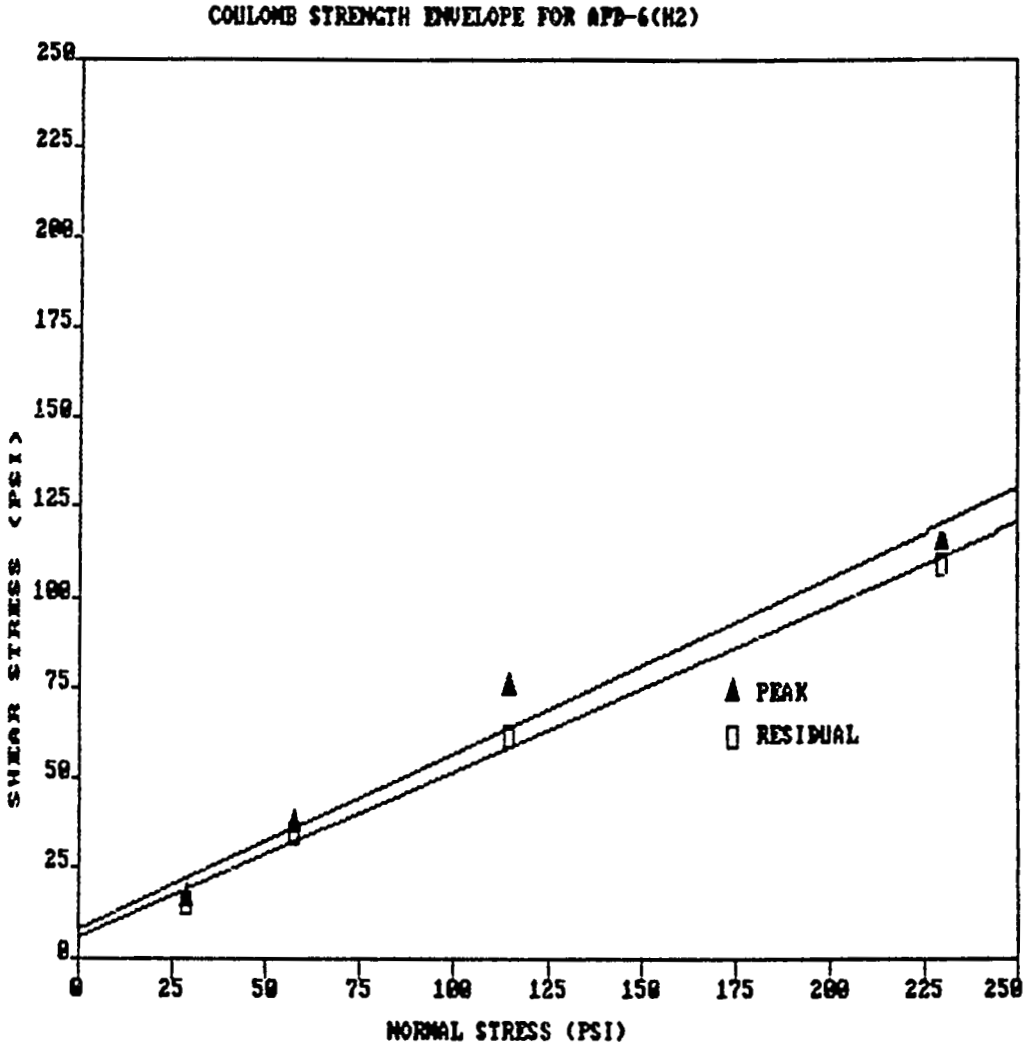

Figure L.7 Mohr-Coulomb strength envelope for cement-on-rock direct shear testing of sample APD-6(H2). Linear regression fit for the peak and residual envelopes.

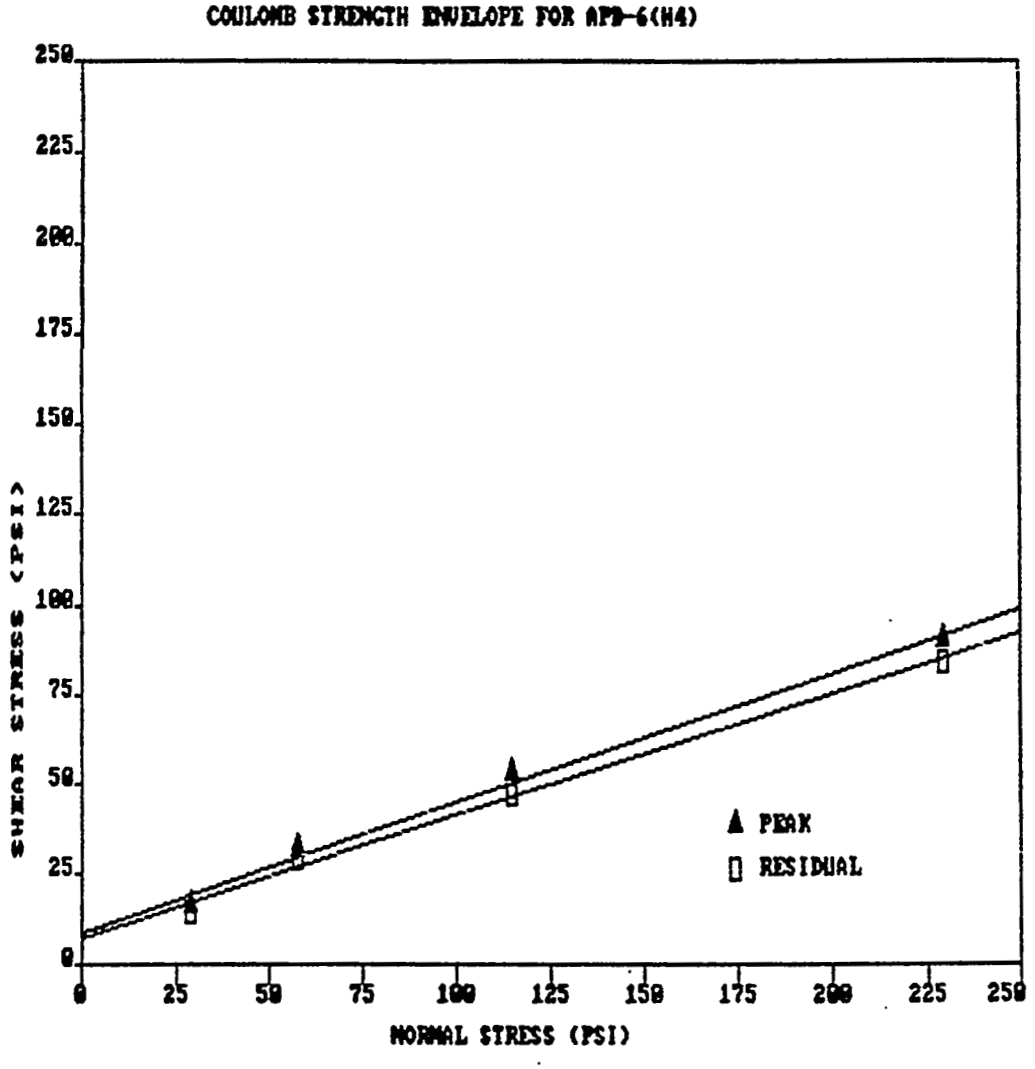

Figure L.8 Mohr-Coulomb strength envelope for cement-on-rock direct shear testing of sample APD-6(H4). Linear regression fit for the peak and residual envelopes.

APPENDIX M

CEMENT SWELLING TEST PROCEDURE

M.1 Objective

The objective of this test procedure is to evaluate the expansive stresses generated by Self-Stress II cement. The cement swelling pressures are measured by pouring cement into steel pipes having inside diameters of 25.4 mm (1 in), 50.8 mm (2 in) and 101.6 mm (4 in). All pipes have wall thickness to inside diameter ratios of 1/16, and hence identical stiffnesses. The cement plugs installed in these steel pipes have length to diameter ratios (L/D) of 1.0. The cement swelling pressures are determined with two tangential strain gages, placed 180 from each other, installed on the outside walls of each steel pipe. An additional objective of this test procedure is to monitor the hydration temperature of the cement plugs with thermocouple probes.

M.2 Procedure for Performing Cement Swelling Tests in Steel Pipes

(1) Cut three 25.4 mm (1 in) inside diameter (ID), 28.6 mm (1.125 in) outside diameter (OD) steel pipes to a length of 101.6 mm (4 in); three 50.8 mm (2 in) ID, 57.2 mm (2.25 in) OD steel pipes to a length of 127 mm (5 in); and three 101.6 mm (4 in) ID, 114.3 mm (4.5 in) OD steel pipes to a length of 177.8 mm (7 in). Check the perpendicularity of the sides of the steel pipes with the top and bottom pipe surfaces by means of a straight edge. If not perpendicular, grind the bottom and/or top steel pipe surfaces until perpendicularity is attained.

(2) Place the steel pipes in a wooden plate with holes drilled through. The holes have the same diameter as the outside diameter of the steel pipes. The wooden plate with holes stabilizes the steel pipes during cement expansion measurements.

(3) Install two tangential strain gages, placed 180° from each other, at the mid-height of the cement plug position on the outside walls of each steel pipe. (Follow strain gage installation procedures given by Measurements Group, Inc., 1979, or Adisoma et al., 1987):

(3a) Mixing instructions for M-Bond 610 strain gage adhesive:

1. Note that the adhesive curing agent bottles must be at room temperature before opening.
2. Using the disposable plastic funnel, empty contents of bottle

labelled "Curing Agent" into bottle of resin labelled "Adhesive". Discard funnel.
3. After tightening the brush cap (included separately), thoroughly mix contents of the "Adhesive" bottle by vigorously shaking it for 10 seconds.
4. Mark date of mixing on bottle in space provided on the label.
5. Allow this freshly mixed adhesive to stand for at least one hour before use.
6. At room temperature M-Bond 610 will last about nine months. The period of adhesive usefulness can be doubled by refrigeration at 0 to 5°C. Refrigerated bottles should never be opened until room temperature is reached.

(3b) Procedure for surface preparation of steel pipes:

1. Wipe off dirt from steel pipe surfaces.
2. Thoroughly degrease the gaging area with a solvent, such as CSM-1 Degreaser or FTF-1 Mild Degreaser.
3. Sand down the gage area with a 220 or 320 grit silicon-carbide paper. Final abrading is done by using a 320 or 400 grit silicon-carbide paper on surfaces thoroughly wetted with M-Prep Conditioner A. Wipe dry with a gauze sponge.
4. Mark lines to align strain gages tangentially using a #4 pencil.
5. Apply M-Prep Conditioner A and M-Prep Neutralizer 5, allowing each to dry before application of the next.
6. Perform final cleaning/degreasing. Apply heat (with a heat gun) to drive out oil, moisture and solvent from the gaging area.
7. Apply M-Prep Conditioner A; scrub and dry.
8. Apply M-Prep Neutralizer 5; let dry.

(3c) Strain gage installation:

1. Apply CEA-06-250UN-350 strain gages as soon as the surface preparation is completed and not longer than 20 minutes afterwards or repeat the surface preparation.
2. Never contaminate gages by handling with fingers. Touching the foil element can lead to long-term changes in resistance. Touching the backing can lead to bonding problems. The gage should always be handled by holding the gage backing as far from the foil as possible using a pair of clean, round-nosed tweezers. It is important that the foil not be scratched or marked as this can seriously degrade the gage performance.
3. Arrange the gages on a clean, degreased surface. Use a 25.4 to 76.2 mm (2 to 3 in) piece of cellophane tape and a pair of tweezers to pick up the gages. Place the foil side of the gages on the tape and position them on the steel pipe outside wall surface so that the strain gages are aligned tangential (form a "hinge" with one end of the tape).

4. By lifting at a shallow angle, peel back one end of the taped assembly so as to raise both gage and terminal. Coat gage backing, terminal and gaging area on steel pipe with a thin layer of adhesive. Do not allow adhesive applicator to touch tape. Permit adhesive to air-dry for 5 to 30 minutes.
5. Return gage/terminal assembly to its original position (tangential) over layout marks. Press the tape holding the gage to the steel pipe surface immediately, using a wiping motion with the thumb. Hold firmly for at least one minute. Overlay gage/terminal area with a piece of Teflon sheet. If necessary, anchor Teflon in position with a piece of tape on steel pipe surface.
6. Repeat steps 4 and 5 for the second tangential strain gage placed 180 from the first one (on the steel pipe outside wall).
7. Cut two 2.5 mm thick silicone gum pads and two metal backup plates to a size slightly larger than the gage/terminal areas. Carefully center these on the two tangential strain gages placed 180° from each other. Use rubber clamps to apply pressures up to 0.48 MPa (70 psi) to the strain gages during curing. Cure the strain gages at room temperature for a week.
8. Upon completion of the curing cycle, remove rubber clamps and tape. Apply a thin layer of M-Coat J to the strain gage surfaces for protection against moisture.

(3d) Strain gage resistance checking:

Check lateral leads of both tangential strain gages (attached to each steel pipe and placed 180° from each other) with an ohmmeter and make sure no current leakage occurs. For the 350 Ω strain gages the resistance should be as follows:

700 Ω from any lateral to lateral lead;
infinite resistance from any lateral lead to steel pipe.

(3e) Strain gage wiring:

The tangential strains are measured by the HP data acquisition system (HP-3497A). The HP-3497A has 20 channels (channels 40 through 49 and 60 through 69) allocated for strain gage data collection. Each channel is connected to one of the strain gages attached to the outside walls of each steel pipe. Each of the HP-3497A strain gage channels has three wires: the white wire (excitation -); the red wire (signal) and the black wire (excitation +). Solder the white and red wires to the upper lateral lead wire and the black wire to the lower lateral lead wire of each tangential strain gage. Place electrical tape on the solder areas. Cut the bridges provided for each strain gage channel (within the HP-3497A strain gage cards) for 1/4 bridge configuration.

(4) Place a rubber stopper into the steel pipes at the level where a central cement plug with a length to diameter ratio (L/D) of 1.0 is to be located.

(5) Place a thermocouple probe (Type J, Omega Engineering, Inc.) in each steel pipe at the mid-height of the cement plug to be poured and at the center of the pipe. Connect each thermocouple probe to the HP-3497A (channels 0-8). Use the thermocouple probe of channel 9 to record the room temperature.

(6) Program the HP-3497A to collect data (10 temperatures and 18 strains) every 5 minutes. Pause the HP.

(7) Mix the Self-Stress II cement according to the cement mixing procedure given in Appendix C. Pour the cement slurry onto the rubber stoppers until a cement plug with a length to diameter ratio of 1.0 is obtained. Start the HP and collect data every 5 minutes.

(8) After 24 hours of cement curing collect data every 6 hours.

M.3 Calculation of the Cement Expansive Stresses and Radial Displacements

(1) Obtain the average of the two tangential strain readings on the outside walls of the steel pipes ($\epsilon_{\theta(r=R)}$) (average readings of the two tangential strain gages placed 180° from each other on the outside walls of each steel pipe) at any stage of cement curing.

(2) Calculate the expansive stresses (σ_s) generated by the Self-Stress II cement poured in the steel pipes according to the formula derived from Eq. M.4, as follows:

The tangential stress on the steel pipe outside walls (r = R) is calculated for a plane strain configuration (i.e. when the vertical strain ϵ_z at r = R is negligible). The radial stress at r = R is zero. From Hooke's law, the tangential stress at r = R is:

$$\sigma_{\theta(r=R)} = \frac{E_s \epsilon_{\theta(r=R)}}{(1-\nu_s^2)} \qquad (M.1)$$

where $\sigma_{\theta(r=R)}$ = tangential stress on the steel pipe outside walls
E_s = Young's modulus of steel pipe
ν_s = Poisson's ratio of steel pipe
$\epsilon_{\theta(r=R)}$ = average induced tangential strain (average of two tangential strain gage readings) on the steel pipe outside walls
r = radial coordinate
R = outside radius of steel pipe.

The tangential stress (σ_θ) distribution in a hollow cylinder with an internal radius a and external radius R, subjected to a radial stress σ_s at r = a (assuming plane strain) is (Jaeger and Cook, 1979, p. 137; Timoshenko, 1956, pp. 205-210):

$$\sigma_\theta = -\frac{\sigma_s a^2}{(R^2 - a^2)}\left(1 + \frac{R^2}{r^2}\right) \qquad (M.2)$$

The tangential stress on the steel pipe outside walls ($\sigma_{\theta(r=R)}$) follows from Eq. (M.2) as:

$$\sigma_{\theta(r=R)} = -\frac{2\sigma_s a^2}{(R^2 - a^2)} \qquad (M.3)$$

Equating Eqs. (M.1) and (M.3) and solving for the radial swelling stress (σ_s) yields:

$$\sigma_s = \frac{E_s \epsilon_{\theta(r=R)}(R^2 - a^2)}{2(1 - \nu_s^2)a^2} \qquad (M.4)$$

(3) Calculate the radial displacement (u_p) induced by Self-Stress II cement poured in steel pipes from Eq. (M.6) as follows:

The radial displacement on the steel pipe inside walls (u_p) follows from Eq. (2.37a) as:

$$u_p = -\frac{\sigma_s(1 + \nu_s)a}{E_s(R^2 - a^2)}[(1 - 2\nu_s)a^2 + R^2] \qquad (M.5)$$

Combining Eqs. (M.4) and (M.5) gives the radial displacement of the plug (u_p):

$$u_p = \frac{\epsilon_{\theta(r=R)}}{2(1 - \nu_s)a}[(1 - 2\nu_s)a^2 + R^2] \qquad (M.6)$$

where $\epsilon_{\theta(r=R)}$ = average induced tangential strain (average of two tangential strain gage readings) on the steel pipe outside walls
ν_s = Poisson's ratio of steel pipe
a,R = inside and outside radii of steel pipe.

The average tangential strain in the plug ($\epsilon_{\theta(r=a)}$) is:

$$\epsilon_{\theta(r=a)} = \frac{u_p}{a} \qquad (M.7)$$

NRC FORM 335 (6 83) U S NUCLEAR REGULATORY COMMISSION

BIBLIOGRAPHIC DATA SHEET

1 REPORT NUMBER (Assigned by TIDC, add Vol No., if any)
NUREG/CR-4295

2 Leave blank

3 TITLE AND SUBTITLE
Bond Strength of Cementitious Borehole Plugs in Welded Tuff

4 RECIPIENT'S ACCESSION NUMBER

5 DATE REPORT COMPLETED
MONTH: June YEAR: 1990

6 AUTHOR(S)
H. Akgun, J. J. K. Daemen

7 DATE REPORT ISSUED
MONTH: February YEAR: 1991

8 PERFORMING ORGANIZATION NAME AND MAILING ADDRESS (Include Zip Code)
Department of Mining and Geological Engineering
University of Arizona
Tucson, AZ 85721

9 PROJECT/TASK/WORK UNIT NUMBER

10 FIN NUMBER
FIN D1192

11 SPONSORING ORGANIZATION NAME AND MAILING ADDRESS (Include Zip Code)
Division of Engineering
Office of Nuclear Regulatory Research
U.S. Nuclear Regulatory Commission
Washington, DC 20555

12a TYPE OF REPORT
Technical

12b PERIOD COVERED (Inclusive dates)
1988-1990

13 SUPPLEMENTARY NOTES

14 ABSTRACT (200 words or less)

This study includes a systematic investigation of the bond strength of cementitious borehole plugs in welded tuff. Analytical and numerical analysis of borehole plug-rock stress transfer mechanics is performed. The interface strength and deformation are studied as a function of Young's modulus ratio of plug and rock, plug length and rock cylinder outside-to-inside radius ratio. The tensile stresses in and near an axially loaded plug are analyzed. The frictional interface strength of an axially loaded borehole plug, the effect of axial stress and lateral external stress, and thermal effects are also analyzed. Implications for plug design are discussed. The main conclusion is a strong recommendation to design friction plugs in shafts, drifts, tunnels or boreholes with a minimum length to diameter ratio of four. Such a geometrical design will reduce tensile stresses in the plug and in the host rock to a level which should minimize the risk of long-term deterioration caused by excessive tensile stresses.

Push-out tests have been used to determine the bond strength by applying an axial load to cement plugs emplaced in boreholes in welded tuff cylinders. A total of 130 push-out tests have been performed as a function of borehole size, plug length, temperature, and degree of saturation of the host tuff. The use of four different borehole radii enables evaluation of size effects. A well-defined exponential strength decrease with increasing plug diameter results. While these extrapolated strengths can be used for the design of large diameter plugs, e.g. in shafts or drifts, it would be desirable to confirm the extrapolations by tests on larger plugs.

15a KEY WORDS AND DOCUMENT ANALYSIS

Borehole sealing
Shaft sealing
Repository sealing
Borehole plugging
Apache Leap tuff

15b DESCRIPTORS

Underground dams
Seal strength
Plug strength
Cement
Tuff
Push-out testing

16 AVAILABILITY STATEMENT
Unlimited

17 SECURITY CLASSIFICATION (This report)
Unclassified

18 NUMBER OF PAGES

19 SECURITY CLASSIFICATION (This page)
Unclassified

20 PRICE
$